Geomechanical characterization of the CO2CRC Otway Project site, Australia

Dissertation

Vom Fachbereich Material- und Geowissenschaften
der Technischen Universität Darmstadt
zur Erlangung des akademischen Grades
Doktor der Naturwissenschaften (Dr. rer. nat.)
Genehmigte Dissertation

TECHNISCHE UNIVERSITÄT DARMSTADT

on

M.Sc. Chiara Maria Aruffo
geboren am. 28. Juni 1986 in Castel San Pietro Terme (Bo), Italy

Referent: Prof. Dr. Andreas Henk
Korreferent: Prof. Dr. Charlotte Krawczyk

Tag der Einreichung: 01 April 2015
Tag der Disputation: 13 July 2015

Darmstadt, July 2015
D 17

Vorsitzender der Prüfungskommission:		Technische Universität Darmstadt
Referent:	Prof. Dr. Andreas Henk	Technische Universität Darmstadt
Korreferent:	Prof. Dr. Charlotte Krawczyk	LIAG Hannover
Prüfer	Prof. Dr. Christoph Schüth	Technische Universität Darmstadt
Prüfer	Prof. Dr. Matthias Hinderer	Technische Universität Darmstadt

Abstract

Storage of CO_2 in the subsurface is one of the options available to lower the amount of CO_2 in the atmosphere, a general priority in mitigating effects of climate change. In this frame, a number of challenges need to be solved to ensure a safe storage containment by avoiding wellbore failure, fault reactivation, leakage of CO_2 along faults, caprock failure and microseismicity. Risks related to those issues can be successfully addressed with an accurate geomechanical characterization prior to injection. The effectiveness of geomechanical methods has been recognized in production of hydrocarbon reservoirs as well as in fluid storage (i.e. waste water and gas).

The case study chosen for this thesis is the CO2CRC Otway Project, launched in 2005 in the state of Victoria (Australia) as first pilot study for CO_2 storage in the southern hemisphere. As international partner of CO2CRC, the PROTECT Research Group was established in 2011 to develop a seismo-mechanical workflow able to predict deformation at sub-seismic level. The work presented in this thesis contributes to the workflow by providing a geomechanical characterization of the storage site. More specifically, finite element forward modelling is used to obtain a description of the 3D state of stress.

A joint effort with partners from PROTECT Research group led to the setup of a geological model based on a detailed 3D seismic interpretation. In particular, it provides the geometry information needed to the buildup of the geomechanical model at the core of this thesis. The inclusion of all lithostratigraphic layers up to the ground surface results in a strengthened reliability of the geomechanical model that can be potentially implemented as a reference in future well planning. Wells logs and a literature review provide rock and fault properties to populate the model, regional stress data are used as boundary conditions for the model and stress measurements from the wells allow to calibrate the model.

In situ local stress is analyzed following two different approaches, both using finite element techniques, to provide a comprehensive knowledge of effective and total stresses in the injection area. The response of the in situ stress field to changes in pore pressure due to CO_2 injection in the reservoir is studied through a one-way flow and geomechanics coupled simulation. The computed effective stresses acting on the reservoir allow to assess caprock integrity and potential fault reactivation in relation to CO_2 injection operations. Vertical rock displacements are also derived from the modelling to understand compaction of the reservoir and subsidence/uplift at ground surface level during the initial gas production and the subsequent CO_2 injection phase. In addition, a parametric study estimates the pore pressure needed to cause fault reactivation for both numerical and analytical models, along with the corresponding maximum allowable daily injection rate. The second approach consists of a structural analysis describing the tectonic present-day in situ stress distribution at reservoir scale. Resolution of the model allows to identify perturbation in stress

magnitudes within the reservoir level, related mainly to the presence of faults. Stability of faults is analyzed from a structural point of view, estimating the slip and dilation tendency of each fault under the computed stress conditions. Identification and modelling of the major tectonic stages allows the reconstruction of the geomechanical evolution of the injection site.

Evidences from the implemented models show some discrepancies in the outcome. Possible sources of divergence between numerical and analytical approach are explored, as well as factors affecting stress modelling using the two different geomechanical simulators. Combination of results aims to analyze and understand the occurrence of local stress rotations and its causes. Finally, the temporal evolution of the fracture network is studied by correlating observed fractures and modelled states of stress.

Finally, a comparison with previous geomechanical models for the CO2CRC Otway Project is conducted in terms of critical pore pressure for fault reactivation. Increasing availability of data used to constrain the models is reflected in an enhanced level of accuracy. However, those models are purely analytical and do not consider variability in rock properties, topographic effects, presence of faults and interaction between adjacent cells. The degree of complexity handled by the numerical model presented in this thesis contributes to increase the confidence on risk analysis results.

To summarize, this thesis presents the first 3D geomechanical model of the CO2CRC Otway project, with the aim to provide a comprehensive geomechanical characterization of the storage site. Description of the 3D state of state and fault stability analysis, taking into account both total and effective stresses, have particular relevance for storage performance and future well planning. Besides this specific case study, the proposed workflow can be potentially applied to other injection sites for pre-injection geomechanical assessment. More generally, the same methodology could be followed for understanding state of stress and faults behavior in hydrocarbon and geothermal reservoirs.

Zusammenfassung

Die Speicherung von CO_2 im Untergrund ist eine der möglichen Optionen, um die Menge an CO_2 in der Atmosphäre zu verringern und so den Effekt des Klimawandels zu mildern. In diesem Zusammenhang müssen eine Vielzahl von Herausforderungen bewältigt werden, um durch die Vermeidung von Bohrlochversagen, Störungsreaktivierung, CO_2 Leckage entlang von Störungen, Versagen des Deckgesteins und Mikroseismizität einen sicheren Speicherort gewährleisten zu können. Mit einer detaillierten geomechanischen Charakterisierung des Speichers können bereits vor der Injektion entsprechende Szenarien untersucht und Risiken vermieden werden. Das generelle Potential von geomechanischen Lagerstättenmodellen für solche Untersuchungen ist aus der Produktion von Kohlenwasserstofflagerstätten bekannt und wird auch allgemein bei der Speicherung von Fluiden (z.B. Abwasser und Gas) im Untergrund eingesetzt.

Als Fallstudie für diese Arbeit wurde das CO2CRC Otway Projekt ausgewählt, die in 2005 im Staat Victoria (Australien) gestartete erste Pilotstudie zur CO_2 Speicherung in der südlichen Hemisphäre. Die PROTECT Forschungsgruppe, als internationaler Partner von CO2CRC, wurde 2011 ins Leben gerufen, um einen seismo-mechanischen Arbeitsablauf zu entwickeln, mit dem Deformationen auf subseismischer Ebene prognostiziert werden können. Diese Dissertation trägt dabei die geomechanische Charakterisierung des Speicherstandorts zu dem generellen Arbeitsablauf bei. Dazu wird mittels Finiter Elemente Methoden der dreidimensionale Spannungszustand im CO_2 Speicher und der Überlagerung berechnet.

Basierend auf einer detaillierten Interpretation von 3D Seismik wurde unter Zusammenarbeit mit Partnern aus der PROTECT Forschungsgruppe ein geologisches Modell erstellt. Dieses liefert die Untergrundgeometrie als eine wichtige Eingabegröße für das geomechanische Modell. Durch die Einbeziehung von Störungen und von mehreren lithostratigraphischen Horizonten bis zur Erdoberfläche kann das geomechanische Modell zukünftig auch für Bohrpfadplanungen genutzt werden. Mechanische Gesteins- und Störungseigenschaften wurden aus Bohrlochmessungen und Literaturquellen kompiliert. Als Randbedingungen für die numerische Simulation wurden regionale Spannungsdaten genutzt. Zur Kalibrierung des Modells wurden lokale Spannungsmessungen aus Bohrlöchern des Speicherprojektes verwandt.

Der in situ Spannungszustand wurde mittels zweier Ansätze analysiert, die beide die Finite Elemente Methode nutzen und umfangreiche Informationen zur effektiven und zur Gesamtspannung im Umfeld des CO_2 Speichers liefern. Die Reaktion des lokalen Spannungsfeldes auf Veränderungen im Porendruck durch CO_2 Injektion im Reservoir wurde durch gekoppelte Strömungs- und Geomechaniksimulationen untersucht. Die berechnete Effektivspannung im Reservoir erlaubt eine Beurteilung der Deckgesteinsintegrität und der potentielle Reaktivierung von Störungen in Bezug auf die CO_2 Injektionen. Ferner wurden die Vertikalverschiebungen in Hinblick auf eine

Kompaktion des Reservoirs und eine Absenkung/Hebung der Erdoberfläche in der initialen Erdgasförder- bzw. der anschließenden CO_2 Injektionsphase untersucht. Zusätzlich wurde mit einer Parameterstudie der Porendruck ermittelt, der nötig ist, um die Störungen sowohl im numerischen als auch im analytischen Modell zu reaktiveren. Damit konnten auch die maximalen täglichen Injektionsraten für einen sicheren Speicherbetrieb bestimmt werden. Der zweite Ansatz besteht aus einer strukturellen Analyse zur Beschreibung der heutigen Spannungsverteilung im Reservoirmaßstab. Die Modellauflösung erlaubt dabei auch die Erkennung von lokalen Spannungsperturbationen im Reservoir, die wesentlich auf die Wirkung von Störungen zurückgehen. Störungsstabilitäten werden unter strukturellen Gesichtspunkten analysiert und für jede Störung die Bewegungstendenz („slip and dilation tendency“) bewertet. Durch die Identifizierung und Modellierung von wichtigen tektonischen Phasen konnte die geodynamische Entwicklung des Arbeitsgebietes rekonstruiert werden.

Die verschiedenen Modellierungsansätze zeigen teilweise Diskrepanzen in den Ergebnissen. Mögliche Quellen für die Unterschiede zwischen numerischem und analytischem Ansatz werden untersucht, insbesondere die Faktoren, die die Spannungsmodellierung mit den zwei verschiedenen geomechanischen Simulatoren beeinflussen. Die Kombination der Ergebnisse zielt darauf ab, das Auftreten und die Ursache von lokalen Spannungsrotationen zu analysieren und zu verstehen. Abschließend wird die zeitliche Entwicklung des Kluftnetzwerks durch Korrelation der beobachteten Klüfte mit modellierten Spannungszuständen untersucht.

Zum Abschluss wird ein Vergleich mit früheren geomechanischen Modellen für das Otway Projekt in Bezug auf den kritischen Porendruck für die Störungsreaktivierung durchgeführt. Durch neue Daten konnten die Modellunsicherheiten weiter eingeschränkt werden, so dass ein erhöhter Grad an Genauigkeit erzielt werden konnte. Allerdings waren diese Modelle ausschließlich analytischer Natur und bezogen keine Variabilität der Gesteinsparameter, topographische Effekte, die Anwesenheit von Störungen und Interaktion zwischen benachbarten Zellen mit ein. Diese Aspekte beinhalten die in dieser Dissertation erarbeiteten komplexen numerischen Modelle, so dass aus den Simulationsergebnissen zuverlässigere Risikoanalysen abgeleitet werden können.

Zusammenfassend behandelt diese Dissertation das erste 3D geomechanische Modell des CO2CRC Otway Projektes und ermöglicht somit eine umfassende geomechanische Charakterisierung dieses CO_2 Speicherstandortes. Diese Beschreibung des 3D Spannungszustandes unter Berücksichtigung von Effektiv- und Gesamtspannungen und die Analyse der Störungsstabilität sind von besonderer Bedeutung für den sicheren Speicherbetrieb und zukünftige Bohrpfadplannungen. Über die konkrete Fallstudie hinaus kann der hier angewandte Arbeitsablauf auch für die geomechanische Beurteilung anderer Speicherstandorte verwandt werden. Die Methodik ist dabei nicht auf CO_2 Speicher beschränkt, sondern kann allgemein zum Verständnis von Spannungszuständen in Kohlenwasserstoff-Lagerstätten und geothermischen Reservoiren eingesetzt werden.

Acknowledgment

The work of this study was accomplished in the framework of PROTECT Research Group funded through the Geotechnologien Program (Grant 03G0797) of the German Ministry for Education and Research (BMBF). Support from the entire PROTECT team was essential and much appreciated. I thank especially Prof. Charlotte Krawczyk (also for the co-supervision of this thesis), Dave Tanner, Jennifer Ziesch and Thies Beilecke. Furthermore, I would like to acknowledge the CO2CRC consortium for sponsoring the project. In particular, I would like to thank Eric Tenthorey and Jonathan Ennis-Kings for the constructive scientific discussions, for their hospitality in Australia and for giving me the opportunity to visit CO2CRC injection facilities.

I thank Prof. Dr. Andreas Henk for giving me the possibility to continue my studies in Germany and for the great opportunity to participate in this project. I am very thankful for his support in these three years and for his guidance. He gave me the opportunity to learn more about geomechanics and encouraged me to present my work and share ideas at conferences and workshops.

Moreover, I am grateful for the time I spent with the Applied Geomechanics team of Schlumberger in Bracknell (UK), in particular I would like to thank Nick Koutsabeloulis for this incredible opportunity. A special acknowledgment goes Jorg Herwanger for sharing his knowledge with me and for his invaluable support.

I also would like to thank the entire staff of the Institute of Applied Geosciences at TU Darmstadt, in particular the engineering geology group: Christoph Wagner, Dennis Laux, Christian Heinz, Bastian Weber, Karsten Fischer, Reimund Rosmann and Stefanie Kollmann.

I want to thank all the people I met in Darmstadt, they made my life much easier and I had great fun with them.

E infine, grazie alla mia grande famiglia e in particolare mamma, papà e Valeria: mi avete supportato e sopportato fino a qui. Il lato positivo è che le feste di laurea non finiscono mai! Grazie a Luigi per i kilometri percorsi in questi tre anni e perché nonostante la distanza c'è sempre stato e mi ha sempre sostenuto. Un pensiero va anche a tutte le persone che ho lasciato in Italia, ma che sono rimaste presenti nella mia vita.

Table of contents

List of Figures

List of Tabs

List of Abbreviations

BHP	Bottom-hole pressure
C_2H_6	Ethane
C_3H_8	Propane
C_4H_{10}	Butane
CO	Carbon Monoxide
CO_2	Carbon Dioxide
CO2CRC	Cooperative Research Centre for Greenhouse Gas Technologies
CPP	Critical pore pressure
DHSR	Differential horizontal stress ratio
DITF	Drilling-induced tensile fracture
DTCO	Compressional wave slowness log
DTSM	Shear waves slowness log
FAST	Fault Analysis Seal Technology
FCP	Fracture Closure Pressure
FFP	Fracture Propagation Pressure
FMI™	Formation MicroImager
GAL	Geocellular algorithm
H_2S	Hydrogen sulfide
InSAR	Interferometric synthetic aperture radar
LNG	Liquified Natural Gas
LOP	Leak-off point
LOT	Leak-off test
MDT	Modular Dynamic Tester
N_2	Molecular nitrogen
NF	Normal faulting regime
PROTECT	PRediction Of deformation To Ensure Carbon Traps
RF	Reverse faulting regime
RHOZ	Bulk density log

SI	International system of units
SS	Strike-slip faulting regime
TDITF	Transverse drilling-induce tensile fracture
THP	Tubing head pressure
TVDss	True vertical depth, subsea
TWT	Two-way traveltime

List of Symbols

A	Reservoir Stress Path
C	Cohesion
c	Lithology-dependent coefficient (decompaction)
cos	Cosinus
d	Diameter
E	Young's modulus
G	Shear modulus
g	Gravitational acceleration
k	Permeability
k_c	Compaction factor (depth conversion)
k_{rCO2}	Relative permeability carbon dioxide
k_{rw}	Relative permeability water
K	Bulk modulus
K_b	Drained bulk modulus
K_g	Grains bulk modulus
l	Length
P	Pressure
P_b	Breakdown pressure
P_p	Pore pressure
P_{vm}	Pore volume multiplier
q	Flux
S	Total stress
S_1, S_2, S_3	Total principal stresses
S_d	Total differential stress
S_{dev}	Total deviatoric stress
S_{HMax}	Total maximum horizontal stress
S_{hmin}	Total minimum horizontal stress
S_{mean}	Total mean stress

S_n	Total normal stress
S_s	Total shear stress
S_V	Total vertical stress
S_{CO2}	Carbone dioxide saturation
sin	Sinus
T	Thickness
T_0	Tensile strength
T_d	Dilation tendency
T_m	transmissibility multiplier
T_s	Slip tendency
tan	Tangent
UCS	Unconfined compressive strength
V	Volume
V_0	Intercept on velocity axis (depth-conversion)
V_i	Interval velocity
v_p	Compressional wave velocity
v_s	Shear wave velocity
Y	Tectonic subsidence
Z	Depth
α	Biot coefficient
δ_{ij}	Kronecker's delta
ε	Strain
ε_1, ε_2, ε_3	Principal strains
η	Viscosity
λ	Lamé constant
μ	Coefficient of friction (faults)
μ_i	Coefficient of internal friction (intact rock)
ν	Poisson Ratio
ρ	Density
ρ_{gr}	Grains density

ρ_m	Mantle density
ρ_w	Water density
σ	Effective stress
$\sigma_1, \sigma_2, \sigma_3$	Effective principal stresses
σ_{HMax}	Effective maximum horizontal stress
σ_{hmin}	Effective minimum horizontal stress
σ_V	Effective vertical stress
σ_n	Effective normal stress
ϕ	Porosity
ϕ_0	Surface porosity
ϕ_*	Decompacted porosity
φ	Angle of internal friction

1 Introduction

1.1 Motivation and objective

In the latest years solving the carbon and climate problem has become an issue of public importance (Pacala and Socolow 2004). Storage of CO_2 in the subsurface has been proven to be one of the options available to mitigate the amount of CO_2 in the atmosphere. Research in this direction has been therefore developing constantly over time and a number of CO_2 storage sites have been set up around the world. Geomechanical characterization of storage sites has a tremendous importance in order to ensure safety during operations and to prevent leakage of CO_2 upwards. Indeed geomechanical modeling provides a tool to understand the state of stress in the reservoir and in the surrounding area and the changes that can occur in response to CO_2 sequestration. Fault stability and potential fault reactivation under reservoir pressure and temperature changes can be also assessed through geomechanical studies. However complexity of reservoir geometries, presence of faults and fractures, response of the in situ stress to the changes in pressure can only be addressed effectively through numerical models.

Main objective of this thesis is to provide a comprehensive geomechanical characterization of the CO2CRC Otway Site, the Naylor Field, a pilot site for CO_2 injection in South Eastern Australia. This work is part of a joint project between research institutes, universities and companies in Germany that under the name PROTECT (PRediction Of deformation To Ensure Carbon Traps) collaborate with the Australian consortium responsible for the project. Fault reactivation risk and leakage of CO_2 represent the principal focus of this work. A brief explanation of the outline of this thesis is provided below to help the reader following the line of the reasoning behind this research.

1.2 Study outline

An introductory part gives a general framework and motivation for this work. Firstly, importance of geomechanics in CO_2 storage and case studies from all over the world (Chap. 1.3) are described with the aim to understand how geomechanics can help in ensure a safe storage. Afterwards, from a general overview, the focus is then shifted directly to the CO2CRC Otway site (Chap. 3.2). A review of the state-of-the-art of the geomechanical analysis and modelling for the Naylor Field (Chap. 3.3) allows to identify potential improvements that motivates the research carried out in this thesis.

The following three chapters outline the basic information required for the subsequent modelling work. Principle of rock mechanics (Chap. 2) are summarized and presented to give a theoretical reference to the practical geomechanical modelling. Regional geology of the Otway Basin (Chap. 4) is then described, giving a background to the geological and structural model of the storage site. A particular emphasis is given to the geodynamic evolution that represents the starting point to retrace the generation of fractures network through paleostresses modelling. Finally,

the present-day state of stress of the Otway Basin (Chap. 5) is reported, and it is then used as boundary condition and calibration reference for the geomechanical models.

Subsequently, the two different modelling approaches, both using Finite Element (FE) techniques, are presented, to provide a comprehensive geomechanical analysis of the injection area. A Petrel® geological model (Chap. 6) provides the geometry for both models, while the rest of input data available are partly directly derived from well logs, partly gathered from a literature review.

Firstly, a one-way flow and geomechanics coupled simulation (Chap. 7) is described to estimate the response of the in situ stress field to changes in pore pressure due to CO_2 injection in the reservoir. History matching technique is applied to build a fluid model to compute those changes in pressure that are also the input for the geomechanical simulation. The resulting coupled geomechanical model provides information on the effective stresses acting on the reservoir throughout all the operation time. Aim of this study is to assess caprock integrity and potential fault reactivation in relation to CO_2 injection operations. In addition to that, a parametric study estimates the pore pressure needed to cause fault reactivation for both numerical and analytical models (Chap. 8). The second methodology outlined is a structural analysis to describe the tectonic in situ stress distribution at reservoir scale (Chap. 9). Present-day state of stress is computed with a particular emphasis on geomechanical behaviour of faults under this stress condition. Stability of faults is analyzed from a structural point of view, estimating the slip and dilation tendency of each fault under the computed stress conditions. Moreover, paleostress distribution of the in situ stress field was simulated to characterize the geomechanical evolution of the site through time (Chap. 10). A schematic workflow valid for both modelling approaches is sketched in Fig. 1.1.

The discussion section (Chap. 11) offers further explanation of the results obtained from the two geomechanical modelling approaches. In particular, reasons behind the difference in fault reactivation analysis for analytical and numerical models are researched, as wells as difference in stress computed following the two geomechanical approaches. Evidence of stress rotation arisen from the steady-state and paleostress models are investigate and a quantitative parameter is proposed to explain their occurrence. Furthermore, a description of the temporal evolution of the fracture network is attempted, based on paleostress modelling.

A conclusion chapter (Chap. 12) summarizes the research carried out in this thesis, and some perspectives (Chap. 13) are depicted for further improvement of this geomechanical workflow.

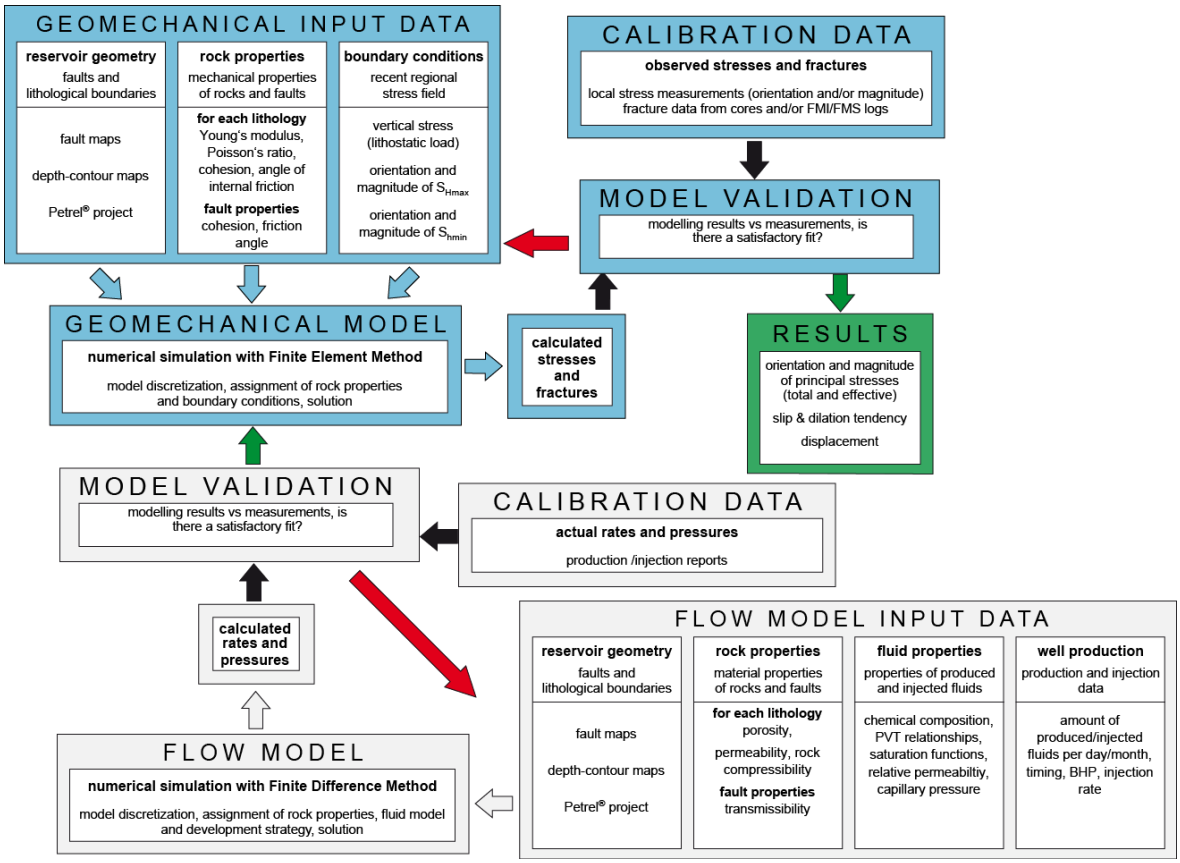

Fig. 1.1: Schematic workflow for geomechanical modelling for one-way coupled simulation and steady-state modelling. For a one-way coupled simulation all the steps need to be followed, whereas a steady-state model requires only the upper part of the sketch (flow model is not included). Modified after Henk (2010).

1.3 Importance of geomechanics for CO_2 storage

Carbon capture and storage (CCS) is promoted as a technology with the potential to achieve significant reduction of anthropogenic greenhouse emissions (Verdon et al. 2013). However, development of CO_2 storage relies mainly on societal acceptability, that from a scientific point of view requires ensuring a safe storage containment if CO_2 injection in the subsurface is planned. Strongest criticism of CCS derives from considerations of geomechanical response to CO_2 injection (Zoback and Gorelick 2012). Indeed, increase of fluid pressure, temperature variation and chemical reaction between fluid and rock affect the state of stress inside the reservoir and its surrounding (Bérard et al. 2007). Stress acting on the Earth's crust controls performance of subsurface operation, therefore an understanding and quantification of stresses and deformation is a crucial issue to ensure safety of geosequestration.

Magnitude and orientation of the present-day local stress field are greatly affected by the presence of discontinuities (i.e. faults and fracture network) resulting in stress perturbations (Zoback 2010). In addition to that, possible changes in effective stress may derived by the influence of changes in pressure related to CO_2 injection (Santarelli et al. 1998). As well as directly changing the effective stress acting on reservoir rocks, inflation of the reservoir could lead to changes in applied stress both

in and around the reservoir (Verdon et al. 2013). The impact of deformation and changes in stress may lead to failure of intact rock (caprock failure) and reactivation of pre-existing faults, with leakage of fluids as a direct consequence, as well as resulting in surface deformation. Related to that, the potential injection-induced microseismicity may impact the long-term integrity of a CO_2 repository (Rutqvist 2012, Zoback and Gorelick 2012). In fact, if CO_2 storage is planned, one of the main precautions is to avoid injection in potentially active faults. Geomechanical studies allow to establish whether a fault is potentially active or not, depending on the orientation of the fault in relation to the current regional stress field (Zoback 2010). Finally, well integrity also depends on the local stress field and its orientation with respect to the drill path (Zoback 2010) and wellbore failure could jeopardize the safety of operations. Bedding-parallel slip in layers above the reservoir or expansion of the reservoir against the overburden, could cause shearing of the wellbore, presenting also a significant leakage risk (Verdon et al. 2013). For all the reasons stated above, a geomechanical assessment of the storage site is necessary in order to properly manage containment performance and leakage-incurred risks. In the latest years a number of pre-injection and monitoring studies have been published for various storage sites around the word. Techniques used often comprise coupled-simulations to match the injection data and microseismic array to monitor CO_2 movements. Some examples are reported below, with a particular focus on methodology used to model the geomechanics of CO_2 storage. A more detailed analysis of geomechanical analysis in the Otway Basin is reported on Chapter 3.3.

Sleipner Project (North Sea, Norway) was the world's first commercial CO_2 storage project, active since 1996. CO_2 is removed from the produced natural gas in order to meet required export specifications and then re-injected into a sand saline aquifer. By late 2011, around 13 Mt had been injected, at a rate of ~1Mt/year (Verdon et al. 2013). Pressure increase in the reservoir due to CO_2 injection was assessed with the used of time-lapse seismic data, on the principle that an increase in pressure reduces seismic velocities and creates a travel time increase through the reservoir. Although no direct measurement of deformation have been made, time-lapse seismic data estimates a small pressure change, that is unlikely to cause significant geomechanical deformation (Chadwick et al. 2004).

The Snøvhit gas field (Barents Sea, Norway) was discovered in the 1980s. The produced gas has a content of 5-8% of CO_2 that needs to be reduced before processing the gas into liquefied natural gas (LNG). Re-injection of the separated CO_2 started in 2008 at a rate of 0.7 Mt per year with the aim to reach a permanent storage of 23 Mt, however in 2010 Statoil announced that storage capacity was lower than expected. A fully coupled hydromechanical simulator GEOCENTRIC was used to understand the geomechanical response of the system to CO_2 injection, with a particular focus on understanding role of the bounding faults and reasons for a lower storage capacity. Results showed that faults can be considered stable in the current stress field and a low storage capacity is due to injection in a compartmentalized sector of the reservoir (Chiaramonte et al. 2011). Furthermore, there is a slight

possibility of interference between CO_2 storage and the natural gas asset that may lead to a relocation of CO_2 injector in the future. For this reason a monitoring program is in place, using time-lapse seismic and reservoir pressure monitoring (Hansen et al. 2011).

At Weyburn oilfield (Canada), CO_2 was first injected in 2000 with the commercial purpose of enhanced oil recovery. However, a significant research component was added to the project with aim to test and examine the abilities of various monitoring techniques to image CO_2 in the subsurface. The expectation is to permanently store 30 Mt of CO_2 by the end of field operation (Verdon et al. 2013). The principal method chosen to monitor geomechanical deformation was to use a microseismic array, however they covered only a small portion of the oilfield. A total of ~100 events were recorded between 2003 and 2010, and after shut-in of the injection well, a further 92 events were recorded. A numerical simulation of the deformation at Weyburn helped to interpret the occurrence of those events, finding that potential for seismicity was not increased by injection. In this case, the geomechanical model has the precise objective to validate microseismic measurements. The methodology chosen was a one-way coupled simulation performed on a 3D synthetic model, using MORE™ (Roxar) for the fluid flow simulation and ELFEN™ (Rockfield) for the geomechanical model (Verdon et al. 2011).

In the vicinity of Otway Basin, the Iona gas storage facility has been subjected to geomechanical analyses (Tenthorey et al. 2013). The Iona field serves as methane storage facility for the state of Victoria (Australia), and experiences every year periods of withdrawal and injection related to gas requirement. Main output for the assessment is to determine the reservoir stress path and how it could affect stability of bounding faults, information about the caprock integrity and the magnitude of possible ground movement during peak periods of injection and withdrawal. A methodology similar to the one presented in this thesis was used to perform a 3D one-way coupled simulation, based on the actual geometry of the reservoir. A dynamic flow model was carried out using ECLIPSE™ simulator and the results were coupled with VISAGE™ to obtain a geomechanical model of the storage site.

The In Salah Gas Project in Algeria is the biggest industrial scale CO_2 storage project (Rutqvist et al. 2010). Natural gas produced directly in the area is then re-injected for geological storage. From its starting in 2004, 3.85 Mt have been stored up to 2013 (Verdon et al. 2013). The main issue encountered in the operations is related to ground deformation on the orders of centimeters, with a rate of uplift approximately 5 mm per year. A preliminary and synthetic geomechanical analysis using TOUGH2-FLAC3D numerical simulator, indicated that surface deformation would be feasible (Rutqvist and Tsang 2002). As a result, it was decided to use InSAR (Interferometric synthetic aperture radar) data (Vasco et al. 2008) to detect ground surface deformation related to CO_2 injection. The observed uplift could be correlated with each injection well, with uplift affecting an area of several km in diameter centered around each injection well. To further characterize the deformation occurring at well locations, a microseismic monitoring array was installed in 2009. Results indicate

that microseismic data are consistent with the inferences about geomechanical deformation drawn from InSAR and seismic data (Verdon et al. 2013). Furthermore, a new 3D synthetic coupled-simulation was performed, again using TOUGH2-FLAC3D simulator, to determine the cause and mechanism of the observed uplift (Rutqvist et al. 2010). Results indicate that the uplift depends on magnitude of pressure change, injection volume and elastic properties of the reservoir.

2 Rock Mechanics

Rock mechanics was first defined by the Committee on Rock Mechanics of the Geological Society of America as „the theoretical and applied science of mechanical behavior of rock to the force fields of its physical environment“ (Judd 1964). Principles of rock mechanics are able to explain and describe properties and behavior of rock masses due to changes in stress or other conditions (Jaeger et al. 2007). In particular, the discipline of geomechanics applies solid and fluid mechanics, engineering, geology and physics to determine how rocks and the fluids they contain respond to force or to changes in stress, pressure and temperature caused by drilling, completion and production (Cook et al. 2007). In oil and gas industry it has common applications to wellbore stability prediction and drilling optimization, sand production and completion design, hydraulic fracturing and reservoir stimulation design (Fjaer et al. 2008). This thesis focuses on aspects of rock mechanics such as state of stress of intact rock and faults, failure of intact rock and potential fault reactivation, perturbation to the total stress field due to presence of faults, variation of effective stress due to production/injection of CO_2.

This chapter has the aim to introduce rock mechanics principles necessary to understand the theory behind the geomechanical study presented. Basic stress principles are explained introducing the concept of stress tensor and principal stress. Components of stress are defined, explaining differences between normal and shear stresses and mean and deviatoric stresses. Subsequently the importance of principal stress in the Earth's crust is addressed in relation with tectonic stress regimes. Role of pore pressure is illustrated to remark the difference between total stress and effective stress, being the latter the most used in geomechanical studies. Finally deformation and failure are described, starting with elasticity and plasticity theories to end with a description of shear and tensile failure.

2.1 Stress principles

Concept of stress was first introduced in 1863 by the French civil engineer and mathematician Cauchy, and it is defined as a force acting over a given area and is measured in SI units in megapascal (MPa) (Zoback 2010). Stress principles will be discussed below in order to have an understanding of the basis of rock mechanics.

2.1.1 Stress components

Stress generally varies with the orientation of the surface on which it is applied, therefore it is conveniently represented as a second-order tensor. Nine components of this tensor are able to describe stresses acting on a homogeneous, isotropic body at depth if a Cartesian coordinate system is considered (Eq. 2-1):

$$S = \begin{bmatrix} S_{xx} & S_{xy} & S_{xz} \\ S_{yx} & S_{yy} & S_{yz} \\ S_{zx} & S_{zy} & S_{zz} \end{bmatrix} \qquad (Eq.\ 2\text{-}1)$$

Where the first subscript of the individual stress components refers to the face of the unit cube upon which the stress component acts, the second to the direction on which the force is acting. Stress components acting perpendicular to the faces of the cube are defines as normal components (S_{xx}, S_{yy}, S_{zz}), while stress components acting parallel to the faces of the cube are defined as shear components (S_{xy}, S_{xz}, S_{yx}, S_{yz}, S_{zx}, S_{zy}) (Fig. 2.1):

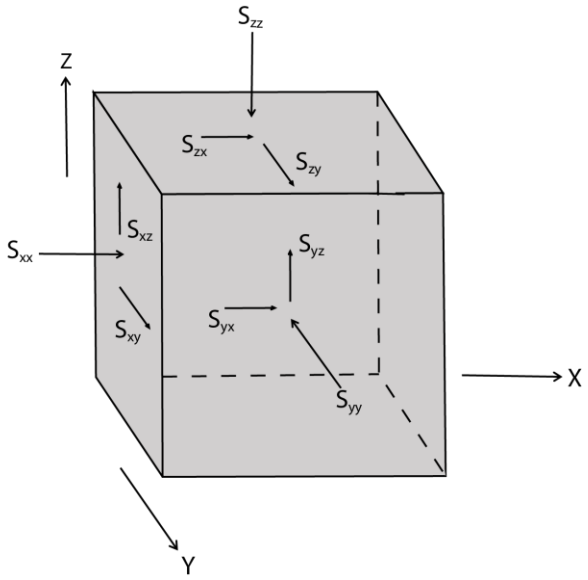

Fig. 2.1: Definition of stress tensor for a 3D unit cube oriented in a Cartesian coordinate system with x,y and z axes (Zoback 2010).

At equilibrium conditions, stresses acting parallel to the faces of the cube (i.e. shear stresses) must be equal, otherwise the cube would rotate around them. Therefore (Eq. 2-2, 2-3, 2-4):

$$S_{xy} = S_{yx} \qquad (Eq.\ 2\text{-}2)$$

$$S_{xz} = S_{zx} \qquad (Eq.\ 2\text{-}3)$$

$$S_{yz} = S_{zy} \qquad (Eq.\ 2\text{-}4)$$

The state of stress acting in a point can be then defined with three normal components (S_{xx}, S_{yy}, S_{zz}) and three shear components.

Stress acting at depth can also be defined in terms of principal stress (i.e. those acting in the principal coordinate system). The principal coordinate system is the one where shear stresses have zero value and the stress field is fully described by three principal stresses, acting in the direction of the principal axes (Zoback 2010).

The stress tensor for this particular case has the form of (Eq. 2-5):

$$S = \begin{bmatrix} S_1 & 0 & 0 \\ 0 & S_2 & 0 \\ 0 & 0 & S_3 \end{bmatrix} \qquad (Eq.\ 2\text{-}5)$$

These three principal stresses are perpendicular to each other and S_1 is the maximum principal stress, S_2 is the intermediate principal stress and S_3 is the minimum principal stress. They can be visualized in a 3D unit cube as (Fig. 2.2):

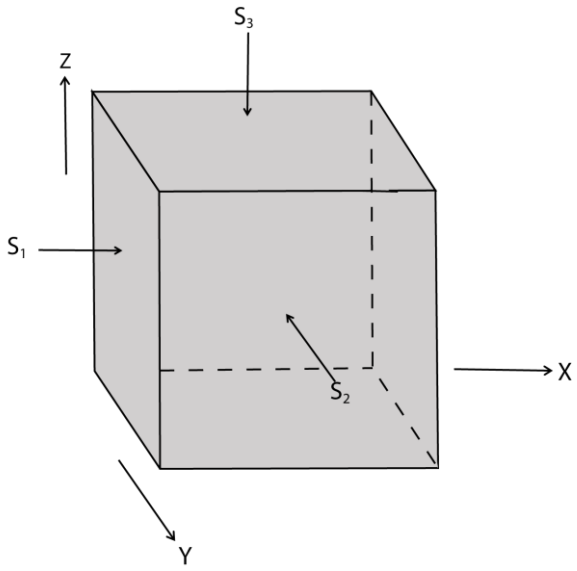

Fig. 2.2: Definition of principal stress components acting on a 3D unit cube oriented in the principal coordinate system (Zoback 2010).

2.1.2 Normal stress and shear stress

In the frame of principal stress system, it is possible to derive some useful relationships, for example between normal and shear stresses. If we consider a fracture plane developed in a sample during a triaxial compression test, we can determine the normal and shear stresses acting on that fracture plane. The principal stresses acting on the sample are *S1* (maximum stress) and *S3* (minimum stress), since the values of *S2* and *S3* are equal in a triaxial compression test (Van der Pluijm and Marshak 2004).

This situation is illustrated in the Fig. 2.3.

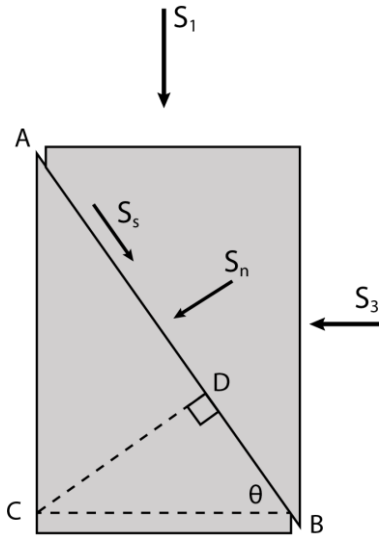

Fig. 2.3: Fracture plane AB developed in a sample under atmospheric conditions. The plane forms an angle θ with S_3. Modified after Van der Pluijm and Marshak (2004).

The fracture plane makes an angle θ with S_3, forming a trace AB of unit length 1. By using trigonometric relationships it is possible to resolve AB along AC (parallel to S_1) and along BC (parallel to S_3). Combining these relationships together with the concept of stress (force acting on a surface), equations for normal (Eq. 2-6) and shear (Eq. 2-7) stresses acting on a plane can be expressed (Van der Pluijm and Marshak 2004):

$$S_n = \frac{S_1 + S_3}{2} + \frac{S_1 - S_3}{2}\cos 2\theta \qquad (Eq.\ 2\text{-}6)$$

$$S_s = \frac{S_1 - S_3}{2}\sin 2\theta \qquad (Eq.\ 2\text{-}7)$$

From these equations it is possible to determine the planes of maximum normal and shear stresses. $\cos 2\theta$ reaches its maximum value for θ=0° (because cos0°=1), therefore plane of maximum normal stress lies at 0° with respect to S_3. On the other hand maximum values of $\sin 2\theta$ is reached for θ=45° (because sin90°=1), hence the plane of maximum normal stress forms an angle of 45° with S_3.

2.1.3 Mean stress, deviatoric stress and differential stress

For a stress applied to a body, as in the case of a rock at depth, it is possible to recognize two different components affecting the deformation of the stressed body. The first component is the mean stress, also known as hydrostatic component or hydrostatic pressure. Mean stress is defined as (Eq. 2-8) (Van der Pluijm and Marshak 2004):

$$S_{mean} = \frac{S_1 + S_2 + S_3}{3} \qquad (Eq.\ 2\text{-}8)$$

Because the magnitude of the mean stress is equal in all directions, it is an isotropic stress component. In the case of a rock at depth is commonly known as lithostatic component (Pollard and Fletcher 2005).

The second component is the deviatoric stress (Eq. 2-9), the difference between the total stresses acting on a body and the mean stress (Van der Pluijm and Marshak 2004):

$$S_{dev} = S_{tot} - S_{mean} \qquad (Eq.\ 2\text{-}9)$$

In the case of a rock at depth the deviatoric component of the stress accounts for tectonic processes, thermo-gravitational processes etc. In contrast with the mean stress is magnitude is not equal in all directions, therefore is an anisotropic component (Jaeger et al. 2007). Deviatoric stresses are many orders of magnitude less than the mean stress (lithostatic stress for rock at depth) (Van der Pluijm and Marshak 2004).

In practice, these two components of the stress influence differently the deformation of a body (Fig. 2.4). Since mean stress is isotropic and acts equally in all directions, it results in a volume change of the body (Fig. 2.4a). On the other hand, the deviatoric component of the stress changes the shape of the body due to its anisotropy (Fig. 2.4b).

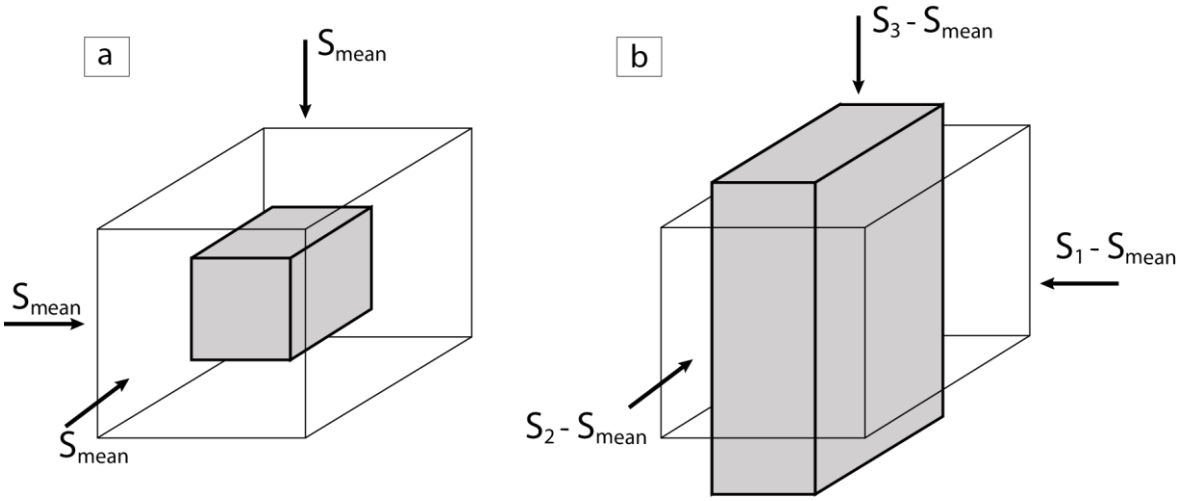

Fig. 2.4: The mean and deviatoric components of the stress. Mean stress causes volume change (a) and deviatoric stress causes shape change (b). Modified after Van der Pluijm and Marshak (2004).

Another useful measure of the part of the stress that acts to change shape is the difference between the maximum and minimum principal stress. It is normally used for situations where the value of the intermediate principal stress is less important than the two extremes. It is commonly referred to as differential stress S_d (Eq. 2-10):

$$S_d = S_1 - S_3 \qquad (Eq.\ 2\text{-}10)$$

2.1.4 Tectonic stress regimes

Concept of principal stresses is normally applied in the study of the earth's crust, considering that the earth's surface is in contact with fluids (air or water) which does not support shear stresses (Zoback 2010). In situ, one principal stress is considered to be normal to the earth's surface, and the other two principal stresses are considered to be acting in a horizontal plane. Following this assumption, state of stress at depth can be fully described if four parameters are known: magnitudes of the three principal stresses (S_V, S_{Hmax}, S_{hmin}) and the direction of the maximum horizontal stress S_{Hmax}. In-situ vertical stress mainly derives from the weight of the overburden. In turn, horizontal stresses account also for tectonic effects, thermal effects and geological structure that have to be added to the gravitational component. Furthermore, factors such as lithology, pore pressure and temperature contribute to influence their magnitude and orientation (Cook et al. 2007).

Stresses acting at depth are not constant, therefore different areas of the earth's crust are subjected to different relative variations between the three principal stresses. In the subsurface however, the three components of the stress are connected to each other, meaning that to any change of stress in one direction corresponds a change in along the two other directions (Cook et al. 2007). A classification of tectonic regimes with respect to relative stress magnitudes of the three principal stresses was first proposed by Anderson in 1951. Anderson established three faulting regimes depending on which of the three principal stresses is the vertical one (Fig. 2.5).

A normal faulting regime (Eq. 2-11) occurs if the maximum principal stress S_1 is vertical, therefore:

$$S_V > S_{Hmax} > S_{hmin} \qquad (Eq.\ 2\text{-}11)$$

In the strike-slip regime (Eq. 2-12) the vertical stress is the intermediate principal stress S_2, and then:

$$S_{Hmax} > S_V > S_{hmin} \qquad (Eq.\ 2\text{-}12)$$

In a reverse faulting regime (Eq. 2-13) the vertical stress corresponds to the least principal stress S_3:

$$S_{Hmax} > S_{hmin} > S_V \qquad (Eq.\ 2\text{-}13)$$

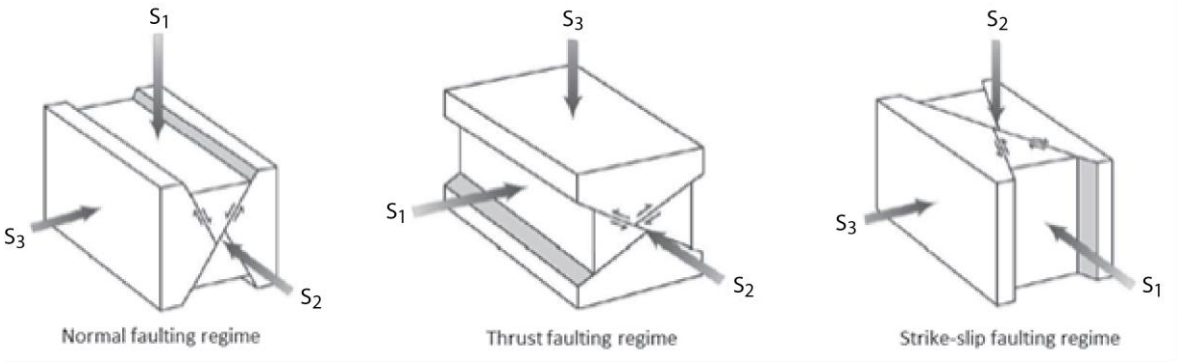

Fig. 2.5: Relationships between the orientation of the principal stress and tectonic regimes (Van der Pluijm and Marshak 2004).

In practice it is observed that at shallows depth the minimum principal stress S_3 is the vertical stress (Pollard and Fletcher 2005), that is because vertical stress is depth dependent, therefore its value increases at greater depth. It can be expressed as follows (Eq. 2-14):

$$S_v = g \int_0^z \rho(z)\, dz \qquad (Eq.\ 2\text{-}14)$$

where ρ is density at depth z, g is the acceleration due to gravity.

2.1.5 Total stress and effective stress

In structural and geomechanical analysis two different types of stress are taken under consideration. The stress externally applied to a mass of rock is known as total stress. However, rocks in the subsurface are filled with cracks and pores, which are saturated with one or more fluid phases (air, water, oil, etc.) (Jaeger et al. 2007). Pressure exerted by the fluid filling the pores has a major influence on the mechanical behavior of rocks and their state of stress, therefore it is important to carefully consider them in geomechanical analyses.

In order to formulate constitutive equations that are able to describe the effective stress, it has to be assumed that a porous medium (a rock, in this case) is isotropic, linearly elastic, fluid saturated and has incompressible grains.

The concept of effective stress was first introduced by Karl Terzaghi who stated that all quantifiable changes in stress are a direct result of a change in effective stress (Terzaghi 1925). He proposed the following equation (Eq. 2-15) to describe the relationship between total stress, effective stress and pore pressure:

$$\sigma_{ij} = S_{ij} - \delta_{ij} P_p \qquad (Eq.\ 2\text{-}15)$$

Where σ is the effective stress, S is the total stress and P_p is the pore pressure. δ is the Kronecker's delta which is defined as $\delta = 0$ if $i = j$ and $\delta = 1$ if $i \neq j$ (Fjaer et al. 2008). It means that pore pressure influences only the normal components of the stress tensor and not the shear components as expected as fluids cannot sustain shear stresses.

The effective stress is the combination of total stress applied to the rock and pore pressure exerted by the fluids contained into the pores. Pore pressure acts on grains and the negative indicates that this direction is opposite with respect to total stress applied to the rock (Fig. 2.6).

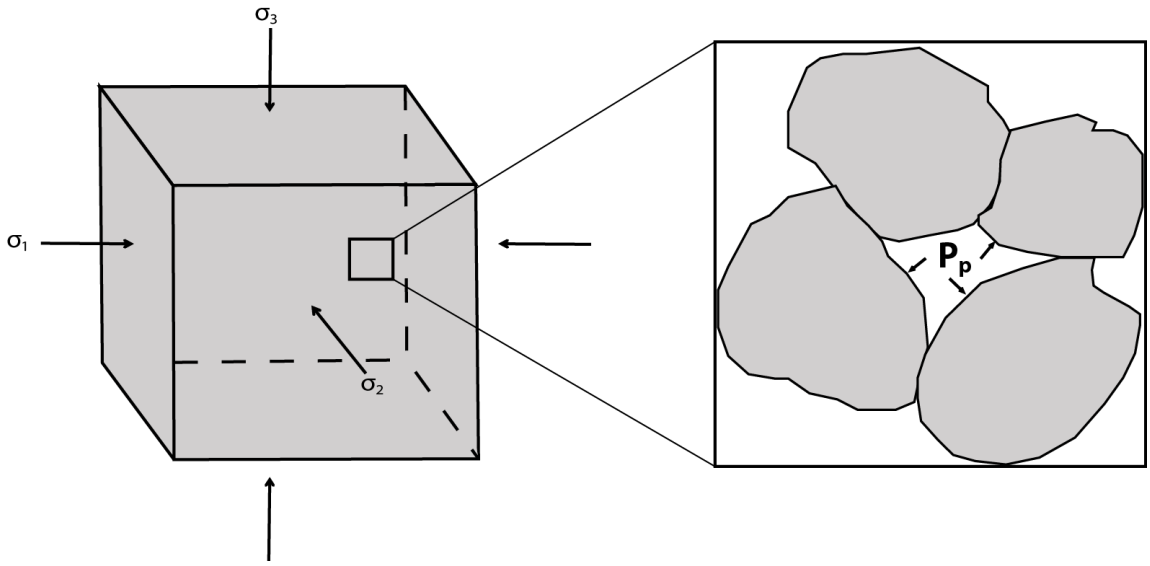

Fig. 2.6: Enlarged view of rock grains in element with pressure acting on grains in pore space.

This concept has been revised and improved by Biot when he developed his theory of poroelasticity (Biot 1941). Biot proposed an equation (Eq. 2-16) to account the following: any change in pore pressure is accompanied by a variation in pore volume, and this change in pore volume affects the overall mechanical response of the rock:

$$\sigma_{ij} = S_{ij} - \delta_{ij} \alpha P_p \qquad (Eq.\ 2\text{-}16)$$

α is known as Biot coefficient and describes the efficiency of the fluid pressure in counteracting the total applied stress. It is defined as (Eq. 2-17) (Nur and Byerlee 1971):

$$\alpha = 1 - \frac{K_b}{K_g} \qquad (Eq.\ 2\text{-}17)$$

Where K_b is the drained bulk modulus of the rock and K_g is the bulk modulus of the rock's individual solid grains. Biot parameter can vary between 0 and 1, depending on

the stiffness of the rock and interconnection between pores. In the case of $\alpha = 1$ the pore fluid has maximum efficiency in counteracting the total overburden stress and therefore implies that the effective stress of the rock is lower. If $\alpha < 1$ the pore fluid is less efficient in counteracting the total overburden stress and the effective stress of the rock is greater. In general it is close to 0 for stiff rocks and close to 1 for rocks with low stiffness.

2.2 Deformation and failure

The application of an external stress to a body of rock may cause different modes of deformation, such as changes in volume and shape which can be accompanied by changes in rock properties. Amount of stress and strain are linked, so that to a higher level of stress corresponds a higher strain affecting the rock. Types of deformation can range from a reversible status (i.e. elastic deformation), to a permanent status (i.e. plastic deformation), before eventually reaching a status of failure in the rock (Fig. 2.7) (Cook et al. 2007). Upon the application of a certain amount of stress, an individual rock's response is mainly driven by rock lithology, degree of cementation, porosity and burial depth.

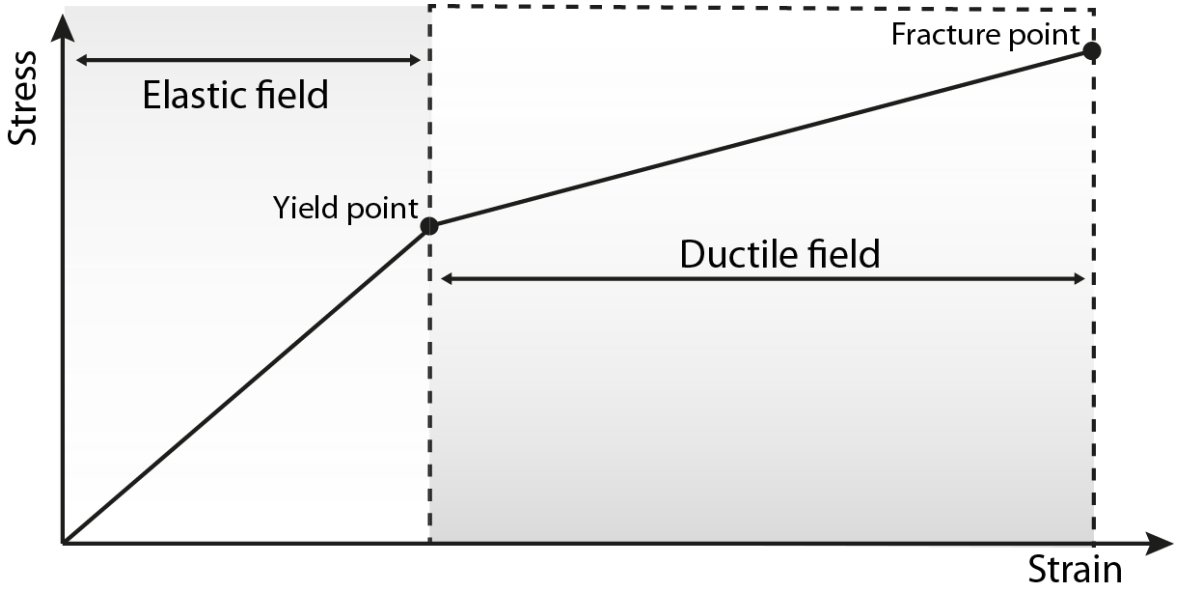

Fig. 2.7: Stress-strain diagram. In the elastic field if the applied stress is removed the rock returns to its original state. With application of greater stress, deformation becomes inelastic and non-recoverable starting at the yield point throughout the ductile field. Higher stresses eventually cause the rock to fail (fracture point) (Cook et al. 2007).

A number of theories have been proposed to determine the relationship between stress and strain (i.e. the constitutive equation of the material under consideration). The simplest explanation is provided by the theory of elasticity that assumes a univocal correspondence between stress and strain, having as a consequence a reversible behavior. Other theories take into account more complex behavior of rock in response to an applied stress, as for example the theory of plasticity (Thiercelin and Roegiers 1989).

2.2.1 Linear elasticity

Strain is the quantity that describes how much deformation is induced in a body by the action of stress. As well as stresses, strain can be normal or shear depending on which face of the rock it occurs. It can also be expressed as principal quantities: three normal strains along perpendicular axes.

The most commonly used form for the stress-strain relationships for rocks is that of linear elasticity, in which the strain tensor is a linear function of the stress tensor (Jaeger et al. 2007). To introduce this theory, let us consider a cylindrical sample with an initial length l and diameter d. If a force is applied to it in the z-direction, the element is compressed in the z-direction by a quantity equal to ΔL (Fig. 2.8), resulting in an axial strain equal to (Eq. 2-18):

$$\varepsilon_1 = \frac{l - l'}{l} \qquad (Eq.\ 2\text{-}18)$$

Where l' is the resultant length.

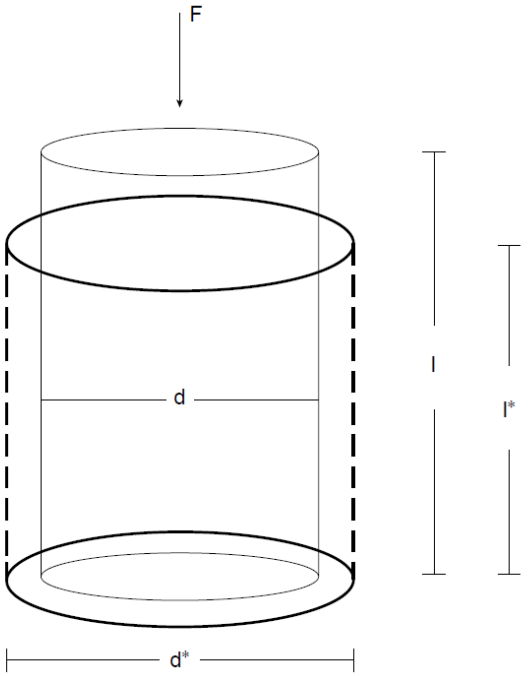

Fig. 2.8: Sample deformation under uniaxial loading (Thiercelin and Roegiers 1989).

The theory of linear elasticity assumes a linear and unique relationship between stress and strain, hence all strain is recovered if the load is removed. A homogeneous isotropic rock can be described, within the field of elasticity, using five elastic moduli (Zoback 2010).

In the case of a uniaxial compression text, such as the one presented above, a linear relationship that links together stress and strain is found through the Young's Modulus E (Eq. 2-19):

$$E = \frac{S_1}{\varepsilon_1} \qquad (Eq.\ 2\text{-}19)$$

Young's Modulus is the ratio of the stress along an axis over the strain along an axis. It is also defined as modulus of elasticity and measures the stiffness of a rock material. It predicts how much material sample extends under tension or shortens under compression (Jaeger et al. 2007).

If a rock sample is compressed in one direction, not only shortens along the loading direction, but it also expands in lateral directions (Fig. 2.8). This effect can be quantified introducing an additional constant, Poisson Ratio ν, defined as the ratio of lateral expansion to longitudinal contraction (Eq. 2-20):

$$\nu = -\frac{\varepsilon_2}{\varepsilon_1} \qquad (Eq.\ 2\text{-}20)$$

Where ε_2 is the transverse strain (measured in relation to the diameter of the cylinder) and ε_1 is the axial strain (measured along the length of the cylinder). By convention expansion is considered negative while Poisson Ratio is positive, thus the negative sign in the equation. It measures the compressibility of material perpendicular to applied stress: if a material is compressed in one direction, it tends to expand in the other two directions perpendicular to the direction of compression. This phenomenon is known as Poisson Effect (Economides et al. 1989). A perfectly incompressible material deformed elastically at small strains would have a Poisson Ratio of exactly 0.5 (Zoback 2010).

If Young's Modulus and Poisson ratio are derived from unconfined uniaxial compression tests as presented above, they are referred to as static moduli. Alternatively, they can be estimated from acoustic wireline logs, and in this case they are referred to as dynamic Young's Modulus and dynamic Poisson ratio respectively. Measurements of acoustic wave velocities together with density information lead to the estimation of dynamic values through the following equations (Eq. 2-21, 2-22) (Fjaer et al. 2008):

$$E_{dyn} = \frac{\rho v^2 (3v_p^2 - 4v_s^2)}{(v_p^2 - v_s^2)} \qquad (Eq.\ 2\text{-}21)$$

$$\nu_{dyn} = \frac{v_p^2 - 2v_s^2}{2(v_p^2 - v_s^2)} \qquad (Eq.\ 2\text{-}22)$$

where ρ is the density of the formation, v_p is the p-wave velocity and v_s is the s-wave velocity. Values of static and dynamic elastic moduli can be quite different, in particular at low stress levels, due to the fact that dynamic values are affected by the loading speed while testing showing a rate-dependency. As a result, dynamic modulus can be several times larger than the static modulus e.g. in a weak sandstone (Fjaer et al. 2008). Empirical relationships between static and dynamic moduli have been established (Mavko et al. 2009, Wang and Nur 2000), however they cannot be considered universal as dynamic elastic moduli depends on the conditions of the measurement. Numerical simulations require using static values for these two elastic moduli, as they are not dependent on frequency and stress level.

In the state of pure shear, stress is related to strain by the Shear Modulus *G*. It is also called modulus of rigidity and it is defined as the ratio of shear stress (S_{xy}) to the shear strain (ε_{xy}) (Eq. 2-23)(Zoback 2010):

$$G = \frac{1}{2}\left(\frac{S_{xy}}{\varepsilon_{xy}}\right) \qquad (Eq.\ 2\text{-}23)$$

Shear modulus is always a positive quantity, except for fluids that have zero value as they cannot sustain shear stresses.

The bulk modulus *K* measures the material's resistance to uniform compression (e.g. hydrostatic compression). It is defined as the ratio of the infinitesimal pressure increase to the resulting relative decrease of the volume (Eq. 2-24) (Halliday et al. 2010):

$$K = -V\frac{dP}{dV} \qquad (Eq.\ 2\text{-}24)$$

Finally, the Lamé constant λ does not have a straightforward physical representation; in a material in which Poisson's ratio is equal to 0.25, λ=G (Zoback 2010).

Although five parameters can be defined for an isotropic material, only two of them are independent. If two of them are know, it is possible to derive the other three from equation of correlation. A compilation of all the thirty relations that can be obtained has been produced by Davis and Selvadurai (1996) .

2.2.2 Plasticity

If a rock is loaded with stresses that exceed the yield point (Fig. 2.7), it is no longer able to react elastically and undergoes a non-elastic deformation. Plastic deformation is not recovered if the rock unloaded, hence the deformation is permanent. The theory of plasticity describes this ductile behavior that starts beyond the yield point (Jaeger et al. 2007). Four major concepts are the basis for the plasticity theory (Fjaer et al. 2008):

- *plastic strain* associated with a stress increment that yield to plastic deformation;
- *a yield criterion* that defines the surface in stress space where plasticity is initiated;
- *a flow rule* that describes how the plastic strain develops for a given load;
- *a hardening rule* that describes how the rock is able to sustain increasing load after the initial plastic failure.

Plastic deformation is often associated with mechanisms such as microcracking, grain rearrangement, mineral dissolution, defect motion etc. Most common yield criteria used for modeling plastic deformation are Mohr-Coulomb yield criterion and Drucker-Prager yield criterion (Drucker and Prager 1952).

2.2.3 Brittle behavior

If a rock is subjected to stresses that overcome the fracture point, they enter the field of brittle deformation (Fig. 2.7). In general, the upper crust is characterized by brittle deformation behavior that makes rocks failing under sufficiently high stresses. Rock failure implies that a rock changes its shape permanently and possibly falls apart, reducing its ability to carry loads (Fjaer et al. 2008). Failure can occur due to different mechanism such as brittle shear, tensile failure or compaction; it is a complex process that is still not fully understood (Zoback 2010). Therefore all models or criteria for failure represent simplified descriptions of realistic rock behavior (Fjaer et al., 2008). The stress level at which brittle failure occurs is commonly called the strength of the rock which varies depending on the respective type of failure (i.e. tensile strength, shear strength).

Failure in rocks is influenced by various factors, for example sample size and shape, moisture content of the sample. Evidences indicate that effective stress governs failure and it is often assumed that only the minimum and the maximum principal effective stress influence failure, considering the intermediate principal effective stress negligible (Mavko et al. 2009).

2.2.3.1 Shear failure and Mohr-Coulomb failure criterion

Shear failure is particularly important as it is the principal mechanism of failure for faults, therefore pre-production and pre-injection studies tend to focus on avoiding shear failure. Indeed, slip on faults can be responsible for damage on wells casing and wellbore instability (Zoback 2010). In addition active faults can provide paths to fluid flow, thus causing leakage in case of CO_2 storage, and eventually can be accounted for inducing microseismicity (Rutqvist et al. 2010). Failure of intact rock has also to be regarded as a potential issue as it concerns, for example, integrity of caprock.

A failure criterion is a relationship between the principal effective stresses and it represents a limit beyond which instability or failure occurs (Thiercelin and Roegiers 1989). Several failure criteria exist and are used for various applications. For the purpose of this thesis the Mohr-Coulomb criterion has been used to evaluate integrity of caprock and fault stability in response to CO_2 injection.

Mohr-Coulomb criterion holds in the case of a rock subjected to a homogeneous state of stress characterized by the three principal stress components S_1, S_2 and S_3 (Pollard and Fletcher 2005). This criterion is based on the assumption that failure is controlled by the minimum and maximum principal stresses, and is unaffected by the magnitude of the intermediate principal stresses (Jaeger et al. 2007).

Mohr-Coulomb criterion establishes a linear relationship between the shear and normal stresses acting on a plane parallel to the potential fracture plane (Eq. 2-25) (Fig. 2.9) (Pollard and Fletcher 2005):

$$S_s = C + \mu_i \sigma_n \qquad (Eq.\ 2\text{-}25)$$

Where S_s is the total shear stress parallel to the fracture when failure starts, C is the cohesion of the rock that quantifies the resistance to shear fracture if the normal stress is zero, μ_i is the coefficient of internal friction and σ_n is the effective normal stress perpendicular to the fracture when failure is initiated. The effective normal stress σ_n accounts also for the pore pressure which mitigates the effect of compression.

An effective tool to visualize Mohr-Coulomb criterion is a Mohr diagram that plots total shear stress against normal effective stress (Fig. 2.9). Only maximum and minimum principal stresses are plotted as the intermediate principal stress is ignored in the Mohr-Coulomb failure criterion. Failure is represented with an inclined line that intercepts the shear stress-axis at a value corresponding to the cohesion of the rock before failure. Slope of the failure line is related to the coefficient of internal friction μ_i through the following equation (Eq. 2-26) (Van der Pluijm and Marshak 2004):

$$\mu_i = \tan \varphi \qquad (Eq.\ 2\text{-}26)$$

where φ is the angle of internal friction.

A stress state whose Mohr's circle lies below the failure line will not give rise to failure on any plane, only when the circle touches the line failure occurs (Jaeger et al. 2007). States of stress exceeding the failure line are not allowed because failure of rock would have occurred prior the rock having achieved such a stress state (Zoback 2010).

The point at which the Mohr circle is tangent to the failure line represents the state of stress of the plane of failure. This plane forms an angle β with the S_1 direction (Jaeger et al. 2007).

Changes in pore pressure in the system would cause a shift on the Mohr circle as they impact directly the effective normal stress. A decrease in pore pressure (e.g. oil production) would cause a shift to the right towards a more stable state of stress, whereas an increase in pore pressure (e.g. injection of fluids) would cause a shift to the left increasing the likelihood of shear failure (Pollard and Fletcher 2005).

In a rock subjected to a higher confinement, that means a larger S'_3, a greater stress S'_1 could be applied before shear failure is initiated. This is a peculiar characteristic of many porous rocks that effectively become stronger the more they are confined (Cook et al. 2007), being their strength dependent mainly on the internal friction. In contrast, rocks such as clays exhibit little internal friction and derive their strength almost entirely from cohesion between grains (Pollard and Fletcher 2005).

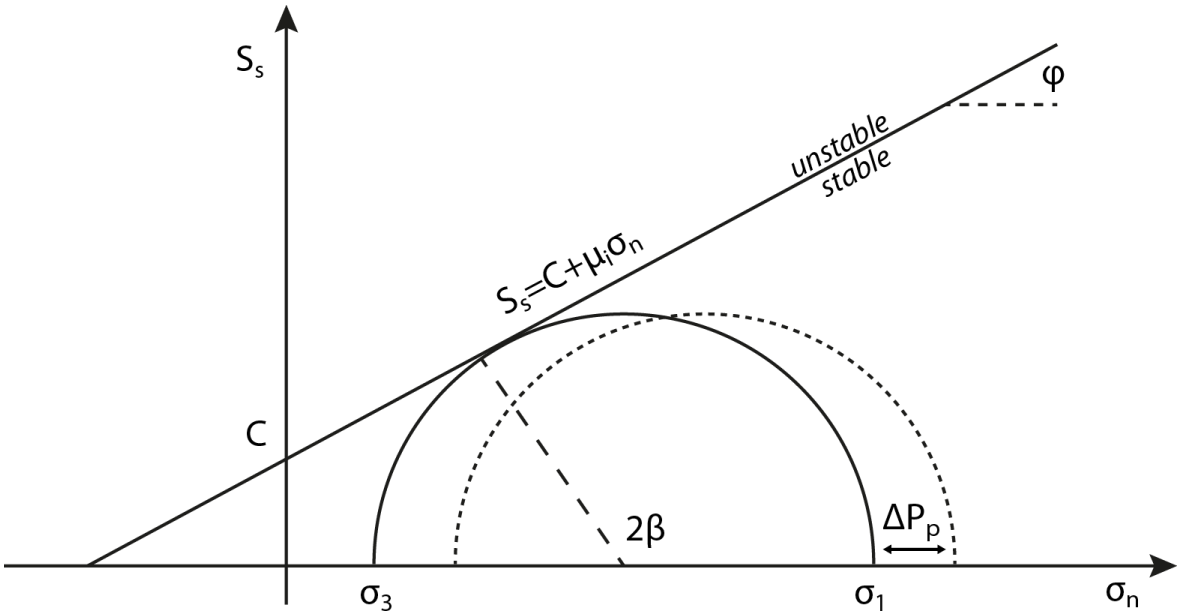

Fig. 2.9: Mohr diagram plotting total shear stress against effective normal stress. Mohr-Coulomb linearized criterion is represented by a failure line. Slope of the line is driven by the coefficient of internal friction (μ_i=tan(φ)), intercept on y-axis is the cohesion of the rock. Effect of pore pressure causes a shift in the Mohr circle: to the right if pore pressure decreases (depletion), to the left if pore pressure increases (injection). Modified after (Fjaer et al. 2008).

2.2.3.2 Tensile failure

Tensile failure is relatively unimportant in rock mechanics, with a predominant role only on hydraulic stimulation. Tensile failure occurs if the effective tensile stress exceeds the tensile strength of the rock, a measure of the resistance of the rock against tensile failure. Tensile strength of rocks is quite low for all rocks, on the order of few MPa (Zoback 2010) and if pre-existing flaws exist it is considered to be close to zero. This implies that rocks cannot sustain significant tensile stress, therefore in situ stress at depth is never naturally tensile (Fjaer et al. 2008). However, tensile fractures can develop around the wellbore because of the stress concentration around the wellbore or due to stimulation in fracking operation. Reservoir stimulation is conducted pumping fluids and propants in the wellbore with the aim to cause hydraulic fracturing in the rock and enhance oil recovery (Economides et al. 1989). Hydraulic fracturing is a form of tensile failure that occurs if fluid pressure exceeds the local effective minimum principal stress (Brudy and Zoback 1999).

The tensile failure criterion that specifies the stress required to reach tensile failure for an isotropic rock is given by the following equation (Eq. 2-27) (Fjaer et al. 2008):

$$\sigma_3 = -T_0 \qquad (Eq.\ 2\text{-}27)$$

Where σ_3 is the effective minimum principal stress and T_0 is the tensile strength of the rock, the maximum stress that a material can withstand while being stretched before failing.

2.3 Reservoir stress path

The changes of pore pressure within a reservoir during depletion and injection operations have an impact on magnitude of horizontal stresses. This was first observed at the Ekofisk field, where reservoir depletion and pore pressure drawdown were correlated to changes in in situ stress and deformation (Teufel et al. 1991). This phenomenon is known as reservoir stress path. Its importance in terms of compaction, surface subsidence, permeability variations etc has long been recognized while remaining poorly understood (Santarelli et al. 1998). It often refers only to minimum horizontal stress magnitude, but the concept holds also for maximum horizontal stress magnitude. The assumption at the basis implies that horizontal stresses are dependent on pore pressure and Poisson Ratio. The latter accounts for the lateral effect of the overburden, known as Poisson effect (Addis 1997).

The theory of poroelasticity can provide a background to understand the concept of reservoir stress path. In a isotropic, porous and elastic reservoir, assuming no lateral strain, if fluid is removed from a reservoir the relationship between vertical effective stress and horizontal effective stresses can be written as (Eq. 2-28) (Zoback 2010):

$$\sigma_{Hor} = \left(\frac{\nu}{1-\nu}\right)\sigma_V + \alpha P_p \left(1 - \frac{\nu}{1-\nu}\right) \qquad (Eq.\ 2\text{-}28)$$

where σ_{Hor} refers to both effective horizontal stresses, ν is the Poisson's Ratio, σ_v is the vertical effective stress, α is Biot coefficient and P_p is the pore pressure. The change in stress magnitude is then calculated taking the derivative of the equation with respect to pore pressure (Zoback 2010)(Eq. 2-29):

$$\Delta\sigma_{Hor} = \alpha\left(\frac{1-2\nu}{1-\nu}\right)\Delta P_p \qquad (Eq.\ 2\text{-}29)$$

Rearranging the equation 2-28 the reservoir stress path A can be defined as (Eq. 2-30) (Yeow et al. 2004):

$$A = \frac{\Delta\sigma_{Hor}}{\Delta P_p} = \alpha\left(\frac{1-2\nu}{1-\nu}\right) \qquad (Eq.\ 2\text{-}30)$$

The reservoir stress path phenomenon is not fully understood yet, and some questions are still open. The reservoir stress path is not known before production and/or injection and even numerical models are sensitive to input parameters (Vidal-Gilbert et al. 2010). Some case studies in the Norwegian North Sea show some sort of irreversibility upon re-pressurization, meaning that the reservoir did not follow the same stress path during depletion and pressure rebound (Santarelli et al. 1998).

2.4 Faults and geomechanics

Faults have an important role in geomechanical studies as they represent planes of weakness within intact rock and they may possibly slip depending on the applied stress. In contrast with intact rock failure which can be detected with the Mohr-Coulomb failure criterion discussed above, in the case of a pre-existing fault, failure

can be compared to a frictional sliding on a plane. This is regulated by the Amontons' law, a modification to Mohr-Coulomb failure criterion, and will occur if the ratio of shear to normal stress reaches the coefficient of friction μ (Eq. 2-31) (Zoback 2010):

$$\frac{S_s}{\sigma_n} = \mu \qquad (Eq.\ 2\text{-}31)$$

Where S_s is the total shear stress, σ_n is the effective normal stress that considers also the role of pore pressure. μ is the coefficient of friction that describes slip on pre-existing fault, in contrast with the coefficient of internal friction μ_i used in Mohr-Coulomb criterion for intact rock studies.

Moreover faults represent a major source of stress perturbations (Yale 2003), resulting in an alteration in magnitude and direction of the regional stress field. Small faults may affect the stress pattern only in an area of few hundred meters around the fault plane, however this behavior becomes more evident in the case of large-scale faults. Especially active faults are able to induce a rotation of the in situ stresses up to 90° with respect to the regional trend (Tamagawa and Pollard 2008).

In the specific case of CO_2 injection, pressures that exceed prevailing formation pressures may potentially reactivate pre-existing faults and generate new faults. Such brittle deformation can increase fault and fracture permeability transforming faults in potential leakage pathways for CO_2 (van Ruth and Rogers 2006).

2.4.1 Slip tendency and dilation tendency

Slip and dilation tendency of faults is one of the techniques used for assessing potential fault reactivation. It has the aim to describe shearing and dilatation behaviors along faults during deformation (Moeck et al. 2009). Amontons' law, already illustrated in equation 2-31, provides the theoretical background for this analysis.

Stability or failure along a plane of weakness (i.e. faults) is determined by the ratio of shear stress to normal stress acting on the plane. This quantity is the slip tendency T_s and is calculated as (Eq. 2-32) (Morris et al. 1996):

$$T_s = \frac{1}{\mu}\left(\frac{S_s}{\sigma_n}\right) \qquad (Eq.\ 2\text{-}32)$$

where μ is the coefficient of friction of fault that normalize the equation.

Dilation of faults is largely controlled by the normal stress which is a function of lithostatic and tectonic stresses. Dilation tendency T_d is calculated as (Eq. 2-33) (Moeck et al. 2009):

$$T_d = \frac{\sigma_1 - \sigma_n}{\sigma_1 - \sigma_3} \qquad (Eq.\ 2\text{-}33)$$

3 Case study – The CO2CRC Otway Project

Reducing greenhouse gas emissions has recently become a topic of main interest and with this purpose the CO2CRC (Cooperative Research Centre for Greenhouse Gas Technologies) has been established in 2003 in Australia. The main target for CO2CRC is to develop economically convenient technologies to decrease CO_2 emissions to the atmosphere within Australian territories, while at the same time continuing to produce fossil fuels to meet industry requirements (Jenkins et al. 2012). Objectives of CO2CRC are, among others: to research new CO_2 storage technologies, to demonstrate that CO_2 capture and storage is sustainable both at economic and environmental level; to decrease Australian carbon monoxide emissions to the atmosphere while maintaining industries at a high level of competitiveness by developing new commercial opportunities (e.g. hydrogen-based technologies); to contribute to solving a global environmental problem by participating in international programs such as the Climate Action Partnership (CO2CRC). Particular care was undertaken in securing and maintaining the consent of the community throughout the operations. The CO2CRC developed a communication strategy, based on market research, to proactively engage communities and decision maker (CO2CRC). Evaluations showed a generally positive attitude in the local community, and also media coverage has been generally balanced and positive over the period of activity of CO2CRC operations (Ashworth et al. 2010). Furthermore, the CO2CRC Otway Project has an important influence on the development of Carbon Capture and Storage legislation in Australia. Indeed, the key performance indicators were agreed together with the Environmental Protection Agency, on the basis of a comprehensive monitoring plan (Ranasinghe 2008).

PROTECT Research Group cooperates with the CO2CRC consortium with the aim to develop a workflow for predicting deformation at sub-seismic level. The study presented in this thesis contributes to the aim of this join project.

3.1 The CO2CRC Otway Project and PROTECT Research Group

The CO2CRC Otway Project is the first operational CO_2 storage pilot project in Australia (Jenkins et al. 2012). It is located in South Western Victoria, about 200 km west of Melbourne in the Otway Basin. Launched in 2005, the project involves the extraction, compression and transport and storage of naturally occurring CO_2. The CO_2 is stored in a depleted natural gas reservoir two kilometres below the Earth's surface. A key project feature is its world-leading CO_2 monitoring program. Designed, developed and implemented by CO2CRC researchers from Australia, New Zealand, the USA and Canada, this comprehensive monitoring program will contribute to the development of new monitoring technologies for safe CO_2 storage.

The Naylor Field in the Otway Basin (Fig. 3.1) has been chosen as a demonstration site (The Otway Project) for the geological storage of CO_2 by the CO2CRC.

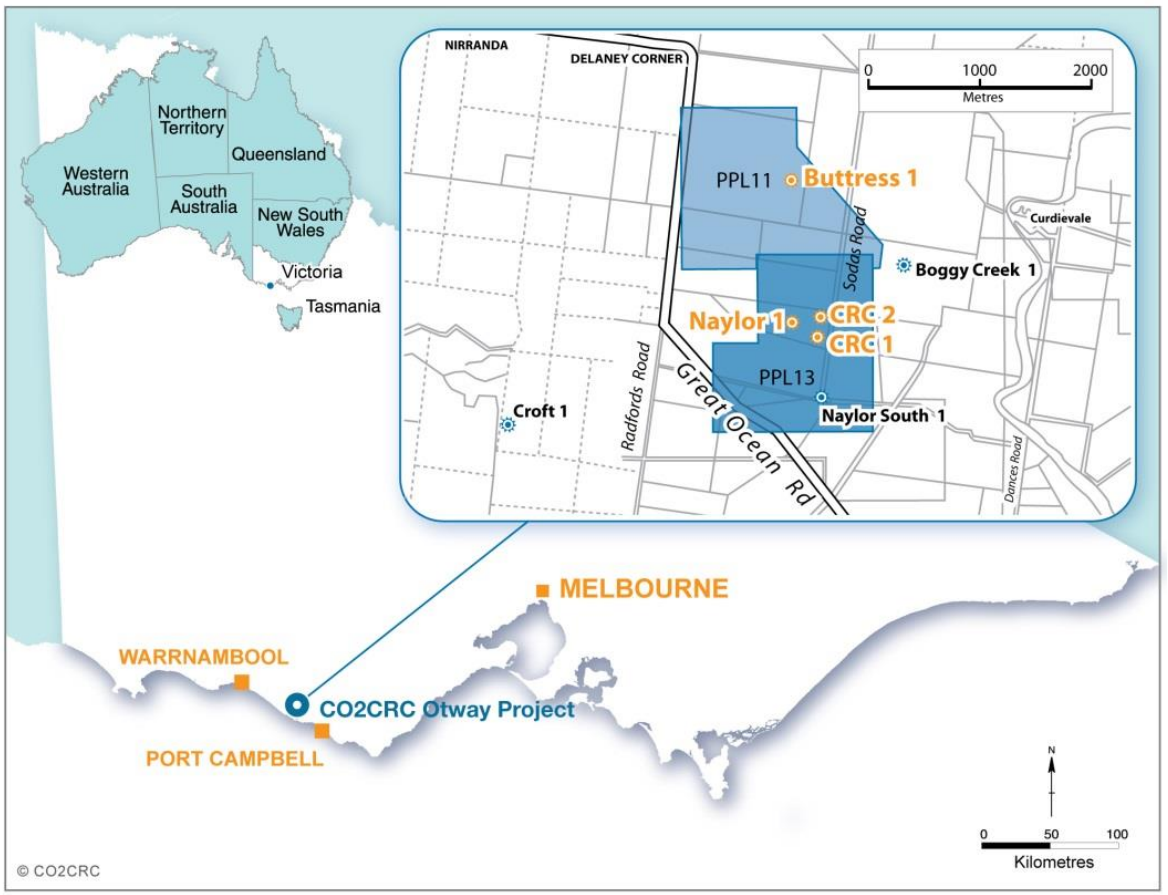

Fig. 3.1: Localization of CO2CRC Otway Project in South Eastern Australia. (CO2CRC)

The Naylor Field is a small depleted natural gas field, with an original cap area estimated at 40 hectares. The composition of the original gas (in mole %) was 88% methane, 4% ethane, 2% propane, 1% carbon dioxide, 2% nitrogen and 3% other components. From June 2002 to October 2003 the total production from the target reservoir has been of 9.5 x 107 m^3 (at standard condition of 15 °C and 0.101325 MPa) that corresponds to 60% of the estimated gas in place (Vidal-Gilbert et al. 2010). Using equivalent volumes at reservoir conditions would indicate a CO_2 storage capacity of ≈210.000 tonnes, but this amount may be reduced by relative permeability and the influx of formation water from the adjoining aquifer.

To demonstrate the viability of geological sequestration of CO_2 in Australia, two different operational stages have been planned and executed in the frame of CO2CRC Otway Project. The first stage aimed to store CO_2 in a depleted gas reservoir, while the second stage had as injection target a saline formation.

During Stage 1 (Fig. 3.2), CO_2-rich gas was produced from the near Buttress Field and then injected into the CRC-1 borehole within the Naylor structure at a depth of ~2000 m. CRC-1 was drilled in February/March 2007 as a CO_2 injection and monitoring well ≈300m to the SE of the original methane production well (Naylor-1). The injected gas has an average composition of (in mole %) 77% carbon dioxide, 20% methane and 3% other gas component. Between March 2008 and August 2009 65,445 tonnes of this gas were injected into the Naylor Field´s Waarre C Formation (van Ruth et al. 2007, Vidal-Gilbert 2008, Vidal-Gilbert et al. 2010). The amount of gas stored is

significantly less than the amount of natural gas originally held in the Naylor field, increasing confidence that the site will be able to safely store the gas.

The geomechanical characterization presented in this thesis focuses on particular on stage 1 of the CO2CRC Otway Project.

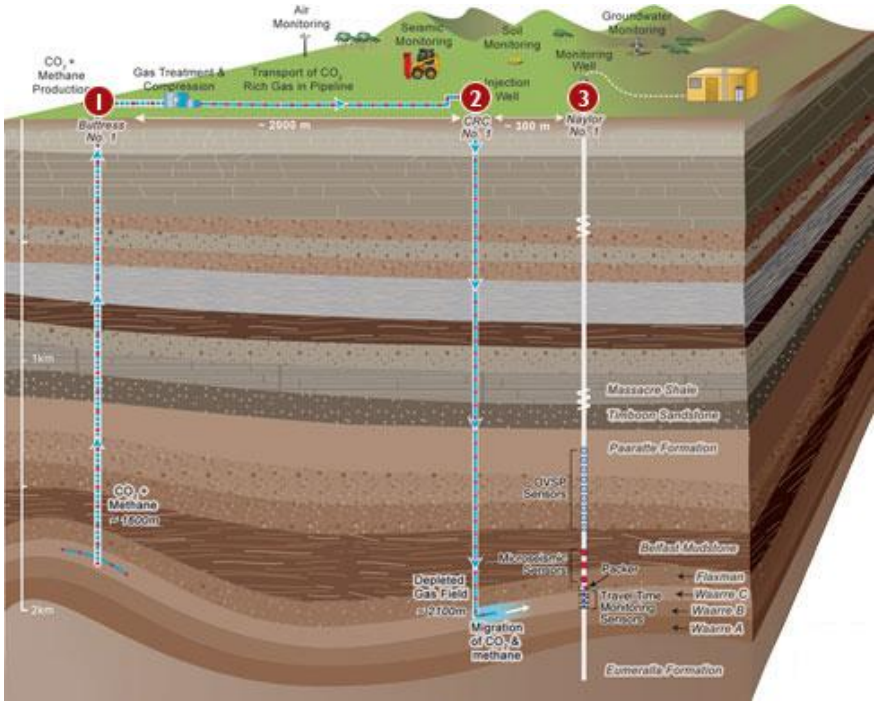

Fig. 3.2: Model of Stage 1 of CO2CRC Otway Project. The geological structure in the cartoon represents a simplification made for better visualize the storage facilities. The more complex actual structure of the subsurface is visualized in Fig. 6.3 and Fig. 6.6. (CO2CRC)

Stage 2 commenced in 2010 with drilling of a new injection well, CRC-2 (Fig. 3.3). In this case, the objective of CO2CRC was to investigate how CO_2 can be permanently stored in saline formations - deep porous rocks containing formation water. This is a very common type of rock formation with the potential to store the amount of CO_2 emissions in a relatively long period.

The first experiment for Stage 2 took place in 2011 and was designed to test an aspect of underground CO_2 storage called residual gas trapping. In residual gas trapping the CO_2 is stored in the porous rock in tiny bubbles, disconnected from each other so they cannot flow out. It is an important aspect of CO_2 storage, because the CO_2 cannot move through the reservoir and so remains fixed underground. To test the effectiveness of this procedure, the research team undertook a series of extraction from and injection into the shallow aquifer at a depth of ~1400 m. Afterwards, formation water with a small amount of pure dissolved CO_2 was re-injected. A series of pressure sensors, tracer concentrations and borehole measurements were used to determine the amount of CO_2 trapped.

Current research of CO2CRC focuses on imaging CO_2 storage in saline aquifer through seismic time-lapse techniques, still using CRC-2 as injection well (Tenthorey et al. 2014).

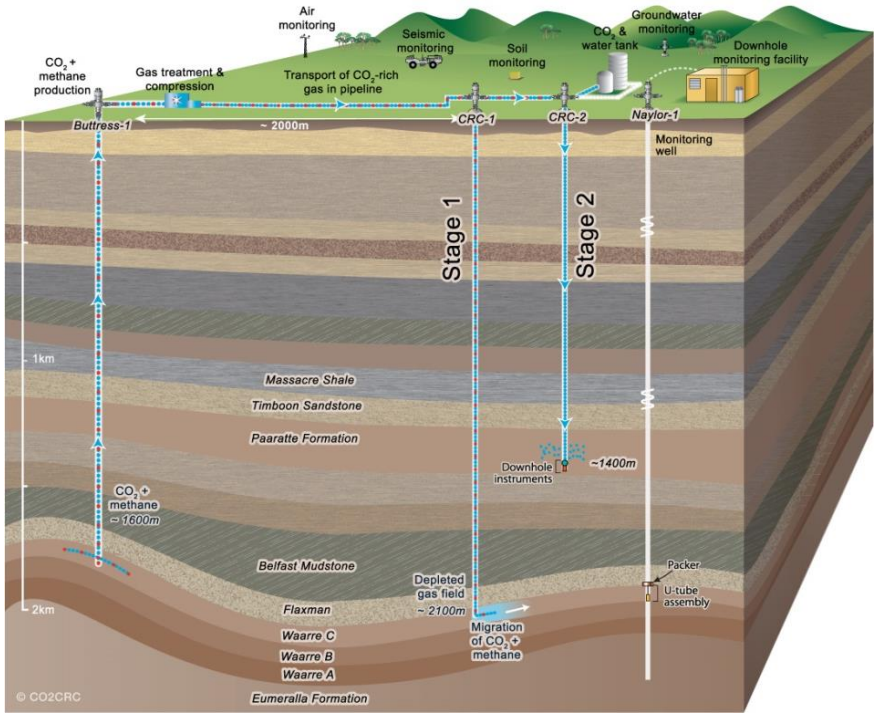

Fig. 3.3: Model of Stage 2 of CO2CRC Otway Project. The geological structure in the cartoon represents a simplification made for better visualize the storage facilities. The more complex actual structure of the subsurface is visualized in Fig. 6.3 and Fig. 6.6. (CO2CRC)

As international partner of CO2CRC, the PROTECT (PRediction Of deformation To Ensure Carbon Traps) Research Group has been established in 2011, with the funding of BMBF (Federal Ministry of Education and research) through the research program Geotechnologien. This joint project gathers universities, research institutes and private companies in Germany and Australia. In particular, scientific partners based in Germany are LIAG (Leibniz Institute for Applied Geophysics), Technical University of Darmstadt, TEEC Geophysics and Helmholtz – UFZ (Centre for Environmental Research), while Curtin University of Technology is the Australian scientific partner. The project uses data from the CO2CRC Otway Project to study the structural framework and recent tectonic stresses to verify potential pathways between reservoir and surface as well as their structural, physical and temporal features. The PROTECT Research Group collaborates to create a dynamic risk profile which is generally applicable to CO_2 reservoirs. Using a combination of methods, the leakage potential of reservoir and overburden will be assessed, thus, providing sensitive monitoring strategies and assuring long-term storage integrity. The main objective of the project is the production of a seismo-mechanic workflow (Fig. 3.4) (Krawczyk et al. 2011), that starts from 3D seismic data and well data to proceed in parallel at large, medium and small scale thus providing an interactive validation between work packages. Results from the different studies will lead to the prediction of sub-seismic faults and fractures, which will be further completed by 2D seismic validation. The PROTECT project is divided into four different work packages with the following aims: sub-seismic deformation prediction by retro-deformation, spatial mapping of fractures and faults by coherency analysis of seismic data, stress and deformation

prediction with geomechanical forward modeling and thermo-hydro-mechanical/chemical benchmarking of geological CO_2 storage processes.

This thesis refers to the "FEM forward modeling and 3D stress field" work package (Fig. 3.4), for which the Technical University of Darmstadt is in charge.

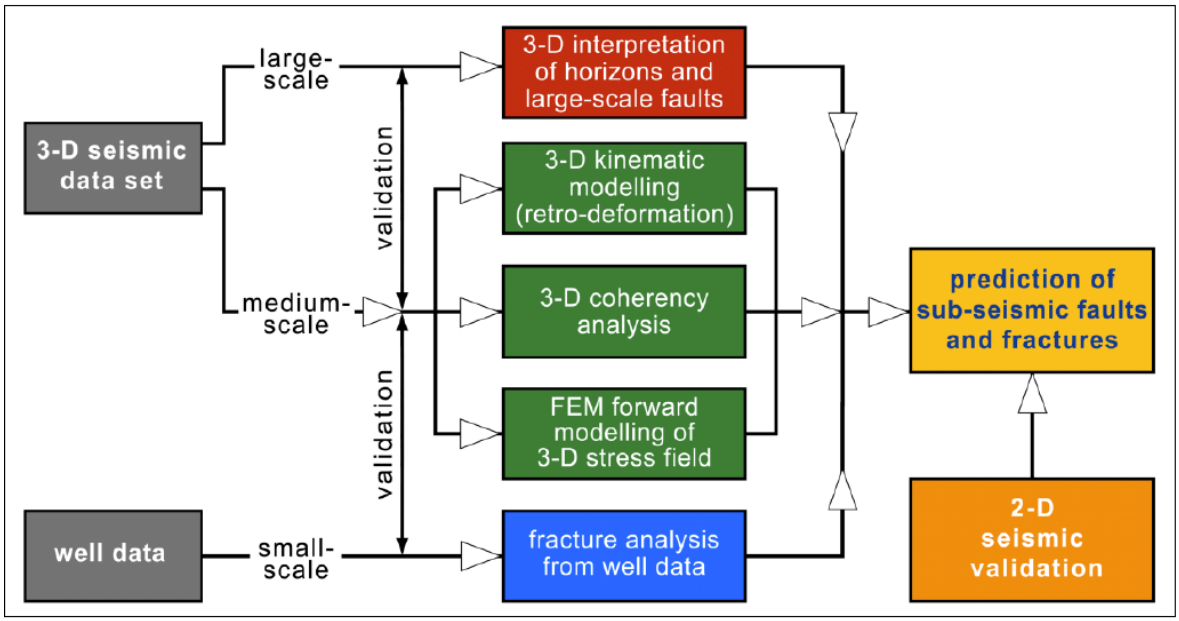

Fig. 3.4: Workflow of the joint project PROTECT, aiming at the combination of different scales of deformation and validating the independently-derived predictions. Modified after Krawczyk et al. (2011).

3.2 Naylor Field

Naylor Field is a depleted natural gas (methane) field located within the onshore Otway Basin, Victoria, Australia. The Naylor Field is a fault-bond trap formed during the development of the passive margin of South-Eastern Australia.

Production from the Waarre Formation Unit C through well Naylor-1 lasted 15 months between 2002 and 2003. At the end of the operations, there was a residual gas cap and the pressure increased following production due to aquifer recharge. This site was selected as the location for a CO_2 injection project due to good porosity and permeability of its reservoir rock (the average permeability was more than 1 Darcy) (Jenkins et al. 2012). The target horizon for CO_2 injection is the Waarre C Formation overlain by the Flaxmans Formation, formerly described as part of the Waarre Fm (cf. Chapter 3 and 5 for complete information about stratigraphy). The primary seal for the CO_2 storage project is considered to be the Belfast Mudstone which acts as regional seal across the area (Daniel 2007).

There are 4 wells in the greater Naylor Field (Fig. 3.5). Naylor-1 was drilled in May 2001 and produced methane from June 2002 until October 2003. Afterwards it was converted to monitoring well for the CO2CRC Otway Project. Naylor-South 1 was drilled in December 2001 to assess the upside potential of the Naylor Field and was not used within the CO2CRC Otway Project. CRC-1 was drilled by the CO2CRC in

March 2007 as a CO_2 injection for Stage 1. CRC-2 was drilled at the beginning of 2010 for Stage 2 of the Otway Project.

The Naylor Field represents a partially-breached structure (van Ruth et al. 2007) (Fig. 3.5). It is bound to the West, below ≈1970 m, by the Naylor Fault, a North-South trending normal fault that does not offset the seal (Belfast Mudstone). The Naylor Fault forms part of the structural closure which will host the injected CO_2 plume, and will be required to act as a long-term seal. To the North the Naylor structure is cut by a normal fault below ≈2000 m, the Naylor East Fault. This fault extends to units shallower than the Belfast Mudstone. The Naylor Field is bound to the South by the Naylor South Fault, which extends to the near surface. Both the Naylor East Fault and Naylor South Fault are not in the expected pathway of the injected CO_2 plume. However, the Naylor Fault and the Naylor East Fault may provide a pathway for movement of CO_2 outside the intended storage area, and are potential containment risks for CO_2 storage in the Waarre Fm in the Naylor Field.

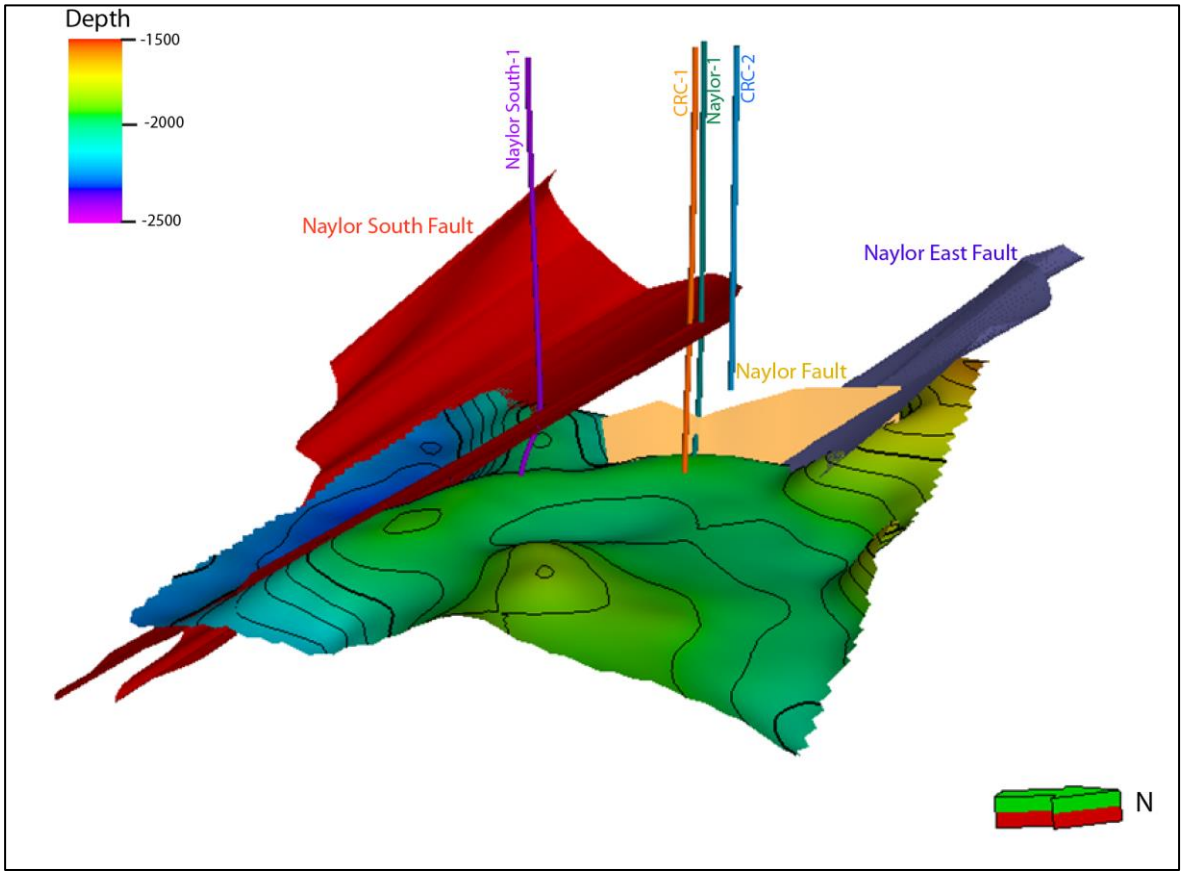

Fig. 3.5: 3D view of the Naylor Field structure at reservoir level (Waarre Fm).

3.3 State of the art – Geomechanical models of Naylor Field

Naylor Field has been subjected to a series of pre-injection and monitoring studies, with the first published report dating back 2006. They are summarized below in order to give an overview of the state of the art concerning the geomechanical understanding of the storage site. The complexity of the models increases through time with the availability of new data from in situ measurements. However, these

models are only analytical and up-to-date there is no numerical model for the CO2CRC Otway site.

The first geomechanical assessment of the onshore Victorian Otway Basin was published in 2006 by van Ruth and Rogers. The study aims to collate existing data (rock strength and in situ stress data from adjacent fields) to constrain the geomechanical model, evaluate the risk of fault reactivation and failure of intact rock and review borehole stability. A NW-SE maximum horizontal stress orientation (152° N) is determined from the occurrence of borehole breakouts. A review of leak-off tests carried out in a number of wells in the basin leads to the determination of an average gradient of 18.62 MPa/km for the minimum horizontal stress. Magnitude of the maximum horizontal stress is derived from the frictional limits theory (Sibson 1974) with a resulting gradient <37 MPa/km assuming the maximum horizontal stress as the maximum principal stress. Thus the stress regime inferred is on the boundary between strike-slip and reverse faulting above 700 m below ground level, and strike slip below 700 m. Pore pressure is established to be almost hydrostatic with a gradient of 9.95 MPa/km from formation interval test pressure measurements. They provide an evaluation of failure of intact rock indicating a maximum sustainable pore pressure increase (ΔP_p) of 9.6 MPa within the reservoir and 16.5 MPa within the seal, before causing brittle failure. Risk of fault reactivation is calculated using the FAST (Fault Analysis Seal Technology) technique (Mildren et al. 2005) that estimates the increase in pore pressure required to cause fault reactivation. Two different scenarios are tested: one for healed faults (C=5.4 MPa; μ=0.78) and one for cohesionless faults (C=0 MPa; μ=0.6) respectively. The resulting orientation of faults with high and low reactivation propensity is almost identical for healed and cohesionless faults (Fig. 3.6), and also the magnitude of reactivation propensity only slightly differs. High angle faults striking NE-SW are unlikely to be reactivated in the current stress regime, whereas high angle faults oriented ESE-WNW and ENE-WSW have the highest fault reactivation risk. For the Naylor Field, the maximum fault reactivation is calculated near the crest of the structure, with a calculated Critical Pore Pressure (CPP) of 0 MPa, thus indicating that faults would not be able to sustain pressure increase without reactivating. However, absolute values of ΔP_p are considered to be affected by large errors due to uncertainties in the geomechanical model and the authors themselves suggest to not use them for planning purposes.

This geomechanical model presents overall a good methodology to assess failure in intact rock and potential reactivation of faults. However, the model is poorly constrained using stress and rock strength data from adjacent fields, and it is not considered to be reliable in terms of injection planning.

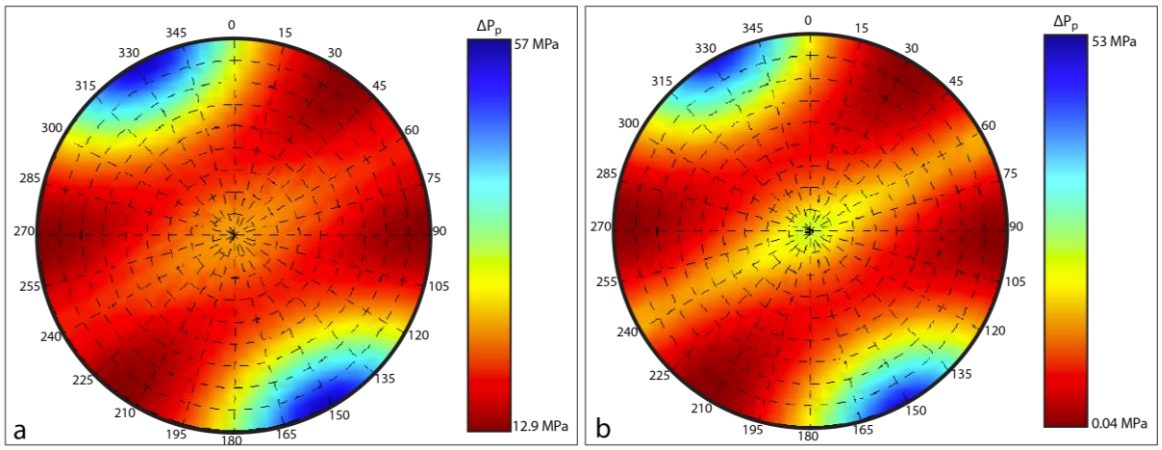

Fig. 3.6: Stereonet showing the reactivation risk (ΔP_p in MPa) for healed (a) and cohesionless (b) faults at 2040 m in the onshore Otway Basin. Modified after van Ruth and Rogers (2006).

In 2007 van Ruth presented a second paper, in collaboration with Tenthorey and Vidal-Gilbert, focusing on pre-injection geomechanical assessment of the Naylor Field. This work follows the previous report (van Ruth and Rogers 2006) and aims to further constrain the already existing geomechanical model and evaluate the risk of fault reactivation and failure of intact rock. A new NW-SE maximum horizontal stress orientation of 142°N is determined from borehole breakouts of the newly-drilled CRC-1 well. Leak-off tests (LOT) undertaken during the drilling of CRC-1 contribute to the comprehension of the minimum horizontal stress magnitude, with an established gradient of 14.62 MPa/km (average from leak-off tests in the onshore Victoria Basin). Magnitude of maximum horizontal stress is calculated using data from CRC-1 leak-off test (Amadei and Stephansson 1997) and frictional limits theory (Sibson 1974), constraining the gradient to an average value of 27.3 MPa/km. As a result, stress regime in the onshore Victorian Otway Basin is considered to be strike-slip if maximum horizontal stress is calculated using frictional limits or normal if maximum horizontal stress is calculated using the CRC-1 leak-off test. Pore pressure is measured in the CRC-1 borehole with a Modular Dynamic Tester (MDT) and has an average gradient of 8.64 MPa/km. The new estimated maximum pore pressure increase (ΔP_p) which can be sustained within the reservoir is 10.9 MPa (frictional limits) and 14.5 MPa (leak-off test); for the seal is 6.3 MPa (frictional limits) and 9.8 MPa (leak-off test). Fault reactivation risk is again calculated using the FAST technique (Mildren et al. 2005). The two scenarios tested are the same as the previous report (van Ruth and Rogers 2006): one for healed faults (C=5.4 MPa; μ=0.78) and one for cohesionless faults (C=0 MPa; μ=0.6). The orientation of faults with high and low reactivation propensity is similar for healed and cohesionless faults. In contrast, this orientation differs depending on the method used for calculating the maximum horizontal stress magnitude (leak-off test and frictional limits) (Fig. 3.7). In both cases high angle faults striking NE-SW are unlikely to be reactivated. In a strike-slip stress regime (frictional limits) the highest fault reactivation propensity is calculated for high angle faults oriented ESE-WNW and NNW-SSE (Fig. 3.7a and Fig. 3.7c), whereas in a normal stress regime (leak-off test) the high angle faults oriented SE-NW are most likely to be reactivated (Fig. 3.7b and

Fig. 3.7d). The fault segment with highest fault reactivation propensity is on the Naylor South Fault near the crest of the Naylor South sub-structure. Critical pore pressure calculated for cohesionless faults and magnitude of maximum horizontal stresses calculated from leak-off test is 5.6 MPa. However, if maximum horizontal stress is derived from frictional limits the CPP is 0 MPa. This has been ascribed to limitations in the frictional limits theory in estimating magnitude of maximum horizontal stress.

The improvements of this work, with respect to the previous report (van Ruth and Rogers 2006) are mainly to be accounted to the new data available from the drilling of CRC-1. Methodology used to assess fault reactivation and failure of intact rock remained the same, with the introduction of new tested scenarios. However a lack of minimum horizontal stress measurements results in an uncertainty in the definition of the stress regime within the Naylor Field.

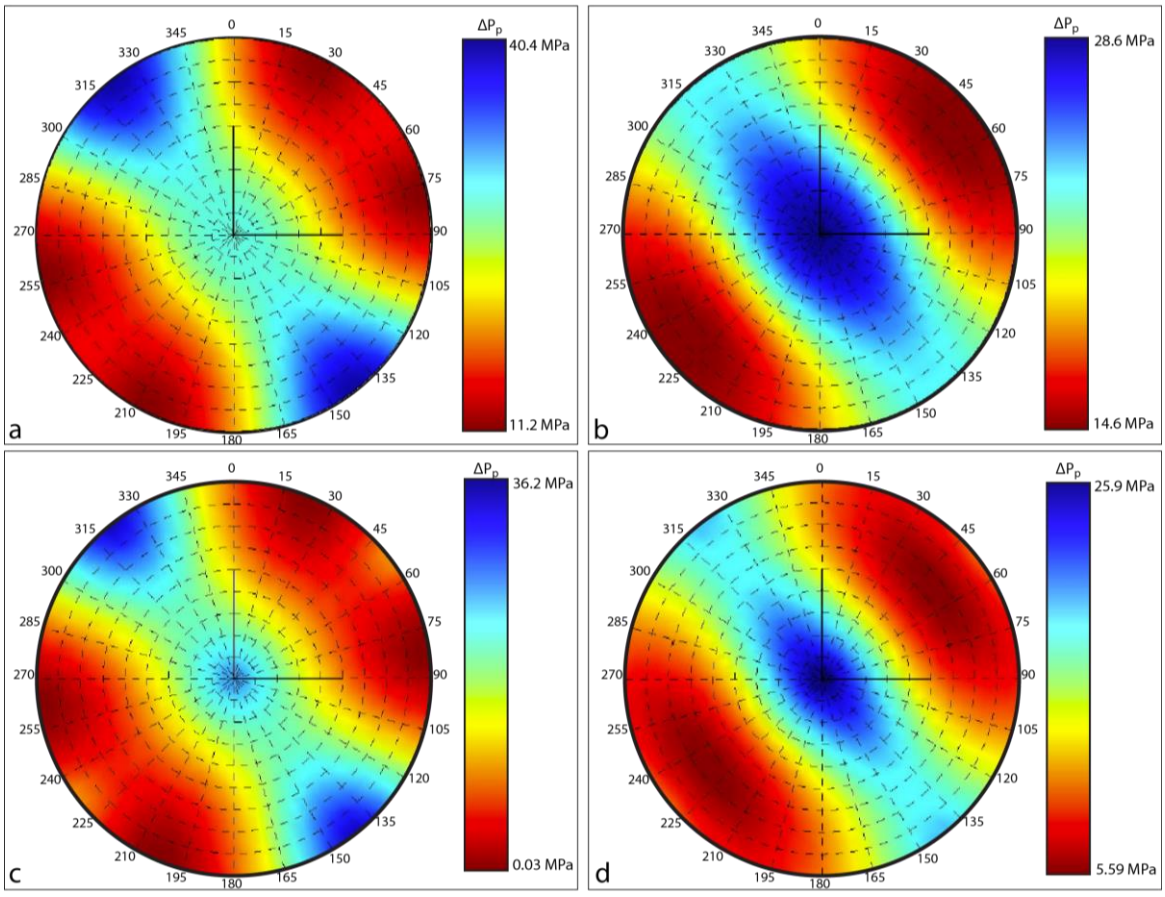

Fig. 3.7: Stereonet showing the reactivation risk (ΔP_p in MPa) for healed faults with maximum horizontal stress calculated using frictional limits theory (a), faults with maximum horizontal stress calculated using leak-off test (b), cohesionless faults with maximum horizontal stress calculated using frictional limits theory (c) and cohesionless faults with maximum horizontal stress calculated using leak-off test (d) at 2025 m in the onshore Otway Basin. Modified after van Ruth et al. (2007).

In 2008 Vidal-Gilbert presented her first paper about reservoir stress path and geomechanical risking in the Naylor Field. Reservoir stress path (*A*) describes the reservoir behavior during depletion/injection and how stresses can be affected by changes in fluid pressure (cf. Chap. 2.3). The aim of her study is to demonstrate that the reservoir stress path is a key point in any fault reactivation analysis technique,

and it may lead to different estimation of the maximum pore pressure increase (ΔP_p) required to cause reactivation. Reservoir stress path is integrated in a synthetic 2D fault stability analysis using pre-existing stress data (van Ruth et al. 2007). In addition to that, a 3D analysis on the basis of previous reports (van Ruth and Rogers 2006, van Ruth et al. 2007) is also carried out introducing the reservoir stress path as pore pressure/stress coupling ratio. The analysis is performed for cohesionless faults with maximum horizontal stress calculated using leak-off test for both constant horizontal stresses (A=0) and for a pore pressure/stress coupling ratio of A=0.5. As a result, the estimated ΔP_p is lower if the horizontal total stresses are considered as constant (ΔP_p =5.6 MPa for A=0) (Fig. 3.8a) with respect to the scenario that introduces a pore pressure/stress coupling ratio into the analysis (ΔP_p =18.5 MPa for A=0.5) (Fig. 3.8b), with a normal fault stress regime assumption.

This study represents a further improvement with respect to previous reports (van Ruth and Rogers 2006, van Ruth et al. 2007), with the introduction of the reservoir stress path into the reactivation risk analysis. The dependence of stresses on changes in pore pressure may better reflect the complexity of poroelastic phenomenon occurring in the reservoir during injection operations. However, lack of constraints on the reservoir stress path value, which is here simply assumed, is a major source of uncertainties in the calculation of fault reactivation propensity.

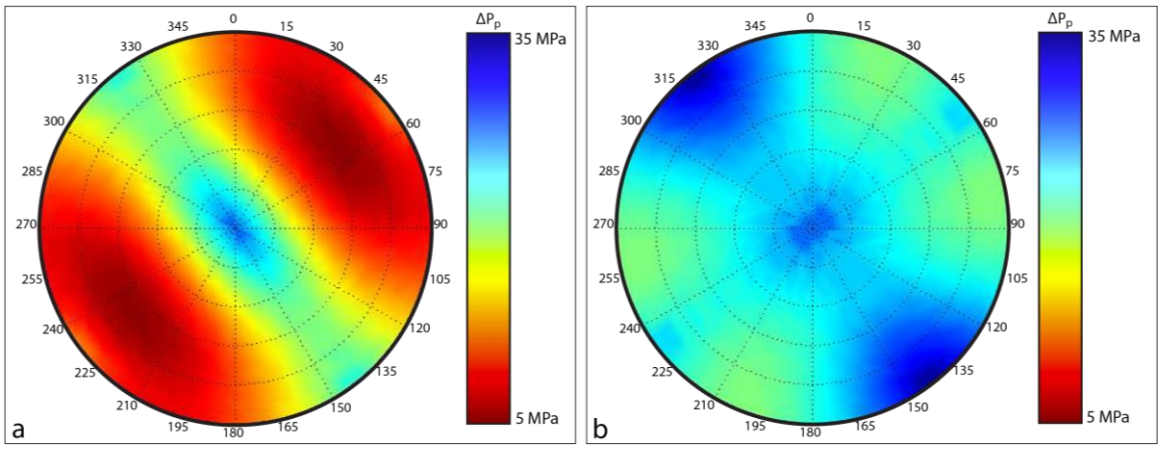

Fig. 3.8: Stereonet showing the reactivation risk (ΔP_p in MPa) for cohesionless faults for constant horizontal stresses (A=0) (a) and for cohesionless faults for a pore pressure/stress coupling ratio of A=0.5 (b). Modified after Vidal-Gilbert (2008).

In 2010 a paper about "Implication for CO_2 injection and storage" has been published by Vidal-Gilbert et al., further improving the work done to investigate the possible geomechanical effect of CO_2 storage in the Naylor Field. Stress data used for the geomechanical model are gathered from previous studies (Bérard et al. 2008, van Ruth 2007). The stress regime computed from this study is inferred to be strike-slip if the maximum horizontal stress is calculated using frictional limits theory (Sibson 1974) and DITF (Drilling Induced Tensile Fracture) or normal if maximum horizontal stress is based on analysis of dipole sonic log data. Reservoir stress path is determined using the solution of Eshelby (Eshelby 1957, Rudnicki 1999) that calculates the effects of geometry and elastic properties on altering the local stress state, resulting in the two extreme estimations: A=0.4 and A=0.8. Stress changes in the

subsurface of the Naylor Field are described by an analytical geomechanical solution, with the reservoir stress path incorporated in the fault reactivation analysis to estimate the minimum pore pressure increase required to cause fault reactivation (ΔP_p). Results of the fault stability analysis indicates that increase of pore pressure (ΔP_p) needed for fault reactivation is generally lower if horizontal stresses are constant (A=0) ranging from 1 MPa in a strike-slip regime (Fig. 3.9a) to 5.3 MPa in a normal stress regime (Fig. 3.9b). Considering a reservoir stress path of A=0.4, these values increase from 1.8 MPa in a strike-slip regime (Fig. 3.9c) to 12.9 MPa in a normal stress regime (Fig. 3.9d). For a reservoir stress path A=0.8 fault stability is not jeopardized in a normal stress regime, whereas it would require an increase in pore pressure of 5 MPa in a strike-slip regime to cause fault reactivation. The orientation of faults with high and low fault reactivation propensity also differs depending on the stress regime assumption. In a normal stress regime, faults orientated NW-SE and dipping 60° have the highest fault reactivation propensity. In a strike-slip stress regime sub-vertical faults that strike 60° from the minimum horizontal stress have the highest fault reactivation propensity.

This latest geomechanical model aims to improve and complete the previous report (Vidal-Gilbert 2008) that first included reservoir stress path into the geomechanical characterization. Here the reservoir stress path is not a simple assumption, but is analytically determined. Limitation of this work is again represented by the lack of a numerical model that could validate the results calculated analytically.

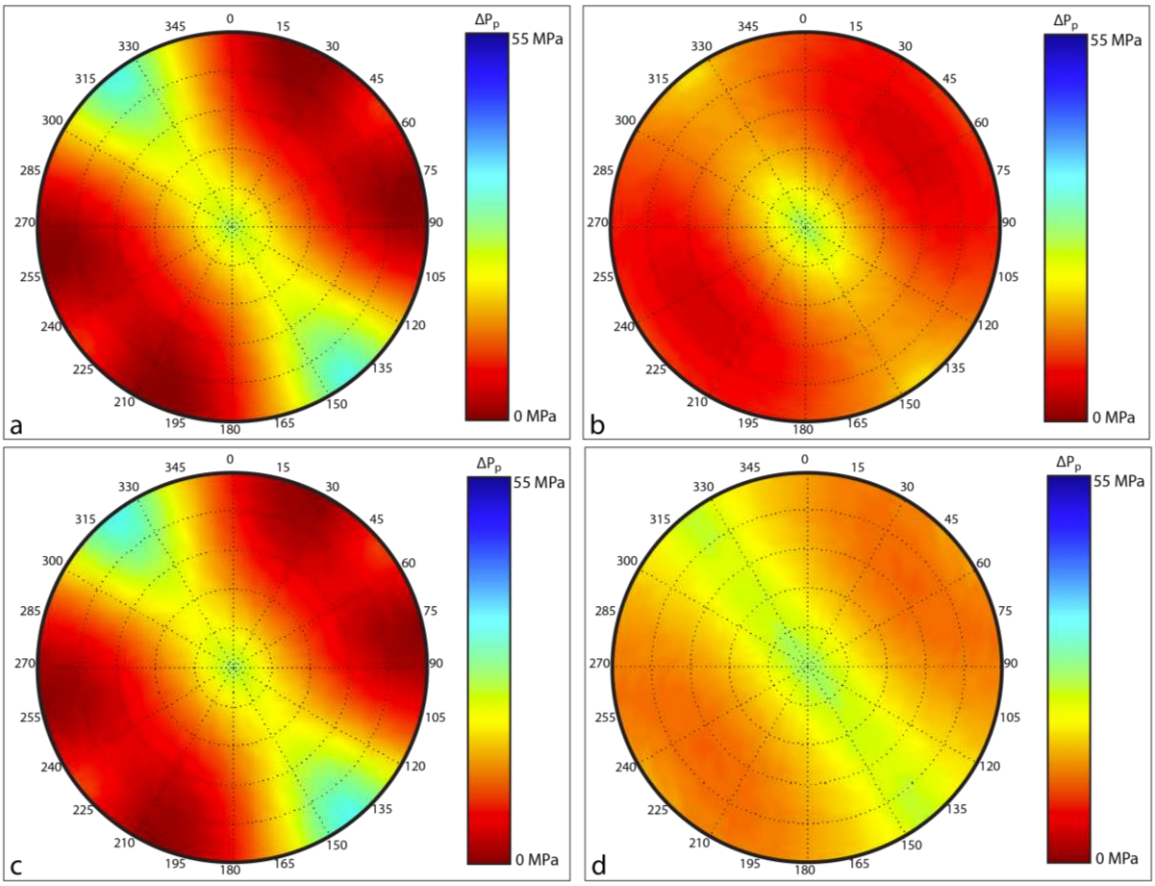

Fig. 3.9: Stereonet showing the reactivation risk (ΔP_p in MPa) for cohesionless faults assuming a reservoir stress path A=0 (constant horizontal stresses) in a strike-slip stress regime (a) and in a

normal stress regime (b), and assuming a reservoir stress path A=0.4 in a strike-slip stress regime (c) and in a normal stress regime (d) at 2025 m depth in the Otway Basin. Modified after Vidal-Gilbert et al. (2010).

To summarize, the four geomechanical models of Naylor Field provide a good indication of the geomechanical characterization of the injection area. However, geomechanical behaviour is analyzed only in terms of analytical solutions that do not take into account the complexity introduced for example by the presence of faults and topology of reservoir layer. Furthermore, these models are sometimes poorly constrained (van Ruth and Rogers 2006, van Ruth et al. 2007) due to lack of in situ measurements that became available later in time. These new rock and stress data, together with the introduction of the reservoir stress path contribute to reduce uncertainties in results provided by the last two studies (Vidal-Gilbert 2008, Vidal-Gilbert et al. 2010). However, some open questions remain and what is certainly missing for validating these analytical results is a numerical model. Furthermore, a flow simulation of CO_2 injection was never attempted before for the Naylor Field and only assumptions were used to account for the change in pressure. Moreover, reservoir compaction and surface subsidence were not investigated in previous models.

This thesis aims to fill this gap and provide the first 3D geomechanical model for the Naylor Field. A list of the data available at this time is provided in Tab. 3.1. Input data for the geomechanical model are chosen in accordance to the previous models here presented, with the aim to compare the results obtained.

	PETREL® MODEL	WELL LOGS	LITERATURE REVIEW
MODEL GEOMETRY			
Horizon geometry	Horizon modelling		
Fault geometry	Fault modelling		
MATERIAL PROPERTIES			
Density		RHOZ – density log	
Young's modulus		DTCO/DTSM – wave slowness	
Poisson Ratio		DTCO/DTSM – wave slowness	
UCS (Uniaxial compressive strength)			Tenthorey et al. (2011)
Angle of internal friction (intact rock)			Tenthorey et al. (2011)
Friction angle (faults)			Vidal-Gilbert et al. (2010)
Cohesion			Tenthorey et al. (2011)
Rock compressibility			Bouquet et al. (2009)
Porosity		SPHI – sonic porosity log	
Permeability		KTIM – permeability log	
FLUIDS PROPERTIES			

Chemical composition			Vidal-Gilbert et al. (2010)
Saturation			Bouquet et al. (2009)
Relative permeability			Bouquet et al. (2009)
Capillary pressure			Bouquet et al. (2009)
DEVELOPMENT HISTORY			
Production data			Operational reports
Injection data			Operational reports
Completions			Operational reports
STRESS MEASUREMENTS			
Orientation S_{HMax}		FMI – Borehole breakouts	Lawrence (2011)
Magnitude principal stresses		Leak-off tests (S_{hmin}), Inversion sonic logs	van Ruth (2007)

Tab. 3.1: Summary table of all input data required for geomechanical modelling and their sources.

4 Regional Geology

An overview of the regional geology of Otway basin is necessary to provide a background to the geological and structural model of the storage site (6), starting point for the geomechanical model. A particular emphasis is given to the geodynamic evolution of the Otway Basin (0), since major tectonic stages are the object of paleostress modelling (10). Knowledge of paleostress regimes acting in the past in Otway Basin allows to understand and explain the generation of fractures network through time (11.4). Most of the information related to the geodynamic evolution of the Otway basin and its stratigraphy has been already summarized in the Releases of Australian Offshore Petroleum Exploration Areas (2009, 2011). However all the authors are cited for the contribution they made in these releases.

4.1 Otway Basin setting

The Otway Basin is located within the state of Victoria and extends both onshore and offshore. It is described as a passive margin rift basin elongated in a NW direction (Schneider et al. 2004, Tassone et al. 2014)(Fig. 4.1). The Otway Basin has been exploited in recent years to provide gas supply to the state of Victoria, with pipelines that connect it to all the surrounding areas, comprising also the nearby island of Tasmania.

Fig. 4.1: Location of Otway Basin in South-East Australia. Courtesy of Geoscience Australia.

The Otway Basin is located in the continental margin of the east central portion of Southern Australia (Von der Borch et al. 1970) and was formed during Gondwana

break-up and the Antarctic-Australian separation, which occurred in two distinct stages in the Early Cretaceous (Williamson et al. 1990). Sediment filling of the Otway Basin dates back to a time range from Upper Jurassic to Holocene, covering both onshore and offshore areas.

The rifting process in southern Australia started during the Oxfordian (about 158 Ma) and then extended towards Otway, Bass and Gippsland basins during the Tithonian (about 150 Ma) (Norvick and Smith 2001). However, presence of rift basalts in the Polda basin suggest that the rifting might have started already during Neoproterozoic (about 600 Ma) (Rankin 1993).

4.2 Tectonic development

The present-day geometry of the Otway Basin is the result of the superposition of basin phases spanning from Late Jurassic to present. These events represents the effects of the Southern Australia breakup, normally divided in three phases (Norvick and Smith 2001).

4.2.1 Phase 1 – Late Jurassic to Early Cretaceous Rift

Early Rifting (Late Jurassic-Early Cretaceous)

Rifting in the Otway Basin began in the Late Jurassic (Fig. 4.2) as a consequence of a NW-SE extension that created a series of E-W to NW-SE asymmetric half-grabens (Cooper and Hill 1997, Williamson et al. 1990) . This structural arrangement has been successfully compared with oblique-rift analogue models (Cooper and Hill 1997), showing a strong influence of the basement during the extension of the basin (Bernecker and Moore 2003, Moore 2002). Lateral extension of the Jurassic half-grabens was not significant, however constant subsidence during Early Cretaceous promoted a further expansion of the rift basins. The half-grabens were mainly filled with non-marine fluvio-lacustrine sediments belonging to the Otway Group (Norvick and Smith 2001).

Fluvial sediments composed mainly by dacitic tuff derived from nearby volcans were deposited in the Otway Basin during the Barremian (120 Ma). As rate of faulting decreased in the Gippsland and onshore Otway Basin, a sagging environment gradually took place within a transtensional regime. In particular, depocentres in Otway ranges formed an en echelon pattern due to a sinistral strike-slip movement along NW trending, pre-existing basement structures, thus producing complex rift geometries (Norvick and Smith 2001). However, this extensional phase it is not yet fully understood especially in the Otway Basin, due to the fact that those structures were overprinted during the Late Cretaceous rifting (Teasdale et al., 2002).

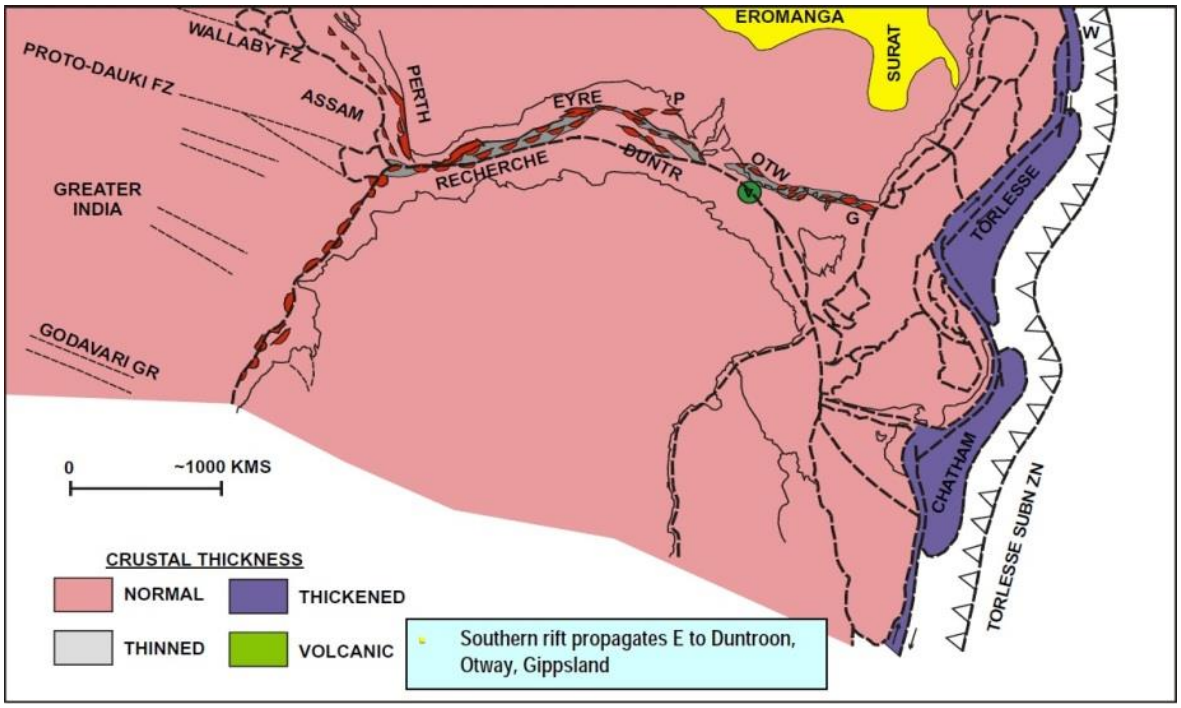

Fig. 4.2: Late Jurassic reconstruction, early Tithonian (145 Ma), after Norvick and Smith (2001).

Rift to Sag Transition (Aptian-Albian)

The extensional faulting system that drove the first phase of early rifting during Late Jurassic and Early Cretaceous decreased its activity in the early Aptian (125 Ma). The consequent thermal subsidence lead to an overprinting of the old footwall blocks across most of the Otway Basin. Sediments deposited during this period are composed by volcaniclastic detritus derived mainly from volcanic complexes located in both Otway and Gippsland Basin (Bryan et al. 1997).

4.2.2 Phase 2 – Mid-Cretaceous to Mid-Eocene Rifting and Breakup

Compression, Uplift and the Otway Unconformity (mid-Cretaceous)

In the late Albian (100 Ma) a significant compression phase marked the end of the rifting, by producing an angular unconformity, the Otway Unconformity, recognized across the entire extent of the basin (Partridge 2001). The associated inversion affected multiple areas such as the Otway Ranges and the Cape Otway. However, magnitude of this inversion was not uniform across the basin, and some areas showed only minor uplift. These uplift and erosion affected the whole basin (onshore Otway, Gippsland and Bass Basins), but they were mostly concentrated in rhombic areas, previously belonging to depocentres. Finally, multiple episodes of inversion lead to a physical separation of the three basins. Also depocentres located in the Otway Ranges, formed in the Early Cretaceous, underwent an inversion phase. Occasionally, faults that originally formed the half-grabens at the beginning of the rifting were affected by overturned folding and thrusting (Norvick and Smith 2001).

Second phase of rifting (Late Cretaceous)

Following a 6.5 Ma hiatus, during Turonian (93 Ma) a new phase of extension and subsidence took place, forming additional rift basins along the boundary of eastern Australia, such as the offshore Otway Basin (Norvick and Smith 2001). Basin development was again strongly controlled by rifting mechanisms, until the continental break up during Maastrichtian (65 Ma) (Lavin 1997).

Direction of extension of this renewed rifting changed to a NW-SE orientation, whereas the early stage of rifting was characterized by a N-S directed extension. As a consequence, if the structural styles from the two rifting stages are compared, the arrangement appears different (Teasdale et al. 2002). Although the setting of rifts in during this second phase of rifting is not yet clear, they are supposed to be arranged according to an X-pattern, with the offshore Otway Basin lying on the NW branch (Norvick and Smith 2001). This new setting caused an overprinting of the structures previously created during the Late Cretaceous. A sinistral-strike movement localized along the eastern margin of the basin lead to the creation of transpressional structures with both extensional and compressional components, particularly in the Shipwreck Trough and Mussel Platform.

Continental Break-up (Santonian - late Maastrichtian)

In the Santonian (85 Ma) ocean crust started forming for the first time along the eastern boundary of the Australian continent, including the southern portion Tasmanian Sea, as a result of a ENE extension occurring between Australia and the Lord Howe Rise (Teasdale et al. 2002). As a consequence of the seafloor spreading, volcanic complexes developed along the boundary of rift margins. In the Great Australian Bight first ocean crust started forming in the early Campanian (83 Ma) (Fig. 4.3) and then during the late Campanian (75 Ma) the spreading extended towards south (Norvick and Smith 2001). This is the result of a NNW extension localised along the southern boundary between Australia and Antarctica, accompanied by significant subsidence along the entire southern margin (Teasdale et al. 2002). The Otway Basin was affected by both of these extensional stress regimes, resulting in a NW-SE directed extension.

The late Maastrichtian break-up between Australia and Antarctica, and the contemporaneous opening of the Southern Ocean, produced a moderate uplift across the basin that eventually resulted in the creation of Late Maastrichtian Unconformity. This unconformity marks the separation between pre-rift and post-rift strata (Lavin 1997). At the end of Cretaceous, the area of Otway Ranges was subjected to minor faulting, extensive uplift and local volcanic activity (Norvick and Smith 2001).

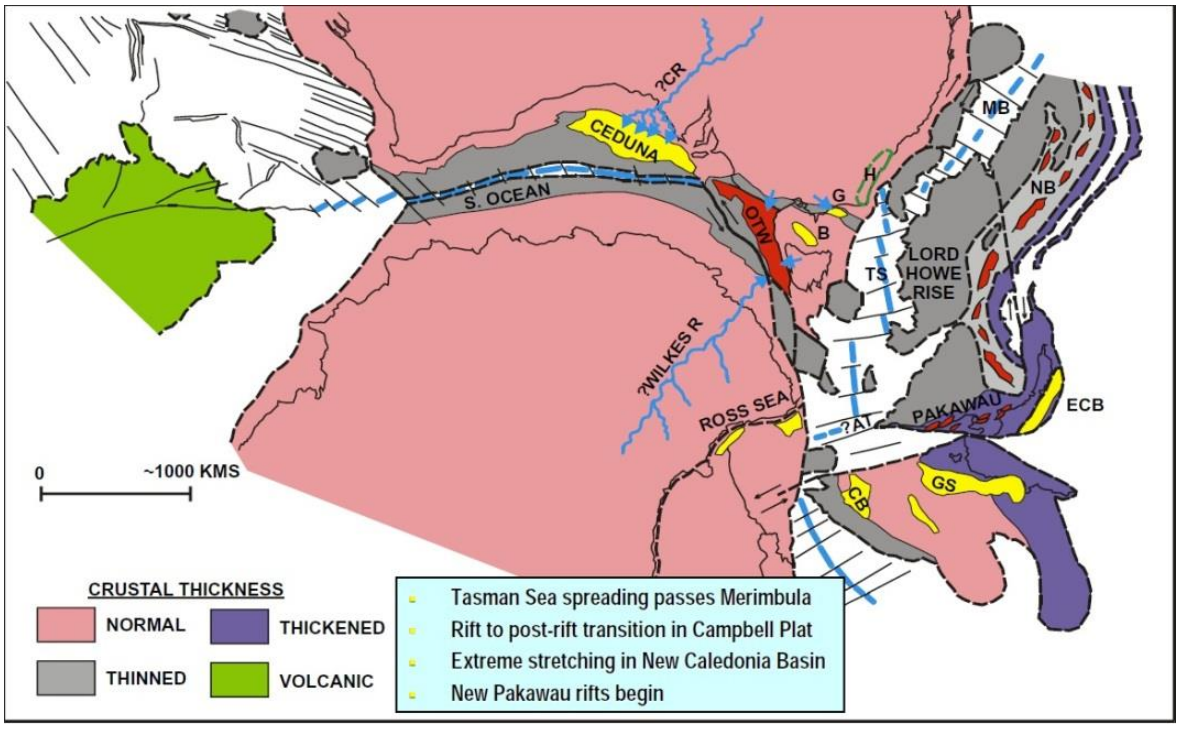

Fig. 4.3: Late Creataceous reconstruction, early-Campanian (80 Ma), after Norvick and Smith (2001).

4.2.3 Phase 3 – Collapse of the continental margin

Seafloor Spreading and local Eocene inversion (Paleocene-early Oligocene)

At the end of Maastrichtian (65 Ma), the peneplain resulting from the formation of the Late Maastrichtian Unconformity was flooded in correspondence with the first major transgression of the newly-formed Southern Ocean (Lavin 1997). During Lutetian (44 Ma), rate of spreading of the Southern Ocean significantly increased. The direct consequence was a rapid thermal subsidence accompanied by marine transgression on several continental margins areas. Subsequently, ocean crust started forming also within the Otway Basin and then expanded offshore towards the western border of Tasmania (Norvick and Smith 2001) (Fig. 4.4). The change from rifting to drifting resulted in a stress regime inversion along the southern border of Australian continent, from NW-SE extension to ~N-S compression, most likely caused by the onset of ridge-push forces. This new compressional phase resulted in minor inversion of structures within the Otway and Gippsland Basins. Slight changes in direction and spreading rate suggest the occurrence of multiple inversion events. That also implies that the distribution of those inversion events along the southern margin of Australia is not evenly distributed (Teasdale et al. 2002). The Middle Eocene Unconformity can be recognised in all basins located along the southern Australian margin. It is associated with minor tectonic activity related to an increase in seafloor spreading rate in the Southern Ocean (Yu 1988). A continued sedimentation was in place during the Tertiary in the Otway Basin, mainly due to thermal subsidence following the continental breakup. Afterwards, oceanic crust start forming also between Antarctica and the South Tasman Rise during the late Eocene (35 Ma): this event is related to the onset of Antarctic glaciation (Norvick and Smith 2001).

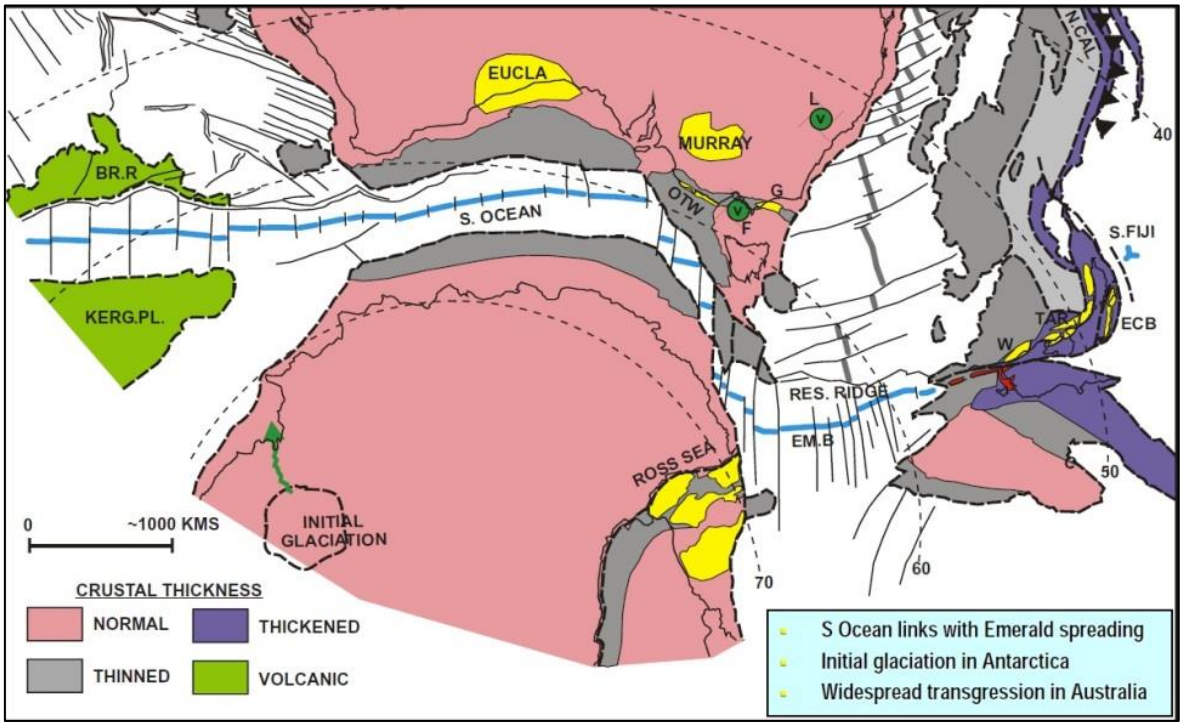

Fig. 4.4: Mid-Eocene reconstruction (45 Ma), after Norvick and Smith (2001).

Basin inversion, desiccation and volcanism (late Oligocene – present day)

In the mid-Oligocene, circum-Antarctic currents were established, along with a significant increase in glaciation of the Antarctic sea and progradation of sediments on the shelf. In the Otway Basin, cool temperate carbonates were sedimented (Norvick and Smith 2001). Following a period of renewed extension in the NW direction, Otway, Gippsland and interior Australia were affected during Miocene by inversion folding. A intraplate stress orientated ~ENE caused the reactivation of weak structures in the Otway ranges. The consequent uplift is responsible for the present-day topography (Teasdale et al. 2002). About 10 Ma, dessiccation started on inland Australia, causing a reduction is size of most rivers, while an intraplate volcanism affected the area of the Eastern Highlands (about 27-14 Ma). During the Pleistocene, dessication continued on the interior of the Australian continent, thus favouring the deposition of aeolian sands. In the Otway Basin, eruption of basalts took place (3-0 Ma), probably connected to a phase of mantle activity (Norvick and Smith 2001). Currently the Otway Basin is subjected to a normal faulting stress regime orientated 142° N (cf. Chapter 5).

4.3 Stratigraphy

Stratigraphy of the Otway Basin is commonly subdivided into five unconformity-bounded successions (Tupper et al. 1993): the Otway, Sherbrook, Wangerrip, Nirranda and Heytesbury groups (Fig. 4.5). During the first rifting phase in Early Cretaceous, fluvial and lacustrine sediments corresponding to the Otway Group were deposited. Subsequently, in the Late Cretaceous, delta and marginal marine environment were in place (Norvick and Smith 2001), leading to the deposition of the Sherbrook Group. Waarre Formation, the main target for exploration, is included in

this group (Miyazaki et al. 1990). Wangerrip and Nirranda groups were deposited in deltaic and nearshore environments during late Eocene. Afterwards, an increase in sea level led to an open marine environment in which carbonates were deposited.

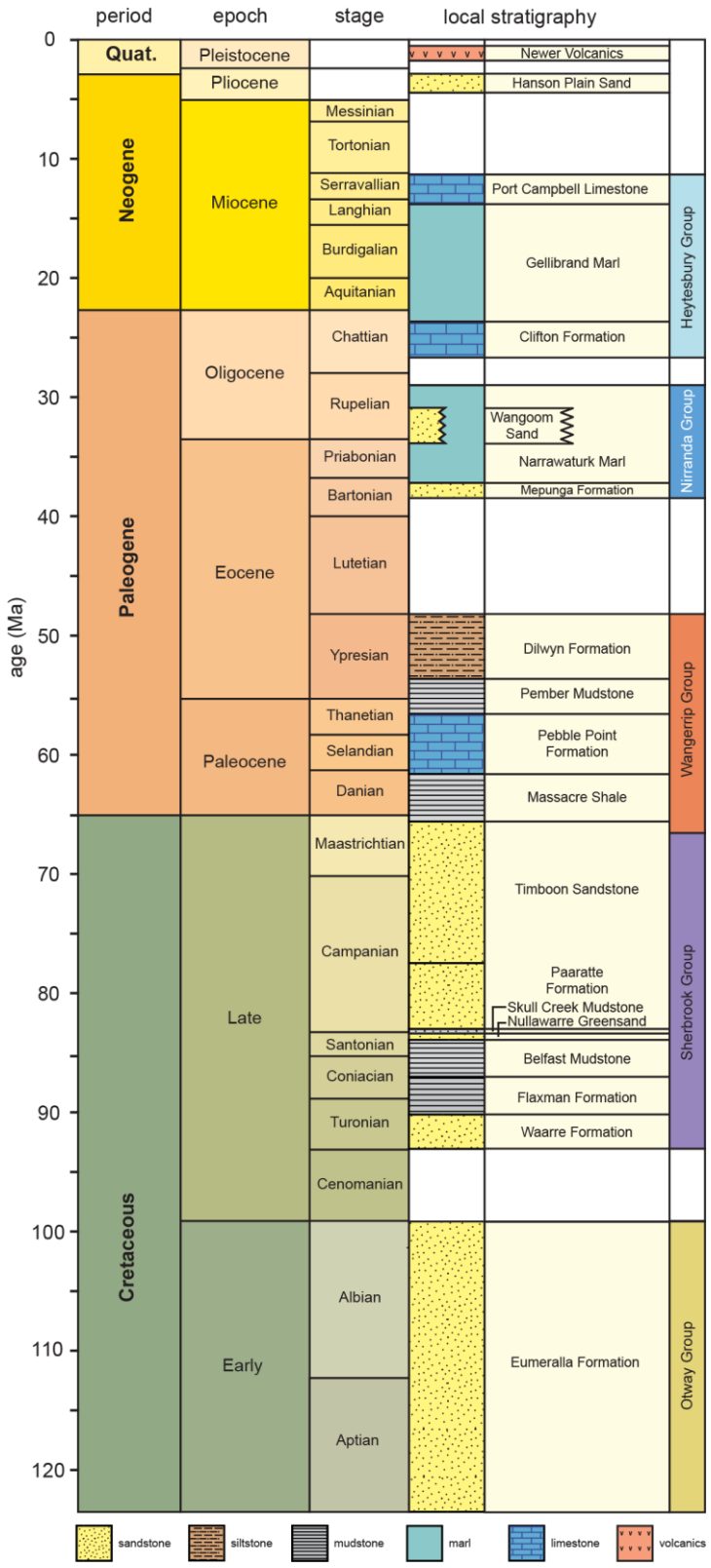

Fig. 4.5: Stratigraphic chart of Otway Basin, from Early Cretaceous to present, modified after Ziesch et al. (subm.).

The **Otway Group** was deposited during the first rifting event, filling grabens and half-grabens (Bernecker and Moore 2003). It is mainly composed by continental and fluvio-lacustrine sediments that may be up to 8000 m thick. The basal formation is the Casterton Formation, comprising syn-rift lacustrine sediments and flow-basalts. The overlying Pretty Hill Formation contains mostly sub-lithic and fluviatile sediments. Proceeding upwards, Laira Formation is composed by lower energy fluvial and lacustrine sediments, while the Katnook Sandstone was deposited in a fluvial environment characterized by higher energy (Kopsen and Scholefield 1990). These lacustrine sediments and coals represent a potential source for both oil and gas (Trupp et al. 1994). These three formations are informally grouped in the Crayfish Subgroup (Kopsen and Scholefield 1990), mainly identified in the onshore portion of the Otway Basin. During the early Aptian (125 Ma) a broad thermal sag basin developed and the earlier half-graben were filled by the Eumeralla Formation, reaching a maximum thickness of approximately 3000 m. Sedimentation of this formation occurred across a series of different depositional environments, such as fluvial flood plain, coal swamp and lacustrine settings. Furthermore, the Eumeralla Formation contains large quantity of volcaniclastic material transported from volcanic complexes located to the east of Otway Basin (Bernecker and Moore 2003, Bryan et al. 1997). Coal inclusions founded within the formation are considered to be a potential source for gas and some oil (Tupper et al. 1993). Indeed, most of the hydrocarbons produced in the fields within the Otway Basin are derived from Eumeralla Formation.

Sherbrook Group was deposited unconformably above the Otway Group, following the first marine incursion into the Otway Basin, and it is formed by sandstones and mudstones up to 5000 m. Deposition of those sediments dates back to the second rift phase and took place in coastal plain, deltaic and restricted marine environments (Partridge 2001). Sedimentation started between the Cenomanian (99 Ma) and the Turonian (93 Ma) with thin barrier-lagoonal sandstones and mudstones in South Australia. The Waarre Formation represents the first clastic influx, following the breakup, into the basin. It is composed by an interbedded sequence of quartzose sandstone, mudstone, carbonaceous mudstone and coal (Mehin and Constantine 1999). Sedimentation occurred in deltaic to marine depositional environments. Similarly to the Eumeralla Formation, coal inclusions are considered as a regional potential source (Bernecker and Moore 2003). The upcoming Flaxman Formation comprises coastal barried sandstones. Sandstones belonging to both Waarre and Flaxman formations have good reservoir characteristics and therefore are a major exploration target in the Otway Basin (Mehin and Constantine 1999). Exploration focused mainly on the Port Campbell Embayment onshore area. Belfast Mudstone was deposited above Flaxman Formation. It is formed by thick, open-marine, prodeltaic, carbonaceous mudstones sedimented during a period of rapid subsidence and high eustatic sea levels. Thanks to its low permeability, the Belfast Mudstone represents a regional seal across for the Otway Basin (Jones et al. 2000). The Paaratte Formation was deposited in a deltaic depositional system that prograded over sediments belonging to the Belfast Mudstone. Lagoonal and proximal deltaic facies

are the majority of sediments forming the Paaratte Formation. In the offshore part of the Otway Basin, sequences of stacked reservoir/seal couplets are attractive exploration objectives (Lavin 1998). In onshore areas, the Paaratte Formation blends laterally into the Timboon Sandstone, a more proximal deltaic formation. Sandstones from both the Paaratte Formation and Timboon Sandstone have very good reservoir characteristics (Miyazaki et al. 1990).

The **Wangerrip Group** marks the onset of passive margin sedimentation after the end of rifting, therefore it lies unconformably above the Sherbrook Group. It may reach up to 700 m and it is composed by sandstone and mudstone deposited in coastal plain, deltaic and inner shelf environments (Miyazaki et al. 1990). The Massacre Shale, a thin basal unit, was deposited between late Maastrichtian and early Paleocene (Partridge 2001). Its characteristics allow it to act as local seal for Sherbrook Group reservoirs. Proceeding upwards, the Pebble Point Formation consists of a ferruginous deltaic succession of fine to very coarse-grained and argillaceous sandstone. It is considered a potential reservoir and multiple occurrence of oil and gas were found in onshore Victoria (Mehin and Constantine 1999). Pember Mudstone overlies the Pebble Point Formation and it is formed by micaceous silty claystone and minor fine-grained sandstone. It is considered to be a potentially good regional seal (Bernecker and Moore 2003). The Dilwyn Formation consists of sandstone and mudstone. Sedimentation occurred in a variety of marine, deltaic and coastal settings (Miyazaki et al. 1990). Evidences of marine incursions are recorded by a complex inter-fingering of the Pember Mudstone together with the Dilwyn Formation.

Wangerrip Group is separated from the **Nirranda Group** by a major unconformity. This unconformity marks the increase in spreading rates in the Southern Ocean occurred during Lutetian (44 Ma). As a result, thermal subsidence and marine transgression took place in the Otway Basin (Norvick and Smith 2001). Mepunga Formation is formed by interbedded sandstone and mudstone that were deposited in nearshore to offshore marine settings. As the transgression continued, an open marine depositional setting was established and Narrawaturk Formation, a fine-grained succession with glauconitic inclusions, was deposited. During Oligocene, a major fall of the sea level led to erosion on the shelf. Subsequently, low-stand turbidite fans were formed on the continental slope (Lavin 1998).

The early Miocene was characterized by the return of marine conditions. Heytesbury Group was deposited, consisting of calcareous mudstone, marls and sandy limestone. During Pliocene the Otway Basin underwent phases of inversion followed by deposition of fluvial sands, which continues up to present day (Norvick and Smith 2001).

5 State of stress

5.1 Present-day state of stress of Southern Australia

Regional stress field magnitude and orientation are essential in geomechanical modelling (7 and 9) to provide boundary conditions. Present-day state of stress is significant for assessing the risk of fault reactivation (including the prediction of breached and live hydrocarbon columns) and to drilling-related issues such as wellbore stability. In particular, its knowledge has been proven effective in understanding geomechanical issues in the South Eastern Australian Basin including: fault reactivation and seal potential in the Penola Through (Lyon et al. 2005), 2005); potential CO_2 sequestration sites in the Port Campbell embayment (Tenthorey et al. 2013, Vidal-Gilbert et al. 2010); wellbore stability/sand production and natural fracture-enhanced permeability in the offshore Gippsland Basin and potential CO_2 sequestration sites in the offshore Gippsland (Nelson and Hillis 2005).

Australia is considered to be a passive margin (cf. Chap. 0). A passive margin is an area located within plates close to the border between continental and ocean crust and therefore not subjected to tectonic activity (Fig. 5.1) (Hillis et al. 2008). Nevertheless, intraplate deformation could still affect passive margins through the transmission of plate boundary forces that may produce local deformation in zones of intraplate weakness (Sandiford et al. 2004). Possible sources of intraplate deformation are also related to mantle activity (Müller et al. 2000) or processes connected to presence of hotspots (Brodie and White 1994).

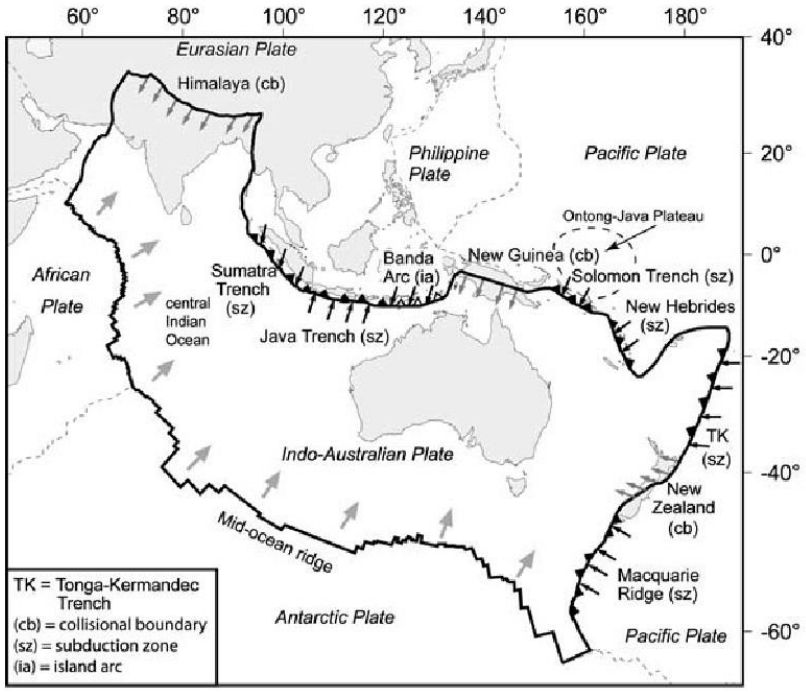

Fig. 5.1: Indo-Australian plate showing the plate boundaries and forces. Large grey arrows indicate the mid-ocean ridge push force, small grey arrows indicate resisting continent-continent collisional forces, the small black arrows indicate slab pull forces (Hillis et al. 2008).

Evidences of Neogene-to-Recent intraplate deformation have been recognized across the Australian continent through structural and geomorphological studies. Main aim of those studies was to investigate a correspondence between stress measurements from earthquake focal mechanism solutions and borehole breakouts, and geological records (Hillis and Reynolds 2000). Furthermore, the objective was to understand whether distant plate boundary forces could be considered responsible for the intraplate tectonic stress field (Hillis et al. 2008).

The Australian continent is entirely located within the Indo-Australian Plate. Orientation of present-day maximum horizontal stress has been determined using different methodologies such as earthquake focal mechanism solutions, borehole break-outs, drilling-induced tensile fractures and hydraulic fracture tests (Hillis and Reynolds 2003). Generally, in situ stress measurements fit well with the regional orientation, which varies across different areas of the continent. Such variation is supposed to be related to the plate boundary forces acting at the margins of the Indo-Australian Plate (Sandiford et al. 2004). Orientation of the present-day maximum horizontal stress is East-West in Western Australia and rotates NE-SW along the northern Australian margin and in central Australia. This NE-SW direction is perpendicular to the collisional boundary of the Indo-Australian plate opposite to New Guinea. This may suggest that collisional plate boundary segments strongly control intraplate stresses (Hillis et al. 2008). Models built balancing the ridge push force associated with the SW boundary of the Indo-Australian plate against the collisional segments of the NE boundary, successfully reproduced rotation in maximum horizontal stress orientation observed at continental scale (Coblentz et al. 1998). Such models confirm that although the present-day maximum horizontal stress orientation is not parallel to the direction of plate motion (as normally it is), it can be explained by taking into account a first-order control by plate boundary forces.

The stress responsible for intraplate deformation can be distinguished in two different components: stress transmitted from plate boundaries and local stresses (i.e. tractions derived from mantle activity or processes related to presence of hotspots) (Hillis et al. 2008). Generally, the present-day maximum horizontal stress orientation in continental areas is constant over large distances and parallel to the direction of absolute plate velocity (Zoback 2010). From this observation, it has been concluded that plate boundary forces are the principal responsible for the generation of the intraplate stress field (Zoback 1992). In the Australian continent in contrast, stress orientations show significant variations and are not often parallel to the NNE direction of plate motion (Fig. 5.2) (Hillis et al. 2008). Moreover, seismicity and related neotectonic deformation are observed in limited areas, thus suggesting that additional factors are involved in the pattern of intraplate deformation (Reynolds et al. 2006). This localization of deformation can be ascribed to three possible causes: the orientation of passive margins in comparison to the present-day stress, overpressuring of faults that facilitates reactivation and thermal weakening of the crust that limits the deformation in weak areas (Hillis et al. 2008).

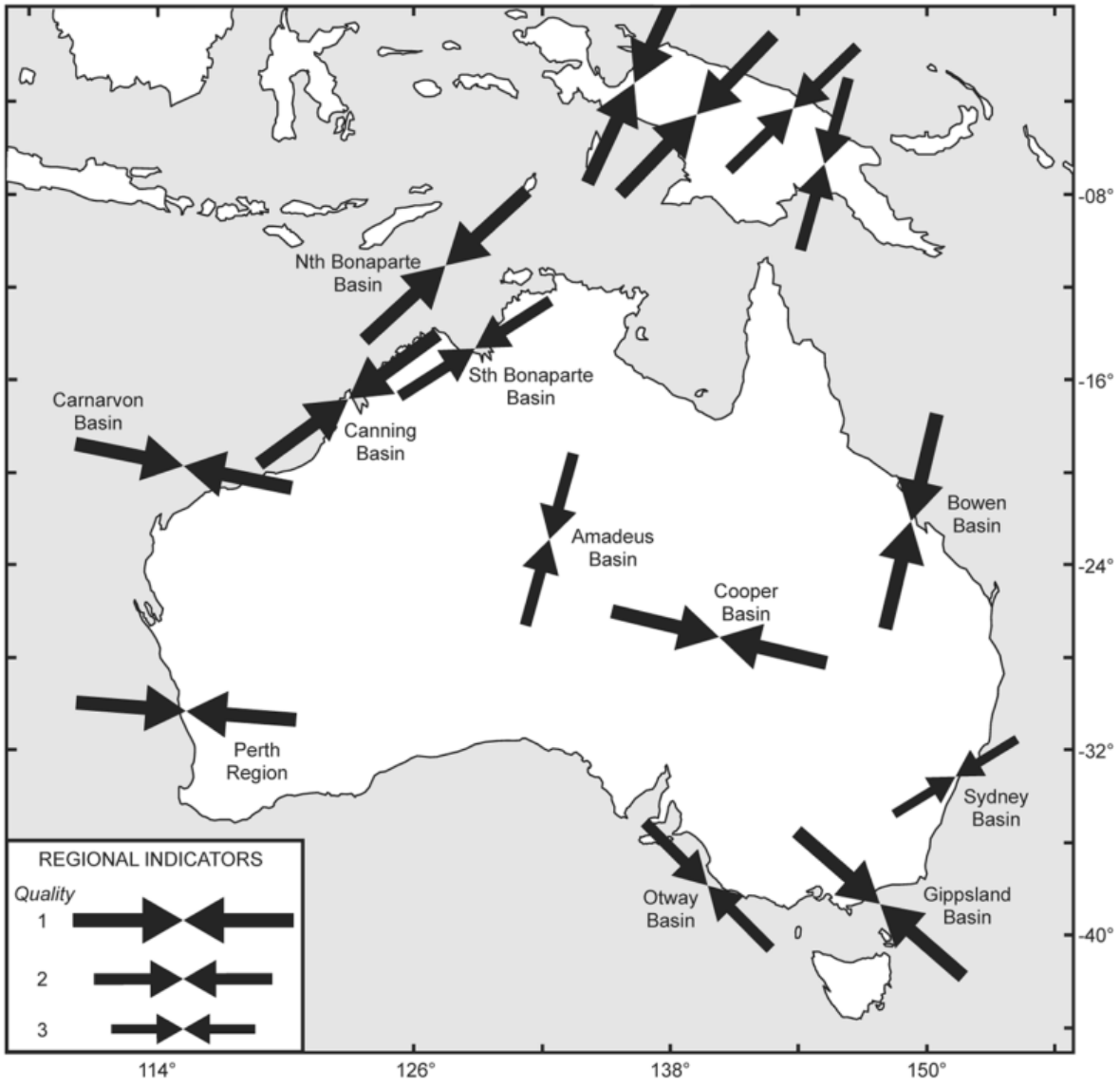

Fig. 5.2: Australia present-day stress map (Hillis and Reynolds 2003).

5.2 Seismicity and neotectonics

The Australian continent has a high level of seismicity since the bulk seismogenic rate varies from $\approx 10^{-17}$ s^{-1} to $\approx 10^{-16}$ s^{-1} in most south-central Australia. Such a rate may lead to a significant amount of deformation (Johnston 1994). In Australia four zones of enhanced seismicity (Fig. 5.3) have been defined by earthquake epicentral locations: SE Seismic Zone; the Flinders Seismic Zone; the SW Seismic Zone of SW western Australia, the NW Seismic Zone (Hillis et al. 2008). Earthquake focal mechanisms suggest a present-day maximum horizontal stress orientated NW-SE along the SE Australian passive margin, with a small rotation from 125°N in the South Australian Otway Basin to 135°N in the Victorian Otway Basin, to 140°N in the Gippsland Basin (Nelson et al. 2006). A composite fault plane solution derived from four eastern Victorian earthquakes indicates the presence of a reverse fault mechanism associated with a present-day maximum horizontal stress oriented 145°N (Allen et al. 2005).

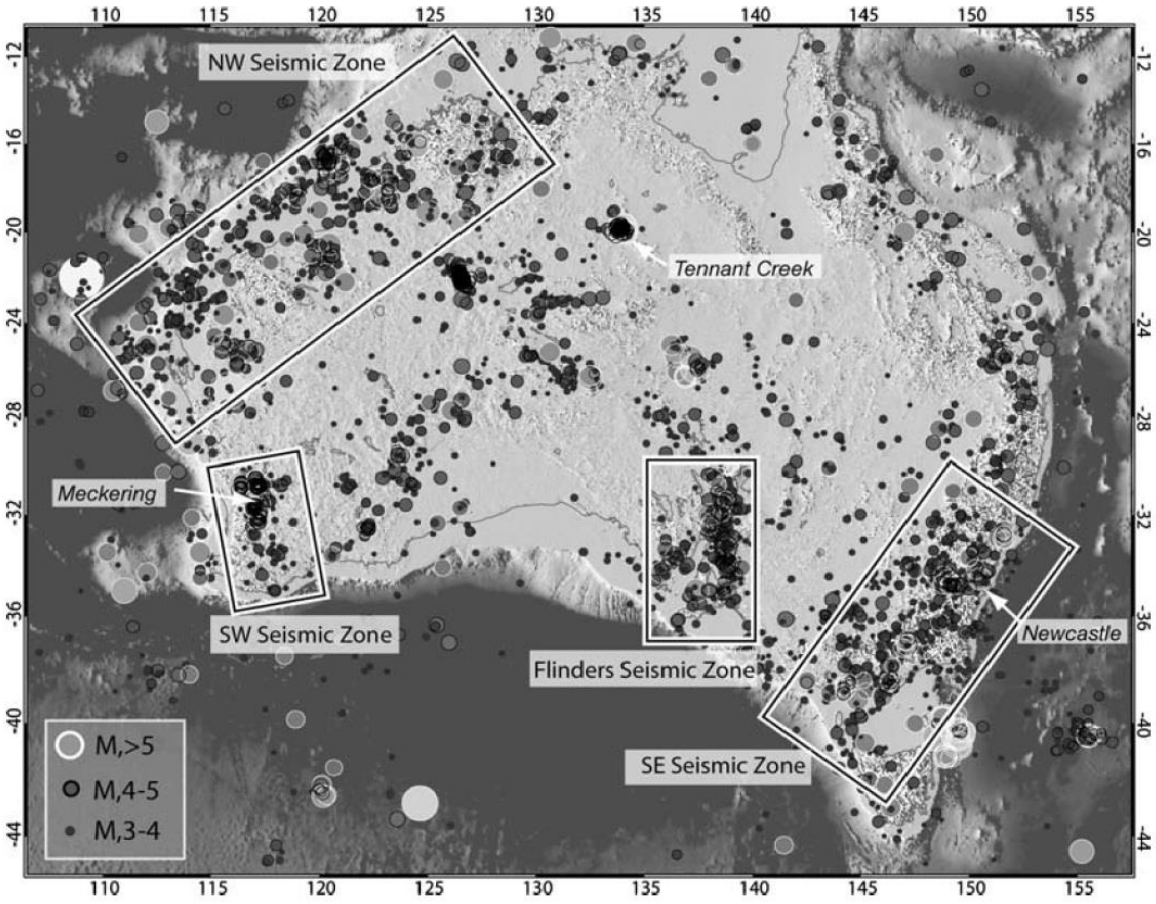

Fig. 5.3: Distribution of M>3 earthquakes and designated seismic zones in Australia (Hillis et al. 2008).

Neogene-to-recent tectonic activity is documented in many areas of Australia, with the presence of prehistoric fault scarps and ongoing earthquake activity. All Quaternary faults identified onshore are related to purely dip-slip or oblique-slip reverse movement. (Hillis et al. 2008). Within the Flinders Seismic Zones, fault kinematic data from palaeoseismicity suggest a palaeomaximum horizontal stress orientation orientated E-W (Sandiford 2003). Prehistoric SE Australian earthquake magnitudes M range from M=5.8 to 7.2 (Clark and McCue 2003), which is aligned with the largest recorded Australian earthquakes. Within the Australian SE passive margin several evidence for Miocene-Recent deformation can be found (Hillis et al. 2008). For instance, the Minerva Gas Field lies on inversion anticline striking towards NE which may be related to a period of compression dating back to Miocene-Recent (Schneider et al. 2004). In the Otway Ranges analysis of strandlines suggests the occurrence of ≈200 m of uplift since early-mid Pliocene (Sandiford et al. 2004).

5.3 *In situ* stress tensor in Otway Basin

A review of the *in situ* stress tensor data collected through years is here exposed to provide information about the present-day regional stress field. Knowledge of orientation and magnitude of the principal stress is essential in any geomechanical analysis. Those stress data are used as input for the geomechanical models presented in this thesis.

5.3.1 Maximum horizontal stress orientation

The maximum horizontal stress orientation (S_{Hmax}) is an important parameter especially in planning of deviated and horizontal wells. Besides, it controls the direction of propagation of fractures and faults. S_{Hmax} orientation is commonly determined from stress-induced borehole breakouts and drilling-induced tensile fractures (DITFs) (Zoback et al. 2003). In vertical wells borehole breakouts elongates along the wellbore in the direction of S_{Hmin} (i.e 90° from the direction of S_{Hmax}) and DITFs forms in the direction of S_{Hmax}.

Measurements of the average S_{Hmax} orientation in SouthEast Australia derived from the interpreted breakouts report an orientation of ≈125±13°N, whereas from the interpreted DIFTs is ≈124°±8N (Nelson et al. 2006). However, information available after the drilling of CRC-1 and CRC-2 reports an *in situ* S_{Hmax} orientation of 142±5°N determined from breakouts interpreted in the resistivity image log (FMI™, Formation MicroImager)(Fig. 5.4)(Lawrence 2011, van Ruth 2007). This orientation is broadly consistent with a NW-SE maximum horizontal stress orientation in the onshore Victorian Otway Basin (Hillis and Reynolds 2000, Nelson et al. 2006).

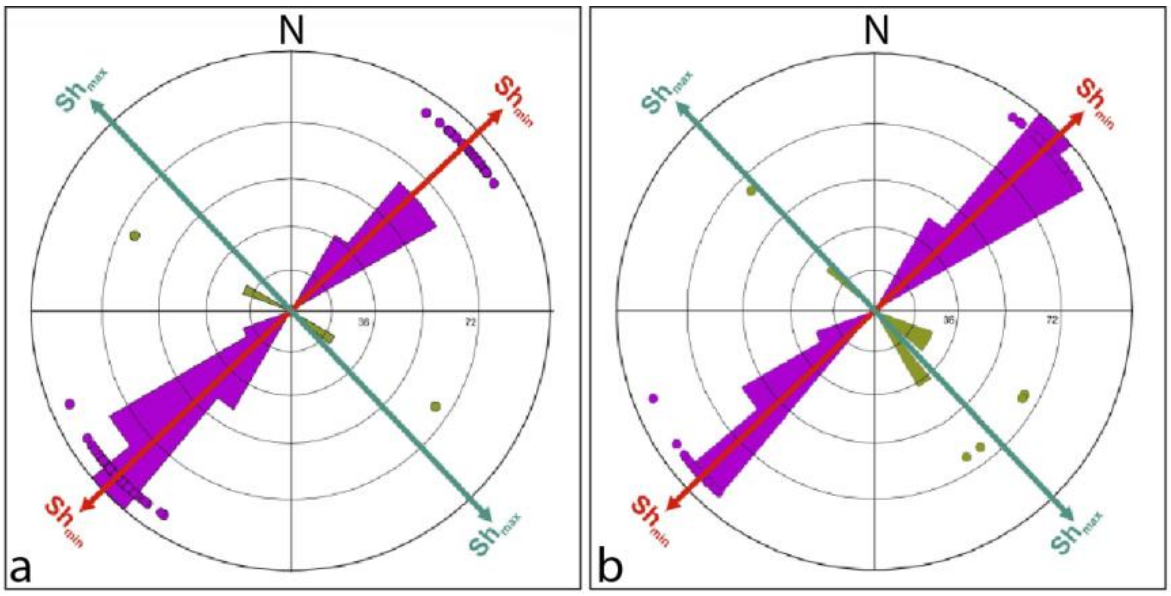

Fig. 5.4: *In situ* stress strike orientation stereonets for wells CRC-1 (a) and CRC-2 (b). Purple color represents borehole breakouts generated in the direction of S_{hmin}, green color represents drilling-induced tension fractures (DITF) propagating in the direction of S_{HMax}. (Lawrence 2011)

5.3.2 Vertical stress magnitude

Vertical stress S_V is the stress applied at any given depth due to the weight of the overlying rock mass and fluids. It is therefore dependent on the densities of the rocks and on the depth (cf. Chap. 2.1.4) (Jaeger et al. 2007).

Onshore, vertical stress gradients are calculated relative to the ground level, whereas offshore they are related to the seabed (in order to remove the effect of varying water depth). The vertical stress calculated in the onshore SA Otway Basin varies from 20 MPa at 1 km depth to 67.5 MPa at 3 km depth. The vertical stress determined offshore shows slight variation in magnitude at depth, probably due to lateral variability of

rocks and then variation in density. It ranges from 20 MPa at 1 km depth to 63-66 MPa at 3 km depth in the offshore wells. The variability of S_V across the Otway basin is described with a power law function (Nelson et al. 2006) (Eq. 5-1):

$$S_V = 21.182\, z^{1.0555} \qquad (Eq.\ 5\text{-}1)$$

where z represents the depth to the reservoir in kilometers.

For the geomechanical model presented in this thesis, the magnitude of the vertical stress is derived from density logs available in wells CRC-1 and CRC-2. The resulting gradient for the vertical stress is 23.3 MPa/km.

5.3.3 Minimum horizontal stress magnitude

The minimum horizontal stress magnitude (Shmin) is determined from leak-off tests and extended leak-off tests, as wells as mini-fracture test data (Zoback et al. 2003). Generally in leak-off tests, a well is pressurized to the point that an hydraulic fracture is created, and magnitude of the principal stress can be determined either from the Leak-Off Point (LOP) or from the Fracture Propagation Pressure (FPP) that should have similar values (Zoback 2010).

The suggested gradient for the South Australian sector of Otway Basin is ≈15.5 MPa/km (Nelson et al. 2006). An extended leak-off test was undertaken in the CRC-1 borehole to obtain more detailed information about the magnitude of S_{hmin} in the Naylor Field (van Ruth 2007). In this case the average fracture closure pressure (FCP) was considered to be the best estimation for the minimum horizontal stress, due to the fact that viscous frac fluid was used as the FPP would increase due to large friction losses (Zoback 2010). The test was conducted at a depth of 512 m and reported a magnitude value of 7.4 MPa, corresponding to a gradient of 14.62 MPa/km.

5.3.4 Maximum horizontal stress magnitude

Magnitude of the maximum horizontal stress is the most difficult component of the stress tensor to estimate since it is not possible to directly measure it (Zoback 2010). However some constraints can be applied, using observations form borehole breakouts and DITFs (Zoback et al. 2003) or through the application of the frictional limits theory (Sibson 1974).

In the Southern Australian sector of the Otway Basin S_{Hmax} magnitude is constrained by the occurrence of DIFTs and transverse drilling-induced tensile fractures (TDITFs) and the S_{Hmax} gradient is calculated equal to ≈29 MPa/km (Nelson et al. 2006), that would indicate a prevailing strike-slip stress regime where the magnitude of the maximum horizontal stress is larger of the magnitude of vertical stress. However, it has to be taken into account that stress measurement were mostly made in the nearby Gippsland Basin, since almost no data were available for the Otway Basin itself. Following the availability of new measurement in the Naylor Field, magnitude of S_{Hmax} is estimated from the CRC-1 extended leak-off test (van Ruth 2007) and is

equal to 9.6 MPa at 512 m depth, corresponding to a gradient of 18.75 MPa/km, following the equation 5-2:

$$S_{HMax} = 3S_{hmin} - P_b - P_p + T_0 \qquad (Eq.\ 5\text{-}2)$$

where P_b is the breakdown pressure, P_p is the pore pressure and T_0 is the tensile strength. Therefore, for the Naylor Field the prevailing stress regime is a normal faulting regime where vertical stress is larger than the two horizontal stresses.

6 Geological model

Reservoir geometry and faults geometry are among the principal input data required for the build-up of a geomechanical model. They can be obtained from structural and geological models derived from 3D seismic interpretation. Within PROTECT Research Group a 3D seismic interpretation (Ziesch et al. subm.) was performed, in collaboration with scientific partners at LIAG (Leibniz Institute for Applied geophysics - Hannover), on the Nirranda-Heytesbury 3D survey, a 3D reflection seismic cube (Urosevic et al. 2011). It is the result of a combination of three different surveys: the OGF93A, the ONH01, and the Curdie Vale 3D (OCV00) surveys, covering an area of 32.3 km x 14.35 km x 4100 ms two-way traveltime (TWT). In particular, the area of study lies within the Curdie Vale 3D subvolume (Fig. 6.1). The geological model derived from the 3D seismic interpretation is the starting point for all the scientific partners of PROTECT Research Group.

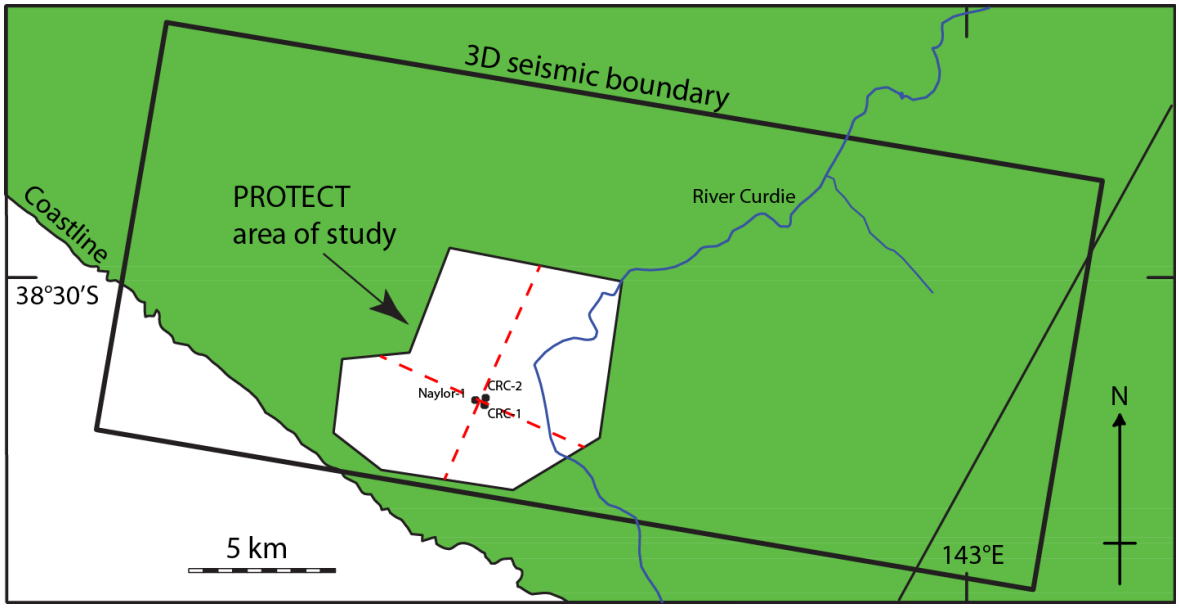

Fig. 6.1: Location of the common area of study for the PROTECT Research Group, showing the extent of the 3D seismic dataset and wells location. Dashed lines indicate the position of the seismic profiles in Fig. 6.3 and Fig. 6.6. Modified after Ziesch et al. (subm.).

The common study area for the PROTECT Research group is focused in a small area around the injection wells CRC-1 and CRC-2 (approximately 8x7 km) (Fig. 6.1 and Fig. 6.2). Although starting from a common geological model, the geomechanical models presented in this thesis have different size (Fig. 6.2). Indeed, the two geomechanical approaches described do not share the same objective, being one focused on total stresses and the other on effective stresses. Therefore the steady-state model is derived directly from the geological model and has the same size, whereas the one-way flow and geomechanics coupled model is slightly smaller. A preliminary one-way coupled model, performed on the entire area covered by the geological model indicated that the area affected by changes in pressure, and consequently by changes in stresses, was located exclusively around the production and injection wells. With the aim to increase the resolution of the model (i.e. keeping the same amount of cells,

but of smaller size), the one-way coupled model covers an area of only 4x4 km and it is centered around the wells. Three wells are located within the area of interest of the models and have been used for the geomechanical modelling: well Naylor-1 is the production well through which the Naylor Field was depleted, wells CRC-1 and CRC-2 are the two injection wells of the CO2CRC Otway Project. As this thesis focuses only on Stage 1 of CO2CRC Otway Project (cf. Chap. 3), only well CRC-1 is used to simulate CO_2 injection in the flow model. However, well log data from well CRC-2 have been used to populate the model with rock properties.

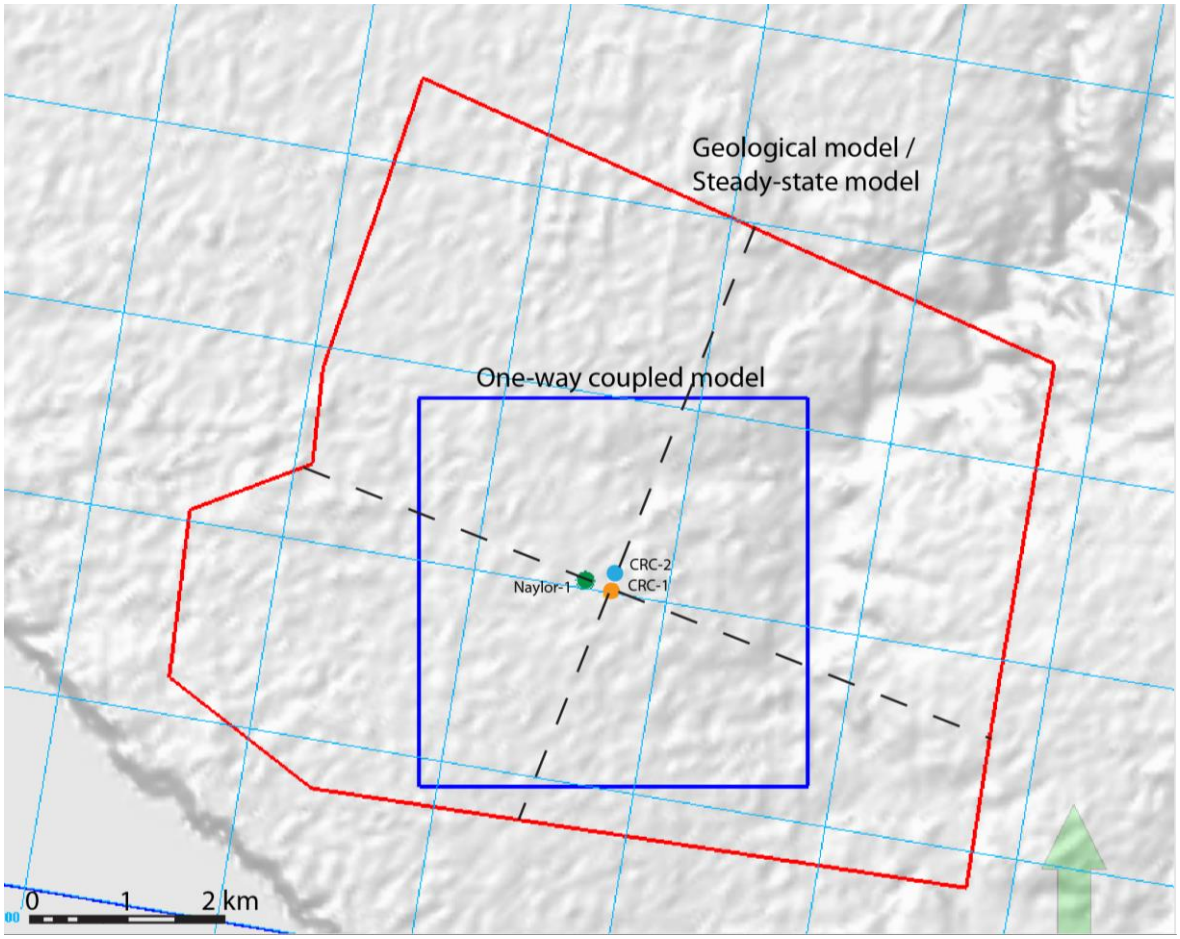

Fig. 6.2: Location of geological and geomechanical models and position of wells. Geological model and steady-state geomechanical model share the same area (red), whereas the one-way flow and geomechanics coupled model is slightly smaller (blue). Dashed lines indicate the position of the seismic profiles in Fig. 6.3 and Fig. 6.6.

6.1 Geological model and depth conversion

A very accurate seismic interpretation was required for reproducing surface morphologies of horizons and faults (Fig. 6.3), therefore a number of different techniques were used to obtain a detailed seismic interpretation. Seismic interpretation has been conducted down to 2.2s TWT, corresponding to ~2800m depth. A SEG standard convention was used during the seismic processing, therefore a negative impedance contrast is shown as a trough. Eight horizons have been interpreted from base of the reservoir formation (Waarre Fm.) up to the highest seismically-visible horizon (Narrawaturk Fm.)(Fig. 6.3)(Ziesch et al. subm.). Available

well tops of the stratigraphy have been used to constrain the interpretation of the horizons. Areas of strong seismic reflection, especially in the upper part of the model, allowed the use of guided auto-tracking. In contrast, in areas with low seismic reflection, a manual interpretation every 100 m in inline and crossline directions was used to improve the quality of output data. Particular care was applied in areas around faults and within strongly-faulted horizons: a series of diagonal lines within the same horizons have been used as double-check features. A number of seismic attributes were used to increase the confidence of the interpretation process.

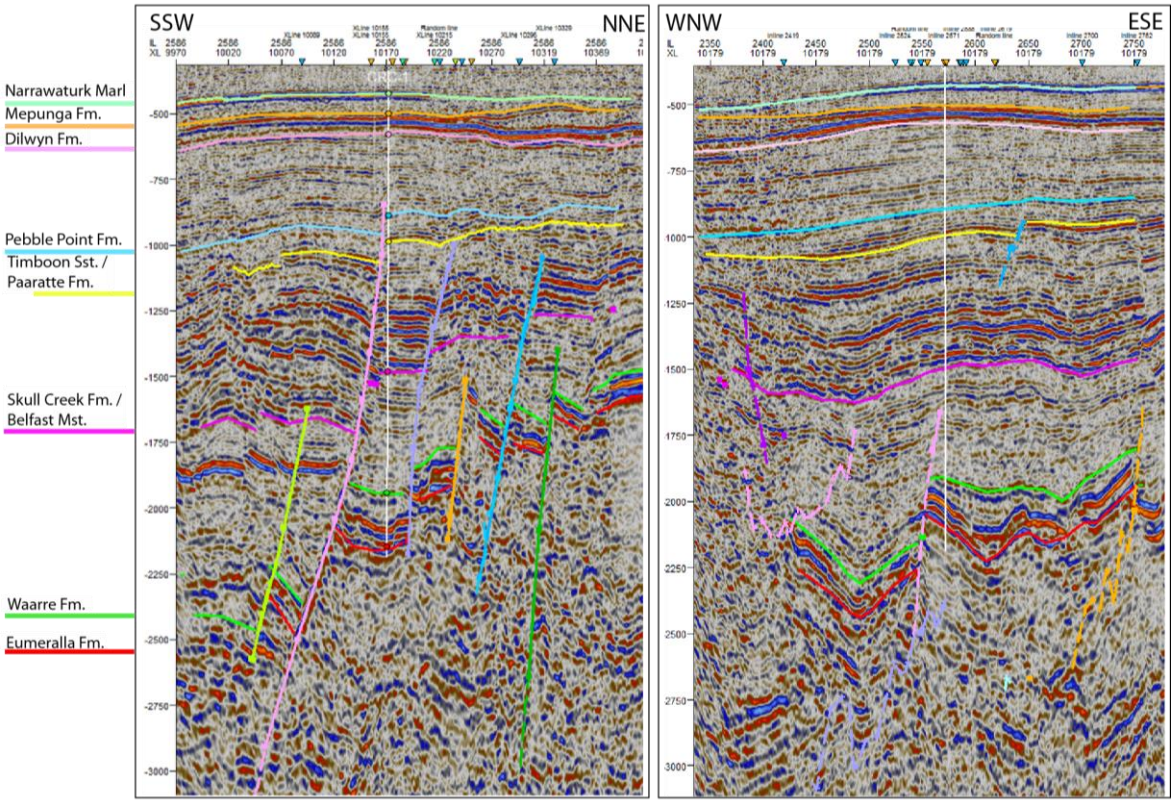

Fig. 6.3: Example from the original interpretation of stratigraphy of CO2CRC Otway Project in the common area of PROTECT Project. Inline is on the left picture, crossline is on the right picture. The injection well is white. Vertical scale is in meters below sea level. Position of the seismic profile is indicated in Fig. 6.1 and Fig. 6.2.

A total of 24 major faults were identified in the 3D seismic cube (Fig. 6.4), through an interpretation process facilitated by the use of the 3D-coherency and curvature processing (Lippmann 2013). Only few faults reach the surface, therefore the geological model appears unfaulted in the upper part where seismic horizons are continuous, and a strongly-faulted lower part, in particular below Pebble Point Fm., where horizons are often displaced by the presence of faults (Fig. 6.3).

Majority of faults strikes NW-SE, the same direction of the maximum horizontal stress orientation (cf. Chap. 5.3.1), and dips towards SW with an angle ~60°, consistent with a normal faulting regime. In this context, it has to be reminded that the coincidence between present-day orientation and orientation of faults depends on the fact that paleostress orientations, under which faults were generated, are similar to those of the present-day stress field. Those normal faults are planar in the NE quadrant of the

geological model and tend to become listric in the SW quadrant with a dip angle of ~30-40° in their lower sections (Ziesch et al. subm.). Moreover, in the SW quadrant a system of antithetic faults developed in response to movement on major listric faults (Fig. 6.4). The offset produced by the major faults increases from North to South, reaching a maximum of 800 m (Ziesch et al. subm.).

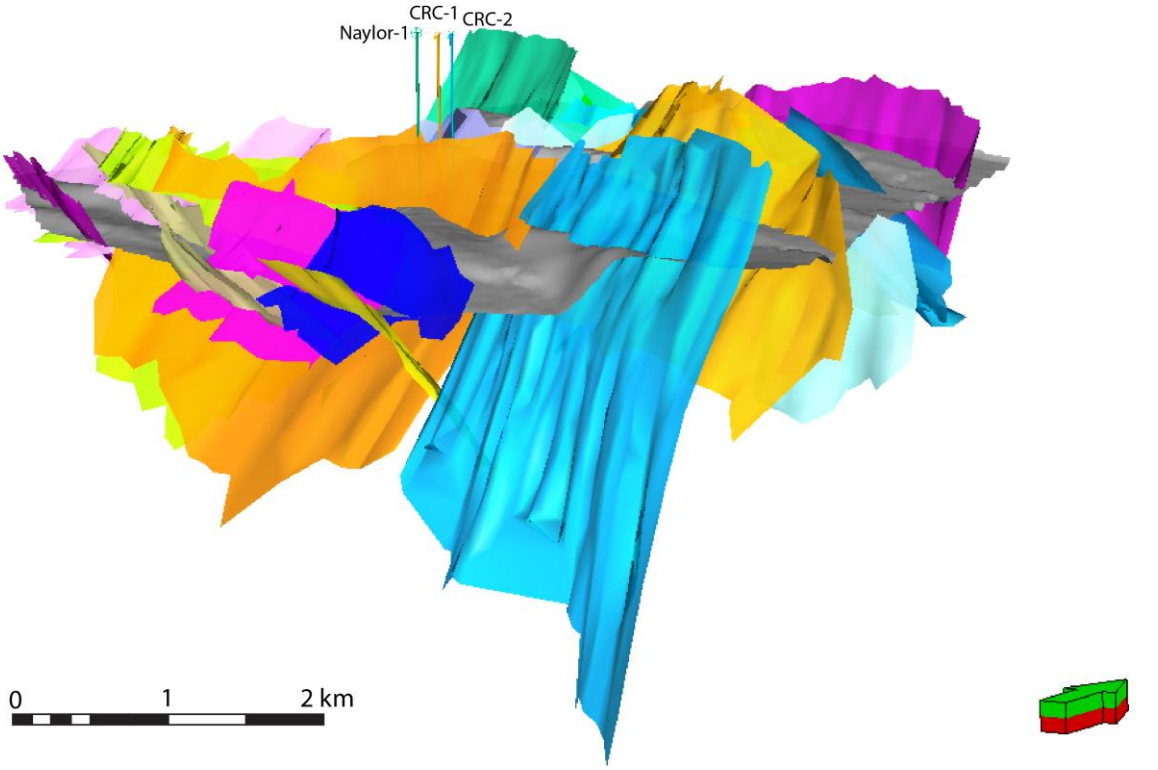

Fig. 6.4: 3D view of the 24 major normal faults interpreted. Most of the faults strike NW-SE and dip around ~60°**.** The horizon shown for reference is the top-reservoir horizon. Vertical scale is equal to horizontal scale.

The velocity model for time-depth conversion was built by the project partners in LIAG (Leibniz Institute for Applied geophysics), based on stratigraphic information from the borehole CRC-1 (Beilecke 2014, pers. comm.). All the eight horizons comprised in the complete geological model (Ziesch et al. subm.) were used. The methodology chosen for the time-depth conversion is the so called "Layer cake depth conversion" (Marsden 1989) that uses interval velocities and reflection times to depth convert a layer at time. In particular, the $V_0 + k_c z$ method was applied (Marsden 1992). The assumption behind this particular type of time-depth conversion is that the interval velocity (Fig. 6.5) increases linearly with depth, following the relationship (Eq. 6-1):

$$V_i = V_0 + k_c z \qquad (Eq.\ 6\text{-}1)$$

where V_i is the interval velocity, V_0 is the intercept on the velocity axis, k_c is the gradient (known as compaction factor) and z is the depth. Interval velocities were then calculated at the tops of the individual formations, together with the velocity gradient within the respective formations.

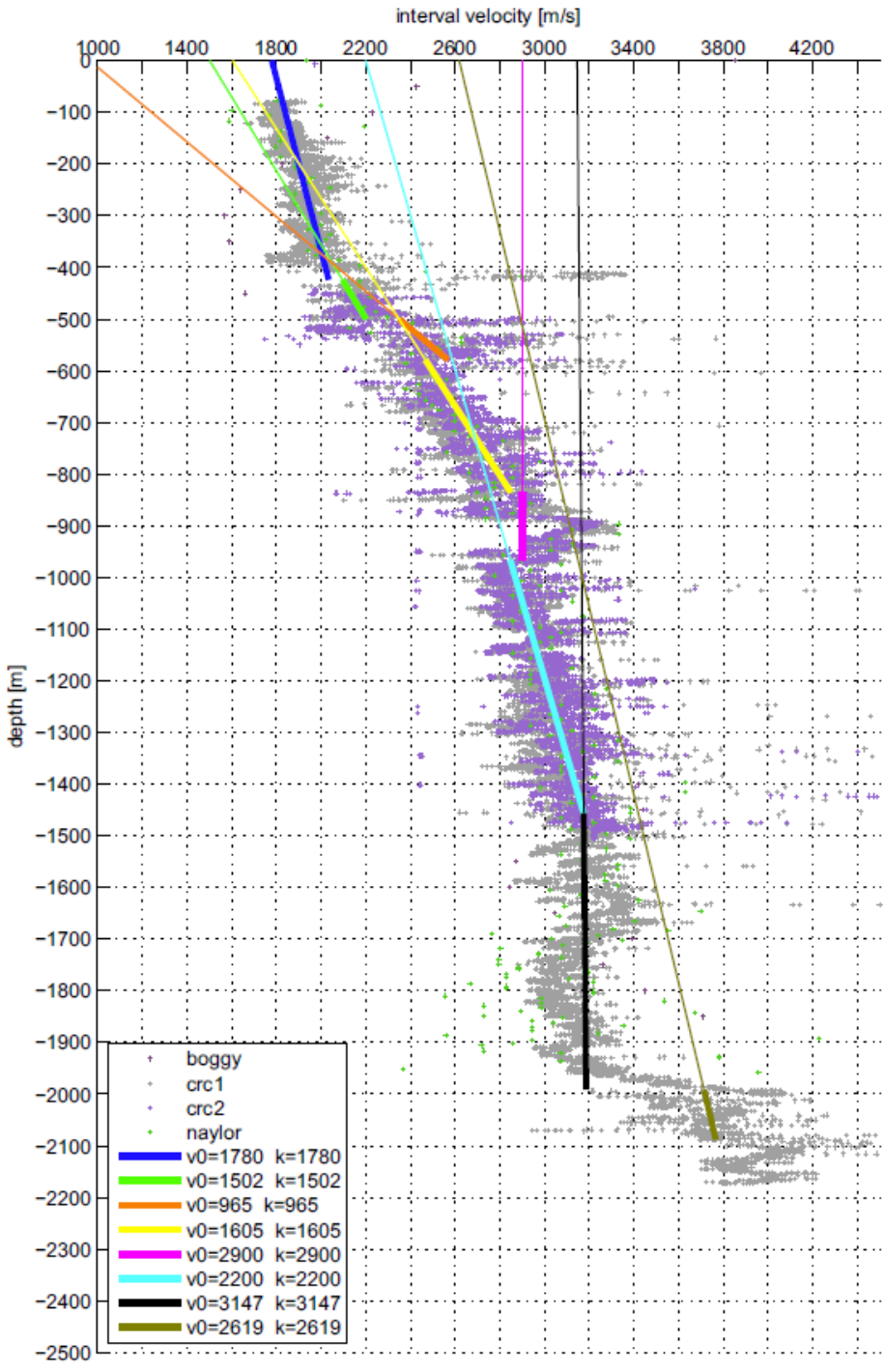

Fig. 6.5: Calculation of interval velocities for each well top. Each dot represents the measured velocity from the sonic log (Beilecke 2014, pers. comm.).

A quality control was performed on 9 wells comprised in the data volume, returning an average depth error of 0.6% of formation depth in the wells, a value acceptable for our study.

A 3D pdf of the depth-converted geological model (Ziesch et al. subm.) is available as appendix to give the reader the opportunity to have a 3D perspective of the geology. All stratigraphic horizons and faults can be displayed in map or oblique and furthermore, customized 2D sections can be created.

6.2 Refined geological model for geomechanical modelling

The geological model used for the geomechanical characterization presented in this thesis represents a simplification of the original model (Ziesch et al. subm.), with a reduced number of interpreted horizons and faults. Indeed, the geomechanical characterization focuses only on major structures, therefore only faults that show significant displacement and size are taken into account. Furthermore, horizons physically very close and with similar rock properties have been grouped to avoid numerical interferences during the geomechanical modeling. 5 representative horizons were chosen for the simplified geological model, covering a time ranging from Late Cretaceous to present-day (Fig. 6.6). The base of the model is represented by the Eumeralla Fm., the source rock for gas (Tupper et al. 1993). It is overlaid by the Waarre Fm., the depleted gas reservoir, target for the CO_2 injection. The Skull Creek Fm/Belfast Mudstone acts as regional seal across most of the Otway Basin and is overlaid by the Timboon Sandstone/Paaratte Formation, a shallow aquifer. The upper part of the geological model comprises a succession of formations not faulted, of which the lower boundary is the Dilwyn Fm.

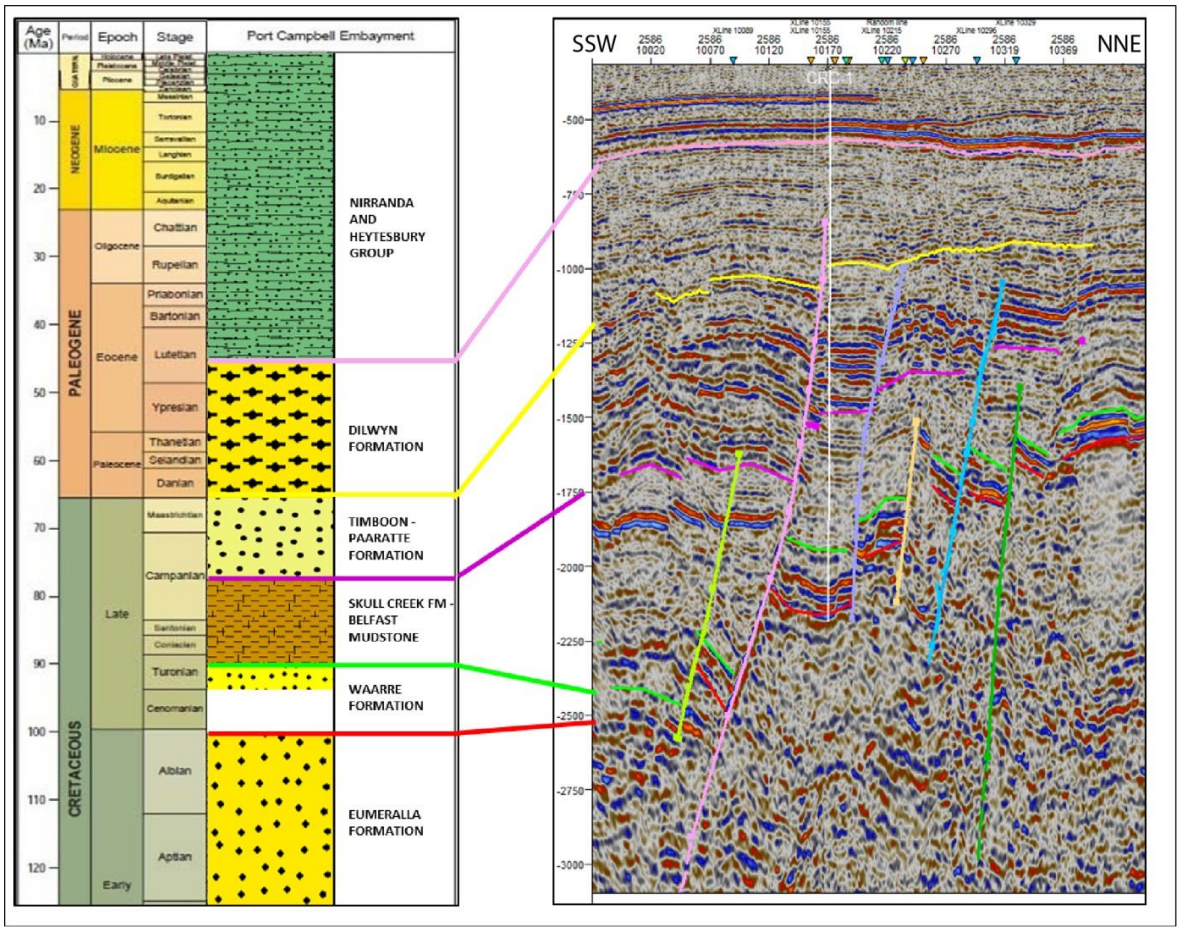

Fig. 6.6: Simplified stratigraphy of CO2CRC Otway Project used for the 3D geomechanical modelling and representative inline across CRC-1 at storage location showing the complex structure of Naylor Field. The injection well is white. Vertical scale is in meters below sea level. Position of the seismic profile is indicated in Fig. 6.1 and Fig. 6.2 (Aruffo et al. 2014).

In general, a geomechanical characterization of a CO_2 storage site has is main focus on caprock and reservoir layers. Caprocks are layers of low permeability rock that

overlay the storage formation, ensuring that buoyant CO_2 does not leak into overlying strata and towards the surface (Kaldi et al. 2011). Storage security is largely influenced by caprock integrity, therefore its assessment is one of the main objectives of geomechanical modelling for CO_2 storage. At the CO2CRC Otway Project site, caprock is represented by Belfast Mudstone, in this geomechanical model grouped together with the overlying Skull Creek Formation. It lies at a depth comprised between 1200-1700 m (Fig. 6.7), with a significant thickness ranging 500 to 700 m (Fig. 6.8). The caprock is intersected by 8 faults, although some of them show a limited displacement. Only one of the two faults bounding the storage reservoir reaches the top of the caprock layer. The reservoir layer corresponds to the Waarre Fm., located at a depth between 1700-2400 m (Fig. 6.7) with an average thickness of ~200 m (Fig. 6.8). In this case, all the faults interpreted displace the reservoir, occasionally with displacements that overcome the thickness of the reservoir itself.

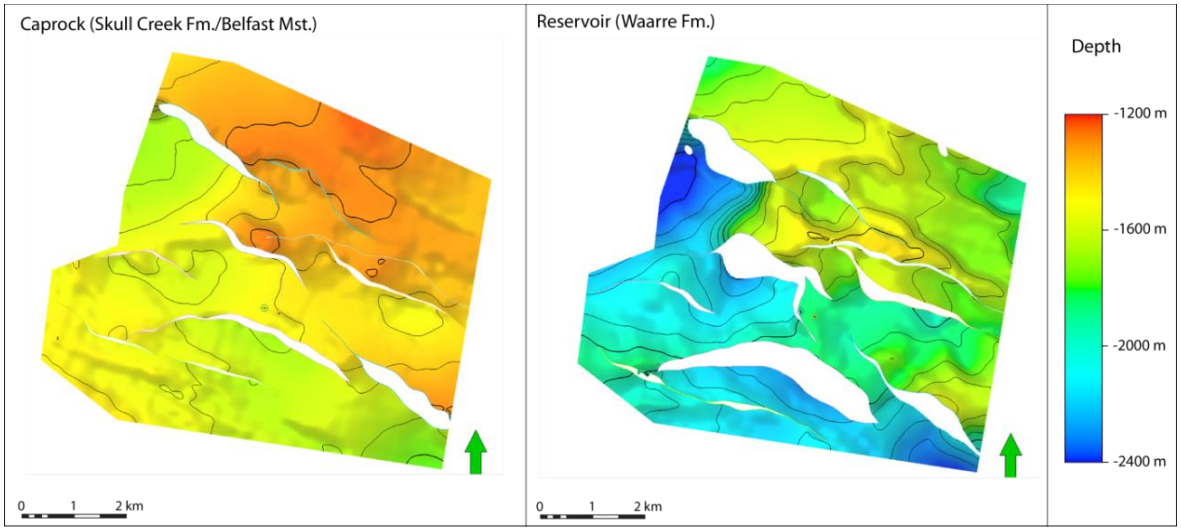

Fig. 6.7: Depth map of top of the caprock layer (left) and top of the reservoir layer (right).

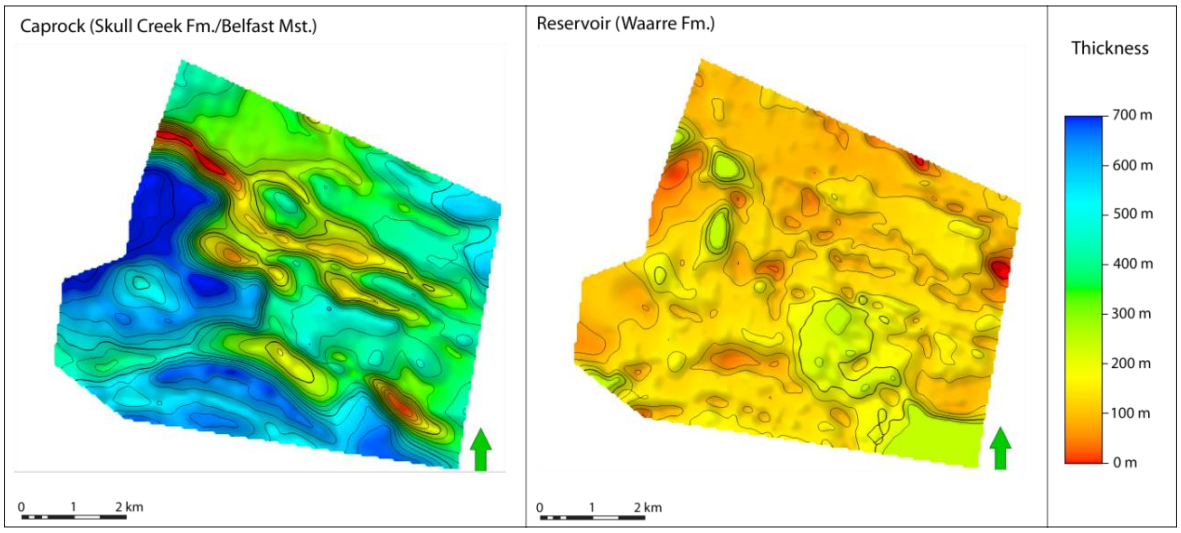

Fig. 6.8: Thickness map of caprock layer (left) and reservoir layer (right). Faults cut-outs are disregarded during the creation of thickness map, although a reduction in thickness horizons can be recognized.

The geological model includes 10 faults, considered as major for size and displacement. The structural arrangement shows a complex of normal faults, three of which reach the uppermost seismically-visible horizon at about 500 m depth (Fig. 6.6 and Fig. 6.9). Faults comprised in the area trends NW-SE, mainly dipping towards SW. In particular, the area of injection is surrounded by three faults: Naylor Fault, Naylor East Fault and Naylor South Fault (van Ruth and Rogers 2006) that form the structural closure which hosts CO_2, and will be required to act as a long-term seal (cf. Chap. 3.3).

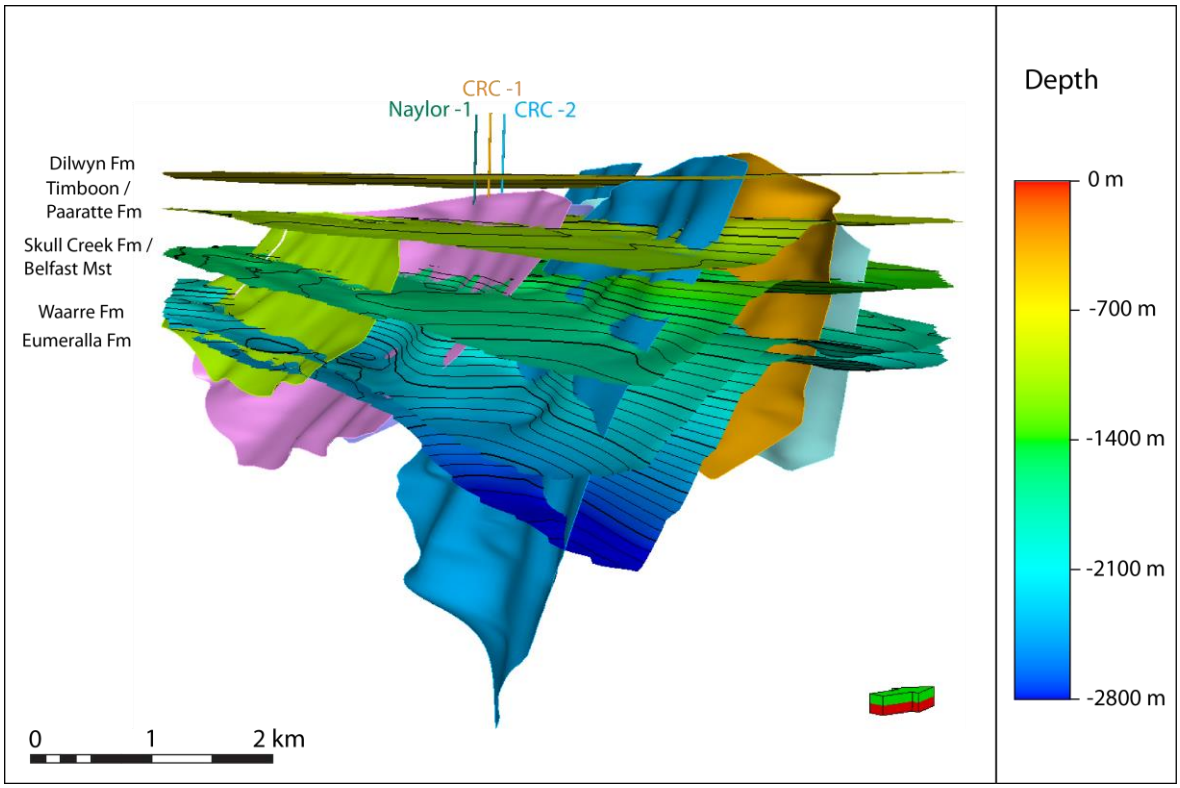

Fig. 6.9: Simplified geological model of the CO2CRC Otway project showing the 5 interpreted horizons and the 10 faults used for the geomechanical characterization. Vertical scale is equal to horizontal scale.

7 One-way flow and geomechanics coupled model

The first geomechanical model presented is this thesis is a one-way flow and geomechanics coupled model. The main aim is to assess mechanical stability of faults at various times in the field's history, in relation to changes in pore pressure occurring during production/injection stages. In this approach, pressure data are transferred from the ECLIPSE™ finite difference reservoir simulator to the VISAGE™ finite element mechanical simulator at regular and/or critical times. The coupling in this approach is one-way coupled, meaning that fluid pressure drives the geomechanics, but mechanically-induced changes to porosity and permeability are not fed back into the dynamic reservoir simulation. So in effect, permeability and porosity are assumed to be the same for each time step in the modelling and not being affected by changes in stresses. This kind of approach is feasible in this particular case study because of the high permeability characterizing the reservoir (more than 1 D). A fully coupled simulation, where permeability and porosity are function of changes in stresses, would not add appreciable benefits to the model results, only increasing the computation time.

7.1 Reservoir simulation for flow modeling

A flow model is normally performed through a so-called reservoir simulation, a form of numerical modelling that quantifies and interprets physical phenomena with the ability to extend these to future performance. A reservoir simulation is a proven and effective method for handling uncertainty during exploration and production and its use within companies nowadays is widespread. Amongst others, reservoir simulation is typically used for determination of recoverable reserves and most economical drilling method, estimation of financial risk of exploration and production (Samier et al. 2003). In the case of geosequestration of natural gas and/or CO_2 it helps to determine the amount of fluids that can be stored in a given reservoir.

The reservoir is divided into several discrete units in three dimensions (cells), and the progression of reservoir and fluid properties is modelled through space and time in a series of discrete steps. The physical concept behind reservoir simulations is based mainly on two principles. First, the Darcy's law that describes the flow of a fluid through a porous medium (Eq. 7-1) (Darcy 1856, Manning 1997):

$$q = -\frac{k}{\eta}\nabla P \qquad (Eq.\ 7\text{-}1)$$

where q is the flux (discharge per unit area), k is the permeability of the porous medium, η is the viscosity of the fluid and ∇P is the pressure gradient. The second principle refers to the application of mass balance that in the case of a reservoir can be generally expressed as (Eq. 7-2):

$$Mass\ flux = Accumulation \pm Injection/Production \qquad (Eq.\ 7\text{-}2)$$

meaning that the mass flux within the reservoir should be equal to the mass accumulated into the reservoir plus/minus the flux that enters/leaves the system during injection/production. The equation solved for each cell and each time step is a combination of these two physical principles. This type of solution is the Finite Difference Method, where governing equations are discretized on a fixed grid.

Fluid composition can be treated in different ways in the frame of reservoir simulations. Black oil simulators assume that oil and gas phases can be represented as one component through time. Properties of this component can change with pressure and temperature, whereas the composition does not change. In contrast, compositional simulators can represent oil and gas phases as multi-component mixtures. Equations of state can model reservoir fluids at all temperatures, pressure and compositions (Dake 1978).

As a general solve method, the reservoir is divided into several cells and for each cell basic data needs to be provided (i.e. porosity, permeability). Wells are then positioned within the cells and well production rates are specified as a function of time. Finally the equations are solved to yield the pressure and saturation for each block, as well as production for each phase for each well. Each cell is solved simultaneously, therefore the number of cells in the reservoir simulation is directly related to the time required to solve a time step.

The simulated flow within the reservoir varies depending on which part of the reservoir model the flow is computed: flow from one grid block to another, flow from the grid block to well completion or flow within the wells and surface networks. More generally, the flow is dependent on transmissibility, mobility and potential difference (Fig. 7.1):

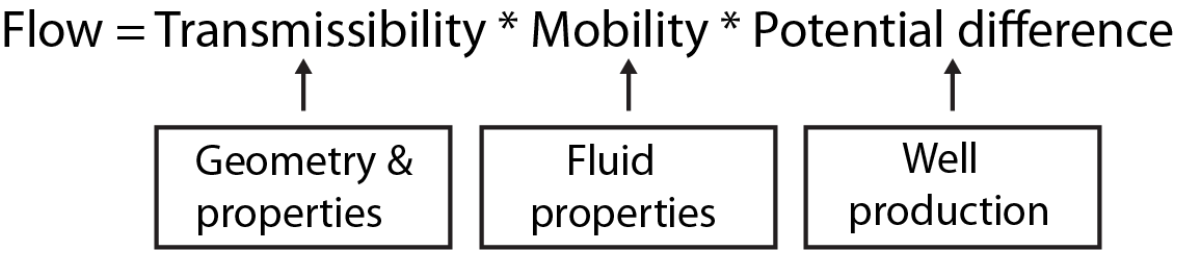

Fig. 7.1: Scheme that illustrated the dependency of flow on transmissibility, mobility and potential difference and their relative causes. Modified after ECLIPSE Manual, Schlumberger (2009)

Dynamic modeling of CO_2 injection and flow in the reservoir using the ECLIPSE300™ (Compositional) simulator has been performed for both production and injection phases in Naylor Field, in order to have a complete overview of the change in pressures before, during and after the injection of CO_2. The input required for the dynamic modeling includes a static model, well logs of porosity and permeability as well as phase behavior (PVT relationships), production and injection data. Injection and production have been simulated with ECLIPSE300™ at reservoir level, where changes in pressure occur. Results from the simulation (i.e. pressure of the reservoir) have been upscaled and used as input for the geomechanical simulation in Visage.

7.1.1 Reservoir model geometry, properties, well completions

The model geometry depends on several factors as for example level of detail, complexity of faulting, number of wells etc. In the case of a one-way flow and geomechanics simulation the main input is the pressure change over time due to production/injection. Changes in pressure occur only in the reservoir, therefore a local reservoir model (Fig. 7.2) is required in order to perform flow modelling. Two wells are included in the model: Naylor-1 (production well) and CRC-1 (injection well). An aquifer has been added to the model to help the pressure recover which occurs in the time between the end of production and beginning of injection.

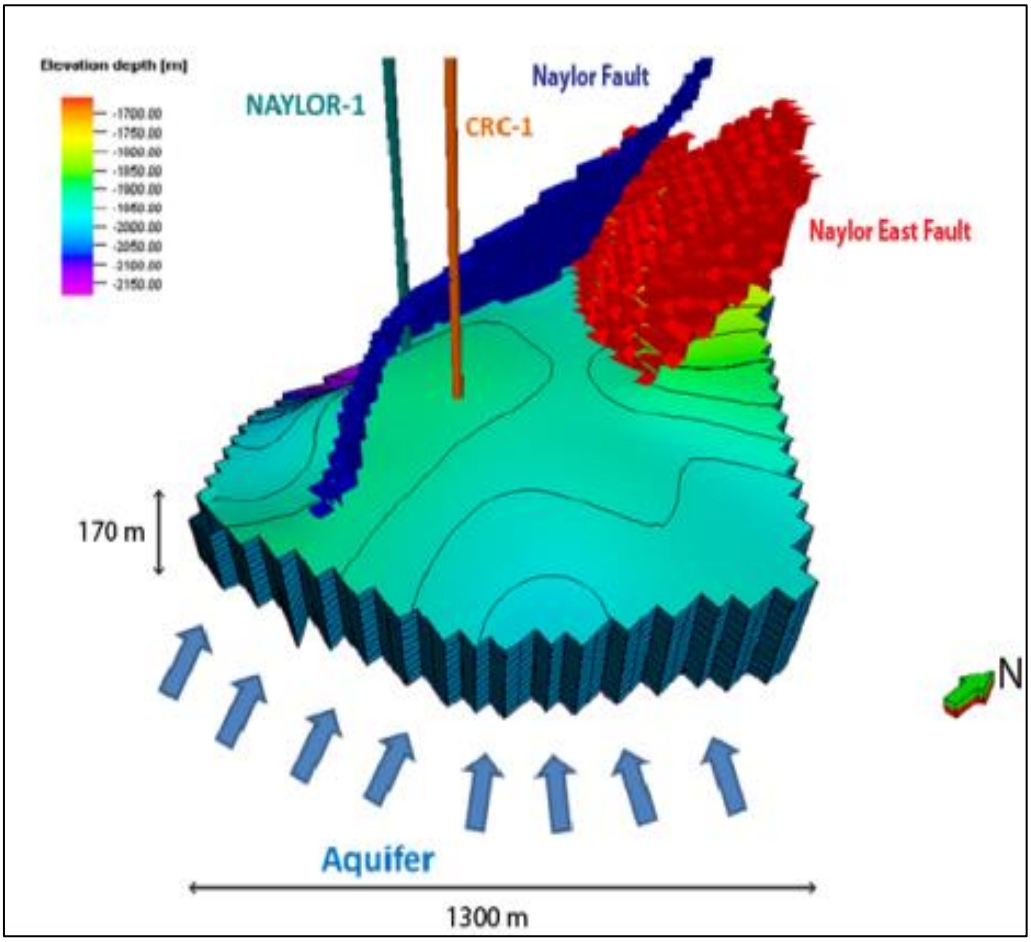

Fig. 7.2: Reservoir model used for flow simulation. Modified after Aruffo et al. (2014).

The grid size of the reservoir model is 36x42x61, with a total number of 92232 cells. The resolution of the grid is 20 m in the horizontal direction and 15 m vertically.

Well logs (data are available only from CRC-1) provide data for populating the model: SPHI (sonic porosity log) is used for porosity and KTIM (CMR permeability using Timur/Coates model) measures the permeability. Average porosity in the reservoir is 0.23, average permeability is 1100 mD in the X and Y direction (Bérard et al. 2008) and 122 mD in the Z direction (from correlations, assuming vertical permeability to be ~10% of horizontal permeability) (Fig. 7.3).

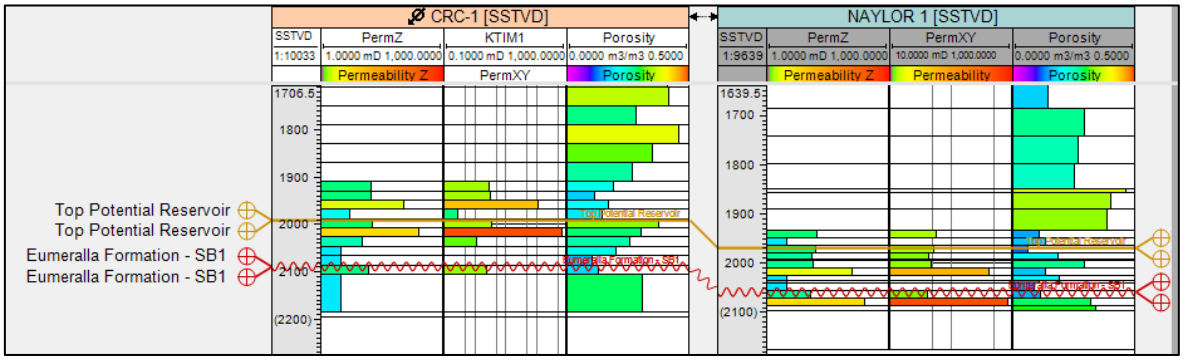

Fig. 7.3: Permeability and porosity well logs used for populating the reservoir model.

Well completions have to be specified as they can be opened or shut at particular times during the history of the reservoir, thus influencing the computation of fluid flow from/into the reservoir. Completion data (Fig. 7.4) are available from well report for both Naylor-1 and CRC-1. The original perforation level in Naylor-1 was from 1977.4 to 1981.4 m TVDss ("True vertical depth, sub-sea"). In late 2003 it has been extended from 1977.8 to 1986 m TVDss to allow production from a deeper formation (Waarre A). CRC-1 has been perforated between 2002.5 and 2008.5 TVDss, and between 2010.5 and 2013.5 TVDss.

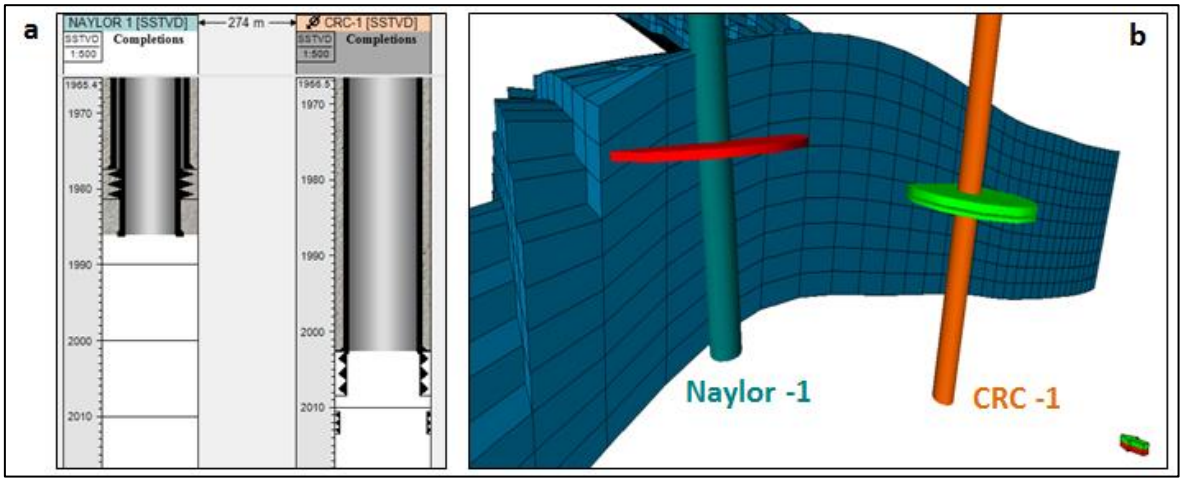

Fig. 7.4: Well completions in well section (a) and in 3D visualization (b). In (b) green and red plates indicate perforation areas, diameter is not indicative.

7.1.2 Fluid model

PVT (Pressure-Volume-Temperature) relationships are a key issue in reservoir simulation as the behavior of the modelled fluid varies depending on temperature, pressures and compositions. Those three elements in turn have a wide range of possible values in relation to whether the processes involved occur in the sub-surface, in the production facilities or in the surface facilities. For example, if a reservoir is produced temperature and pressure drop and the fluid may reach the bubble or dew point pressure. If gas is injected into the reservoir, it could be either miscible or immiscible and a proper PVT behavior has to be predicted.

During the reservoir simulation, material balance is calculated for each cell at each time step requiring the density of each phase to be calculated. Because the density of

each phase depends on pressure and the quantities of dissolved components in each phase, calculation PVT properties for each phase is the ideal mean to specify fluid characteristics. The PVT data allow to translate produce volume to reservoir condition and subsequently to convert these into mass that can be solved as mass balance equations by the simulator.

The composition of the gas (Tab. 7.1) produced through the Naylor-1 well (Vidal-Gilbert et al. 2010) has been used for the fluid model, created with the PVTi software. The gas is mainly composed by ethane (C_2H_6) and contains also propane (C_3H_8), butane (C_4H_{10}), hydrogen sulfide (H_2S), molecular nitrogen (N_2) and carbon dioxide (CO_2). The water salinity is 0.52 molal. PVT relationship table (Fig. 7.5) for each component of the gas has been exported for a compositional simulation taking for a reservoir temperature of 85 °C (Bérard et al. 2008).

COMPONENT	COMPOSITION %	WEIGHT FRACTION %
CO_2	1	2.4148
N_2	2	3.0741
H_2S	3	5.6092
C_2H_6	88	77.463
C_3H_8	4	6.5996
C_4H_{10}	2	4.8391

Tab. 7.1: Composition of gas produced from Naylor-1.

PVT relationships are often represented with a phase envelope as the one computed for the gas produced from well Naylor-1 (Fig. 7.5). Phase diagrams show the conditions for stability of a fixed mixture of components as function of pressure and temperature conditions. Inside the envelope, two phases are present: liquid and gas in equilibrium. The green line bounding the phase envelope is the bubble point line, above which the gas is in a liquid state. The red line on the right side of the plot is the dew point line, to the right of which the gas is in a vapor state. At pressure and temperature condition of the simulated reservoir, ~20 MPa and 85°C, the gas is in a supercritical state being way above the critical point.

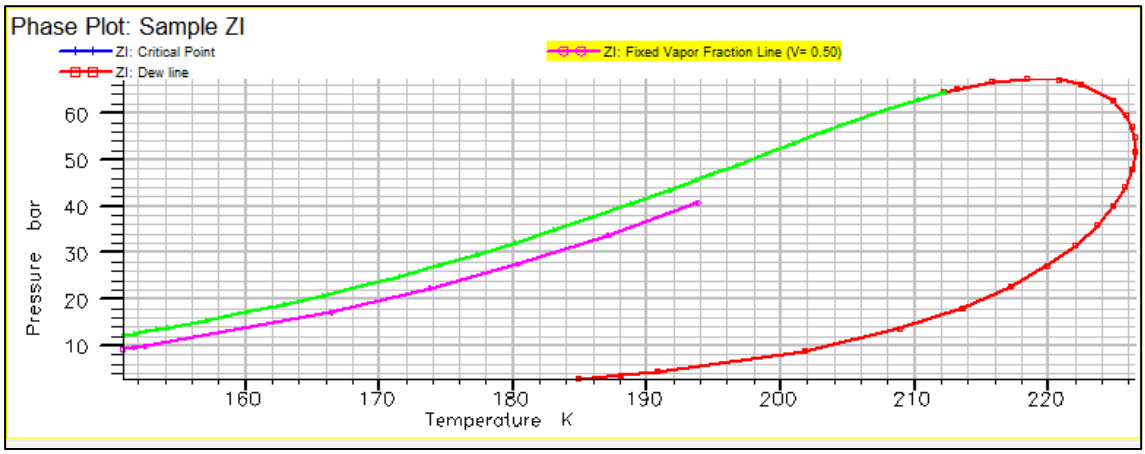

Fig. 7.5: Phase plot of gas produced from Naylor-1.

The gas injected in CRC-1 has a different composition with respect to the original gas in place produced through Naylor-1. The average composition of 77 mole % CO_2, 20 mole % methane and 3 mole % other gas components (Vidal-Gilbert et al. 2010), and again at reservoir conditions it is in a supercritical state.

7.1.3 Rock physics functions

Rock physics functions relating the physics of fluids and rock have been computed directly into Petrel and comprise saturation function and rock compaction, used during the simulation to represent the physics of the fluids, the physics of the rock and their mutual interaction.

According to the ECLIPSE simulation manual (Schlumberger 200), information on capillary pressure and relative permeability for each active phase is the minimum requirement to compute a saturation function. The specification of a saturation function allows to establish the upper and lower boundaries of the saturation for each active phase. Those limits are then used to determine the initial saturation of each phase in the gas and water zones. In turn, capillary pressure is used to calculate the initial transition zone saturation of each phase. Finally, the relative permeability allows to calculate fluid mobility and solving the flow equations between cells and from cells to well.

The saturation function takes into account the relative permeability between gas and water (Tab. 7.2 and Fig. 7.6) and capillary pressure to compute the initial saturation for each phase in each cell. Data from cores in CRC-1 well are available and have been used (Bouquet et al. 2009), and a compositional fluid model has been used.

SCO_2	$KrCO_2$	KrW
0	0	1
0.1319	0.002785	0.514199
0.177	0.009745	0.378783
0.197	0.014323	0.324768
0.235	0.02535	0.246349
0.2683	0.034304	0.222242
0.278	0.044646	0.185943
0.35	0.055842	0.149051
0.4144	0.086914	0.135666
0.4508	0.157555	0.080584
0.5563	0.608532	0

Tab. 7.2: Data used to compute the saturation function: S_{CO2} is the CO_2 saturation, Kr_{CO2} is the relative permeability of the gas and Kr_w is the relative permeability of water.

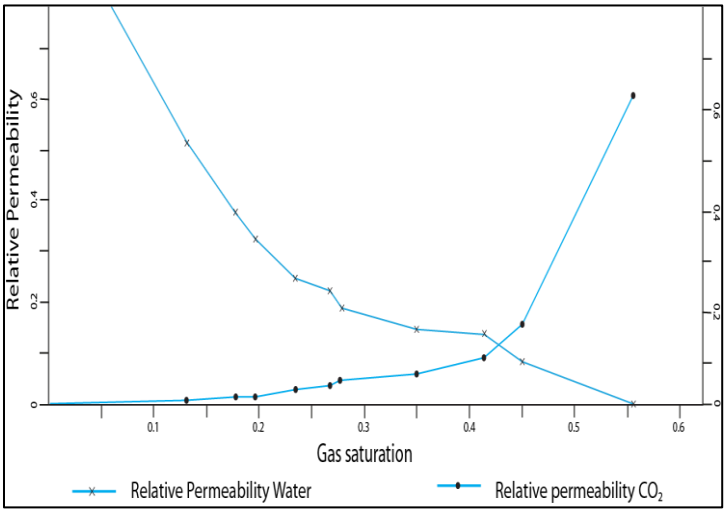

Fig. 7.6: Relative permeability curve for gas and water used for the simulation.

Capillary pressure used for simulation is 0.00248 MPa (average at a pressure of 19.3 MPa) at the gas-water contact. It is used to determine the extent of the transition zone: the higher the capillary pressure, the larger the transition will be.

ECLIPSE™ uses the cell pore volume and transmissibility (Fig. 7.7) for the calculation of fluid flows, instead of using grid cell dimension and properties. The input required to calculate cell pore volume and transmissibility comprises, besides porosity and permeability, is a multiplier factor applied to each cell depending on rock compressibility. Therefore rock compressibility must be specified as the pore volume varies under different pressure conditions.

Rock compaction function (Tab. 7.3 and Fig. 7.7) has been computed using a rock compressibility of 0. 815 Pa^{-1} for a reference pressure of 27.5 MPa (Bouquet et al. 2009).

Pressure (bar)	Pvm (pore volume multiplier)	Tm (transmissibility multiplier)
137.5	0.99888	1
165.1	0.99910	1
192.7	0.99933	1
220.3	0.99955	1
247.9	0.99978	1
275.5	1	1
303.1	1.0002	1
330.7	1.0004	1
358.3	1.0007	1
385.9	1.0009	1
413.5	1.0011	1

Tab. 7.3: Rock compaction data used for the simulation.

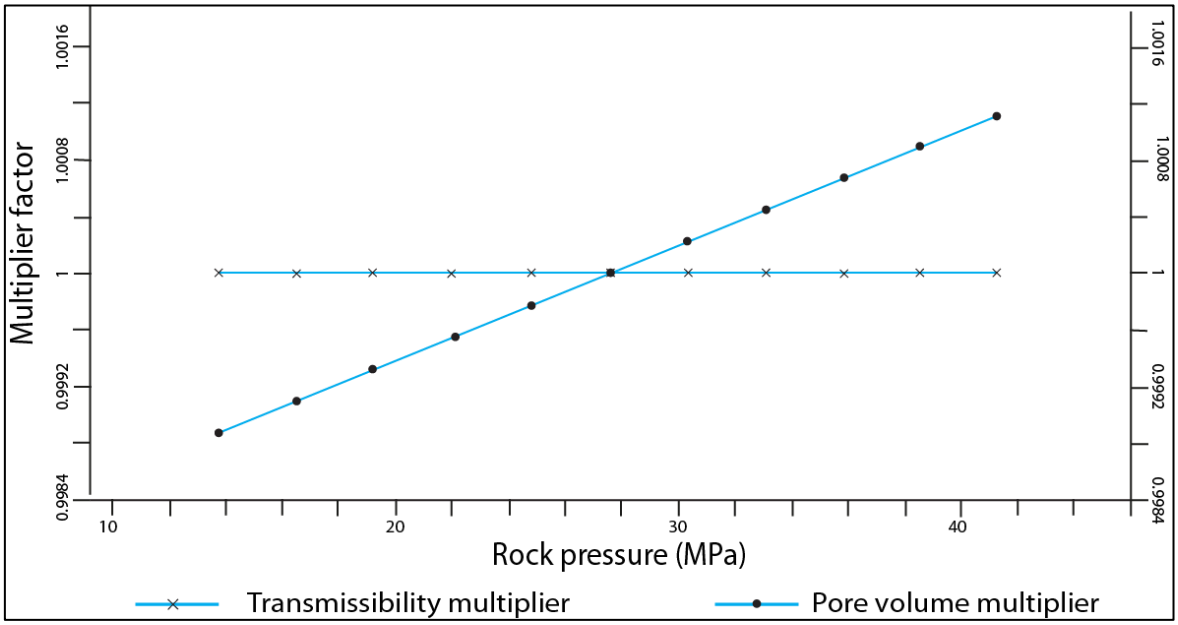

Fig. 7.7: Rock compaction plot showing pore volume multiplier and transmissibility multiplier used for the simulation.

Faults are modelled as cells and also have been assigned with a transmissibility multiplier, i.e. a multiplier which is applied to the transmissibility that is present between the cells that are juxtaposed on either side of the fault. In this simulation a value of 0 has been chosen, which produces a sealed fault as reported in data from literature (Vidal-Gilbert et al. 2010).

7.1.4 Development strategy

The approach used for the simulation is the *history matching* (Fig. 7.8) which has the aim to compare numerical simulation results with real data observed in the field (from literature review and well data). In a general way, a reservoir model is built using interpreted geology, geophysics and petrophysics. Once the ECLIPSE model runs, the modelled rates and pressures are compared with actual rates and pressure from production/injection data. If there is a match, then the ECLIPSE model is validated. On the contrary, if there is no match between modelled and observed data, a series of sensitivity models are run to identify the uncertain properties. Those properties are then modified in the tuning runs until the model and actual rates match and the ECLIPSE model can be validated. The accuracy of the history matching depends on the quality of the reservoir model and the quality and quantity of pressure and production data. For this specific case study, a validation of the flow model against history was required to get the right pressure information for the coupled simulation. Uncertain properties comprised horizontal permeability (from correlations), transmissibility multiplier for cells and faults.

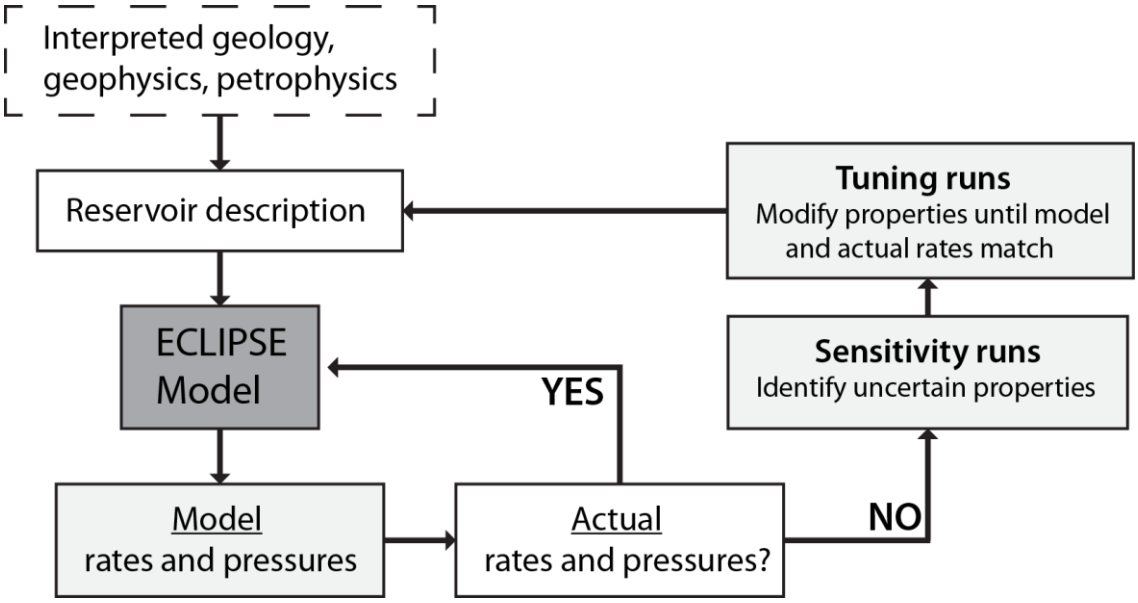

Fig. 7.8: History matching scheme for a reservor simulation. Modified after ECLIPSE Manual, Schlumberger (2009)

Naylor-1 well has produced 9.5 x 10^7 m^3 of gas (Vidal-Gilbert et al. 2010) from the Waarre Fm between 1st June 2002 and 27th October 2003. The discovery pressure (before production) was 19.58 MPa at reference depth of 1993.34 m TVDss, indicating an almost-hydrostatic pressure gradient before production. The downhole temperature was estimated at 85°C. The original pre-production gas-water contact (GWC) was located at 2015 mSS (van Ruth et al. 2007), although there are no wells intersecting it before production. The simulation has been constrained using the BHP (borehole pressure) as control mode and gas production rate as limit. Production data are available and comprises BHP and monthly averaged production (Tab. 7.4).

Month	Elapsed days	Production (kg/s)	BHP (MPa)
June 2002	30	1.2754	18.5754
July 2002	61	1.2485	17.6441
August 2002	92	1.3354	17.382
September 2002	122	1.6948	16.7184
October 2002	153	0.9046	16.2815
November 2002	183	1.0235	16.8651
December 2002	214	1.2283	16.3051
January 2003	245	1.0109	16.0061
February 2003	273	1.5426	15.6334
March 2003	304	0.9832	15.2719
April 2003	334	2.0009	13.7454
May 2003	365	1.1765	13.560
June 2003	395	2.5703	11.6204
July 2003	426	2.5043	9.9498

August 2003	457	1.7826	10.997
September 2003	487	0.9174	12.3964
October 1-11 2003	498	0.9130	
October 12-20 2003	507	0	
October 21-27 2003	514	1.1935	11.8612

Tab. 7.4: Production data used to constrain the flow simulation. Production is averaged for each month.

Injection of CO_2 through CRC-1 well started the 18th March 2008 and lasted until 29th August 2009, reaching a total amount of gas injected equal to 65445 tonnes (Jenkins et al. 2012). Pre-injection pressure was 17.80 MPa at 2013.1 m TVDss, slightly below initial reservoir pressure, while the temperature was 82°C at 2016.3 m TVDss. Also for this simulation, BHP has been set up as control mode and gas injection was the target. Injection data are reported as BHP and daily injection rate averaged for each month (Tab. 7.5). It is important to note that BHP never exceeds initial pressure, giving already the indication that caprock failure would be highly unlikely.

Month	Elapsed days	Injection (kg/s)	BHP (MPa)
March 18 2008	1		17.9006
March 2008	13	0.6895	17.9502
April 2008	44	1.0949	18.1296
May 2008	75	1.0092	18.2737
June 2008	105	1.4386	18.4566
July 2008	136	1.5935	18.5896
August 2008	167	1.6752	18.6002
September 2008	197	1.7878	18.8501
October 2008	228	1.7522	18.9363
November 2008	258	1.6940	19.0351
December 2008	289	1.2474	18.9531
January 2009	320	1.0902	19.0711
February 2009	348	0.7527	18.9584
March 2009	379	1.4031	19.0068
April 2009	409	1.5934	19.0822
May 2009	440	1.4583	19.1311
June 2009	470	1.5876	19.1763
July 2009	501	1.5752	19.2192
August 29 2009	530	1.5378	19.2226

Tab. 7.5: Injection data used to constrain the flow simulation. Injection is a daily rate averaged for each month.

7.1.5 Results of the flow model

The main objective of the flow model was to simulate production and injection of CO_2 in the Naylor Field, in order to obtain pressures at different time-steps to be used as input in the coupled geomechanical simulation with Visage. For this reason history matching has been chosen as simulation approach, using production and injection data available from operational reports. Pressures computed with the Eclipse simulation (Fig. 7.9) are comparable with pressure data from reports and literature review, and follow the same trend of the BHP imposed as control mode.

The discovery pressure before starting production in 2002 was 19.58 MPa, almost hydrostatic considering the reservoir depth is ~ 2 km. All the production phase is characterized by a constant drop in pressure inside the reservoir with a minimum value of 11.05 MPa (at CRC-1 location) reached at the end of the production (October 2003). This value of pressure corresponds to almost half of the original discovery pressure. The period between the end of the production and the beginning of the injection of CO_2 into the reservoir lasts approximately 4.5 years, during which a recovery in pressure is seen in the observed data. This behavior has been simulated in the reservoir model by adding an aquifer that forces the pressures to increase again up to 15.76 MPa (lower value in the model on 18th March 2008).

Pressures keep increasing during all the injection phase, as expected and the average pressure in the reservoir registered the last day of injection is 20.23 MPa (at CRC-1 location). Note that the reservoir pressure at the end of injection only slightly exceeds pre-production pressure of 19.58 MPa. Furthermore this value corresponds to an almost hydrostatic gradient, providing already an indication for the geomechanical simulation and the fault reactivation study where no failure is expected for such a pressure change.

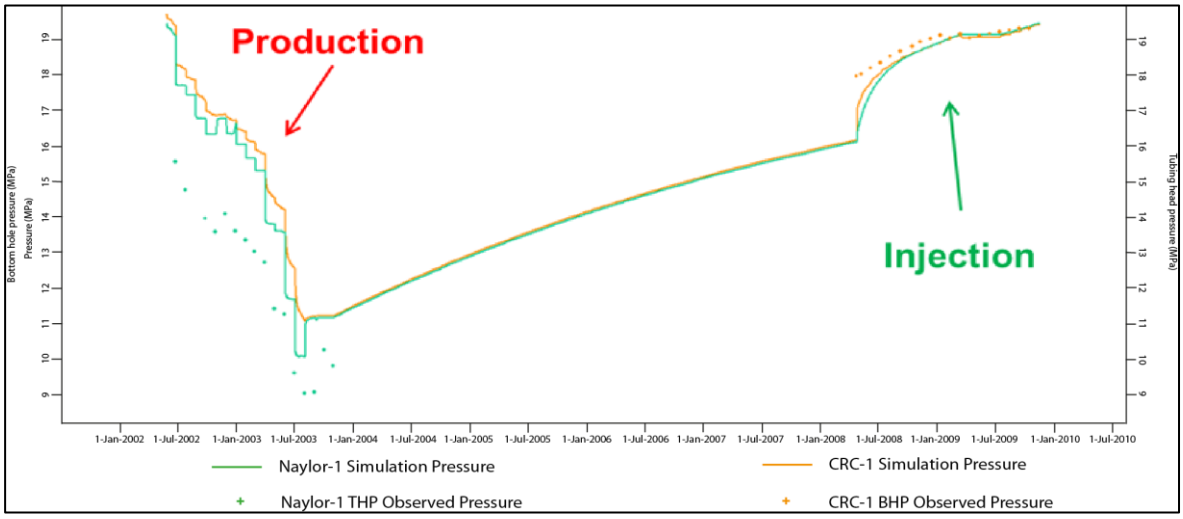

Fig. 7.9: Pressure profile at wells location computed with the flow simulation. Observed data from literature are represented by dots (green: THP tubing-head pressure from Naylor-1 during production; orange: BHP bottom-hole pressure from CRC-1 during injection).

Results for Gas Saturation (Fig. 7.10) in the reservoir have also been computed, with the aim to analyze the behavior of the gas volume inside the reservoir. An increase of

the gas saturation during the production phase is computed, due to the expansion of the gas in place. The Gas Saturation further increases during the injection phase as expected due to injection of new gas into the reservoir.

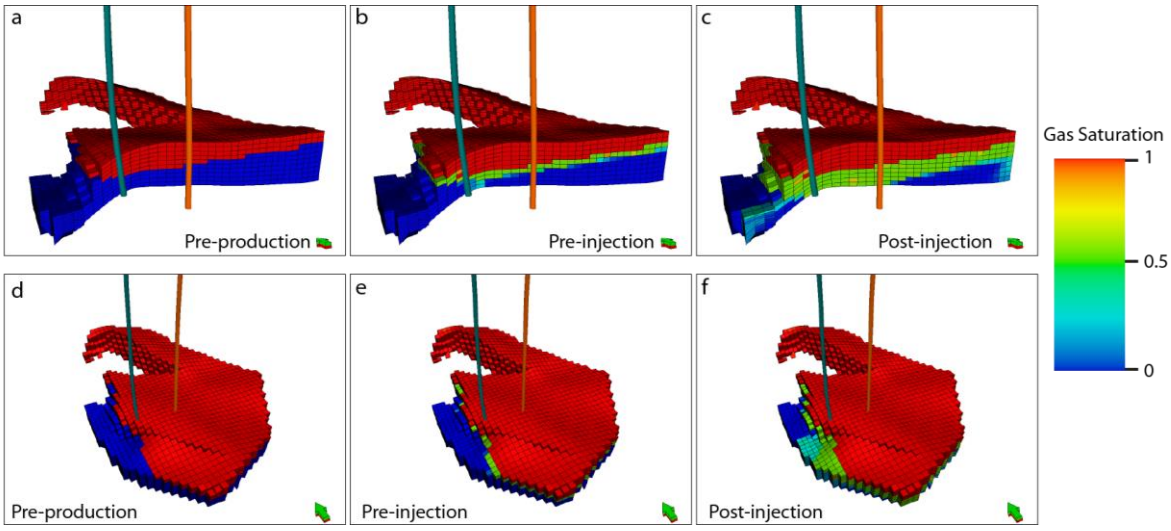

Fig. 7.10: Gas saturation computed pre-production (a and d), pre-injection (b and e) and post-injection (c and f). Gas saturation increases during both production and injection due firstly to expansion of gas (production phase) and then to the injection of new gas into the reservoir.

7.2 Geomechanical model

A preliminary elastic analysis has been performed starting from the geological model geometry, with aim to understand the extension of the area affected by the CO_2 injection in terms of changes in pore pressure and, consequently, effective stress. Size of the model was ~7x8 km, with a horizontal resolution of 100 m to avoid a too long computational time. Vertical resolution used for this preliminary model was 25 m.

Changes in pressure have been found to occur only in area directly surrounding the well location, therefore suggesting the need for a refinement in this particular location. The area chosen for the refinement has sides of 4km and is centered at the well location (Fig. 7.11). The horizontal cell size has been decreased from 100 m in the preliminary model to 25 m in the refined model in order to provide a more detailed analysis. Similarly, the vertical cell size has been decreased from 25 m to 15 m.

The following chapters will focus only on the refined model as its results are more relevant for the geomechanical characterization of the CO2CRC Otway Project. Results derived from the preliminary model are in any case comparable with results from the refined model.

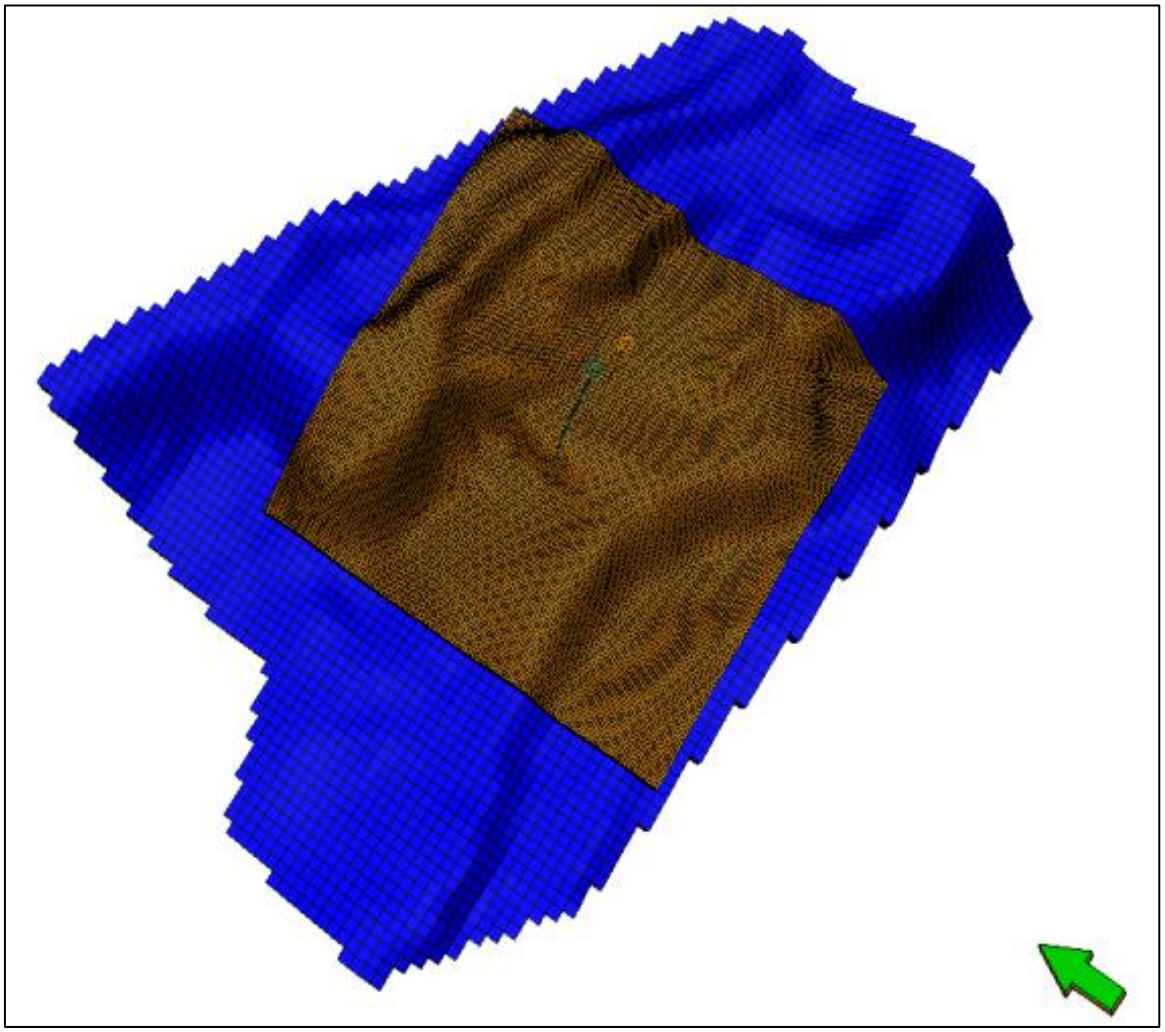

Fig. 7.11: Location of the refined geomechanical model (orange) with repsect to the geometry of the original geological model (blue). Horizontal resolution for the refined model is 25 m, for the preliminary model is 100 m.

7.2.1 Geometry and properties

The geomechanical model is built using only the two horizons bounding the reservoir: Waarre Fm top horizon and Eumeralla Fm top horizon. It has 159x159x10 grid cells, which correspond to a total number of 3D grid cells equal to 252810. The width of the model is 4x4km and the average thickness of the reservoir is 170 m. The embedded grid (Fig. 7.12) has been converting the simple grid surfaces into nodes and grid cells on which properties can be populated. Sideburden, overburden, and underburden have been added to the model selecting a number of cells by which the grid will be extended in each XX and YY (I and J) direction and a scale factor. The grid is created much finer in the area of interest at the centre of the grid and progressively coarsen towards the extremities. The grid width to depth ratio should ideally be less than 3:1. The embedded grid has a width of 12x12 km and is 4.5 km deep.

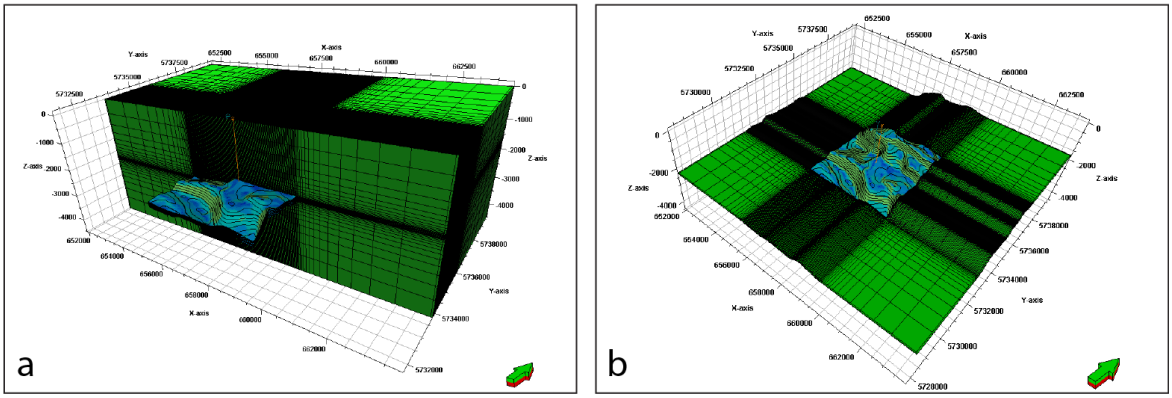

Fig. 7.12: Embedded grid of the geomechanical model in cross section and plan view.

Well logs provided data for populating the model with mechanical properties. DTCO (compressional waves slowness), DTSM (shear waves slowness) and RHOZ (bulk density) were available for CRC-1 and CRC-2 wells (Fig. 7.13). The Quantitative geocomputing plug-in (GAL – geocellular algorithm) was used to compute material properties such as Shear Modulus, Young's modulus (dynamic), Poisson's Ratio (dynamic) and Bulk Modulus using DTCO, DTSM, RHOZ (Tab. 7.6). Fuller's correlation (Mavko et al. 2009) allowed us to compute static Young's modulus from dynamic Young's modulus. For this simulation dynamic Poisson Ratio has been used as there is a good correspondence with data from literature (Tab. 7.7).

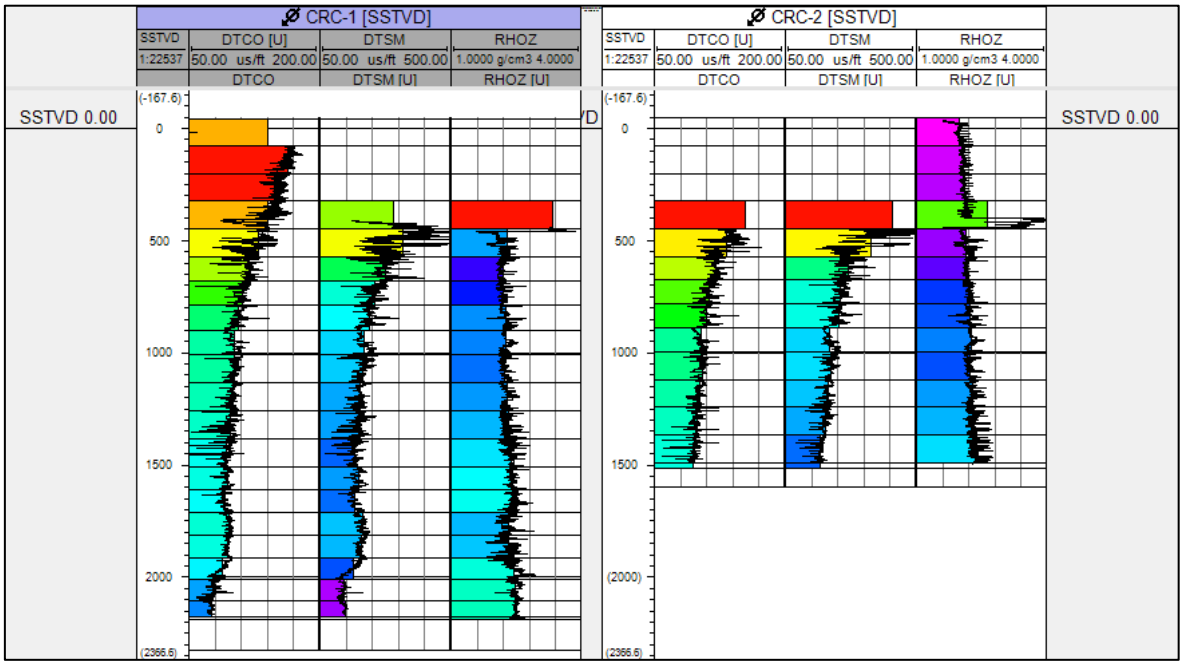

Fig. 7.13: Well logs used for populating the model and correlating properties. DTCO, DTSM and density logs were available for both CRC-1 and CRC-2 wells.

Property	Calculation
V_p - P- wave velocity (ft/s)	$= \frac{10^6}{DTCO}$
V_s – S-wave velocity (ft/s)	$= \frac{10^6}{DTSM}$
G - Shear Modulus (Pa)	$= RHOZ \times V_s^2$
K – Bulk Modulus (Pa)	$= RHOZ \times V_p^2 - \frac{4}{3}G$
E_dyn – dynamic Young's Modulus (Pa)	$= \frac{9.0 \times G \times K}{G + 3.0 \times K}$
ν – dynamic Poisson Ratio	$= \frac{3.0 \times K - 2.0 \times G}{6.0 \times K + 2.0 \times G}$
E_stat – static Young's Modulus (GPa)	$= 0.032 \times E\_dyn^{1.632}$

Tab. 7.6: Equations and correlations used in the Quantitative geocomputing plug-in GAL to compute material properties.

A literature review (Tab. 7.7) has been conducted to obtain the missing data needed for the geomechanical model. They include UCS (Unconfined Compressive strength) and angle of internal friction (Tenthorey et al. 2011, van Ruth et al. 2007, Vidal-Gilbert et al. 2010). For this study Biot Elastic constant has been assumed to be 1.

	Biot elastic constant	UCS (MPa)	Angle of internal friction (°)	Young's modulus (GPa)*	Poisson Ratio*	Density (kg/m3)*
Nirranda & Heytesbur	1	4.28	21.5	4.80	0.25	1950
Dilwyn Fm.	1	4.28	23.4	4.57	0.25	2323
Timboon Fm.	1	13.2	22.77	7.95	0.28	2298
Skull Creek	1	14.83	28.06	16.07	0.30	2391
Waarre Fm.	1	21.21	37.23	12.07	0.24	2498
Eumeralla Fm.	1	30	32.2	13.27	0.31	2495

Tab. 7.7: Summary of material properties used for the geomechanical model. Biot coefficient, UCS and Angle of internal friction are derived from a literature review. Reported values of Young's Modulus, Poisson Ratio and Density are averaged from well logs to give a reference value, since they are directly upscaled from well logs in the population process.

All the properties, from both logs and literature, have been upscaled to the embedded grid with an arithmetic averaging (volume-weighted). Then, they have been extrapolated in the horizontal direction into the sideburden using the Extrapolate function in Petrel. This operation fills value layers by layer: the algorithm looks at each layer separately, and does not use the values below or above. The underburden has been populated with properties of the lowermost layer in the model.

Six faults are included in the model and are mapped to the embedded grid. In PetrelRG faults are modelled as discontinuities (Fig. 7.14) and each object created contains a list of cells which intersect with the fault (including the dip value and dip direction of the fault within each cell) and a set of fault properties. As no data about stiffness of fault was available, a parametric study has been conducted which indicates an appropriate value of 40 MPa/km for the normal stiffness and 15 MPa/km for the shear stiffness over a range of values (Tab. 7.8).

A friction angle of 31° (corresponding to a coefficient of friction of 0.6) is assumed for this geomechanical model, on the basis of previous geomechanical models (van Ruth et al. 2007, Vidal-Gilbert et al. 2010) with the aim to be able to compare the results. Although being an assumption, the value is reasonable, being smaller than the coefficient of internal friction of the corresponding host rock (μ_i=0.75) (Tab. 7.7) as expected in lithologies like sandstone (Townend and Zoback 2000). Furthermore, there is no evidence of clay minerals that would contribute to lower its value, promoting sliding on fault planes.

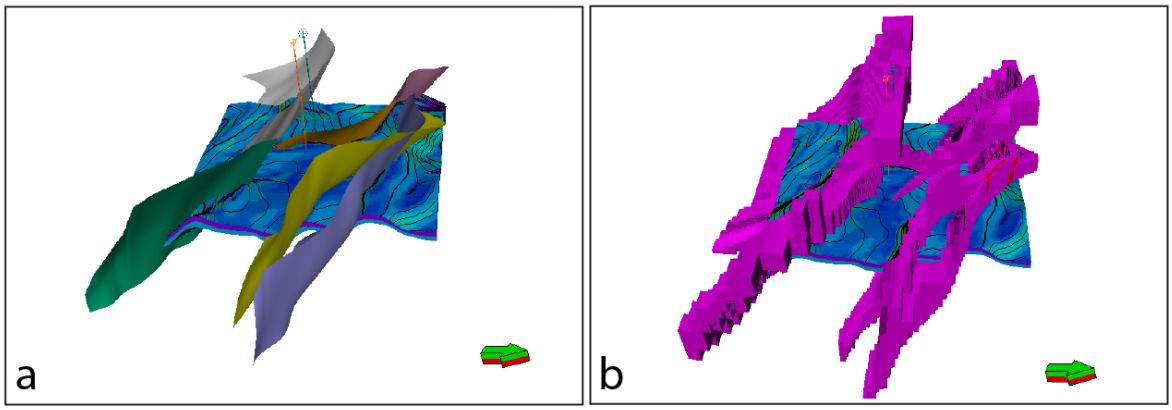

Fig. 7.14: Fault model (a) from the geological model and faults mapped into the geomechanical model (b).

Normal stiffness (MPa/km)	Shear stiffness (MPa/km)	Cohesion (MPa)	Friction Angle (°)	Dilation Angle (°)	Tensile Strength (MPa)
40	15	0.001	31	10	0.001

Tab. 7.8: Faults properties used for the geomechanical model.

7.2.2 Pressure data and boundary conditions

Pore pressure data (Fig. 7.15) are derived from the flow simulation previously performed and upscaled to be embedded grid with the Scale Up properties process. Pressure results from Eclipse simulator are available in the reservoir only, therefore a hydrostatic gradient of 0.956 MPa/m (Bérard et al. 2008) has been assigned to the rest of the model. Initial pressure condition has been set up at the beginning of the production phase, and then 13 steps have been included into the simulation in order to monitor the change in pore pressure every 3 months.

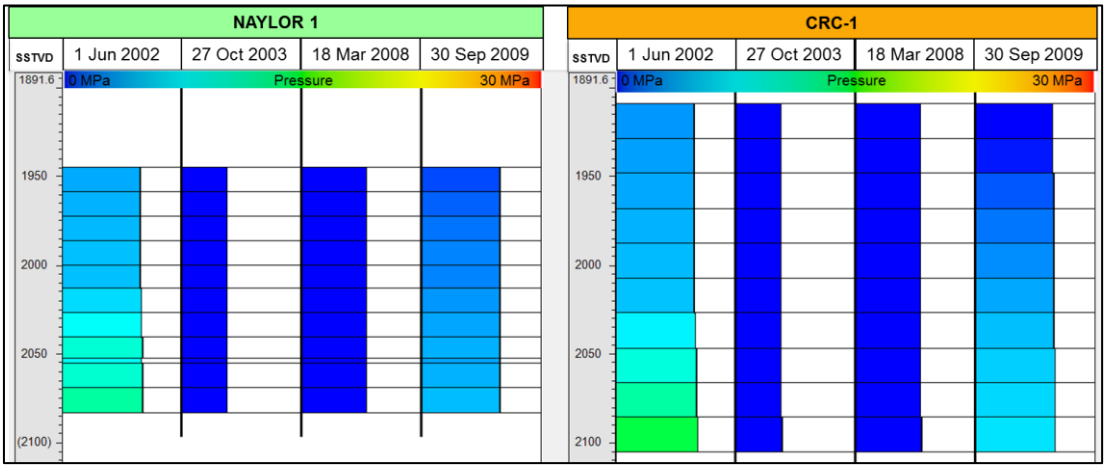

Fig. 7.15: Pressures in the reservoir computed in the flow model and used as input for the geomechanical simulation. Pressures pre- and post-injection are shown.

Geomechanical model performed through numerical solutions require the application of boundary conditions to simulate the correct physical conditions (Herwanger and Koutsabeloulis 2011). In this case stress boundary conditions are applied at the sides of the model to generate a stress field that matches observed stress attributes. At the base of the model, zero-displacement boundary conditions to prevent the occurrence of any movement. Stress data used as boundary conditions are derived from a literature review (Lawrence 2011, Nelson et al. 2006, van Ruth 2007, van Ruth and Rogers 2006). A more comprehensive description of the present-day state of stress in the Otway Basin can be found in Chapter 4.3. The minimum horizontal stress gradient is equal to 14.62 MPa/km and the ratio between maximum and minimum horizontal stresses applied to the model has been calculated as 1.13. Azimuth of the minimum horizontal stress is 52°, taking into account the direction of the maximum horizontal stress in the Otway Basin (142°). Calibration of the model has been accomplished with the comparison of observed stress data available at well location (Bérard et al. 2008, van Ruth 2007).

7.2.3 Coupling scheme

In a one-way coupled flow and geomechanics simulation approach, pressure data are transferred from the Eclipse™ finite difference reservoir simulator to the Visage™ finite element mechanical simulator at regular and/or critical times. The coupling is referred to as “one-way” meaning that fluid pressure affects the geomechanics computation, but mechanically-induced changes to porosity and permeability are not fed back into the dynamic reservoir simulation. So in effect, permeability and porosity are assumed to be constant for each time step in the modelling and not being affected by changes in stresses. This kind of approach is feasible in this particular case study because of the high permeability characterizing the reservoir (more than 1 Darcy). A fully coupled simulation, where permeability and porosity are function of changes in stresses, would not add appreciable benefits to the model results, only increasing the computation time. A schematic illustration of the one-way coupling scheme is shown in Fig. 7.16.

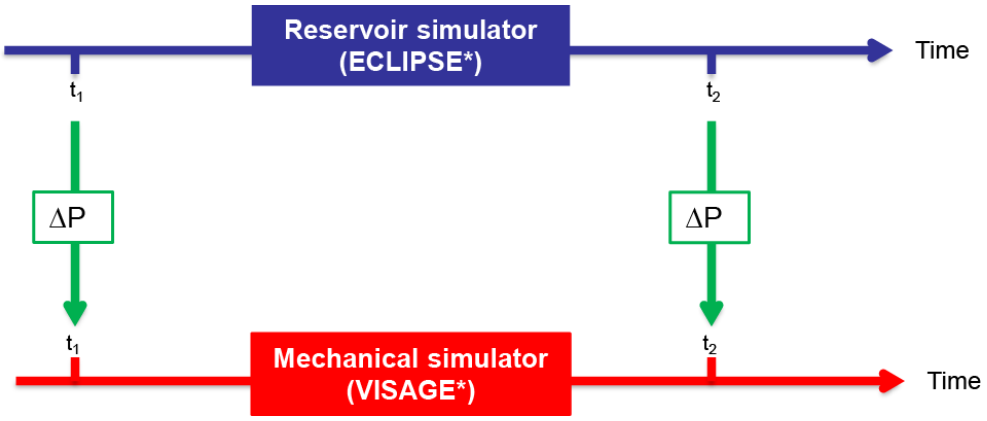

Fig. 7.16: Coupling scheme for a one-way coupling flow and geomechanics simulation. At chosen-time steps pressures from flow simulation are transmitted as input to the geomechanical simulator. This accounts for the influence of pressure changes in the in situ stress. Modified after (Bérard et al., 2008)

This coupling scheme can reproduce the pressure-dependence of stresses acting in the reservoir, which are modified in orientation and magnitude due to changes in fluid pressure (Addis 1997, Yeow et al. 2004). Thirteen time steps have been used for coupling the flow and the geomechanics simulation: every four months during production phase, then two check-points during the period the field has not been exploited and again a time step every four months during CO_2 injection into the reservoir (Fig. 7.17).

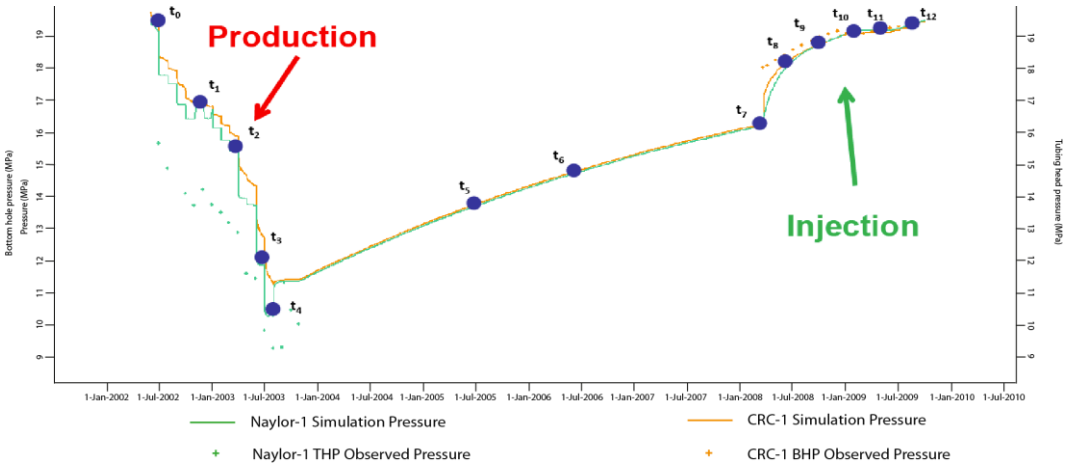

Fig. 7.17: Pressure profile along wells computed with the flow simulation. Blue circles indicate time-step when pressure data are transferred from the reservoir simulator to the geomechanical simulator.

7.2.4 Results of the geomechanical simulation

A one-way coupled simulation allows to compute at different time steps the vertical and horizontal rock displacement caused by production and injection. Furthermore, stress changes can be calculated and used to assess whether sufficient conditions exist for the onset of failure in either faults or intact rock around the wells. As the geomechanical simulations were elastic, rock failure is modelled explicitly by means of a failure function which directly evaluates if the elastic stress solution exceeds a given failure criterion. In this way only the onset of failure is estimated and subsequent plastic deformation is not modelled.

Vertical rock displacement (Fig. 7.18) is observed throughout the entire operations period. During the production phase, the overburden has a negative vertical displacement i.e. a downward movement with respect to pre-production surface elevation. Conversely, the underburden exhibits a positive vertical displacement, albeit smaller in magnitude. Maximum values of displacement are observed at the end of the production phase and compared to the surface elevation before production which is used as zero-value reference. A negative downward movement of ~150 mm is exhibited in the immediate overburden and ~30 mm at the ground surface. Rock displacement recovers during the injection phase, returning to values of ~7 mm in the overburden and ~1 mm at surface level due to the increase of pressure during the injection phase. A comparison of rock displacement along the two wells allows to better visualize the trend followed by the rock displacement, which is strictly connected to the change is pressure during operations. At the end of the production phase a change in pressure of ~9.5 MPa with respect to the initial pressure (19.58 MPa at well CRC-1 location) is computed, resulting in a significant vertical movement of the rock mass (~150 mm in the overburden and ~30 mm at surface level). On the contrary, at the end of the injection phase the difference between the final computed pressure (20.23 MPa at well CRC-1 location) and the initial discovery pressure is less than 1 MPa, which is reflected by a relatively small residual vertical displacement (~7 mm in the overburden and ~1 mm at surface level). No direct observational data are available to confirm surface displacement computed with the simulation.

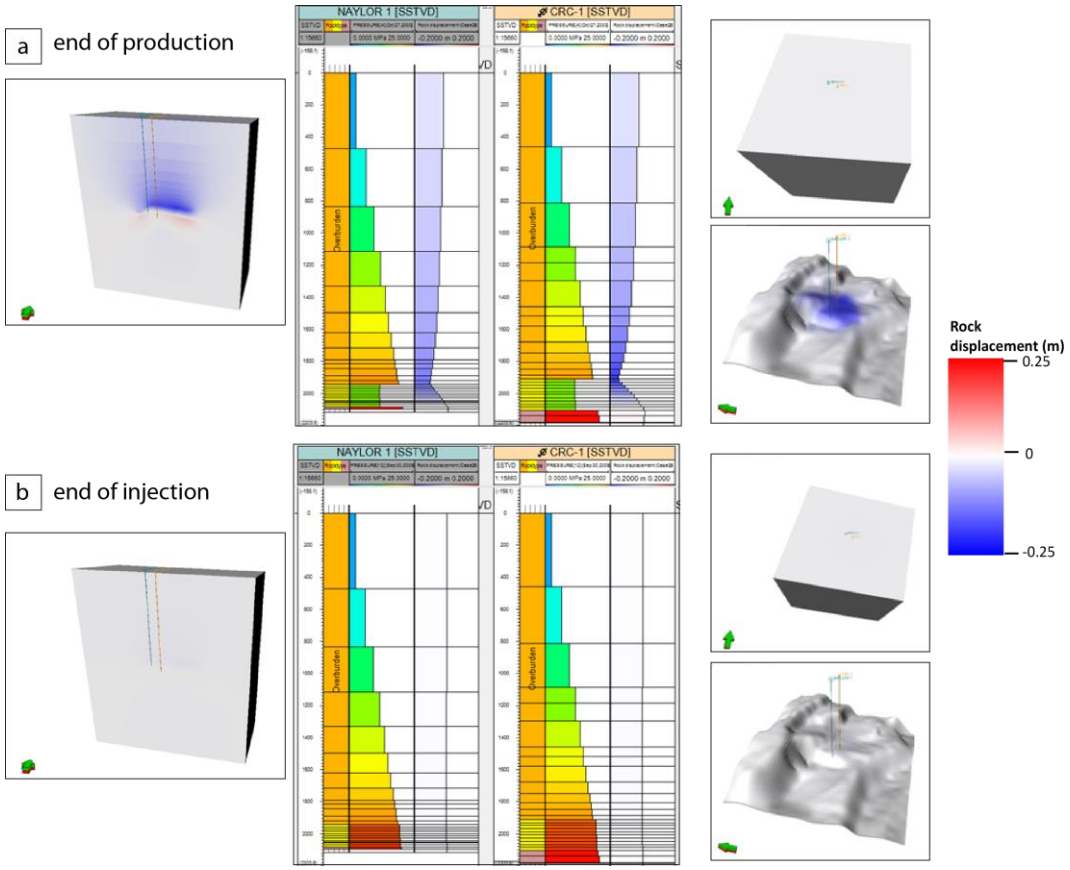

Fig. 7.18: Vertical rock displacement shown in cross section, along wells together with pressure data, in 3D view and in plan view at caprock level post-production (a) and post-injection (b). Length of the edges is 4 km.

The elastic differential vertical strain (Fig. 7.19) computed in the caprock has very low values and reaches ≈0.1 millistrain at the end of the production phase, and it is equal to zero at the end of the injection phase. No plastic strain is observed throughout the model.

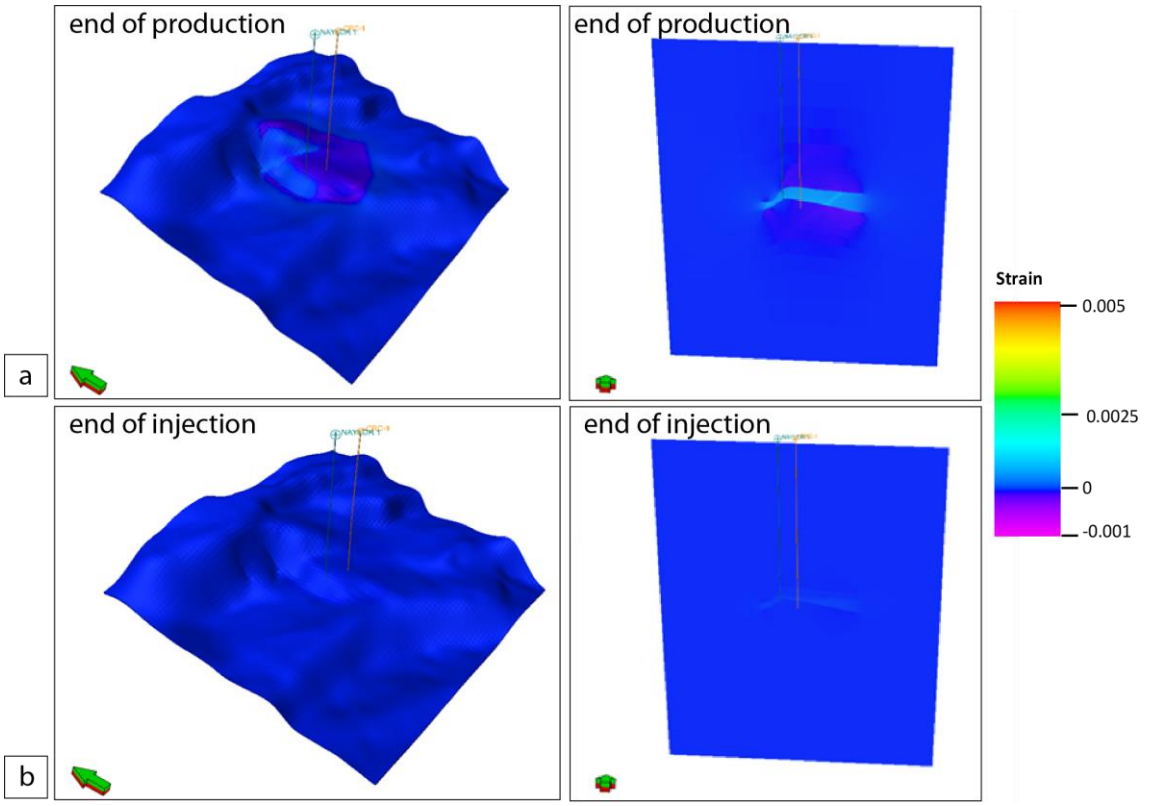

Fig. 7.19: Differential vertical strain computed at the end of the production stage (a) and at the end of the injection stage (b) in plan view at caprock level and in cross section. Length of the edges is 4 km.

Observations of stress rotation do not show substantial changes over time (Fig. 7.20). The vertical component of the effective stress increases with time during the production phase as pore pressure inside the reservoir decreases. During the injection phase a decrease in effective stress is computed as result of the increase in pore pressure inside the reservoir. However only the magnitude of effective stress is affected and stress directions do not show any appreciable change over time.

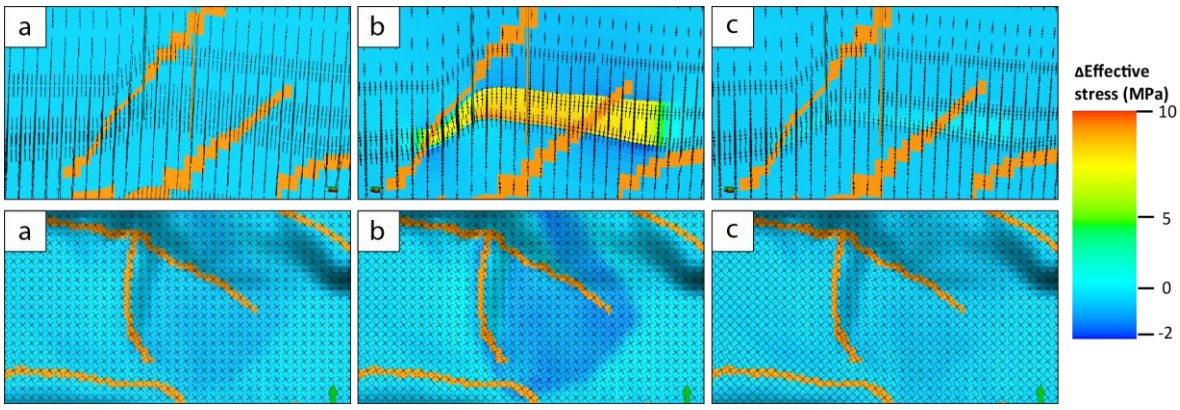

Fig. 7.20: Orientation and differential magnitude of the vertical component of effective stress in cross section (above) and plan view (below) pre-production (a), post-production (b) and post-injection (c). Top row pictures cover a depth of 600 m, the top view plots in the second row have a width of 1km.

Variation of stress orientation due to depletion can occur in reservoirs bounded by impermeable faults. More specifically, changes in pore pressure and the subsequent isotropic change in stress create perturbations in relation to the initial stress state. These perturbation can result in a rotation of the principal stress directions (Zoback et al. 2008).

Fault stability is studied computing for each cell belonging to faults the distance to the envelope failure of the Mohr-Coulomb Failure Criterion (Fig. 7.21). It has been assumed that the vertical stress is the vertical principal stress, according to the present-day normal stress regime, in order to calculate the distance to failure in terms of normal and shear stress. The equation of the failure envelope for the Mohr-Coulomb criterion of failure (Eq. 7-3) is:

$$S_S = C + \mu\sigma_n \qquad \textit{(Eq. 7-3)}$$

where S_s is the shear stress on the fault plane, σ_n is the normal stress, C is the cohesion of the faults and μ is the coefficient of friction of the faults. Coefficient of friction of faults is only assumed to be 0.6 (corresponding to an angle of friction of 31°) for this geomechanical model (7.2.1) and it is considered to be one of the most uncertain parameters in the calculation. In this case, no failure in the faults has been detected, as none of the cells reach the failure envelope for both linear and non-linear analysis (Fig. 7.21). However, lower values of coefficient of friction (e.g. μ= 0.36, corresponding to an angle of friction of 20°) would decrease the slope of the failure line, thus determining a state of failure for cells belonging to faults.

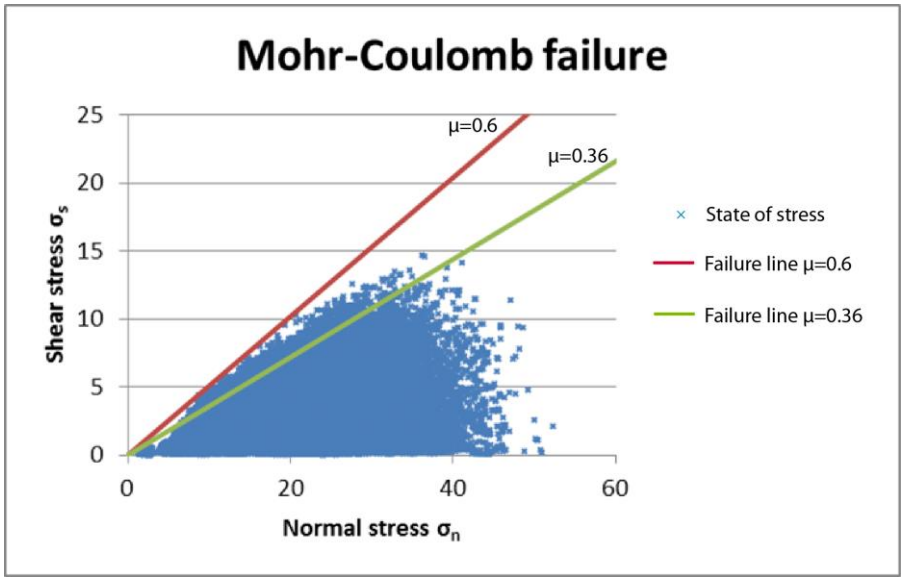

Fig. 7.21: Mohr-Coulomb failure plot for faults.

The same methodology is applied to assess possible failure in the caprock. As well as for faults, no failure is computed for the intact rock at both caprock and reservoir level if a Mohr-Coulomb criterion of failure is chosen. On contrast with the observation made for failure of fault, angle of internal friction of caprock (Tab. 7.7) and reservoir has been measured with triaxial tests (Tenthorey et al. 2011) and it is not considered an uncertain parameter for the simulation.

8 Potential fault reactivation analysis

8.1 Pore pressure for fault reactivation

Fault reactivation is one way of failure in geomechanics and can jeopardize the safety of operations, cause microseismicity and provide a path for leakage of CO_2 up to the surface. In the frame of Mohr- Coulomb criterion, slip will occur if the maximum shear stress acting on the fault plans exceeds the shear strength of the fault. Pore pressure required to reactivate fault in the Mohr-Coulomb criterion is expressed by (Fjaer et al. 2008)(Eq. 8-1):

$$P_p = \frac{1}{\alpha}\left[\frac{1}{2}(S_1 + S_3) + \frac{1}{2}(S_1 - S_3)cos2\theta - \frac{1}{2}(S_1 - S_3)\frac{sin2\theta}{\mu}\right] \qquad (Eq.\ 8\text{-}1)$$

where α is the Biot's coefficient (assumed to be 1), S_1 is the maximum principal stress and S_3 is the minimum principal stress and θ is the angle between the dip line of the fault and the S_3 direction. We refer to this pore pressure as the critical pore pressure or CPP. In the case of a normal stress regime, we can assume that S_1 is vertical ($S_1 = S_v$) and S_3 is horizontal and corresponds to S_{hmin}. It is then possible to apply this equation to the geomechanical model and estimate the critical pore pressure that would cause fault reactivation.

This study comprises calculation of the critical pore pressure both analytical and numerical approaches, with the aim to observe possible differences in pore pressure required for reactivation of faults. The grid built from the geological model is the basis for both approaches, but what changes is the input state of stress for the critical pore pressure calculation. Pore pressure derived from the history matching scenario is multiplied for a fixed factor until it matches the reactivation pressure previously calculated. Factors used for this operation were 1.1, 1.15, 1.2, 1.25, 1.3, 1.35, 1.4, 1.5. It is then possible to evaluate the change in pressure in the reservoir needed for causing fault reactivation. For all the different tested scenarios, fault reactivation affects only the two faults directly bounding the reservoir: Naylor Fault and Naylor East Faults.

8.1.1 Fault reactivation for the numerical analysis

In the case of the numerical simulation, total stresses needed for the fault reactivation analysis come directly from the Visage results, meaning that stresses have been computed numerically taking into account interaction between adjacent cells, topographic effects and presence of faults.

Following the methodology outlined above, the pore pressure from the history matching scenario is multiplied for increasing factors (Fig. 8.1). At a pressure of 1.15 times the original pore pressure, corresponding to a final Bottom Hole Pressure (BHP) of 22.73 MPa, both Naylor Fault and Naylor East Fault start reactivating. The amount of failure in the cells becomes more significant as pore pressure increases in the different scenarios.

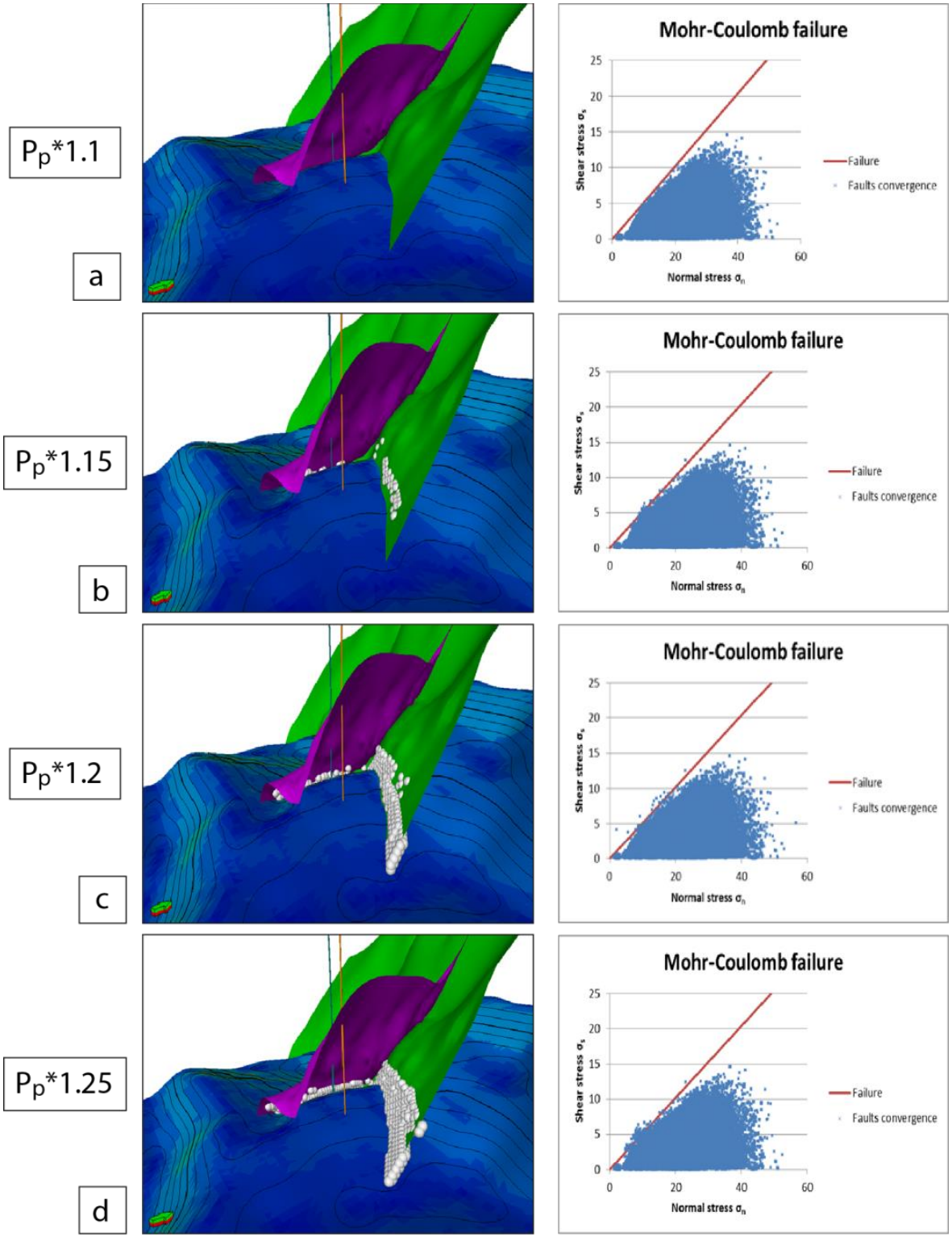

Fig. 8.1: Fault reactivation computed for the numerical analysis for pressure multiplied by a factor of 1.1 (a), 1.15 (b), 1.2 (c) and 1.25 (d). White dots indicate cells whose state of stress exceeds the failure criterion. The failure line corresponds to a coefficient of friction of 0.6.

8.1.2 Fault reactivation for analytical analyses

The second part of the fault reactivation analysis aims to calculate pore pressure that would cause fault reactivation in the case of analytical analyses. The methodology

used is the same as for the first part of the study, what differs is the state of stress used as input for the calculation. Two different assumptions have been made: a first case considers the total horizontal stresses to be constant during injection, a second case includes a dependence on pore pressure also known as Reservoir stress path. The workflow for computing analytically the state of stress is explained below.

Total vertical stress is calculated with the equation 8-2 (Fjaer et al. 2008):

$$S_v = g \int_0^z \rho(z)\, dz \qquad (Eq.\ 8\text{-}2)$$

where ρ is density at depth z, g is the acceleration due to gravity. Density log, the same used for the numerical simulation, has been used for the calculation. In the first assumption maximum and minimum horizontal stress are considered to be constant during injection and therefore independent by the change in pressure. They can be calculated using the following equation (Eq. 8-3 and Eq. 8-4) (Fjaer et al. 2008):

$$S_{HMax} = \frac{\nu}{1-\nu} S_v + \frac{E}{1-\nu^2}\varepsilon_y + \frac{E\nu}{1-\nu^2}\varepsilon_x \qquad (Eq.\ 8\text{-}3)$$

$$S_{hmin} = \frac{\nu}{1-\nu} S_v + \frac{E}{1-\nu^2}\varepsilon_x + \frac{E\nu}{1-\nu^2}\varepsilon_y \qquad (Eq.\ 8\text{-}4)$$

where ν is the Poisson ratio, S_v is the total vertical stress calculated before, E is the Young's modulus, ε_x and ε_y are respectively the horizontal and the vertical strain, which have values of 0.02 and 0.05 millistrain (from pre-injection strain calculated in the geomechanical simulation), thus assuming constancy through space and time. Calibration of the 1D analytical model with respect to the 3D numerical simulation has been done at the injection well location, where numerical values for strain has been extracted to be used as input for the calculation of analytical horizontal total stresses.

The pore pressure required for reactivate faults is calculated using the Mohr-Coulomb criterion as expressed in the Eq. 7-1, following the same methodology as for the numerical analysis. This first analytical analysis exhibits the first occurrence of reactivation at a pressure 1.2 times the original pressure (Fig. 8.2), corresponding to 23.93 MPa at well location.

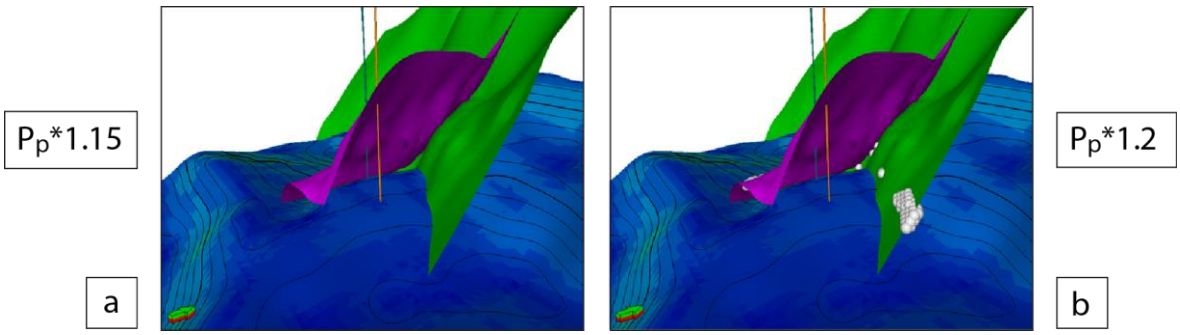

Fig. 8.2: Fault reactivation computed for the analytical analysis, considering horizontal stresses to be constant, for pressure multiplied by a factor of 1.15 (a) and 1.2 (b). White dots indicate cells whose state of stress exceeds the failure criterion.

A second assumption has been made, where stresses are considered to be dependent on the Poisson's ratio and pore pressure (Addis 1997, Santarelli et al. 1998, Yeow et al. 2004). This impact of pore pressure on regional tectonic stress is also known as the *reservoir stress path* and it was first observed in the Ekofisk Field where reservoir depletion and pore pressure drawdown were correlated to changes in *in situ* stress and deformation (Teufel et al. 1991). The reservoir stress path is defined as the ratio of the change in minimum horizontal stress S_{hmin} to the change in pore pressure P_p (Addis 1997). In general, the two horizontal stresses are affected by this poro-elastic effect (Santarelli et al. 1998). Information about reservoir stress path A can be extracted from the 3D geomechanical model, with reference to the injection stage, simply computing the ratio between the change in total minimum horizontal stress and the change in pore pressure pre- and post- injection (Eq. 8-5)(Zoback 2010):

$$A = \frac{\Delta S_{hmin}}{\Delta P_p} = \frac{1-2\nu}{1-\nu} \qquad \textit{(Eq. 8-5)}$$

Throughout the reservoir the reservoir stress path ranges from 0.25 to 0.60, with a concentration of higher value at the crest (close to the injection well location) and lower values at the flanks of the reservoir. This dependence on the relative location with respect to the depletion/injection point has been described analytically and suggests a differential distribution of radial and tangential stress (Altmann et al. 2014). Analytical studies on reservoir stress path report values ranging between 0.5 – 0.8 (Addis 1997, Santarelli et al. 1998) during reservoir depletion. Reservoir stress path related to injection of fluid is still poorly studied, however a dependence on loading and/or unloading path is expected in the stress rebound (Santarelli et al. 1998) and this could explain the lower values of reservoir stress path in this study.

The reservoir stress path effect has been incorporated for the analytical solution and for each time step according with the aim to account for changes in the two horizontal effective stresses related to changes in pore pressure. Maximum and minimum total stresses are then calculated using the relationships (Eq. 8-6 and Eq. 8-7)(Jaeger et al. 2007):

$$S_{HMax} = \frac{\nu}{1-\nu} S_v + \frac{E}{1-\nu^2}\varepsilon_y + \frac{E\nu}{1-\nu^2}\varepsilon_x + \frac{1-2\nu}{1-\nu} P_p \qquad \textit{(Eq. 8-6)}$$

$$S_{hmin} = \frac{\nu}{1-\nu} S_v + \frac{E}{1-\nu^2}\varepsilon_x + \frac{E\nu}{1-\nu^2}\varepsilon_y + \frac{1-2\nu}{1-\nu} P_p \qquad \textit{(Eq. 8-7)}$$

where the last term is the reservoir stress path and in particular P_p is the pore pressure at the initial stage i.e. before starting the injection.

In the fault reactivation analysis if the reservoir stress path and its dependence on pore pressure changes are considered, the pressure needed for reactivation is increased to 1.35 times the original pressure (Fig. 8.3),corresponding to 26.8 MPa at well location.

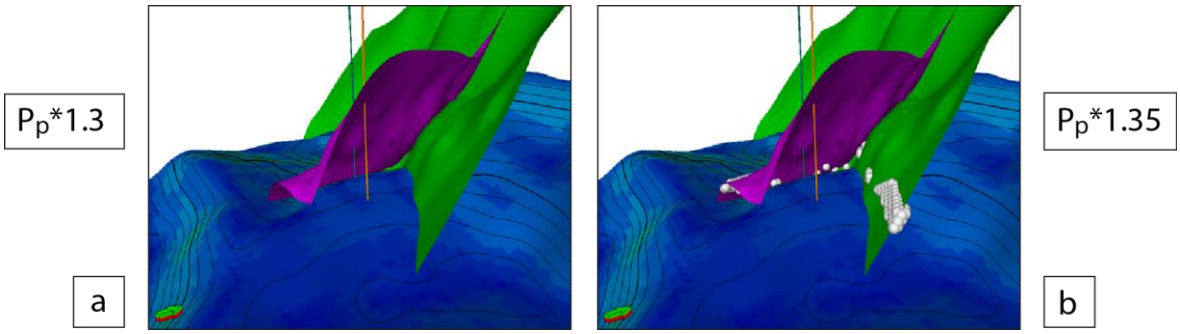

Fig. 8.3: Fault reactivation computed for the analytical analysis, taking into account the reservoir stress path, for pressure multiplied by a factor of 1.3 (a) and 1.35 (b). White dots indicate cells whose state of stress exceeds the failure criterion.

The pore pressure required for causing fault reactivation can also be expressed as so-called critical pressure perturbation (Fig. 8.4). This value shows how close the fault element is to failure, given a reference pore pressure (Zoback 2010). In this case the reference pore pressure is the pore pressure determined from the history matching flow simulation.

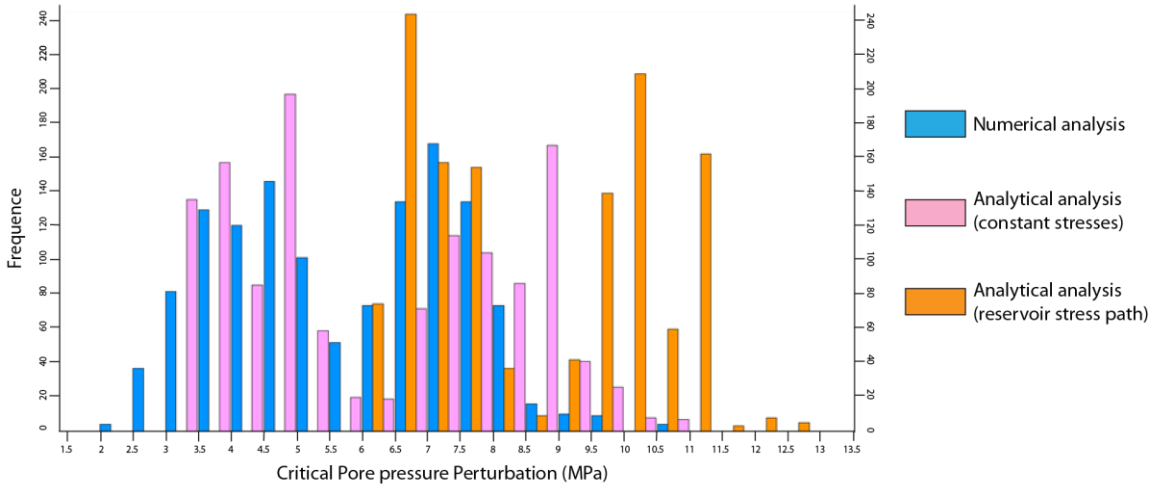

Fig. 8.4: Critical pore pressure perturbation calculated for the three different fault reactivation scenarios, using as reference pore pressure the history matching scenario.

8.2 Injection rate for a safe storage

Pore pressures for fault reactivation calculated for the different scenarios give an estimation of the pressure at the borehole which is necessary to reactivate faults, assuming high permeability and consequently high pressure diffusion. Therefore those popre pressures can be used then as BHP (Bottom Hole Pressure) control mode in a new flow model simulation (Fig. 8.5) in order to estimate the injection rate that causes fault reactivation, thus indicating an upper boundary for possible injection rates.

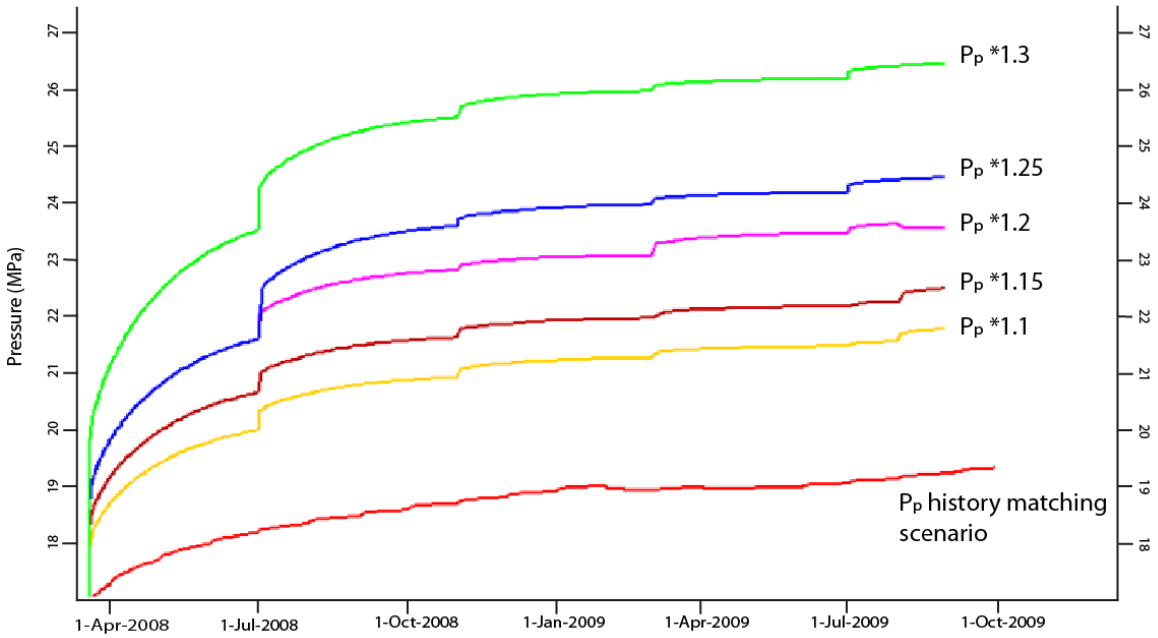

Fig. 8.5: Pressure profile for new flow simulations using as BHP control mode the reactivation pressures.

Results from the new flow models in terms of daily injection rate are significantly different for numerical and analytical analyses. Numerical analysis estimates that the CO_2 injection rate could be increased up to ~90.000 Sm^3/day, but if we consider analytical analyses the limit increases to ~100.000 Sm^3/day and ~140.000 Sm^3/day for constant stresses and stresses dependent on change in pressure, respectively (Tab. 8.1). Those differences are not negligible and could have a significant impact on risk management and operation set-up.

Pressure multiplier	Average final BHP (MPa)	CO_2 injection rate (SM^3/day)	Type of analysis
1.0	19.58	64741	History matching (numerical)
1.15	22.73	91301	Numerical
1.2	23.93	102257	Analytical – constant stresses
1.35	26.80	143662	Analytical – reservoir stress path

Tab. 8.1: Results from the new flow simulations in terms of CO_2 daily injection rate for each different reactivation scenario.

9 Steady-state geomechanical model for present-day stress

The second model presented in this thesis is a steady-state geomechanical model, describe the tectonic contribution of the *in situ* state of stress, thus accounting only for total stresses. As a consequence, pore pressure is not included in the computation. Furthermore, faults behavior is characterized from a structural point of view and quantified through slip and dilation tendencies under the computed stress conditions.

9.1 Geometry transfer

Specific requirements of the finite element software Ansys®, chosen for this second approach, do not allow a direct transfer from the geological model already used in the one-way coupled model.

The workflow for the geometry transfer (Henk and Fischer 2011) is based on the extraction of points from the grid created in Petrel® and the re-construction of a model geometry with the same spatial coordinates in Ansys® workspace. For a single horizon, horizon lines (i.e. the intersection lines between the horizon and the faults surfaces) are converted to polygons and further to points to obtain xyz-coordinates in ASCII format which can be exported from Petrel® and imported into Ansys® (Fig. 9.1). In some cases it has been necessary to introduce auxiliary surfaces ('pseudo-faults') in order to provide a more accurate topology inside these blocks.

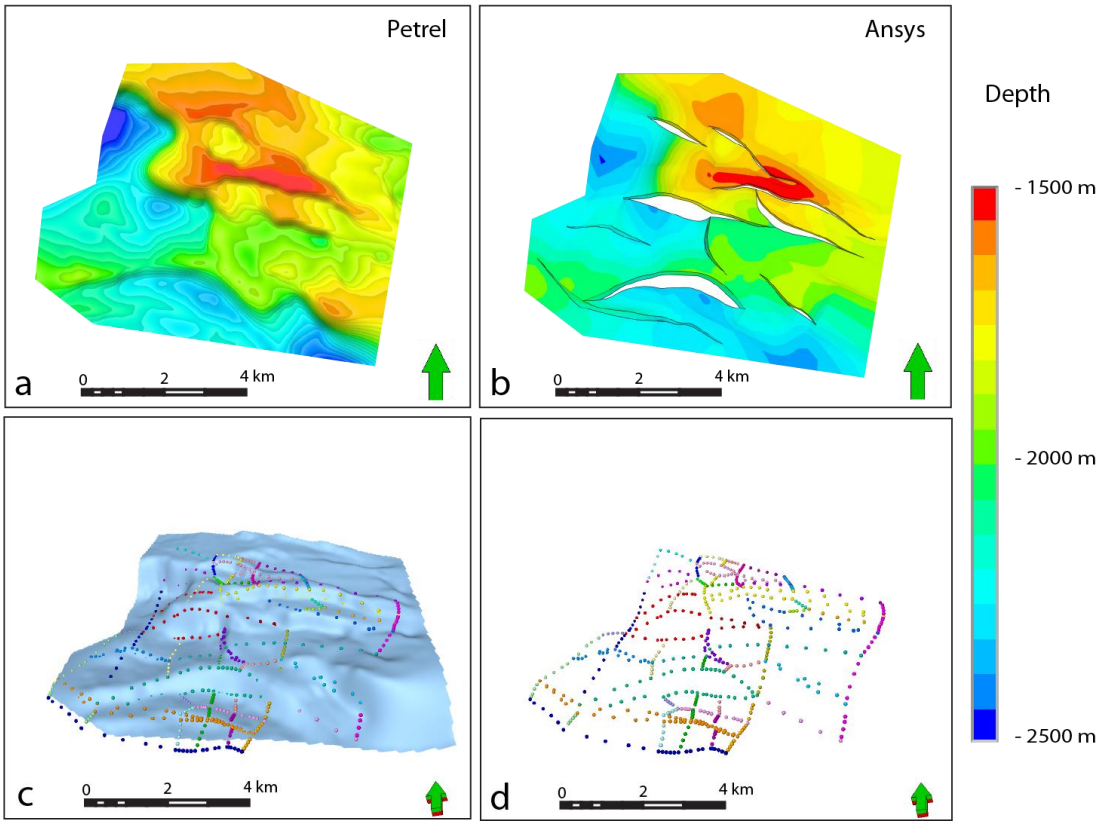

Fig. 9.1: Creation of points to recreate the geometry of the top reservoir level (top Waarre Fm): depth-contoured view of the horizon in Petrel® software (a) and in Ansys® software (b), horizon + points created (c) and the layer of points that is imported into Ansys® (d).

In Ansys® points are reconnected by splines that follow exactly the fault traces. Multiple splines are then combined to create a so-called Coon's patch of the internal area. A Coon's patch is a surface whose topology is interpolated by the slope of the bounding lines (Barnhill 1982, Goodman and O' Rourke 2004). The same workflow, starting from horizon and auxiliary lines to the re-construction of the patches, is followed for each horizon belonging to the original geological model. At this point, corresponding patches of two adjacent horizons can be used as input to re-generate volumes (Fig. 9.2).

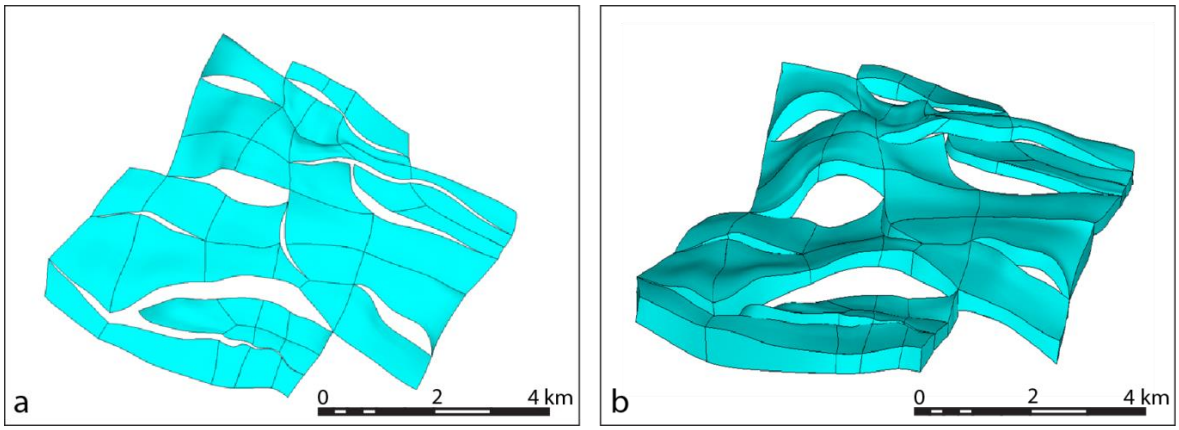

Fig. 9.2: Recreation of the geometry in Ansys®: multiple splines are connected into Coon's patches (a), superimposed layers of patches are used to recreate volumes (b).

Each lithostratigraphic layer chosen for the geometrical model is then re-created into Ansys® and the entire geometry of the geological model is re-built. However, the irregularity of the edges of this re-created model does not allow for a direct use of the geomechanical model. To solve this issue, additional volumes are built in the exterior part of the model with the aim to create a circular-shaped model on which boundary conditions can be easily applied (Fig. 9.3).

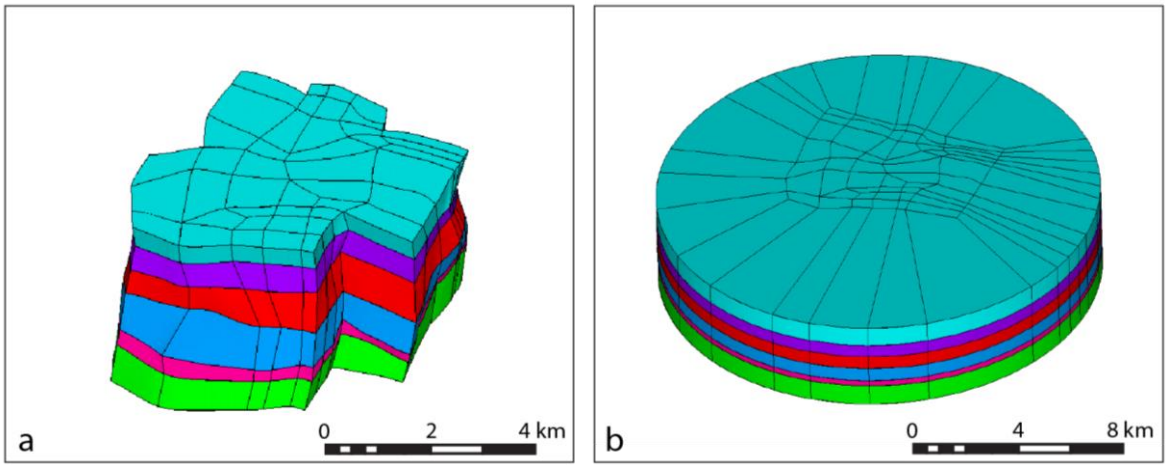

Fig. 9.3: Re-created geometry of the geological model (a) and final geometry used for the geomechanical model, with the addition of extra-elements to create a circular-shaped model (b).

9.2 Discretization of the model

Discretization of the model in 3D mechanical elements is accomplished by dividing each horizontal side of the volumes in 10 segments. The resulting mesh consists of 1000 3D variously sized elements created for each volume, leading to a non-uniform horizontal resolution ranging from 50 to 100 m (Fig. 9.4). Similarly, the vertical resolution depends on the thickness of the meshed layer, with a higher resolution for thinner layers (e.g. reservoir level which has a vertical resolution of ~15-20m). The total number of elements forming the geomechanical model is about 522.000.

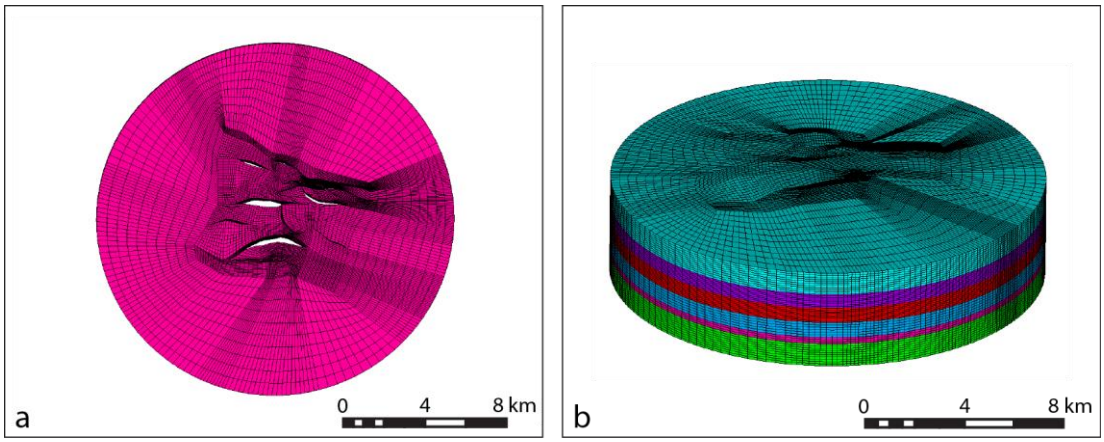

Fig. 9.4: Discretization of the model in 3D mechanical elements: details of the mesh at reservoir level (a) and final meshed geomechanical model (b).

Discretization of faults is done through 2D contact elements (Ansys 2012) that are assigned to both sides of fault plane (i.e. hanging-wall and foot-wall). This kind of discretization is very different with respect to the one-way coupled geomechanical model built in Visage® where faults where treated as cells (cf. Chap. 7.2.1). In a surface-to-surface contact as the one used for modelling faults, one side of the fault plane is modeled as "contact", the other one as "target" (Fig. 9.5). A real constant identifies each contact pair composed by contact and target elements. After the meshing process the edges of volumes not belonging to faults are merged together along the auxiliary surfaces created for exporting the points, to obtain a continuous mesh.

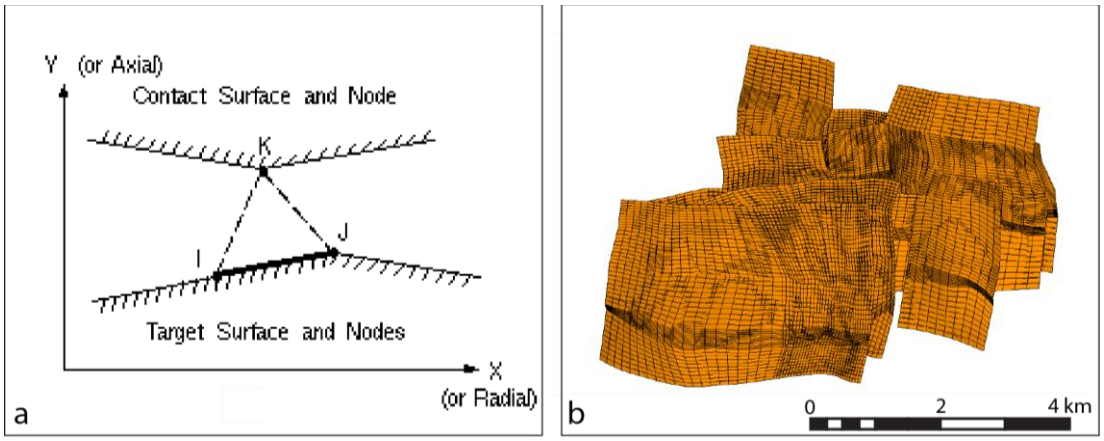

Fig. 9.5: Sketch of 2D contact elements (a) and discretization of faults in the geomechanical model (b). (a) is modified from Ansys® manual.

The use of contact elements allows a better accuracy on reproducing the geometry of the faults and, in addition to that, can recreate the potential slip occurring on faults. For this reason a contact-parameters are assigned to the contact elements, such as stiffness and a coefficient of friction that drive the slip occurring along faults. During the simulation, contact is researched at the location of the integration point (i.e. center of contact/target element) in a normal direction between contact and target elements (Ansys 2012). The contact element status is determined by the position and motion of a contact element relative to its associated target surface. Possible contact statuses are: open far-field contact, open-near field contact, sliding contact, sticking contact. Ideally, in the initial geometry contact pairs should be in contact, however this may not be straightforward, due to curvature and inclination of faults. Small gaps may exist between the integration points of the contact elements and target surface elements. Conversely, too much initial penetration between target and contact surfaces can occur. Various techniques can be used to solve this issue, such as defining a small initial contact closure (Fig. 9.6a), specifying an initial allowable penetration range (Fig. 9.6b), specifying a contact surface offset, increasing or decreasing the pinball region (i.e. the region where contact is researched, centered on the integration point of contact elements) (Ansys 2012).

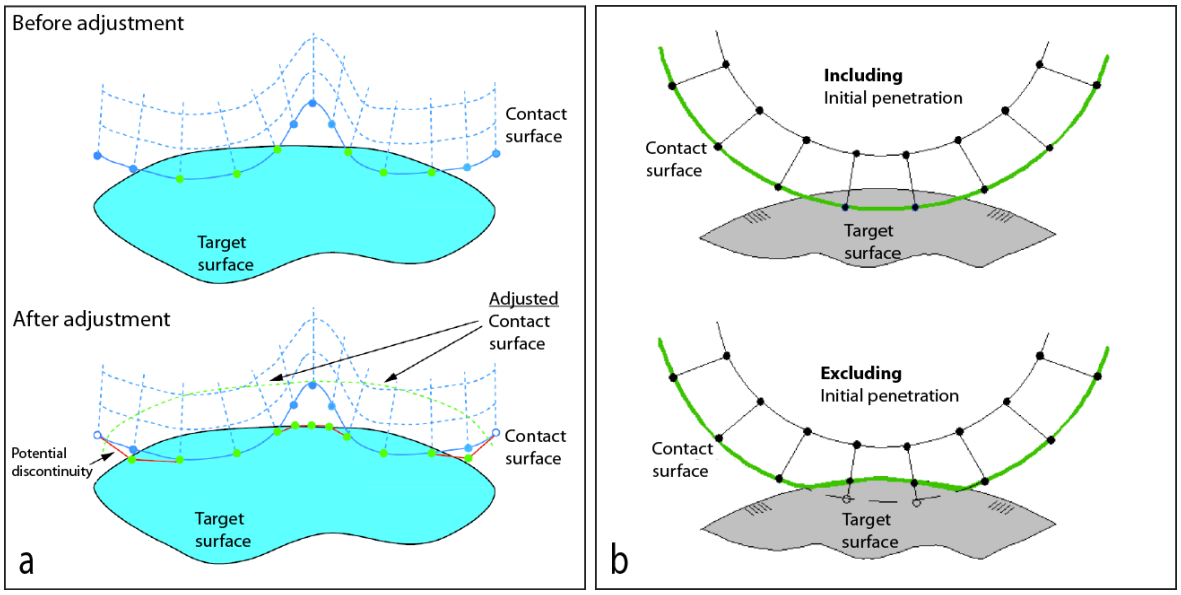

Fig. 9.6: Example of initial contact status issues and relative solutions: adjustment of contact surface introducing a small initial contact closure (a) and specification of an initial allowable penetration range (b). Modified from manual of Ansys (2012).

9.3 Material properties

The discretized model is populated with material properties derived from the well logs available and from a review of literature data (cf. Chap. 7.2.1). Contrary to the material population in the one-way coupled model, lateral and vertical variations are not included. Instead the six different lithostratigraphic layers are assigned with one single value for each parameter. This value is extrapolated as average for that

particular layer from well logs data. Material properties assigned to the intact rock include Young's modulus, Poisson ratio and density (Tab. 9.1).

	Young's Modulus (GPa)	Poisson Ratio	Density (kg/m^3)
Nirranda & Heytesbury group	4.80	0.25	1950
Dilwyn Fm	4.57	0.25	2323
Timboon Fm /Paaratte Fm	7.95	0.28	2298
Skull Creek Fm / Belfast Mst	16.07	0.30	2391
Waarre Fm	12.07	0.24	2498
Eumeralla Fm	13.27	0.31	2495

Tab. 9.1: Table containing the three material parameters assigned to each layer.

Contact elements belonging to faults are assigned with a coefficient of friction of 0.6 as in the previously exposed one-way coupled model. It is also the same value used in the analytical models carried out for the CO2CRC Otway Project (van Ruth et al. 2007, Vidal-Gilbert et al. 2010), so that the different models can be compared.

9.4 Boundary conditions

The application of boundary conditions in this steady-state geomechanical model occurs through a cut-boundary interpolation (Ansys 2012). This submodeling method requires the setup of a new external loadframe on which calibrated displacements are applied. The external loadframe is located in the same position of the internal model, but it is significantly bigger as it needs to contain completely the internal model and ensure the generation of a homogeneous stress field within it. The same mechanical properties are assigned to this model that has the same thickness and vertical division of the internal model (i.e. 10 divisions for each layer), but a much coarse grid. The nodes at the bottom of the model are fixed with zero displacement constraints. The external loadframe is rotated until it is aligned with the direction of the maximum horizontal stress (142° for this case study). Calibrated displacements are applied horizontally to the nodes belonging to the sides of the model, again with the aim of reproducing a stress field inside the model to match the desired state of stress that comprises a minimum horizontal stress gradient of 14.62 MPa/km and a ratio between maximum and minimum horizontal stresses of 1.13 (cf. Chap. 7.2.2). Observed stress data from the injection well are not included at this point, as they will be used for calibrating the model later on. Regional stress data used as boundary conditions are derived from a literature review (Lawrence 2011, Nelson et al. 2006, van Ruth 2007, van Ruth and Rogers 2006). A more comprehensive description of the present-day state of stress in the Otway Basin can be found in Chapter 4.3. Displacement values are calculated iteratively until they generate the desired magnitude of stress at a calibration depth (at this point depth from reservoir and sealing formation were considered). Amount of displacement applied is ~15 m and ~19 m in the direction of minimum and maximum horizontal stress, respectively.

Moreover, a small gradient increasing with depth has been included to better reproduce the horizontal stresses at the chosen calibration depths.

Once the external loadframe is solved and displacements are determined it is possible to perform the cut-boundary interpolation with the internal model. Coordinates of nodes located on the outer boundary of the internal model are exported and re-imported on the solved external loadframe. Specific displacements calculated in the external loadframe are interpolated for all the nodes and are used as boundary conditions for the internal model (Fig. 9.7).

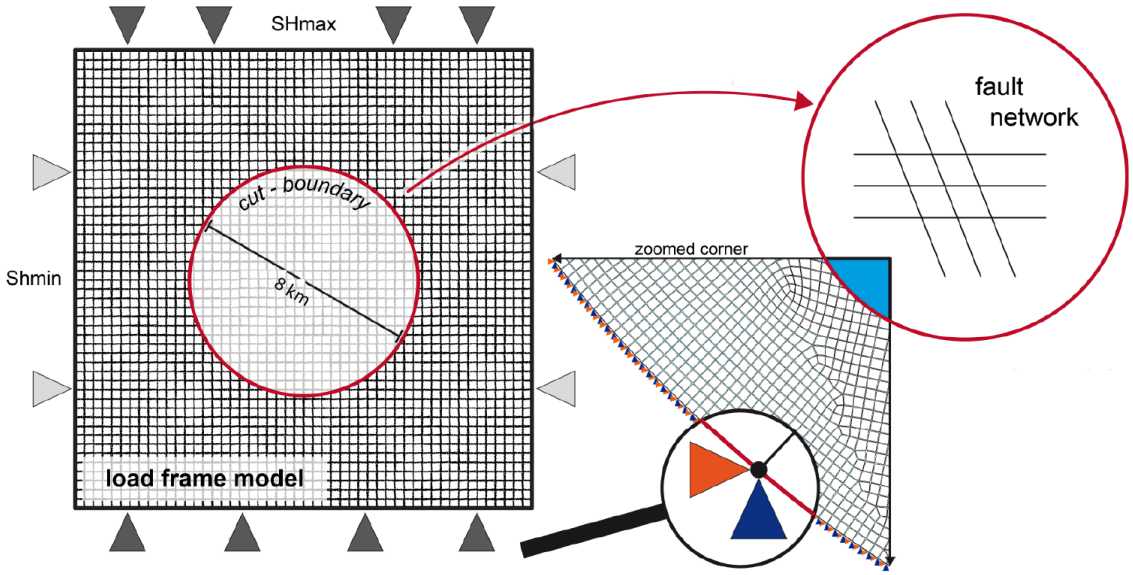

Fig. 9.7: Workflow for the cut-boundary interpolation method. Calibrated displacements are applied to an external loadframe and subsequently transferred to the internal model. Modified after (Fischer 2013).

9.5 Model calibration

The main aim of calibrating a geomechanical model is to check whether it matches observed stress data in terms of magnitudes and orientation. For this case study only the calibrated displacements are considered to be an uncertain parameter. Indeed, mechanical parameters for both intact rock and faults have to be preserved in order to allow comparison with previous geomechanical models. Stress measurements for the calibration process are obtained from leak-off test conducted in CRC-1 well (van Ruth 2007) and dipole sonic log data inversion (Bérard et al. 2008, Lawrence 2011, Vidal-Gilbert et al. 2010). The measured stress data are compared to a stress profile extrapolated along the trace of CRC-1 well in a pre-calibration stage. New calibrated displacements are applied to the model iteratively with aim to reduce the gap between the modeled and measured values. Generally, the difference in magnitude between pre-calibration modeled values and measured values is of the order of about 2-3 MPa.

Pre-calibration modeled values of S_{hmin} are smaller than the measured values at shallower depth. An inversion of the trend is registered after 960m depth where modeled values start overcoming the measured values. The calibration in this case aims to reduce the values of modeled S_{hmin} (Fig. 9.8).

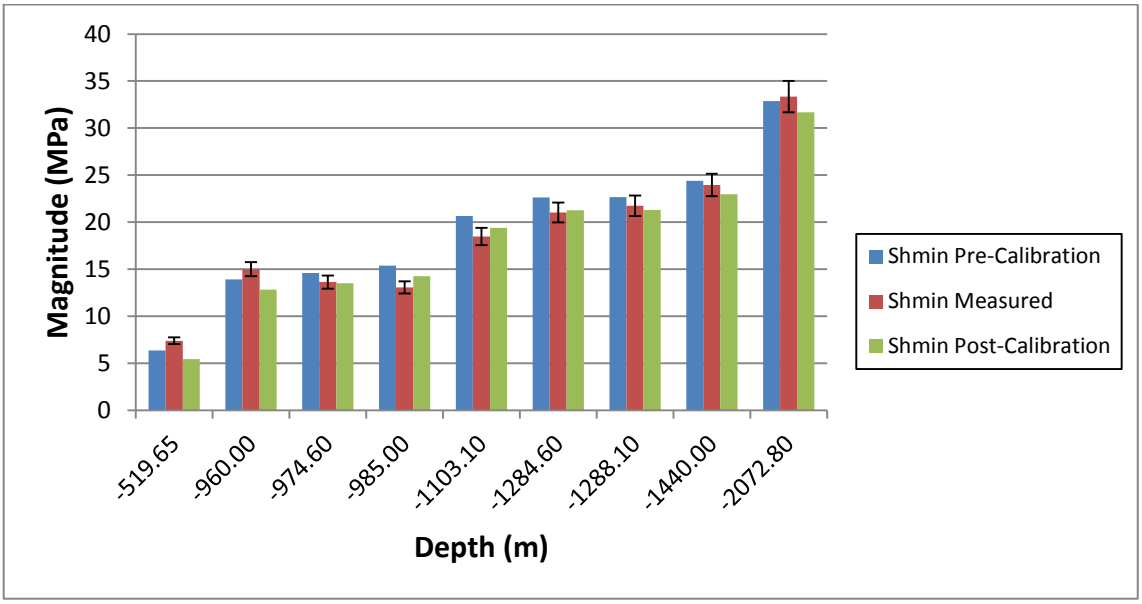

Fig. 9.8: Diagram comparing pre-calibration modeled values (blue), measured values (red) and post-calibration modeled values (green) of minimum horizontal stress (S_{hmin}). A 5% error is taken into account for measured values.

The analysis of pre-calibration S_{HMax} values in comparison with measured values describes an opposite scenario. In this case pre-calibration modeled values are generally smaller with respect to the measured values. The calibration process aims to increase the magnitude of the modeled S_{HMax} to reduce the gap with the measured values (Fig. 9.9).

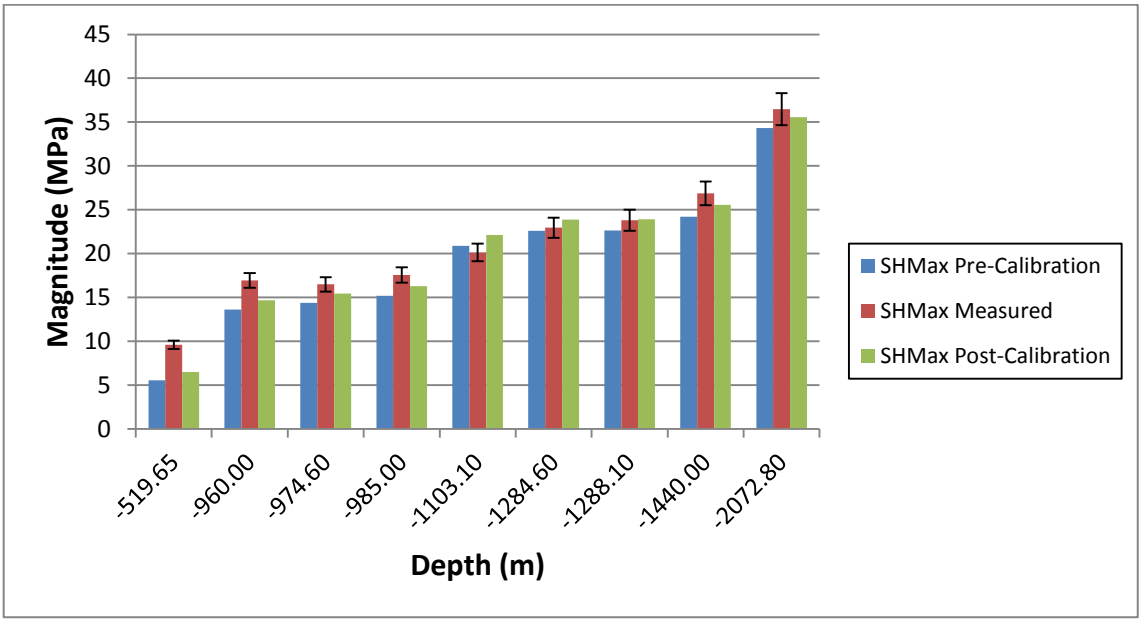

Fig. 9.9: Diagram comparing pre-calibration modeled values (blue), measured values (red) and post-calibration modeled values (green) of maximum horizontal stress (S_{HMax}). A 5% error is taken into account for measured values.

9.6 Results of the steady-state geomechanical model

In the following pages, results from the steady-state geomechanical model are presented. In particular, distribution of the present-day in situ stress is described in terms of both magnitudes and orientation. Focus of this geomechanical analysis is on the reservoir layer, therefore top view of the reservoir formation is shown in the results plots. The reservoir formation is divided into 10 elements in the geomechanical model (cf. Chap. 9.2) and to avoid numerical influences from different material parameters the middle element layer is chosen for visualization. Slip and dilation tendency of faults contributes to characterize faults from a structural point of view.

9.6.1 In situ stress distribution

The first set of results includes magnitudes of the three principal stresses. The present-day stress regime in the Otway Basin is a normal faulting regime, where S_1 is the vertical stress, S_2 is the maximum horizontal stress and S_3 is the minimum horizontal stress. The variations of magnitudes reported for all the three principal stress show a correlation with depth, where magnitudes increase with depth. The mid-reservoir level in examination has complex topography, with depth ranging almost 1 km between -1500 m and -2500 (Fig. 9.10). In particular a shallow area is located in the NE quadrant of the reservoir with shallowest values comprise in a zone of connection between two faults. On the other hand, the NW quadrant and the SE quadrant host the two areas at greatest depth, leading to higher values in magnitude.

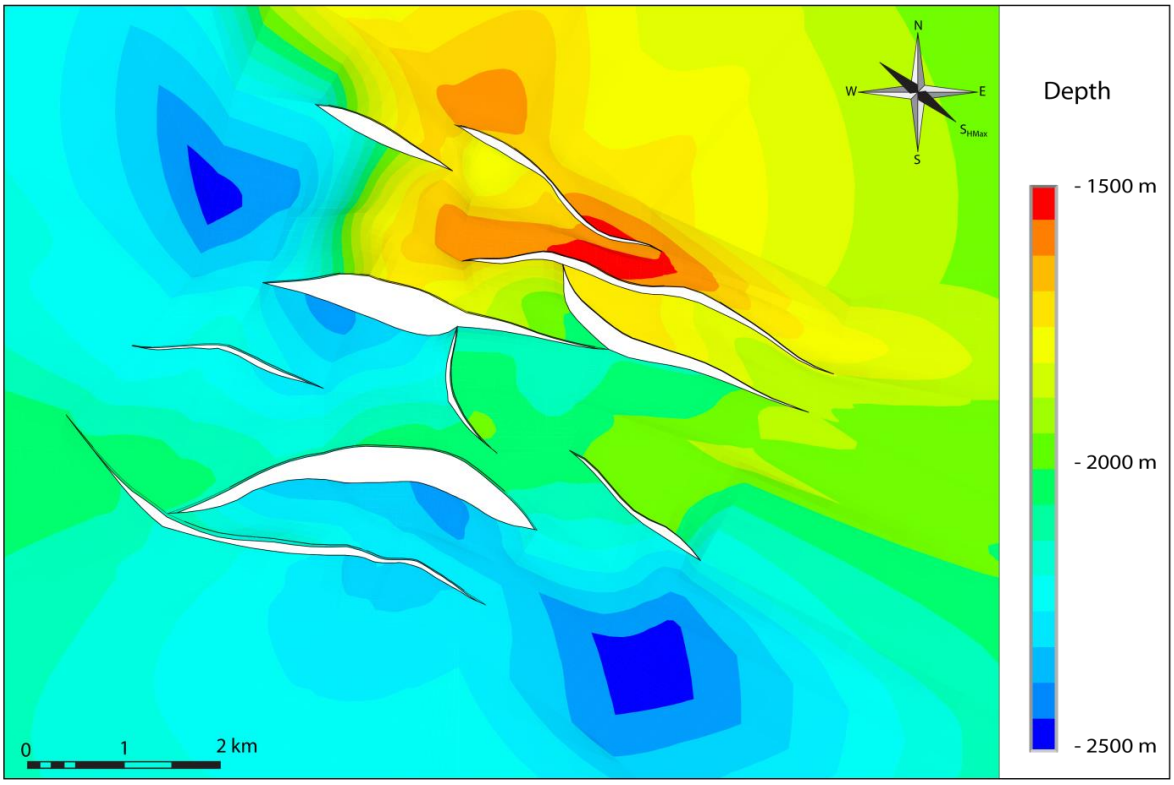

Fig. 9.10: Depth map of the mid-reservoir level, the layer chosen to plot the results of the steady-state geomechanical model.

The vertical stress distribution shows a good correlation with depth (Fig. 9.11). Lowest values are located in the NE quadrant, while areas with higher values lie in NW and SE quadrants. Local perturbations occur around faults mostly in the southern part of the plot, probably due to numerical noise caused by contact elements with different curvatures. The vertical stress is a measure of the weight of the rock column above a certain depth, therefore it describes the lithostatic load acting at reservoir level.

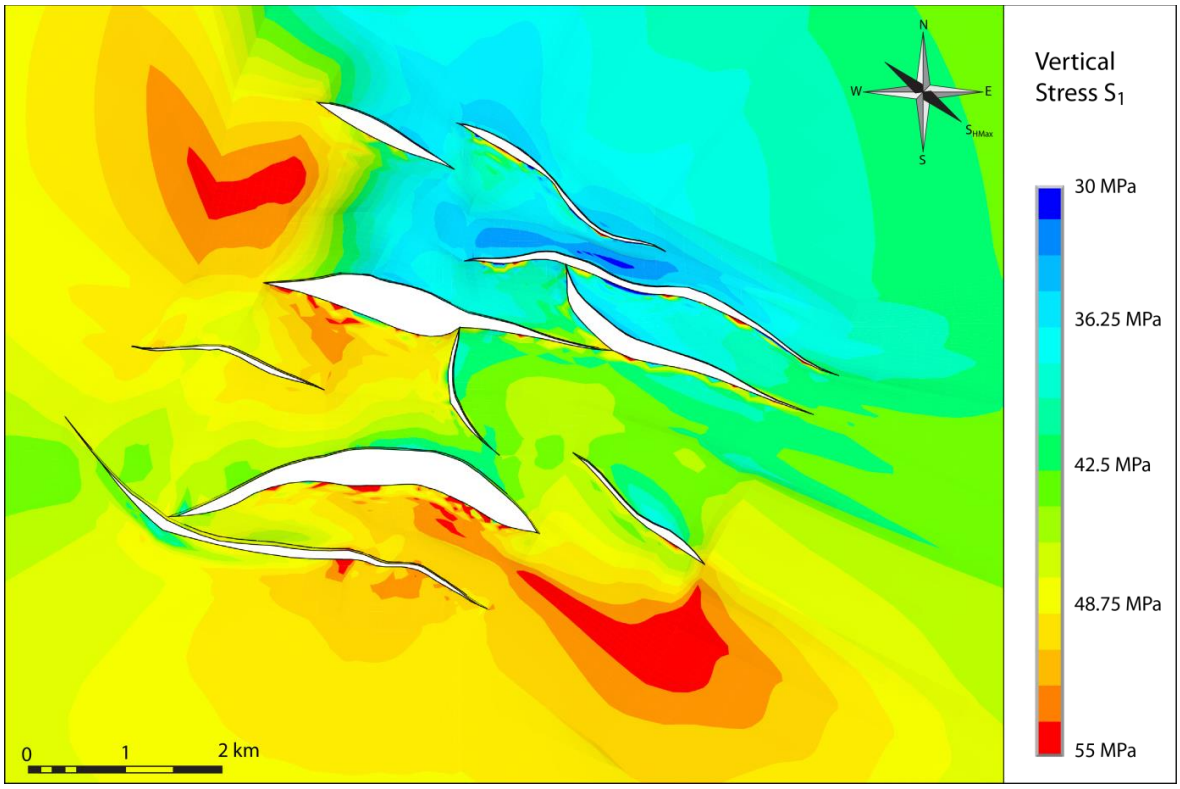

Fig. 9.11: Top view of the mid-reservoir level showing contoured plot for the magnitude of vertical stress S_1.

The distribution of both horizontal stresses S_2 and S_3 correlates well with depth (Fig. 9.12 and Fig. 9.13), having the same high-magnitude areas in NW and SE quadrant although some differences in shape and intensity occur. They both show the highest magnitudes in the SE quadrant. Local perturbations occurring at the footwall of the faults tend to be exaggerated by the contact elements with different curvature, as already seen for the vertical stress. More specifically, the maximum horizontal stress S_2 is more affected by perturbations towards higher values, most of all in the southern area of the reservoir. On the other side, the minimum horizontal stress S_3 develops more low-value perturbations in the northern part of the reservoir.

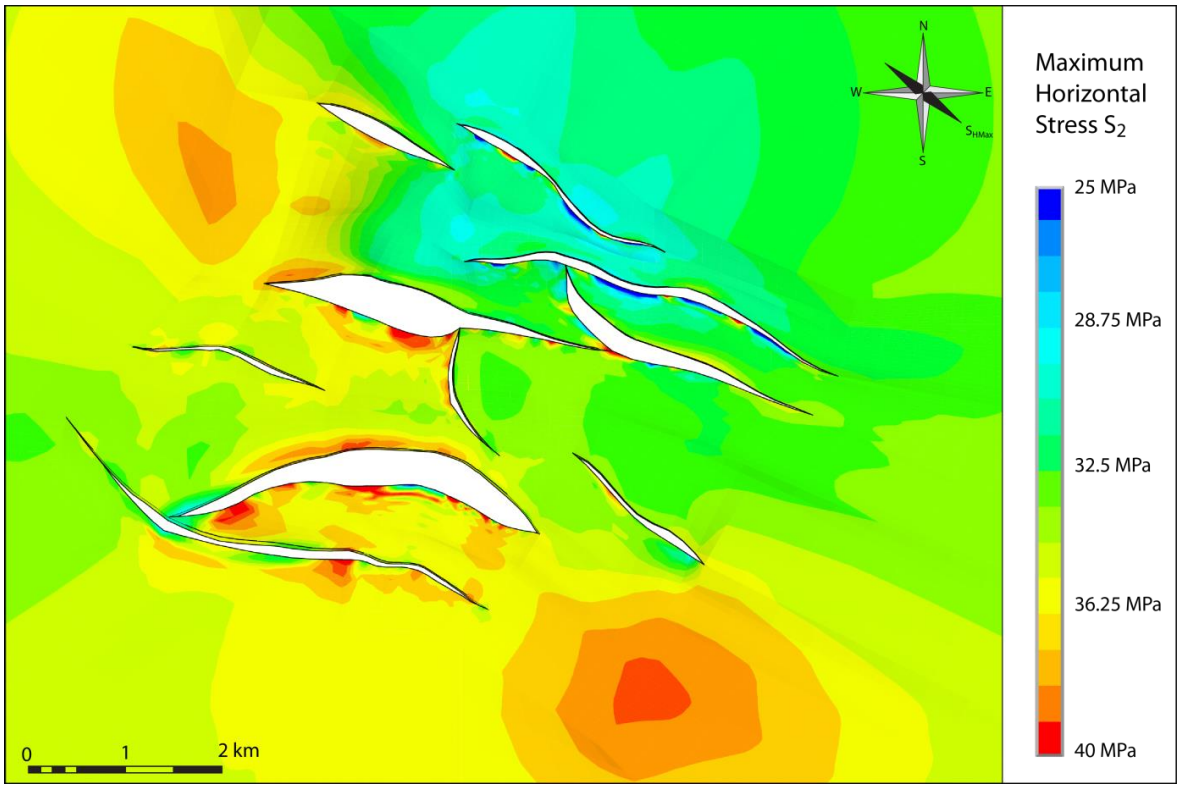

Fig. 9.12: Top view of the mid-reservoir level showing contoured plot for the magnitude of maximum horizontal stress S_2.

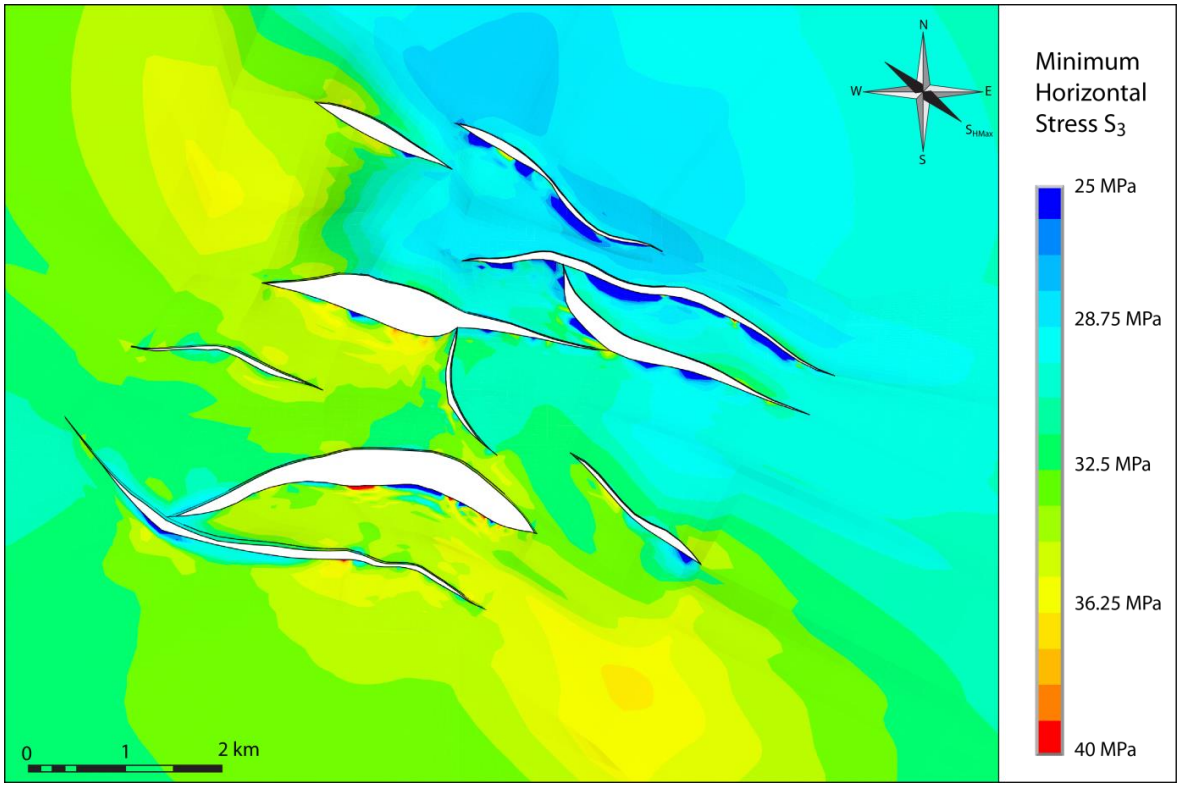

Fig. 9.13: Top view of the mid-reservoir level showing contoured plot for the magnitude of minimum horizontal stress S_3.

To fully describe the state of stress of a reservoir, the knowledge of the magnitude of the three principal stresses is not sufficient. Indeed, it is necessary to establish the orientation of the maximum horizontal stress component with respect to North. For

the Otway Basin, regional studies and borehole measurements indicate an orientation of 142° from North (Lawrence 2011, Nelson et al. 2006, Vidal-Gilbert et al. 2010).

The computed orientation of the maximum horizontal stress S_2 (Fig. 9.14) can be extracted from the direction cosines of the components of the stress. The resulting vectors have an uneven spatial distribution due to the not uniform mesh: vectors are plotted at the center of the elements, therefore as the size is not equal for each element, also spacing of vectors is not uniform. The regional trend NW-SE is observed in most of the model. Local rotation of the stress occurs around faults, where the vectors tend to become perpendicular to the faults orientation. However, not all the faults produce stress rotation which seems to show a dependence on fault throw and orientation of the fault with respect to the orientation of the regional stress. The bigger the fault throw, the more the stress rotates, also due to the fact that throw sometimes exceeds the thickness of reservoir. In such conditions, in correspondence of the throw of the faults, different mechanical properties will be present at the two sides. As a result, the numerical simulation is affected by the interference caused by this difference in rock properties, thus enhancing the occurrence of local stress rotation. Faults oriented parallel to the regional stress are less affected by stress rotation, whereas fault that form an angle with the maximum horizontal stress direction are more favorable for occurrence of local stress rotations. Further observations about local stress rotation are included in the discussion chapter, following evidences also from paleostresses modelling (11.3).

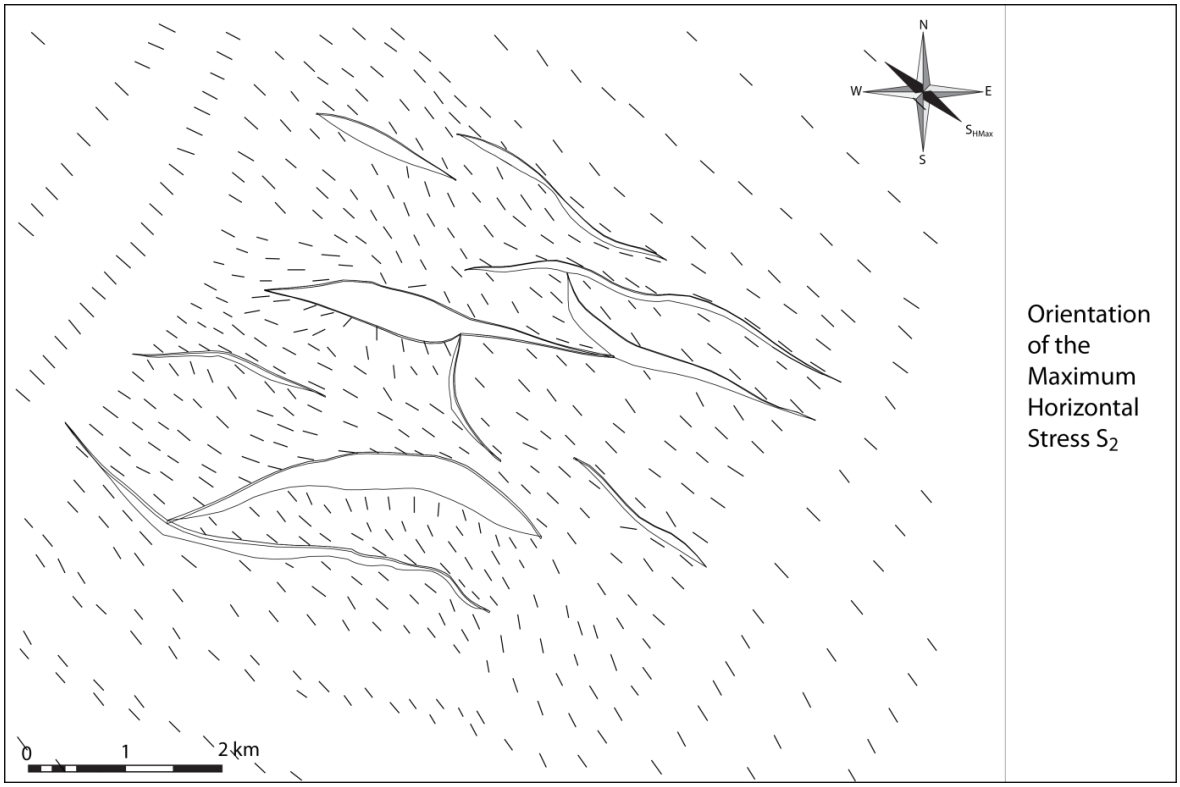

Fig. 9.14: Top view of the mid-reservoir level showing vector plot for the orientation of the maximum horizontal stress S_2.

Starting from the knowledge of three principal stresses is possible to calculate other stress quantities that concur to a comprehensive geomechanical characterization of the reservoir.

The first quantity derived is the mean stress, given by the arithmetic mean of the three principal stresses (Fig. 9.15). It is an isotropic stress component and is also known as lithostatic component (cf. Chap. 2.1.3). Its magnitude distribution follows the general dependence on depth of the three principal stresses. Areas of high-magnitude are located in the NW and SE quadrants, with highest values computed in the SE quadrants. The NE quadrant hosts the low-magnitude area, with a uniform distribution. Perturbations of the magnitude of the mean stress are less evident than in the case of the three principal stresses plotted singularly (compare with Fig. 9.11, Fig. 9.12 and Fig. 9.13).

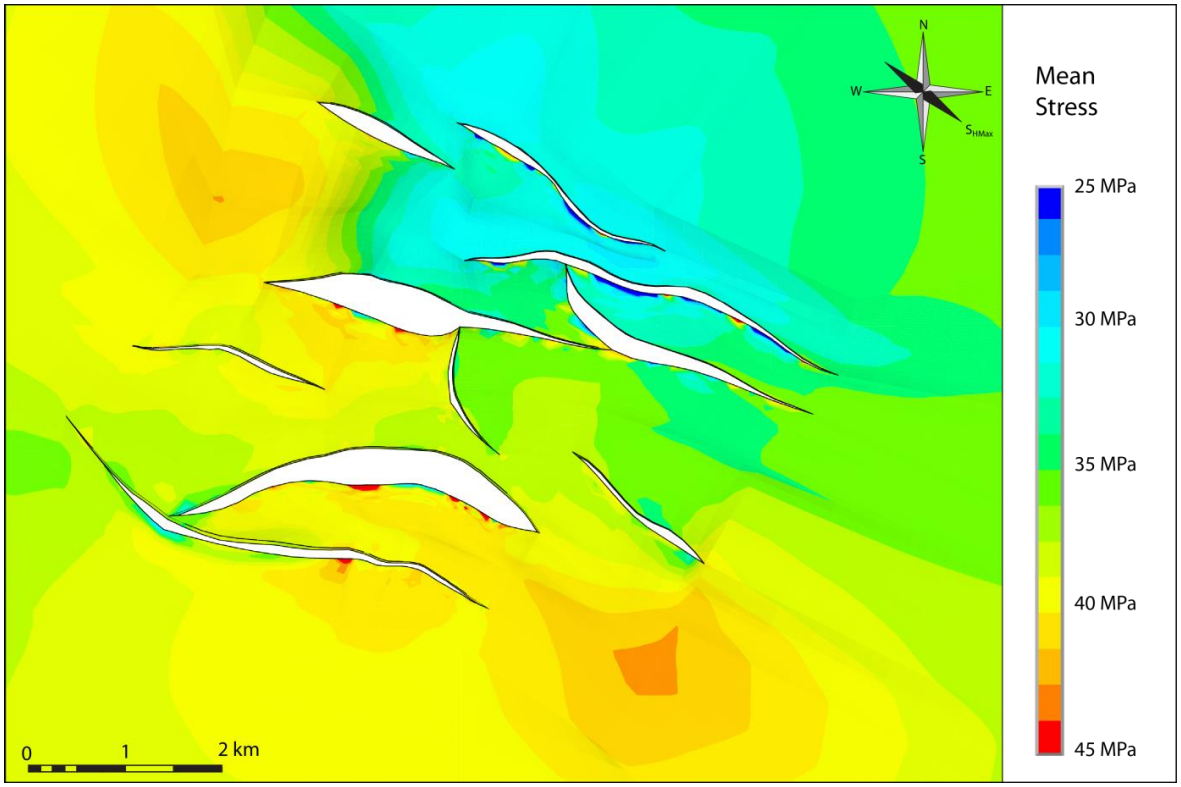

Fig. 9.15: Top view of the mid-reservoir level showing contoured plot for the magnitude of mean stress.

The second stress quantity derived is the differential stress (Fig. 9.16), the difference between the maximum and minimum principal stress (S_1-S_3)(cf. Chap. 2.1.3). Dependence on depth is very pronounced with a distribution of magnitude similar to the vertical stress S_1 plot. Local perturbations represent the highest magnitude in the plot, while they represented the lowest magnitude when the minimum horizontal stress S_3 was plotted individually. In the same area the vertical stress S_1 was not significantly affected by perturbations.

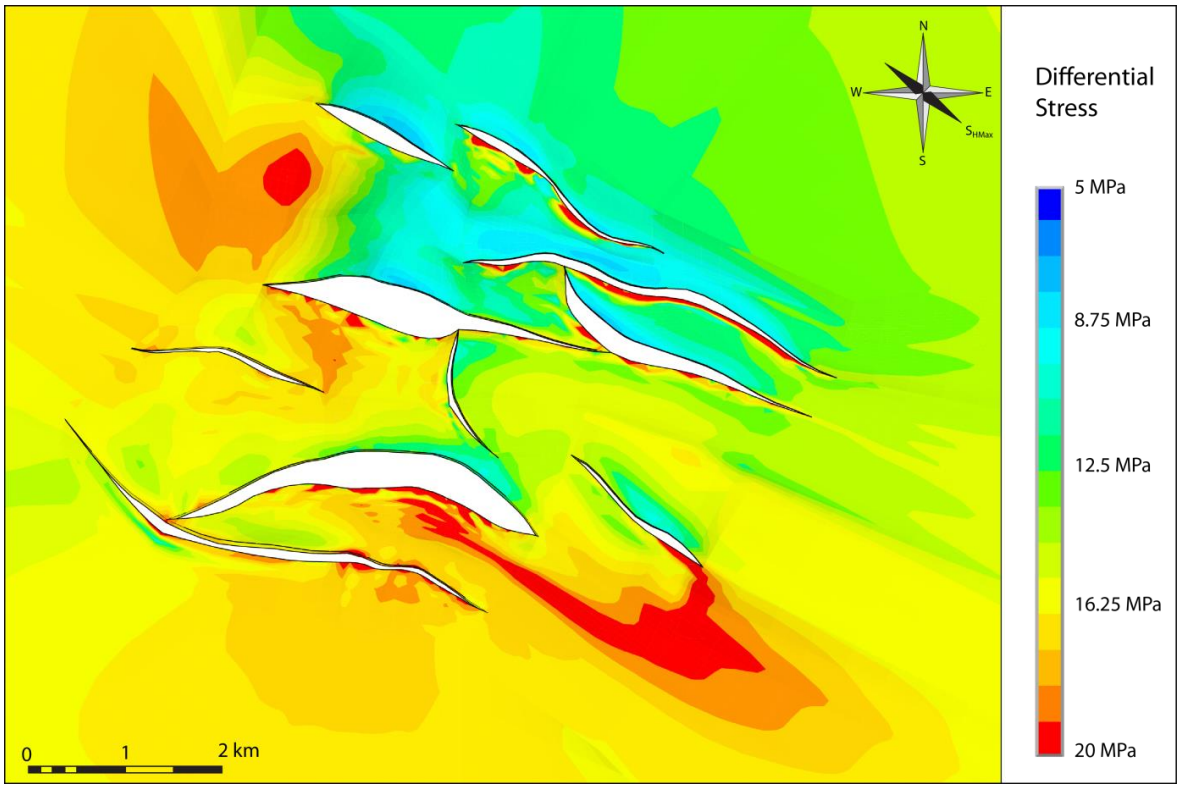

Fig. 9.16: Top view of the mid-reservoir level showing contoured plot for the magnitude of differential stress.

9.6.2 Fault characterization

The second major outcome of the steady-state geomechanical model is the characterization of faults from a structural point of view. This is possible thanks to the contact-element approach that uses 2D elements for faults for which is possible to calculate normal and shear stress acting on the fault plane. Following the computation of these two components of the stress, fault can be characterized in terms of slip and dilation tendency. Coefficient of friction is considered to be one of the most uncertain parameter of the modelling (cf. Chap. 7.2.1), although it has a significant influence in fault behavior. For this reason, in addition to the history-matching scenario modelled with a coefficient of friction of 0.6, fault characterization from a second scenario is presented where the coefficient of friction is lowered to 0.2. Distribution of stress magnitudes is not significantly affected by a lower coefficient of friction, only an intensification of perturbations is observed. However, slip along fault is enhanced and this is reflected by higher slip tendency values.

Shear stress computed for the two scenarios shows values ranging 0-10 MPa (Fig. 9.17). Shear stress magnitude computed using a coefficient of friction of 0.6 has slightly higher values with respect to the simulation carried out using a coefficient of friction of 0.2. A dependency on mechanical stratigraphy and on curvature of faults can be recognized, with the highest magnitude observed at reservoir level in the southernmost fault.

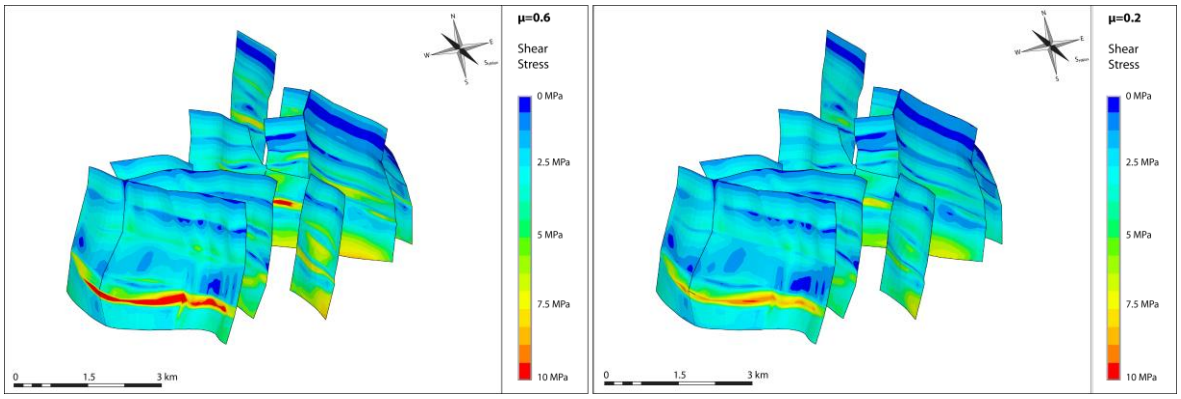

Fig. 9.17: Oblique view of the faults showing contoured plot of shear stress for a coefficient of friction of 0.6 (left) and 0.2 (right).

Normal stress has higher magnitude with respect to shear stress, ranging 0-60 MPa (Fig. 9.18). It has a strong dependency on depth, with magnitudes progressively increasing from the surface to the bottom of the faults. In contrast, impact of mechanical stratigraphy does not seem to affect significantly the distribution of magnitude. Normal stress calculated using a coefficient of friction of 0.6 has lower magnitude in comparison with normal stress calculated using a coefficient of friction of 0.2.

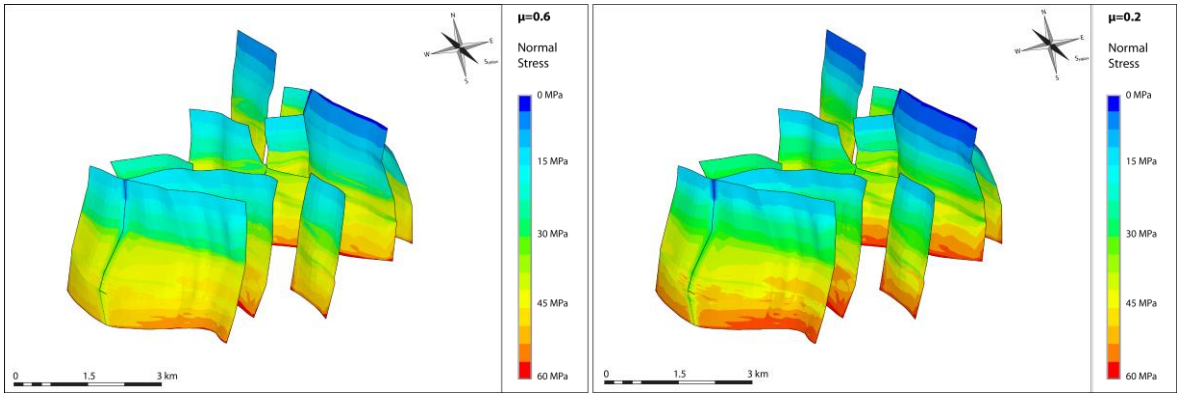

Fig. 9.18: Oblique view of the faults showing contoured plot of normal stress for a coefficient of friction of 0.6 (left) and 0.2 (right).

Slip tendency controls the stability or failure along a plane of weakness and is determined by the ratio of shear stress to normal stress acting on the plane, normalized by the coefficient of friction, which has a value of 0.6 for this first scenario (cf. Chap. 2.4.1). Results for faults in the CO2CRC Otway project area show a slip tendency generally very low (Fig. 9.19). Low values of shear stress (0-10 MPa) and higher values of normal stress (0-60 MPa) are the reason for low values of slip tendency. Only the two faults reaching the surface have in the shallowest layer higher values. However, within the thickness of the different layers is possible to recognize a zonation of values, increasing with depth.

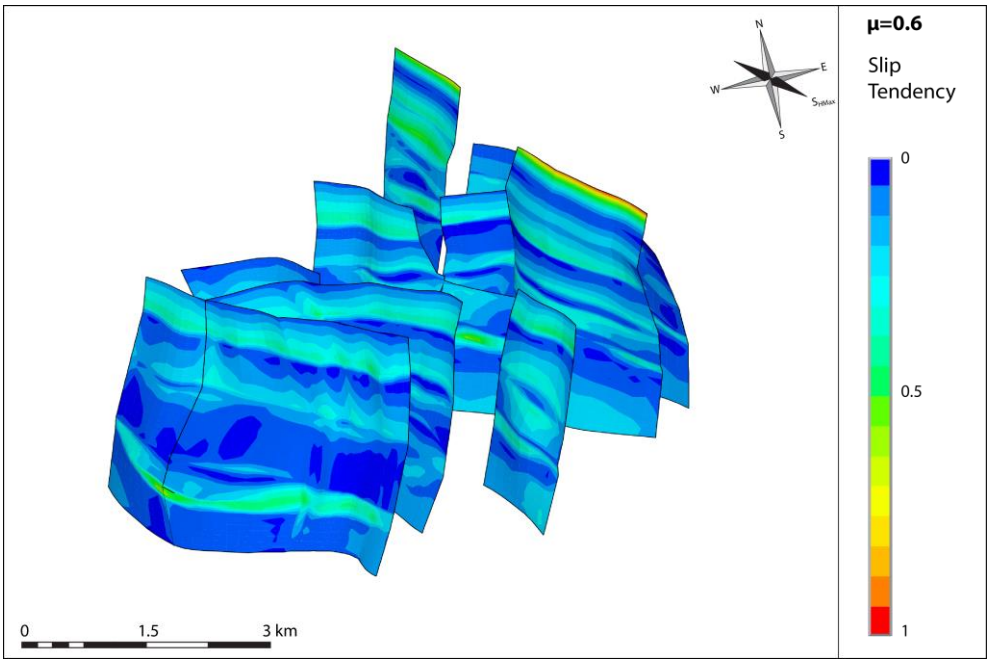

Fig. 9.19: Oblique view of the faults showing contoured plot of slip tendency for a coefficient of friction of 0.6.

The second scenario proposed uses a value of 0.2 for the coefficient of friction (Fig. 9.20), with the aim to better understand the role of the coefficient of friction in fault slip. Such a low value is an indication of a weak fault, and would be appropriate in case of presence of clay minerals or graphite in the fault zone (Zoback 2010) or as a result of cataclasis due to small movements along the fault plane. The low friction coefficient results in higher slip tendency value for all the modelled faults. The two faults reaching the surface show the highest slip propensity, in particular at shallower depth. The impact of mechanical stratigraphy becomes more evident and again within each layer is possible to recognize a zonation of values increasing with depth.

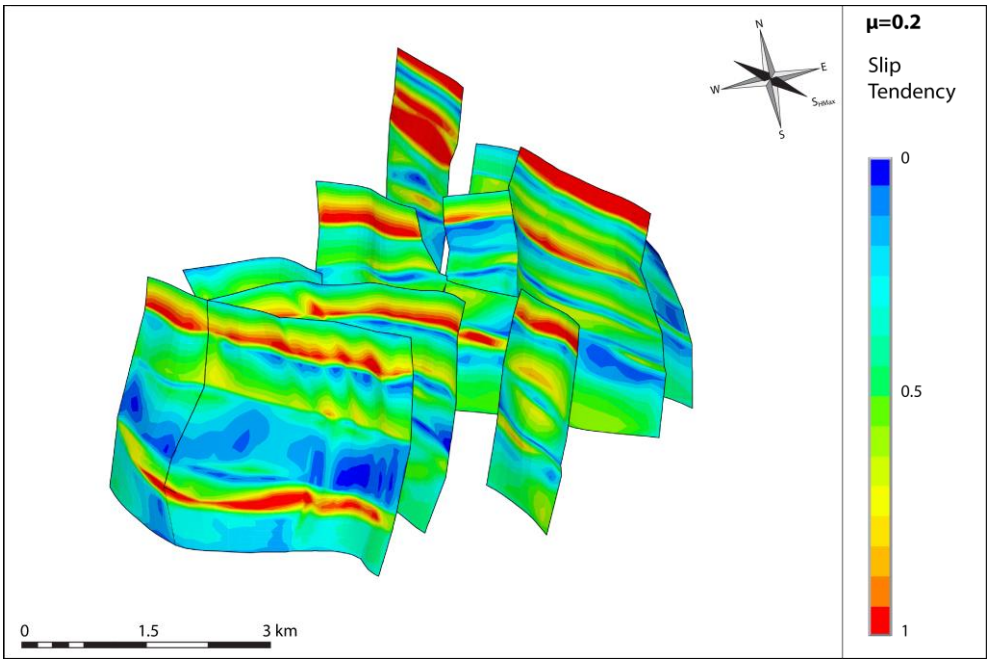

Fig. 9.20: Oblique view of the faults showing contoured plot of slip tendency for a coefficient of friction of 0.2.

Dilation tendency accounts for the fault proximity to open and it is largely controlled by the normal stress and differential stress acting on the faults (cf. Chap. 2.4.1). In the first scenario, the coefficient of friction used is 0.6 (Fig. 9.21). The computed dilation tendency shows significantly higher values than slip tendency which is in turn controlled by a low-magnitude shear stress. However, the distribution is not uniform being affected by changes in mechanical properties from one layer to another, internal curvature and orientation of the fault plane.

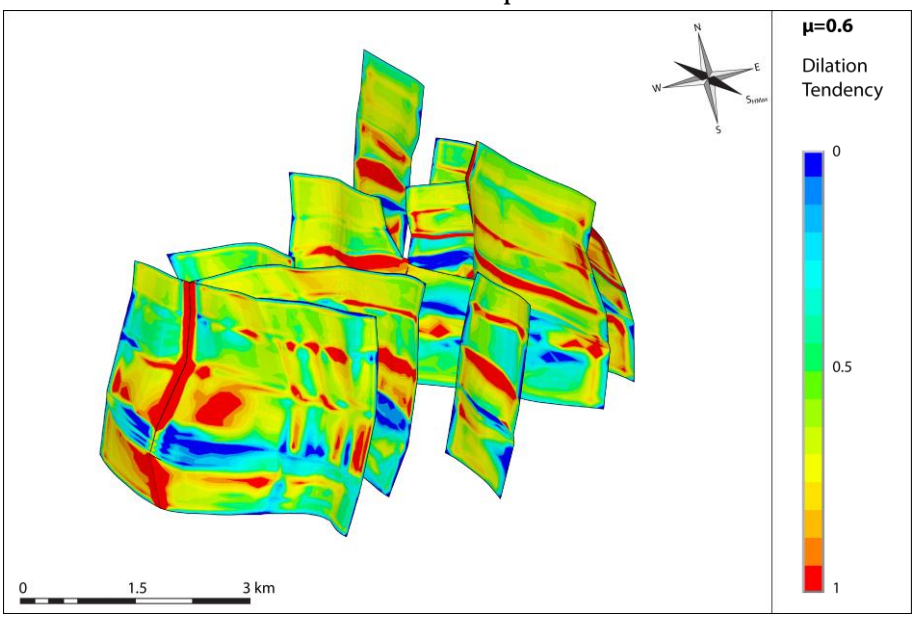

Fig. 9.21: Oblique view of the faults showing contoured plot of dilation tendency using a coefficient of friction of 0.6.

In contrast with slip tendency, changes in the friction coefficient do not significantly affect the distribution of dilation tendency. No appreciable change in distribution of dilation tendency values is observed if a coefficient of friction of 0.2 is used for the modelling (Fig. 9.22).

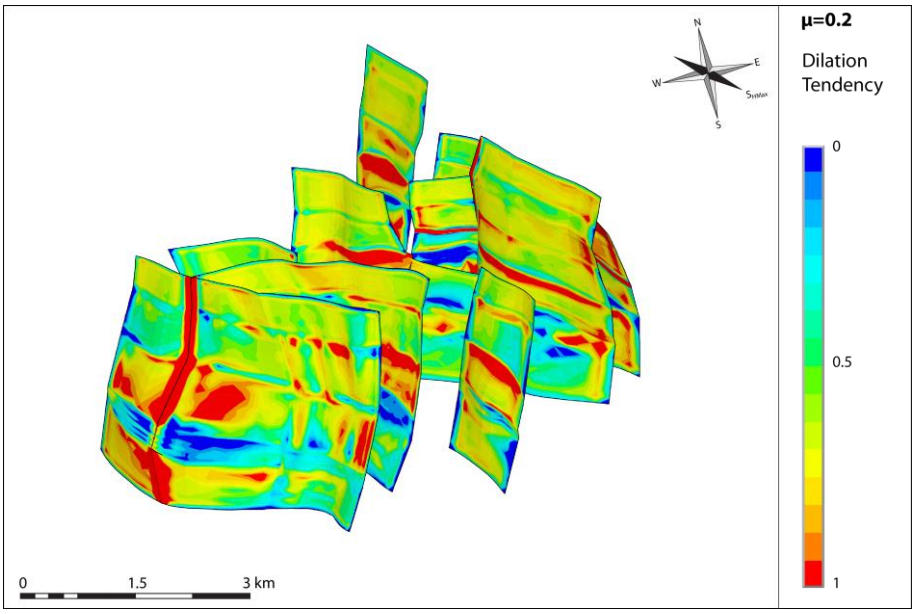

Fig. 9.22: Oblique view of the faults showing contoured plot of dilation tendency using a coefficient of friction of 0.2.

10 Paleostress modeling

Following the modeling of the contemporary state of stress, a forward-modeling of paleostress regimes starting from Mid-Cretaceous is hereby presented. Information concerning paleostress regimes allows to reconstruct the development of fracture networks and frameworks for fault reactivation through time. In particular, this issue is relevant to Australia due to the fact that most of the Australian reservoirs occur in structural traps formed by reactivation of geological structures (Dyksterhuis et al. 2005), including the Otway basin. Previous studies of paleostress regimes in Australia investigated and modeled mainly the stress regime of the entire Indian-Australian plate (Dyksterhuis et al. 2005, Müller et al. 2012), thus providing a general understanding of paleostress for the Australian continent. Inferring magnitudes and orientation of paleostress regimes at local scale is one of the biggest challenges in paleostress modelling.

The paleostress analysis focuses on the Otway basin tectonic history after the deposition of the reservoir formation (~90-80Ma). The main objectives are to describe the development of fracture network through time and to characterize faults behavior during the different stages. The description of the in situ paleostress acting during major past tectonic stages is the starting point for this study, for both intact rock and faults. Four different scenarios are presented, which are significant in terms of time length and tectonic activity for the Otway Basin.

The modeling approach takes advantage of the characteristics of the submodeling technique already used for modeling the present-day stress. The external loadframe on which boundary conditions are calculated to be transferred to the internal model, can be easily rotated in the direction of the maximum horizontal stress for the different tectonic stages. Elastic properties assigned to model are the same as for the present-day stress model, while density is recalculated for the different tectonic stages using a decompaction method.

10.1 Major tectonic stages from Mid-Cretaceous to present

Tectonic history of Otway Basin can be mostly extrapolated from geodynamic studies (Norvick and Smith 2001) and paleostress studies (Dyksterhuis et al. 2005, Müller et al. 2012) covering the entire Australian continent. The level of accuracy and resolution of this type of studies with respect to Otway Basin is therefore relatively low, however it still represents a good starting point to define the major tectonic stages (cf. Chap. 0). In addition to that, a useful source of information was found in one of the report for the SEEBASE Project focusing on Otway and Sorell Basins evolution (Teasdale et al. 2002). The geometry of the geomechanical model covers a range of time from Early Cretaceous onwards (~125 Ma). The modeled period with respect to the paleostress analysis is subsequent the deposition of the reservoir formation occurred in the Mid-Cretaceous (~90-80 Ma).

Based on the major tectonic stages definition, four different paleostress models are proposed covering the tectonic history of the Otway Basin. In particular, three models reproduce the three different stress regime occurred between Mid-Cretaceous and Paleogene, while the last model covers the compression period during Miocene.

In Late Cretaceous (~80-45 Ma), during the final phases of breakup between Australia and Antartica, Southeast Australia was affected by a NE directed extension that reactivated pre-existing NW trending basement structures (Fig. 10.1) (Teasdale et al. 2002). After a short inversion period, the same extensional regime in NE direction due to the first marine incursion in Otway Basin ~40 Ma was reinstalled again, lasting up to Miocene (Fig. 10.1) (Norvick and Smith 2001). Therefore a single paleostress model is used to cover both extensional periods. Maximum horizontal stress orientation for this stage is NW-SE, therefore the external loadframe is rotated 45° counter-clockwise with respect to North. The extensional setting of this tectonic stage is associated with a normal faulting regime (Fig. 10.1).

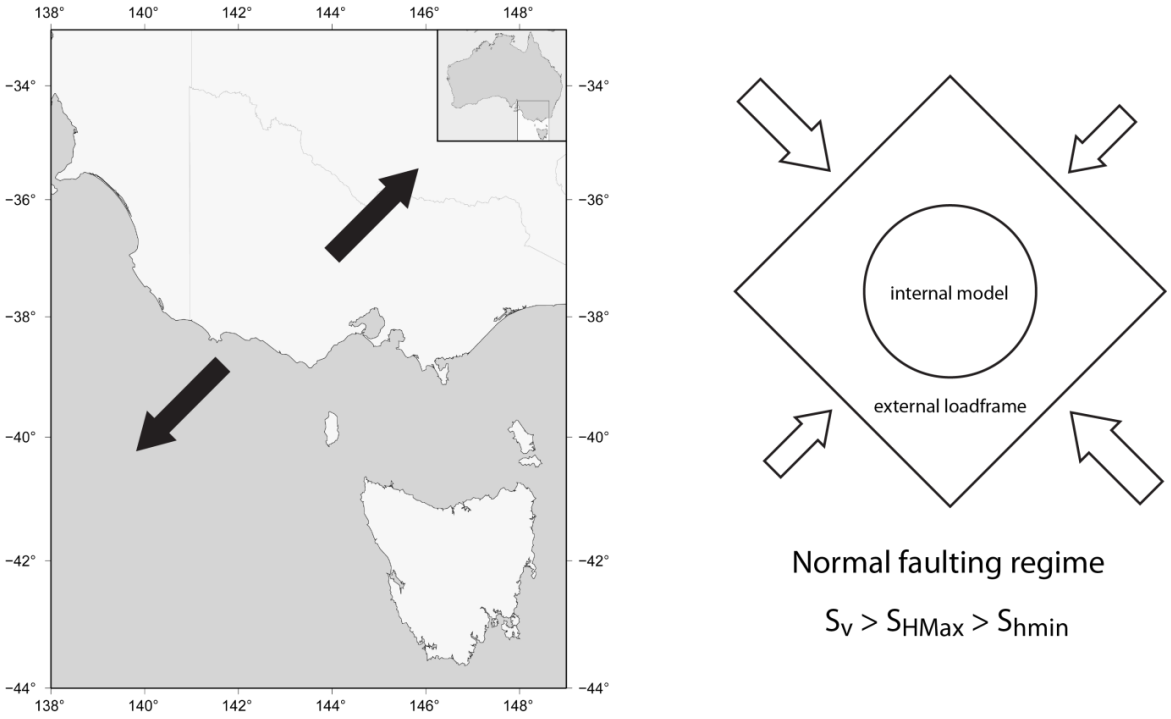

Fig. 10.1: Representation of the extensional tectonic stage in place in the Otway basin from Late Cretaceous to Early Eocene, then again from Late Eocene to Miocene. The boundary conditions for this paleostress model use a loadframe rotated 45° with respect to North and normal faulting regime.

In the arrangement of rifting during extension, an X-pattern is recognized of which the Otway Basin is the northwest branch. It has been associated with a sinistral intra-cratonic transcurrent faulting that developed along the boundary between Antartica and Tasmania-North Island New Zealand (Fig. 10.2) (Norvick and Smith 2001). For this tectonic stage a strike-slip faulting regime is chosen to include the transcurrent nature of the stress regime. The maximum horizontal stress orientation is again NW-SE, with a rotation of 45° counter-clockwise of the external loadframe (Fig. 10.2).

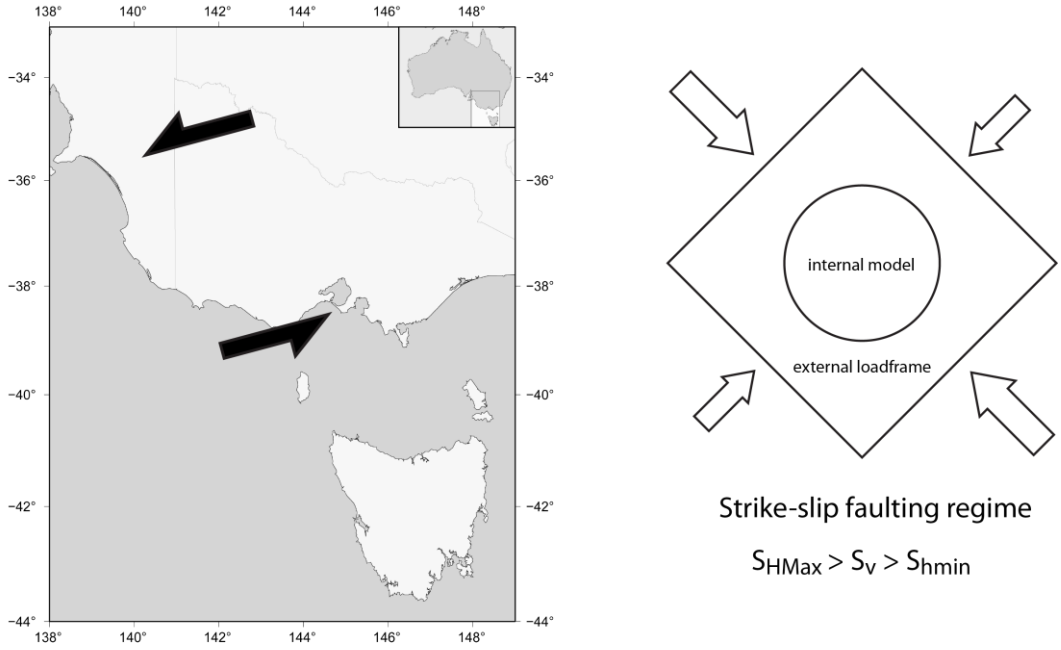

Fig. 10.2: Representation of the sinistral transcurrent component of tectonic stress during Late Cretaceous extension. The boundary conditions for this paleostress model use a loadframe rotated 45° with respect to North and strike-slip faulting regime.

During the final rifting stage in Eocene the Otway basin was affected by a short period of local inversion (~45-40 Ma), caused by the change from rifting to drifting and the onset of ridge-push forces (Fig. 10.3). The resulting compression caused minor inversion of some pre-existing structures in the Otway and Gippsland Basins (Teasdale et al. 2002). This tectonic stage is modeled as reverse faulting regime, with an orientation of the maximum horizontal stress NNE-SSW as deduced from interpretation of fractures (Fig. 10.3).

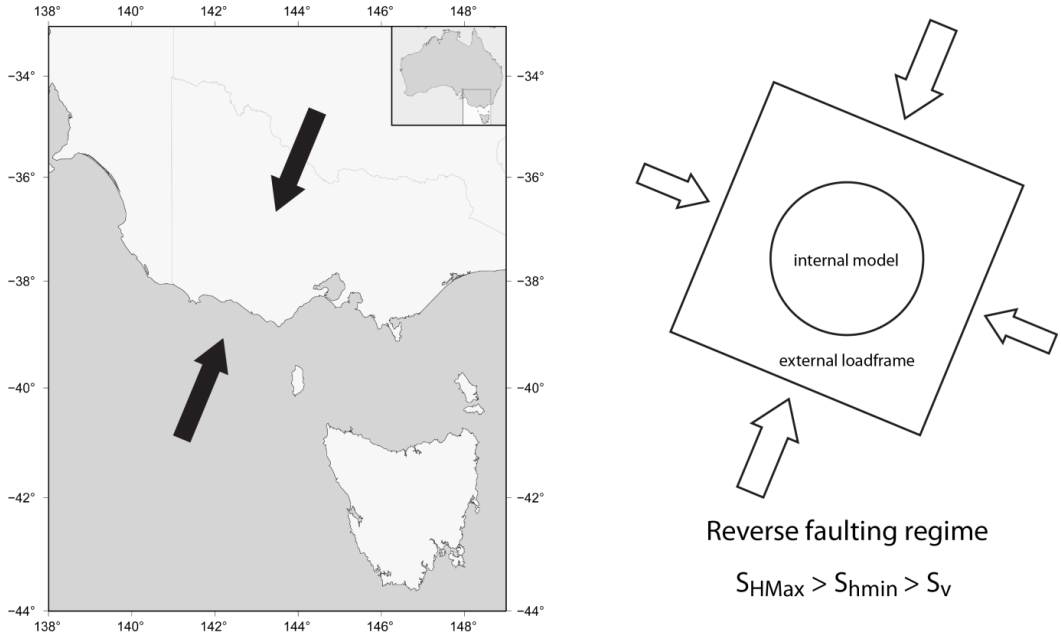

Fig. 10.3: Representation of the compressional tectonic stage occurred locally in the Otway basin during Eocene. The boundary conditions for this paleostress model use a loadframe rotated 22.5° with respect to North and reverse faulting regime.

During the Miocene (~16-6 Ma) an ESE directed intraplate stress reactivated weak basement structures nearby the Otway basin. This compression led to uplift which formed the present-day topography at regional scale in the Otway Basin. However, only minor inversion occurred at this time in the Otway and Sorell Basins (Teasdale et al. 2002, Tassone et al. 2014). In this case, the orientation of the maximum horizontal stress is ESE-WNW, with a resulting rotation of the loadframe of 22.5° counter-clockwise with respect to North (Fig. 10.4). The stress regime modeled is a reverse faulting regime.

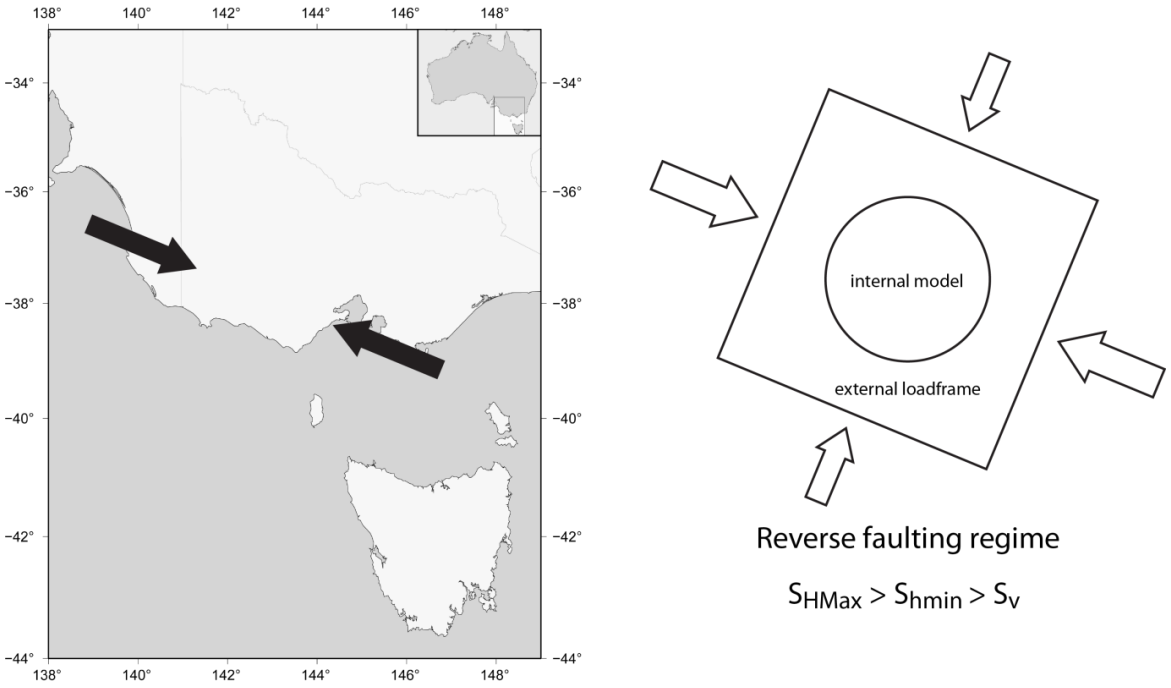

Fig. 10.4: Representation of the compressional tectonic stage occurred during Miocene. The boundary conditions for this paleostress model use a loadframe rotated 22.5° with respect to North and reverse faulting regime.

10.2 Geometry and material properties

As a consequence of the identification of the major tectonic stages, it is necessary to address the change in geometry and material properties for the paleostress models. Burial history and the consequent compaction of sediments vary for the different tectonic stages through time. Decompaction and backstripping methods can be used for calculating decompaction of sediments and subsequently assign the corresponding depths and densities to the different paleostress models.

10.2.1 Decompaction and backstripping methods

For the purpose of updating the geometry of the model (cf. Chap. 10.2.2), two subdivisions have been included in the shallower layer of the model (Nirranda & Heytesbury Group). The first at -84.51m where is located the top of the intra-formation marl, and the other at -225.36m at the top of the intra-formation claystone. Nevertheless, the initial parameters are the same for all the three resulting sublayers. On the contrary, depths, porosities and densities are reported as separated results for

each sublayers, following the time division in eight instead of six time-steps of deposition.

The burial of sediments in a basin causes porosity loss, which is normally assumed to be driven by mechanical compaction. Estimates of porosity form borehole logs suggest an exponential relationship between porosity and depth (Eq. 9-1) (Allen and Allen 2013):

$$\phi = \phi_0 e^{-cy} \qquad (Eq.\ 9\text{-}1)$$

where ϕ is the porosity at any depth y, ϕ_0 is the surface porosity and c is a coefficient dependent on lithology that describes the rate at which the exponential decrease in porosity takes place with depth. The surface porosity ϕ_0 is derived from the equation 9-1 for a given porosity ϕ (from well logs) at corresponding depth, while the lithology-dependent coefficient c is assigned depending on the lithology of the layer according to Allen and Allen (2013) (Tab. 10.1).

Lithostratigraphy layer	Surface porosity ϕ_0	Lithology-dependent coefficient c
Intra-Level 1	0.35	0.27
Intra-Level 2	0.36	0.27
Intra-Level 3	0.39	0.27
Dilwyn Fm.	0.38	0.27
Timboon Fm./Paaratte Fm.	0.39	0.27
Skull Creek Fm./Belfast Mst.	0.60	0.51
Waarre Fm.	0.40	0.27
Eumeralla Fm.	0.35	0.27

Tab. 10.1: Table summarizing the input parameters for the decompaction analysis: surface porosity ϕ_0 is estimated from sonic log and the lithology-dependent coefficient c is assumed according to Allen and Allen (2013).

To calculate the thickness of a sediment layer at any time in the past, it is necessary to move the layer up to the appropriate porosity-depth curve. It is basically equivalent to remove overlying layers of sediment in order to allow the layer of interest to decompact. The assumption behind is to consider the mass as constant and take into account only changes in volumes and therefore thickness. This method is commonly known as backstripping and includes, if needed, a paleobathymetric correction and a eustatic correction.

To backstrip multiple layers it is necessary to restore all the stratigraphic units in a sequence for each time step, by decompacting the younger units and compacting the older ones (Fig. 10.5).

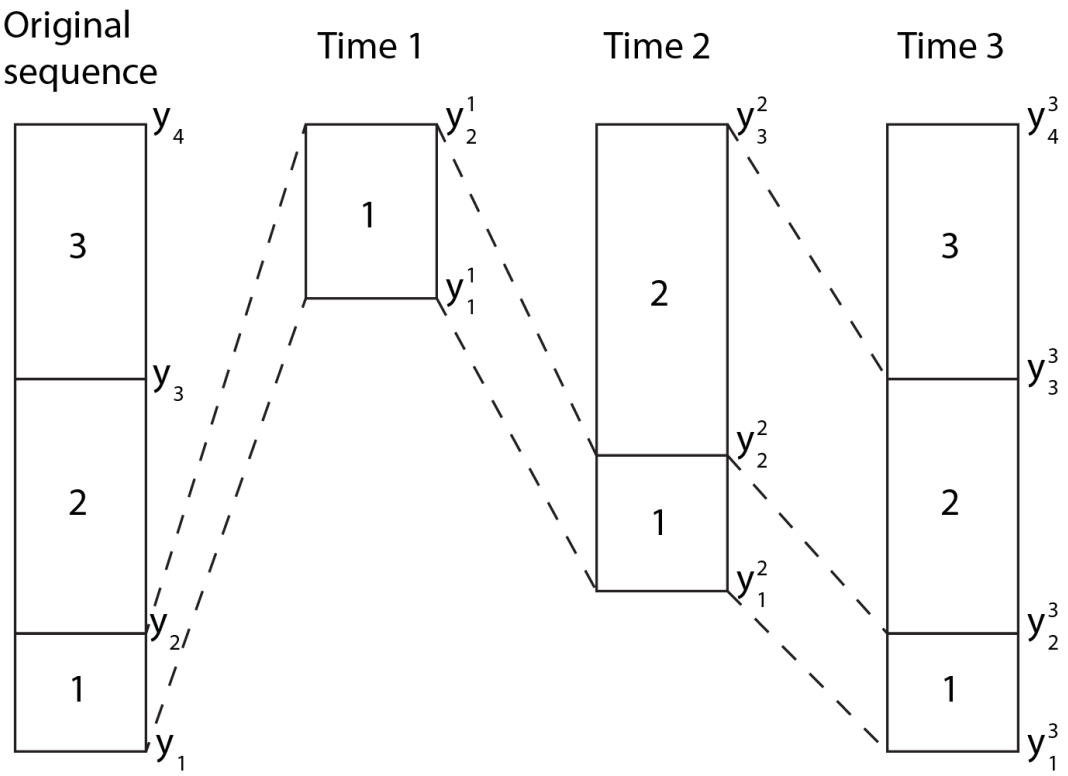

Fig. 10.5: Sketch illustrating the successive stages in decompaction. Each layer is first decompacted and then subsequently compacted again in the following stages. Modified after Allen and Allen (2013).

For this study, decompacted depths and porosities have been calculated through a Matlab script modified from Allen and Allen (2013) that allows to find the solution of the decompaction equation, and the software Backstrip (Cardozo 2005). First of all, the entire column of sediments overlying the layer 1 is removed and it is moved up from depths y_1 and y_2 (respectively top and base of the layer) to the new depths y_1^1 and y_2^1. Assuming that the top depth y_2^1 of the decompacted layer 1 is at a zero-depth reference, the bottom depth y_1^1 is calculated following the equation 10-2 (Allen and Allen 2013):

$$y_1^1 = y_1 - y_2 - \frac{\phi_0}{c}\left[e^{(-cy_2)} - e^{(-cy_1)}\right] + \frac{\phi_0}{c}\left[e^{(-cy_2^1)} - e^{(-cy_1^1)}\right] \qquad (Eq.\ 10\text{-}2)$$

where y_1 and y_2 are the compacted depths, y_1^1 and y_2^1 are the decompacted depths, ϕ_0 is the surface porosity and c is a coefficient dependent on lithology. For the following stages, it is necessary to add the depth of the overlying layers to the previously compacted layers (Eq. 10-3):

$$y_1^2 = y_1 - y_2 - \frac{\phi_0}{c}\left[e^{(-cy_2)} - e^{(-cy_1)}\right] + \frac{\phi_0}{c}\left[e^{(-cy_2^2)} - e^{(-cy_1^2)}\right] + y_2^2 \qquad (Eq.\ 10\text{-}3)$$

Results of the compaction calculation are commonly visualized as compaction diagram (burial history plot) showing compaction curves for each layer of the sedimentary column (Fig. 10.6). At local scale around the Naylor Field, there is information available about the amount of uplift that may have occurred after the deposition of the reservoir. However, analysis of sonic transit time data on the nearby well Boggy-Creek 1 indicates that Eumeralla Fm. experienced a net exhumation of

~20 m (Tassone et al., 2014). Furthermore, evidences from thermal studies suggest that the Naylor Field area is at present time at his maximum burial depth (Duddy et al., 1997, Gallagher et al., 2004). As a conclusion, compressional phases and related erosional unconformities such as Otway Unconformity (between Eumeralla Fm. and Waarre Fm.) and Middle-Eocene Unconformity (between Dilwyn Fm. and Nirranda Group) (cf. Chap.4.3) represent a big uncertainty in this decompaction model.

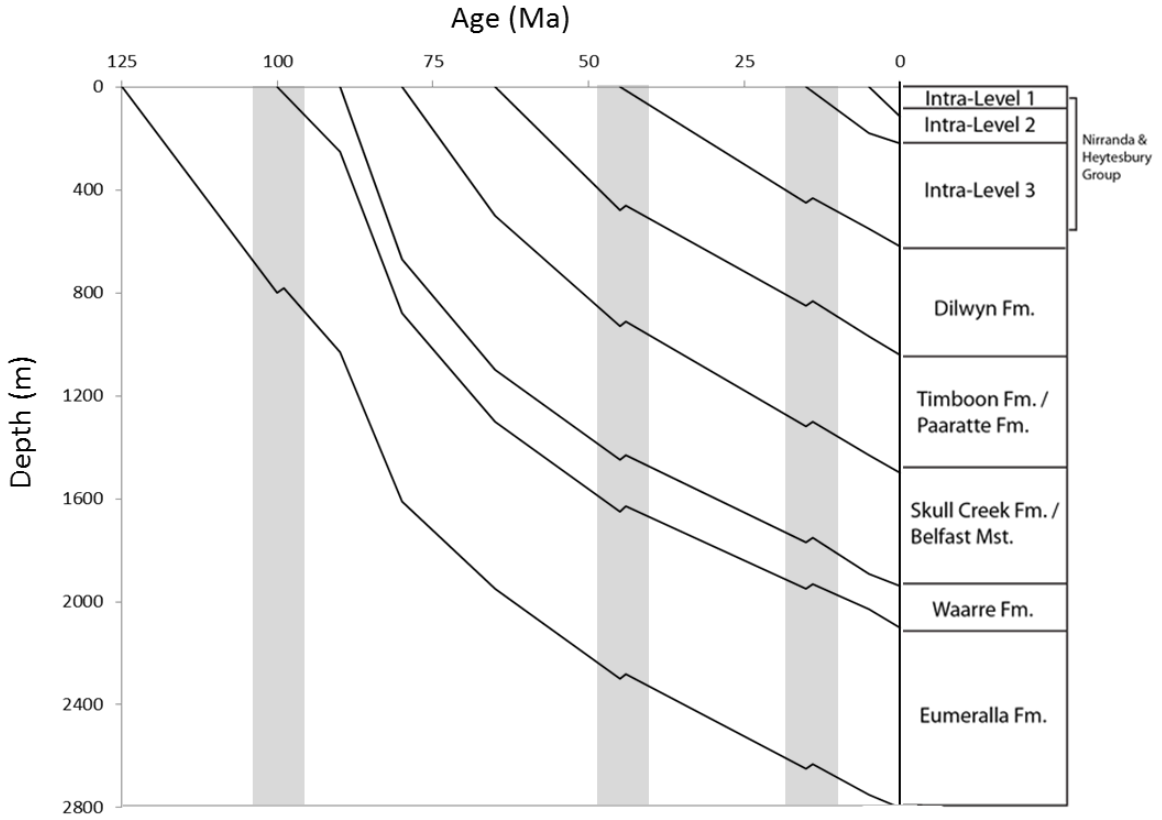

Fig. 10.6: Compaction curves calculated for each layer of the paleostress models. Shaded area indicates periods of possible minor uplift occurred at local scale in the Naylor Field. Magnitude of absolute exhumation is uncertain.

Given the new depths y_1^1 and y_2^1 of the decompacted layer and the surface porosity ϕ_0, the porosity of the decompacted layer ϕ^* can be derived (Eq. 10-4):

$$\phi^* = \frac{\phi_0}{c}\left[\frac{e^{(-cy_1^1)} - e^{(-cy_2^1)}}{y_2^1 - y_1^1}\right] \qquad (Eq.\ 10\text{-}4)$$

It is now possible to calculate the decompacted porosity ρ^* for each layer (Eq. 10-5):

$$\rho^* = \{\rho_w \phi^* + [\rho_{gr}(1 - \phi^*)]\} \qquad (Eq.\ 10\text{-}5)$$

where ρ_w is the sea water density (1030 kg/m^3), ϕ^* is the porosity of the decompacted layer and ρ_{gr} is the density of the grains (Tab. 10.2), derived for given present-day porosity and density.

Lithostratigraphic layer	Density of grains ρ_{gr} (kg/m3)
Intra-Level 1	2436.7
Intra-Level 2	2435
Intra-Level 3	2426.9
Dilwyn Fm.	2857
Timboon Fm./Paaratte Fm.	2762.5
Skull Creek Fm./Belfast Mst.	2812.6
Waarre Fm.	2922.5
Eumeralla Fm.	2815

Tab. 10.2: Table summarizing the input parameter density of grains ρ_{gr} assigned to each layer.

Along with depths and porosity it is also possible to calculate the total subsidence experienced by the basin and the loading effect of the sediments (i.e. tectonic subsidence). Tectonic subsidence Y (Fig. 10.7) can be treated as a problem of local isostatic balance (Airy isostasy), where sediment is replacing a column of water (Eq. 10-6):

$$Y = T\left(\frac{\rho_m - \bar{\rho}}{\rho_m - \rho_w}\right) \qquad (Eq.\ 10\text{-}6)$$

where T is the thickness of the sediment column, ρ_m is the mantle density (3300 kg/m^3), $\bar{\rho}$ is the mean density of the sediment column taken into account. As a consequence of the lack of information on exhumation and erosion already described, amount of uplift related to compressional is considered to be uncertain.

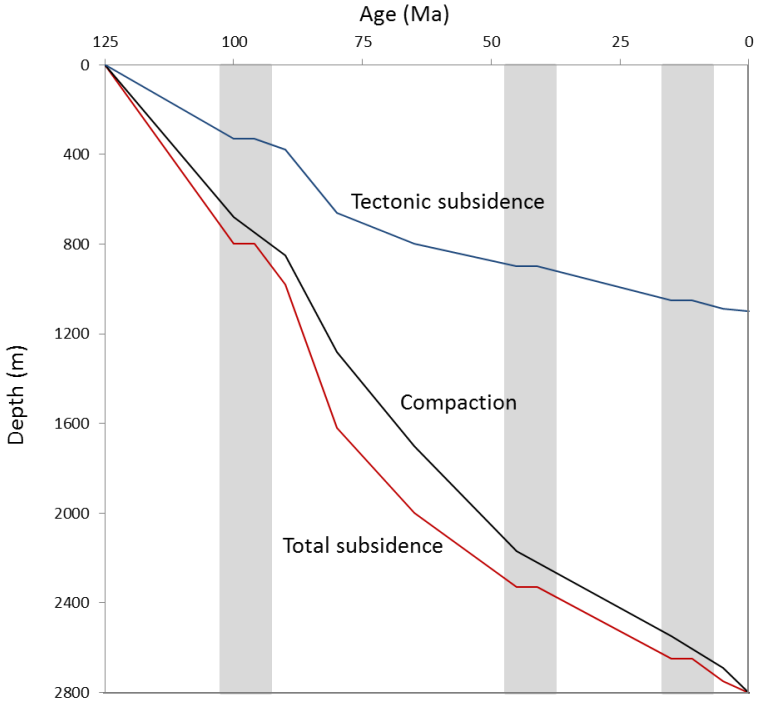

Fig. 10.7: Backstrip curves for the Otway basin considering a continuous deposition. Blue curve describe the loading effect of sediments (tectonic subsidence), the black line indicates the compaction

curve and the red line represents the total subsidence. Shaded area indicates periods of possible minor uplift occurred at local scale in the Naylor Field. Magnitude of absolute exhumation is uncertain.

10.2.2 Updating geometry and material properties

Updating the geometry of the model presents challenges due to the workflow followed to build the geomechanical model in Ansys® (cf. Chap. 9.1). Ideally, fault restoration should be taken into account when paleo-tectonic stages are modelled, in order to reproduce exactly the horizon geometry at different stages of faults activity and to progressively introduce faults according to their generation. Up-to-date no restoration information are available and besides incorporating the geometrical balancing into the modelling would require a separate build up for each tectonic stage. Therefore, a simple adjustment of the depth of the top of the model has been performed to take into account depth changes during the past. This assumption is supported by a structural analysis of the Naylor Field (Ziesch et al. subm.) based on evidences from 3D seismic interpretation and Allan Maps indicate that majority of faults were continually active from Early Cretaceous to Late Cretaceous. However, two of them continued their activity at least up to Oligocene. Temporal activity of faults can be also related to the presence of unconformities that seal older faults, in particular the Mid-Eocene Otway Unconformity separates Wangerrip Group from Nirranda Group and most of the faults are visible only below this major seismic event. Combining information obtained from the structural analysis study and seismic interpretation, it could be concluded that recent major tectonic stages occurring after Eocene (when most of the faults end their activity and are subsequently sealed by the Otway Unconformity) can be modelled using the present-day geometry, since only subsidence is considered to be source of deformation after this temporal boundary. However, older major tectonic stages (i.e. Paleo 2 and Paleo 4 models) would require the incorporation of retrodeformed layers to increase the degree of accuracy. LIAG (Leibniz institute of applied geophysics) is currently carrying out a retrodeformation analysis that could be potentially used to set up new models for the identified major tectonic stages.

In this light, for this paleostress modelling only depth of the top layer is updated, together with density provided by the decompaction analysis. Following the division in major tectonic stages, it is possible to group the first three paleostress models (Paleo2, Paleo3, Paleo4) in one single setting that covers a time range from the deposition of the reservoir formation up to Miocene (~16 Ma). This temporal boundary lies within the first stratigraphic layer of the geomechanical model (Nyrranda & Heytesbury Group), therefore the top of the model is adjusted to a depth of -225.36 m (top of the intra-formation of claystone) for the models Paleo2, Paleo3, Paleo4 (Fig. 10.8). However, it has to be taken in mind that these models would benefit from the inclusion of restored layers, since they cover a time range where fault activity was still in place. The same procedure can be followed to address the change in geometry for the Miocene inversion stage, with the top of the model lowered down to -84.51 m (top of the intra-formation of marl) for model Paleo 1(Fig. 10.8). In this case, the assumption of maintain the present-day geometry is supported

by the fact that during Miocene, deformation was related only to subsidence as faults already ended their activity.

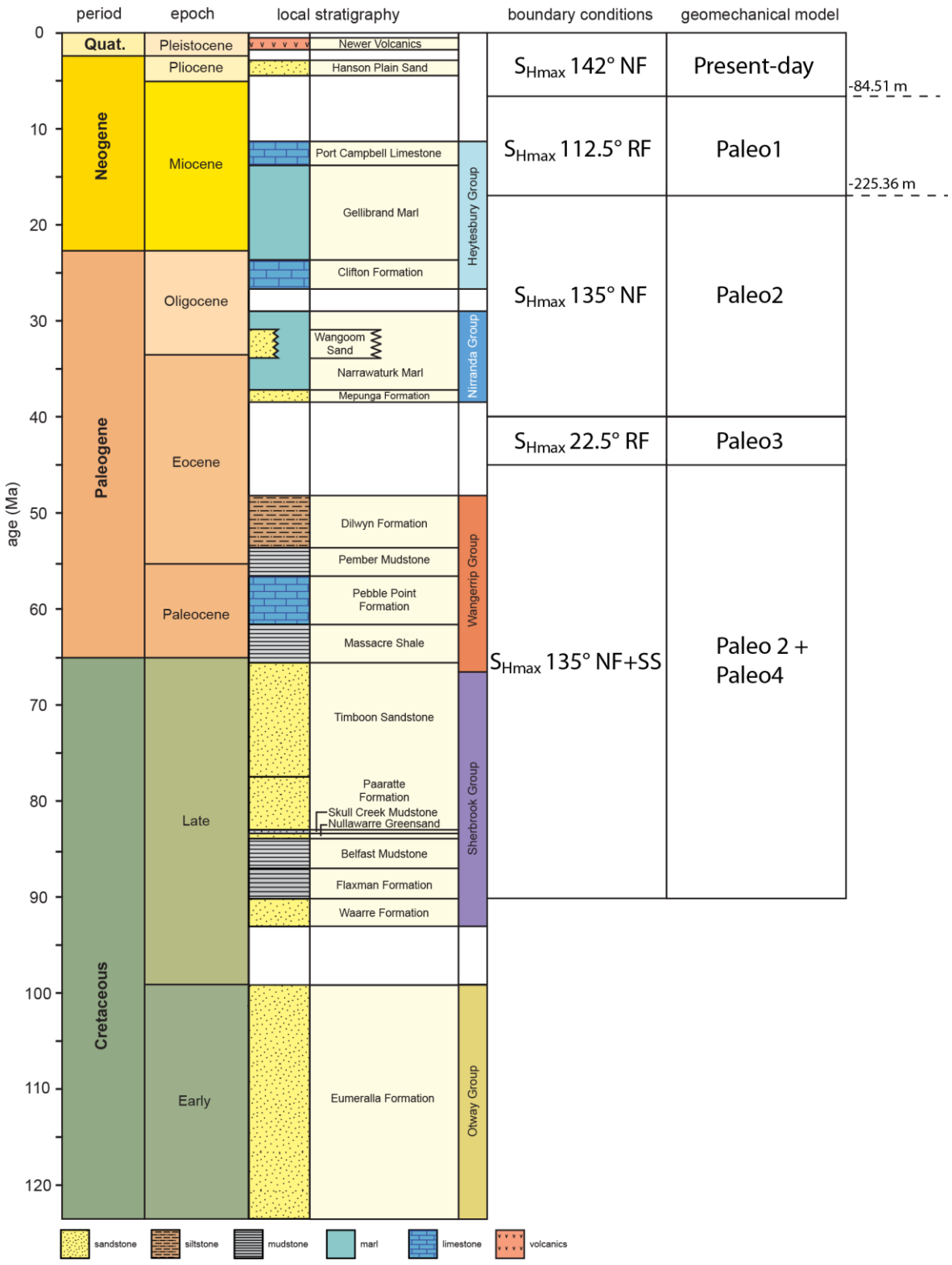

Fig. 10.8: Summary of the paleostress models stratigraphy, boundary conditions, name given to the model and depth of the top of the model (Paleo2, Paleo3 and Paleo4 have the same top depth).

Following the definition of the new geometry of the paleostress models, also material parameters need to be updated. The three parameters assigned to the intact rock are

density, Young's Modulus and Poisson Ratio. Density can be derived from the compaction study, while Young's Modulus and Poisson Ratio are not corrected for the paleostress modelling. This is due to the fact that the temporal evolution of these two parameters is affected by a number of factors, which are yet not fully understood. The same applies to the coefficient of friction of faults, for which the development through time is not yet established. A reasonable estimation of paleo-values of Young's Modulus, Poisson Ratio and coefficient of friction can not be provided at this stage, therefore values from the steady-state geomechanical model are used also for the paleostress analysis.

The compaction analysis allows the derivation of density for each layer of the model at every time-step of deposition (cf. Chap. 10.2.1), according to Eq. 9-5. Porosity of the decompacted layer should be known, as well as the density of the grains (Tab. 10.2). According to the updated geometry of the paleomodels, density results from the last two stages of decompaction (i.e. removal of Intra-Level 1 and Intra-Level 2 respectively) are used to populate the model (Tab. 10.3).

Lithostratigraphic layer	Paleo 2-3-4	Paleo 1	Present-day
Intra-Level 1	----	-----	1950 kg/m^3
Intra-Level 2	----	1932.9 kg/m^3	1950 kg/m^3
Intra-Level 3	1912 kg/m^3	1932.9 kg/m^3	1950 kg/m^3
Dilwyn Fm.	2272.3 kg/m^3	2292.5 kg/m^3	2323 kg/m^3
Timboon Fm./Paaratte Fm.	2257 kg/m^3	2273.6 kg/m^3	2298.8 kg/m^3
Skull Creek Fm./Belfast Mst.	2321.7 kg/m^3	2349.9 kg/m^3	2391.55 kg/m^3
Waarre Fm.	2464.5 kg/m^3	2478 kg/m^3	2498.6 kg/m^3
Eumeralla Fm.	2478.5 kg/m^3	2488.1 kg/m^3	2495.88 kg/m^3

Tab. 10.3: Table summarizing the updated density for the paleostress model, together with density used for the steady-state present-day geomechanical model.

10.3 Paleostress magnitudes

The final step for the setup of the paleostress models is to define the paleostress magnitude to constrain the models. The orientation of the maximum horizontal stress has already been derived from the definition of the major tectonic stages and determines the rotation of the external loadframe (cf. Chap. 10.1).

Magnitude of the vertical paleostress is easily computed through the integration over depth of the corrected decompacted densities (Tab. 10.3). The determination of the horizontal stress magnitudes, on the contrary, is more uncertain since they can not be correlated with known parameters as in the case of vertical stress and density. Knowledge of the faulting regime acting during the period covered by the paleostress models, allows to establish the relative magnitudes according to Anderson's classification scheme (Anderson 1951). Limits to the in situ stress can be derived by the frictional strength of faults as stated in the frictional faulting theory (Zoback

2010). Basically, the difference in magnitude between maximum and minimum stresses is limited by the frictional strength of faults and fractures. In particular, values of maximum principal stress S_1 and minimum principal stress S_3 that correspond to the situation of a critically oriented fault at his frictional limit are given, neglecting the pore pressure, by (Eq. 10-7) (Jaeger et al. 2007):

$$\frac{S_1}{S_3} = \left[\left(\sqrt{\mu^2 + 1} + \mu\right)\right]^2 \qquad (Eq.\ 10\text{-}7)$$

that for a coefficient of friction μ of 0.6 becomes (Eq. 10-8):

$$\frac{S_1}{S_3} = 3.1 \qquad (Eq.\ 10\text{-}8)$$

This equation can be adapted for each faulting regime, simply determining the correspondence between the principal stress (i.e. S_V, S_{HMax} and S_{hmin}) and S_1, S_2 and S_3. Absolute horizontal stress magnitudes assigned to the paleostress models (Tab. 10.4) lie within the lower and upper boundaries provided by the frictional faulting theory.

	Paleo 1	Paleo 2	Paleo 3	Paleo 4
S_{HMax} orientation	112.5° N	135° N	22.5° N	135° N
Stress regime	Reverse faulting	Normal Faulting	Reverse Faulting	Strike-slip faulting
Stress order	SHMax > Shmin > Sv	Sv > SHMax > Shmin	SHMax > Shmin > Sv	SHMax > Sv > Shmin
S_V at reservoir level	41.42 MPa	40.26 MPa	40.26 MPa	40.26 MPa
S_{HMax} at reservoir level	55.52 MPa	35.28 MPa	51.09 MPa	43.06 MPa
S_{hmin} at reservoir level	47.06 MPa	23.83 MPa	43.39 MPa	24.73 MPa

Tab. 10.4: Table summarizing the four paleostress models and their characteristics in terms of stress regime, stress orientation and stress magnitudes at reservoir level.

10.4 Results of the paleostress models

Results of the paleostress models are derived in a similar way with respect to results for the steady-state geomechanical model and are presented in the following pages. The main objectives of the paleostress models is to reveal the distribution of paleostress magnitudes and orientations to explain the generation of fracture networks, along with the characterization of faults behavior. As for the steady-state geomechanical model, the focus is on reservoir layer, therefore top view of the reservoir formation is shown in the results plot (cf. Chap. 9.6). The middle layer of the reservoir formation is chosen to avoid numerical influences from changes in material parameters.

10.4.1 Distribution of paleostress magnitudes and orientations

Distribution of paloestress for the four major tectonic stages is the first important outcome of the paleostress modelling. Magnitudes and orientations change according to the boundary conditions proposed and so does the occurrence of local perturbations. Indeed, intensity and location of perturbation vary in the different scenarios, showing a dependence on orientation and magnitude of the regional stress field. As already seen for the steady-state present-day geomechanical model they also differ depending on the principal stress component. Results of the distribution of maximum and minimum horizontal stress for the four major tectonic stages are presented in the following pages.

Model Paleo1 represents the first major tectonic stages, that is the Miocene inversion that interested the Otway Basin. The orientation of the maximum horizontal stress is ESE-WSW and the stress regime is a reverse faulting regime, where the horizontal stresses overcome the vertical stress. Distribution of magnitudes tends to correlate with depth as already seen for the steady-state present-day geomechanical model (Fig. 10.9) (cf. Chap. 9.6). However, if the two magnitude distributions are compared, locations and shapes of high-magnitude areas show some differences. Local perturbations occur, for both horizontal stresses, mostly at the footwall of the faults and are exaggerated by the contact elements with different curvature. Minimum horizontal stress S_{hmin} is slightly more affected by perturbations than the maximum horizontal stress S_{HMax}, and also it has a less uniform distribution of magnitudes.

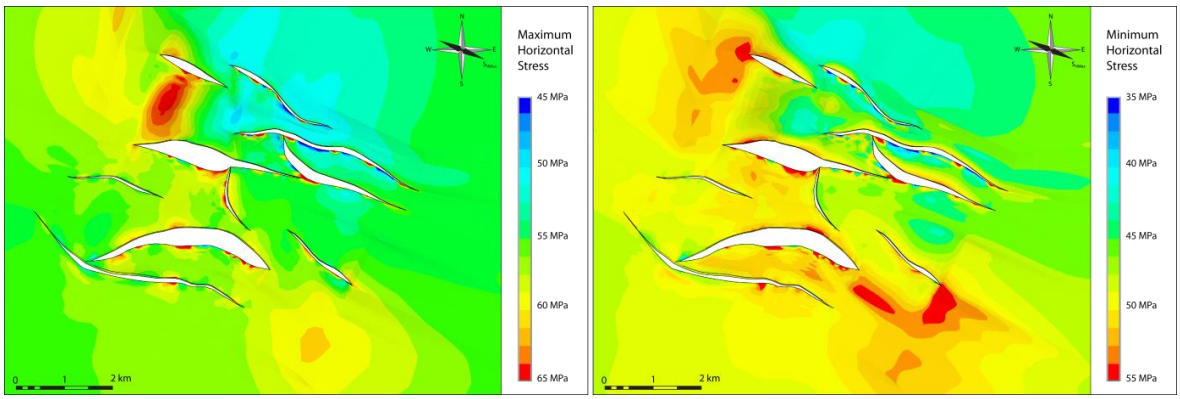

Fig. 10.9: Maximum horizontal paleostress (left) and minimum horizontal paleostress (right) distribution for the first major tectonic stage (Paleo1 model).

Model Paleo 2 covers the extensional regime in place in the Otway basin from Late Creataceous to Early Miocene. The orientation of maximum horizontal stress is NW-SE and the stress regime is a normal faulting regime, where the two horizontal stresses are smaller than the vertical stress. A comparison of the two horizontal stresses shows a more uniform distribution of the minimum horizontal stress S_{hmin} with respect to the maximum horizontal stress S_{HMax} where high- and low-magnitude areas are more pronounced (Fig. 10.10). The maximum horizontal stress S_{HMax} is more affected by occurrence of high-magnitude perturbation in the southern part of the reservoir, not only at the footwall of faults but occasionally also at the hangingwall. On the contrary, the minimum horizontal stress S_{hmin} shows a minor amount of local

perturbation, generally low-magnitude perturbation in the northern part of the reservoir.

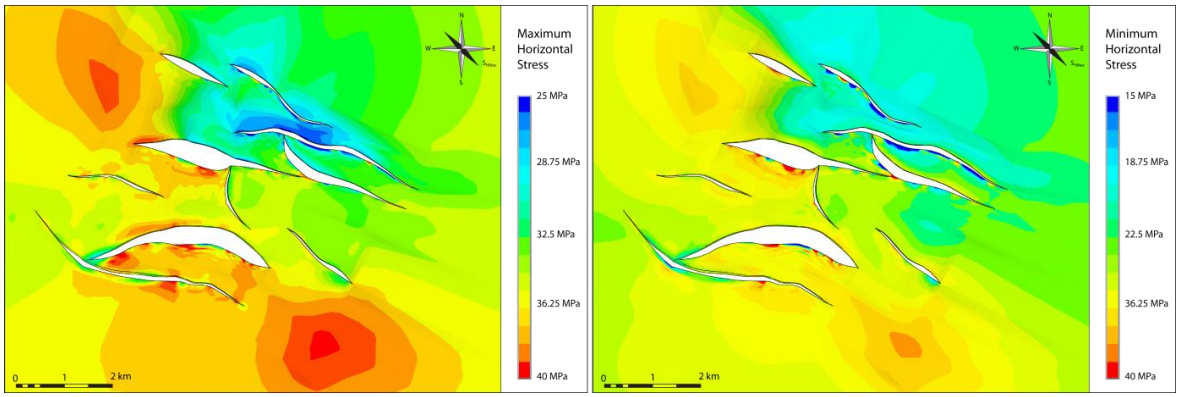

Fig. 10.10: Maximum horizontal paleostress (left) and minimum horizontal paleostress (right) distribution for the second major tectonic stage (Paleo2 model).

Model Paleo 3 reproduces the local inversion that for short time during Eocene affected the Otway Basin. The orientation of the maximum horizontal stress is NNE-SSW and the stress regime is a reverse faulting regime, where the horizontal stresses overcome the vertical stress. Magnitude of maximum horizontal stress S_{HMax} is slightly more uniform with respect to the minimum horizontal stress S_{hmin} (Fig. 10.11). Minor local perturbations affect both horizontal stresses, particularly at the footwall of faults. Minimum horizontal stress S_{hmin} develops a greater amount of low-magnitude perturbation in the northern part of the model, while maximum horizontal stress S_{HMax} tends to develop high-magnitude perturbations.

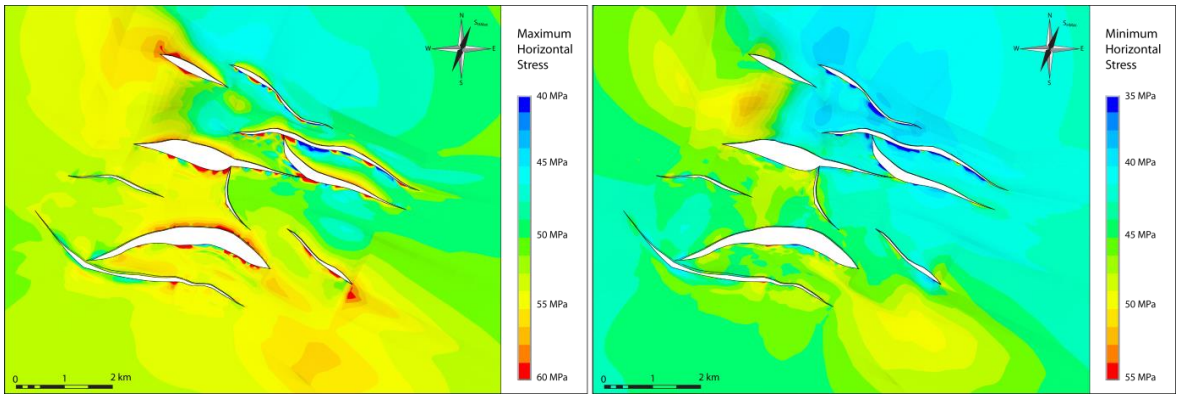

Fig. 10.11: Maximum horizontal paleostress (left) and minimum horizontal paleostress (right) distribution for the third major tectonic stage (Paleo3 model).

Model Paleo 4 incorporates the transcurrent component affecting the rifting extension from Late Cretaceous to Mid-Paloegene. The orientation of the maximum horizontal stress is NW-SE and the stress regime is a strike-slip faulting regime, where the vertical stress is greater than the minimum horizontal stress but smaller than the maximum horizontal stress. A comparison of the two horizontal stresses distribution shows a significant variation of high-magnitudes, particularly affecting the minimum horizontal stress S_{hmin} (Fig. 10.12). Local perturbations affect both horizontal stresses at the footwall of faults. Minimum horizontal stress S_{hmin} is more affected by local perturbation both of low- and high-magnitude.

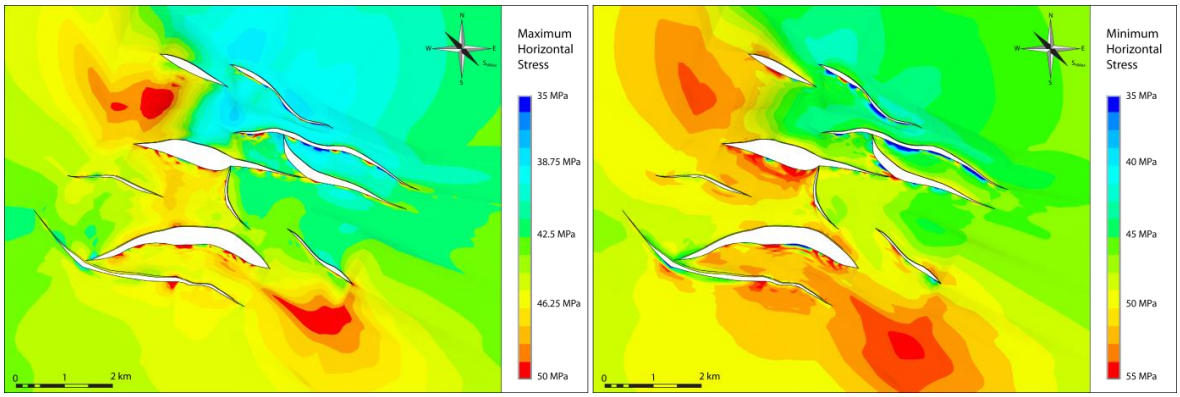

Fig. 10.12: Maximum horizontal paleostress (left) and minimum horizontal paleostress (right) distribution for the fourth major tectonic stage (Paleo4 model).

The orientation of the maximum horizontal stress S_{HMax} for the four paleomodels is derived from the direction cosines of the stress components (cf. Chap. 9.6.1). Generally, orientations computed for all the models tend to follow the regional stress orientation provided by the boundary conditions (Fig. 10.13). However, Paleo 1 model shows significant local stress rotation in particular in the vicinity of faults where stress tends to reorient perpendicular to them (cf. Chap. 9.6.1).

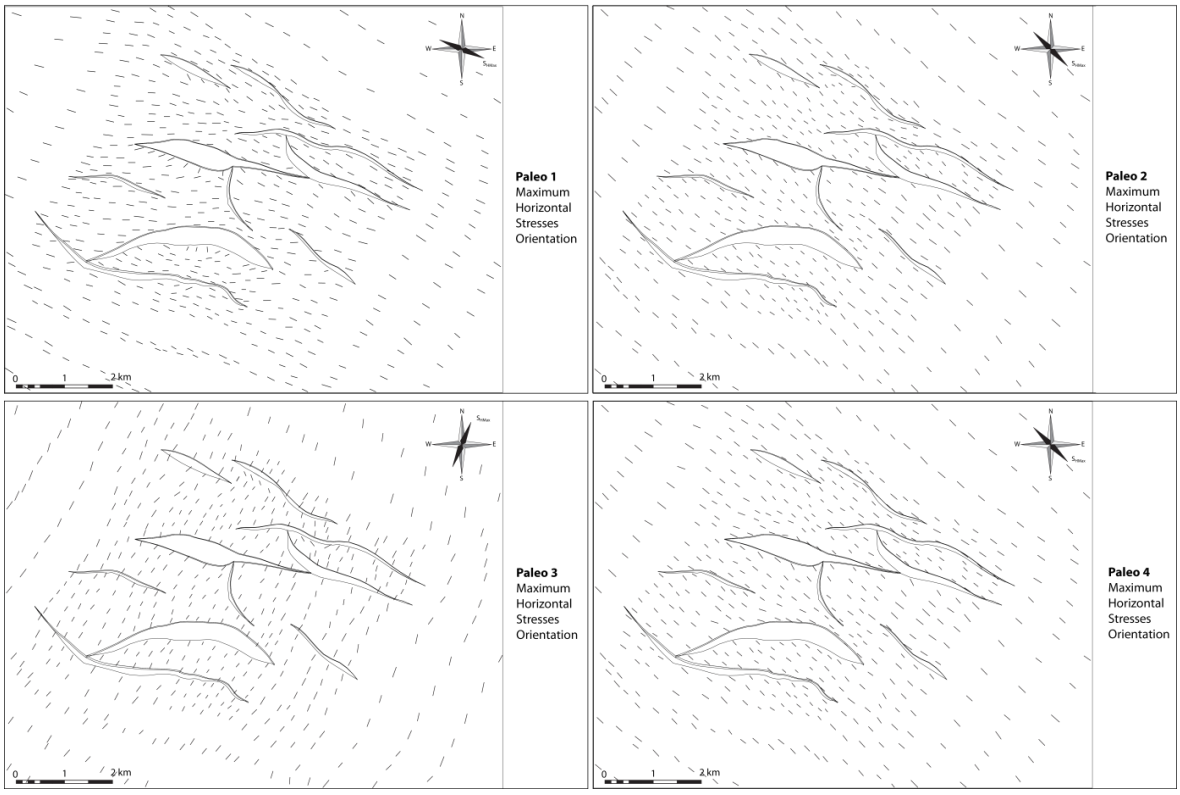

Fig. 10.13: Top view of the mid-reservoir level of the four paleostress models showing vector plot for the orientation of the maximum horizontal stress S_{HMax}.

10.4.2 Fault characterization

The last outcome of the paleostress modeling is the fault characterization, through time, from a structural point of view. As previously seen in the results of the present-day steady-state geomechanical model, fault characterization is described in terms of slip and dilation tendency (cf. Chap. 9.6.2).

Slip tendency shows low values for all the four tectonic stages (Fig. 10.14), although relatively higher values are computed for the model Paleo 3. Slip tendency is mainly dependent on shear stress acting on faults planes and quantifies the likelihood of movement along the faults planes. Generally, the four paleostress models show similar distribution of slip tendency. The two faults reaching the surface have high-values of slip tendency in the shallowest layer in all the models, however this observation can be considered valid only for model Paleo 1 since it is the only one covering a time range where those faults were actually active.

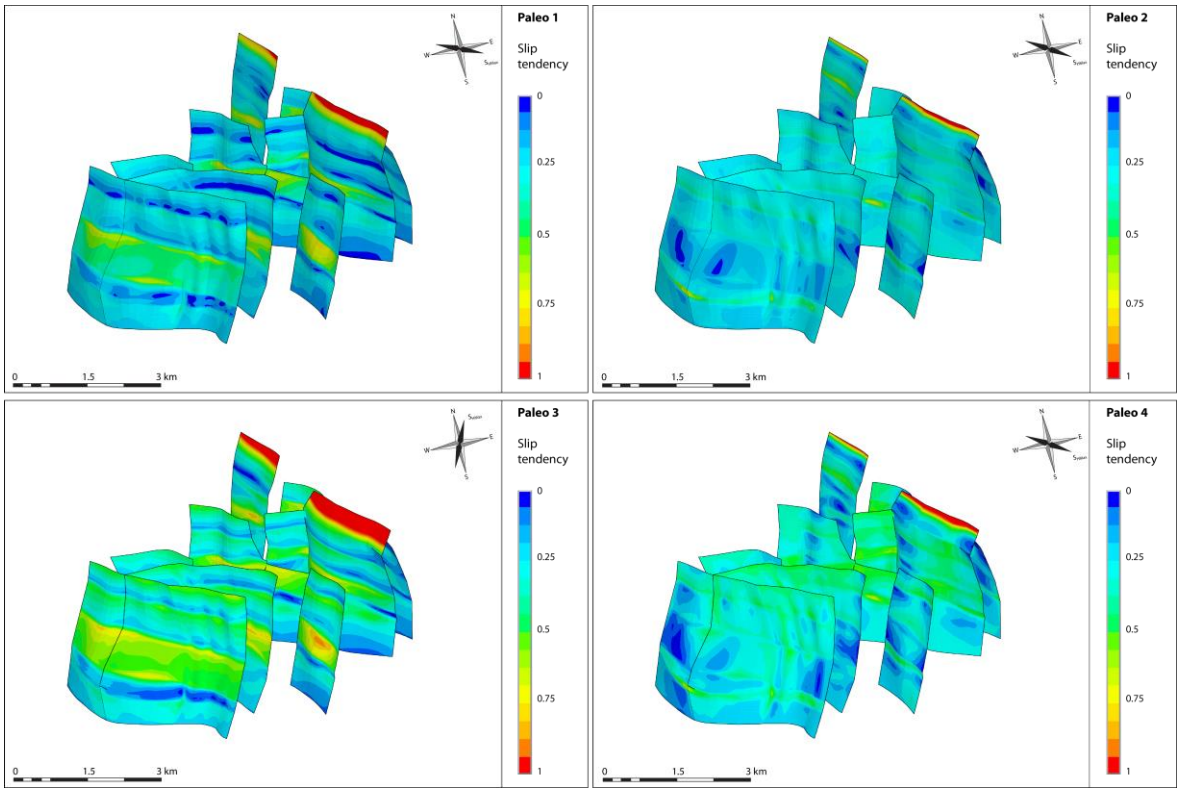

Fig. 10.14: Oblique view of the faults showing contoured plot of slip tendency for the four major tectonic stages.

Dilation tendency shows relatively medium-high values for the modeled four major tectonic stages, with differences among the paleostress models (Fig. 10.15). Models Paleo 1 has a medium-high (0.5-0.75) dilation tendency, Paleo 2 and Paleo 4 reach higher values (up to 1) and Paleo3 has very low tendency (0-0.5) if compared to the other models. Dilation tendency is primarily controlled by normal stresses and differential stress (cf. Chap. 2.1.3) acting on fault planes. As a result, if the differential stress is small (i.e. S_1 and S_3 are closer) as in the case of the models Paleo 2 and Paleo 4, dilation tendency will be higher. On the contrary, a greater differential stress corresponds to lower values of dilation tendency. Also the relative orientation between faults and maximum horizontal stress affects dilation tendency as it impacts directly on the normal stress acting on fault planes.

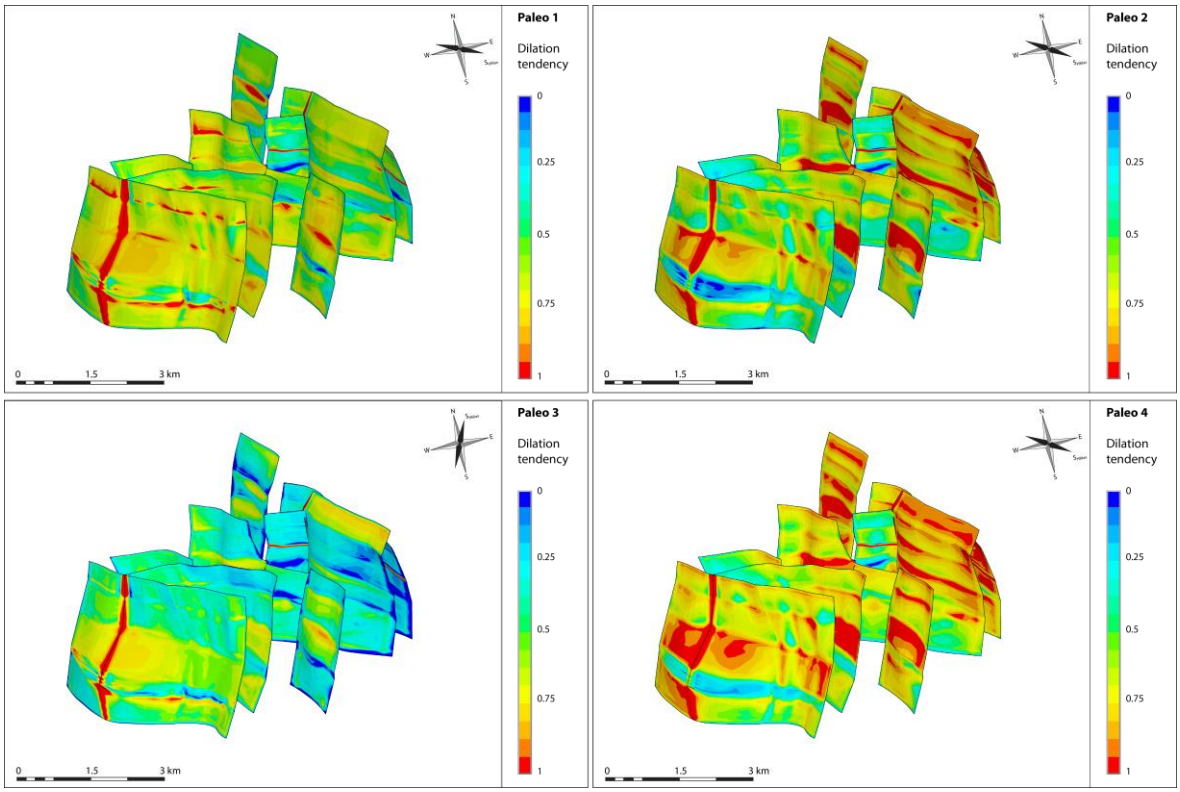

Fig. 10.15: Oblique view of the faults showing contoured plot of dilation tendency for the four major tectonic stages.

11 Discussion

Geomechanical studies have come to prominence due to their importance for modern conventional and unconventional energy exploration and also for ensuring safe operations in the CCS space. The failure to employ adequate geomechanical workflows in advance of operational activities can lead to catastrophic effects, as evidenced by well blowouts (i.e. Montara etc.) and unwanted caprock failure during gas injection (i.e. In Salah; Rinaldi and Rutqvist (2013)). A series of observations is outlined in the following pages on the basis of the results of the two geomechanical approaches adopted in this thesis. The aim is to combine the results obtained to provide a full geomechanical characterization of the CO2CRC Otway site and find possible explanations to differences arisen during the modelling.

First of all, the pore pressure analysis showed how analytical and numerical approaches can lead to quite significantly different results, thus affecting the geomechanical risk during operations. Possible sources of those differences have been explored.

This thesis proposes two different geomechanical approaches to analyze the response of the reservoir to changes in pressure due to CO_2 injection (i.e. effective stresses) and to understand the tectonic contribution to the stress field acting on the reservoir and its surroundings (i.e. total stresses). Although the different aims of the two geomechanical models presented, it is still possible to compare them in terms of modeled pre-production total stresses.

The analysis of the results computed to study the tectonic contribution of stresses in the present-day stress field and in the past, lead to the observation of occurrence of local stress rotation for some of the models. An attempt to explain possible source and factors that may cause local stress rotation is proposed.

Finally, the steady-state models that cover a period of time that last from the deposition of the reservoir formation until present-day, allow to understand the timing of fracture generation. Strike and dip angle of fractures are the two parameters used to sort the different set of fractures and they are subsequently assigned to the corresponding model according to Anderson's faulting theory.

11.1 Pore pressure analysis: Analytical vs Numerical approach

Analytical geomechanical studies can provide very useful information regarding the geomechanical behavior of reservoirs exposed to production and/or injection. However, they are simplified and do not incorporate finer details of the reservoir and surrounding rock, and therefore the use of numerical simulations can increase the accuracy of the model results. Numerical models that are coupled to dynamic reservoir simulations represent a cutting-edge workflow in this field of research, as they are able to combine changes in pressure and stress occurring in reservoir subject to production and/or injection of fluids. This coupled methodology has been

applied in the oil and gas industry (Koutsabeloulis and Zhang 2009, Zhang et al. 2011) and also recently in the CCS space for example for the In Salah CO_2 injection project in Algeria (Rutqvist et al. 2010) and for modeling the Iona gas storage facility in Australia (Tenthorey et al. 2013). The importance of numerical modeling for solving important geomechanical issues is highlighted in this thesis by comparing the numerical and analytical models for fault reactivation. Results from the modeling indicate that the numerical approach predicts fault reactivation at a significantly lower fluid pressure than the two analytical models (cf. Chapter 8). In this case, a mechanical study based only on analytical solutions would therefore have predicted higher allowable fluid pressures, thereby introducing a greater degree of risk also in terms of injection rates. Furthermore, the analytical approach is only able to predict fault reactivation related to changes in pore pressure during injection, but is unable to predict it in case of depletion. Limitations to the applicability of analytical approach in fault reactivation reduce its applicability only inside the reservoir where changes in pressure effectively occurs. This is a direct consequence of the way how stresses are analytically calculated, cell by cell, without taking into account any interaction. The numerical approach on the other hand would be able to predict fault reactivation due to compaction in the reservoir rock during depletion due to a great displacement of rock. Moreover in the numerical model interactions between cells are incorporated and the computed state of stress outside the reservoir includes effects from the changes in pressure occurring at reservoir level. The reasons for the numerical modelling yielding lower estimates for the critical pore pressure are likely to come from several different sources. A comparison of the different components of the total stress calculated for both numerical and analytical models helps to visualize those possible sources (Fig. 11.1).

Firstly, and most obviously, numerical models capture the inherent heterogeneity of the system, including the variability in porosity and permeability as well as topographic effects on the faults and at horizon boundaries. The mean stress difference (Fig. 11.1) shows how the analytical total stress tends to be underestimated in the topographic highs and overestimated in areas of depression. The main responsible for this result is the total vertical stress that shows the biggest difference in value between numerical and analytical models and reflects the tendency of the mean stress. Maximum horizontal stress is generally underestimated in the analytical solution, while the minimum horizontal is overestimated (Fig. 11.1).

Complex interactions between individual cells and the far field stress are also things that are hard to quantify, but which are not taken into account by analytical models. Finally, there are other effects such as stress arching effects which are incorporated into numerical models. The stress arching effect during CO_2 injection would lead to a heterogeneous vertical stress profile across the reservoir (Santarelli et al. 1998). In the case that the cap rock possessed sufficient stiffness, reservoir expansion during injection would lead to an increase in the vertical stress above the reservoir, which would be accompanied by reduced vertical stress at the edges of the injection zone.

However this would require also a greater volume of injected CO_2 and a bigger change in pore pressure to be effectively observed.

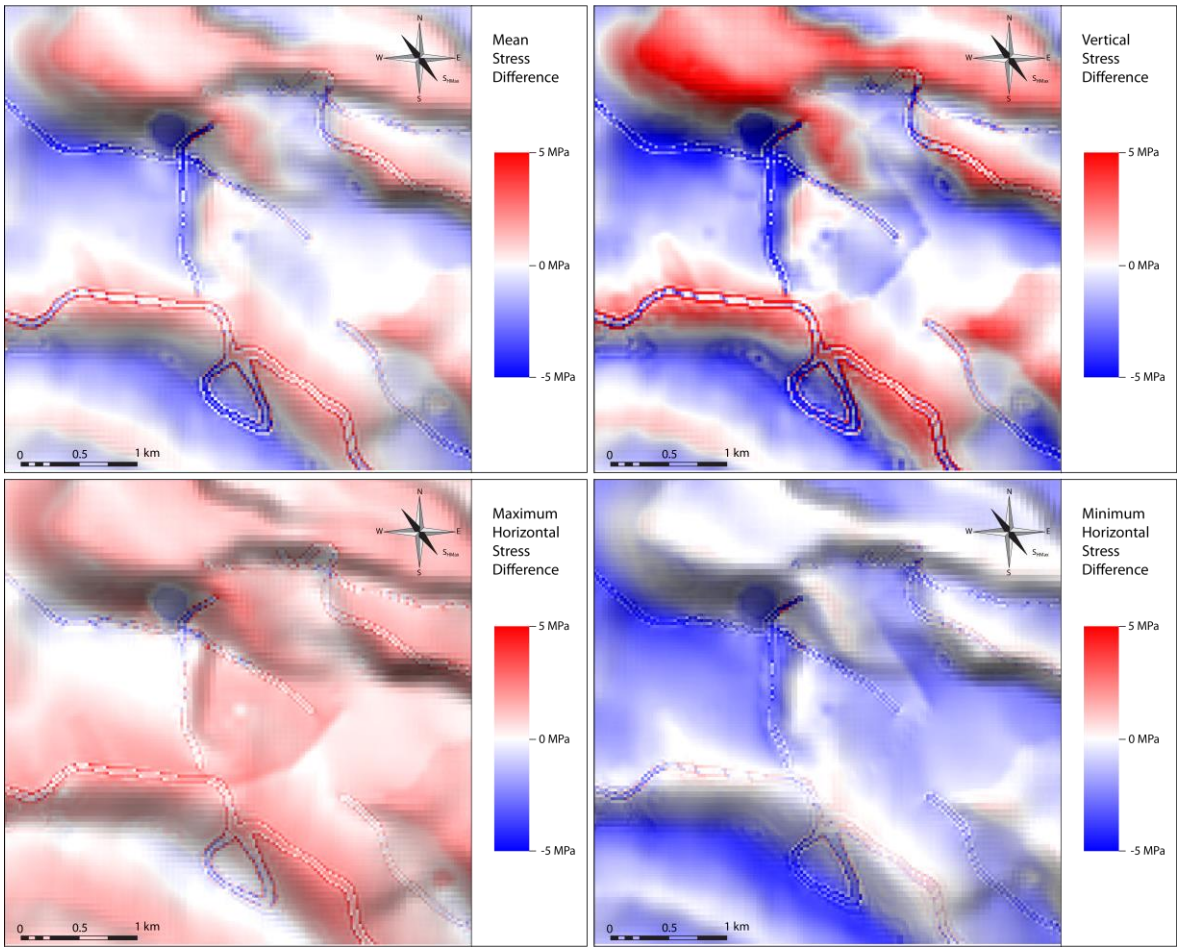

Fig. 11.1: Differences between numerical and analytical models in terms of mean stress, vertical stress, maximum horizontal stress and minimum horizontal stress. Total stresses for both numerical and analytical model are computed at the initialization of the model. Red zones indicate areas where numerical-computed stresses are greater than the analytical-computed stresses, blue zones represents areas where analytical-computed stresses are greater than the numerical-computed stresses. Location of the model can be seen in Fig. 6.2.

11.2 Stress modelling differences between Ansys® and Visage®

The two geomeachanical approaches presented in this thesis allow to characterize, from a geomechanical point of view, the target reservoir in two different manners.

The one-way flow and geomechanics coupled simulation focuses on the understanding of the variation in effective stresses due to changes in pressure related to CO_2 injection in the subsurface. In other words, the emphasis is on the pore pressure changes during operations. On the contrary, the steady-state model neglects pore pressure and takes into account only the local total stress field. Nevertheless, it is possible to compare the total stress modeled with both geomechanical simulator Visage® and Ansys® and analyze what differs in the two outputs obtained.

The comparison is done at pre-production stage for the one-way coupled model to avoid any influence on total stress due to reservoir stress path during

production/injection. Factors to be considered are the geometry of the model, material population and how faults are incorporated in the computation. Firstly, the geometry of the Ansys® model is a derivation of the geometry of the geological model (cf. Chap. 9.1), therefore loss of information could have occur during the geometry transfer process. Indeed, only sides of block volumes transferred are constrained to the original geometry, whereas the internal topology is reconstructed as Coon's patches. Visage® model instead is directly built starting from the geological model (cf. Chap. 7.2.1), therefore in terms of geometry can be considered more accurate.

Material population for the Ansys® model is implemented through a layer-cake approach where each lithostratigraphic layer is assigned with a single value for each parameter (cf. Chap. 9.3). Material properties in the Visage® model are upscaled from well logs and their population retains information about original vertical and horizontal variations (cf. Chap. 7.2.1).

The biggest difference between the two geomechanical approaches is the way faults are included in the model. Ansys® software allows the introduction of contact elements on the model (cf. Chap. 9.2): planar elements that can slip along each other are used to reproduce faults. Each fault is therefore modeled a pair of contact and target elements (one for the hanging wall, one for the footwall). On the contrary, Visage® simulator treats faults as 3D cells with different material parameters with respect to the surrounding rocks (cf. Chap. 7.2.1). That implies that the area modeled as fault is much bigger with respect to the planar area in Ansys®. As a consequence, visualization of 2D horizontal slices through the horizons in the two models may be misleading as the visual output of the two softwares is quite different (Fig. 11.2, Fig. 11.3 and Fig. 11.4). In Ansys® the displacement of faults is visualized as such, meaning that it results in a "void space" as effectively the horizon does not exist at that location having being displaced above or below. On contrast, output of Visage® model is continuous through space and presence of faults can be recognized by abrupt change in depth at displacement location, even though technically the horizon does not exist at that location.

The first comparison between the two models shows the distribution of total maximum horizontal stress at mid-reservoir level (Fig. 11.2). Generally, magnitudes correlate well with depth for both models with an increase from the northern part of the reservoir towards the southern part. Ansys® model is much more affected by local perturbation around faults, even if it has to be taken into account that they may be exaggerated by numerical noise at contact elements location. Distribution of magnitudes is more uniform in the results provided by Visage® and perturbations due to presence of faults are less regular since cells belonging to faults may not exactly follow the displacement geometry.

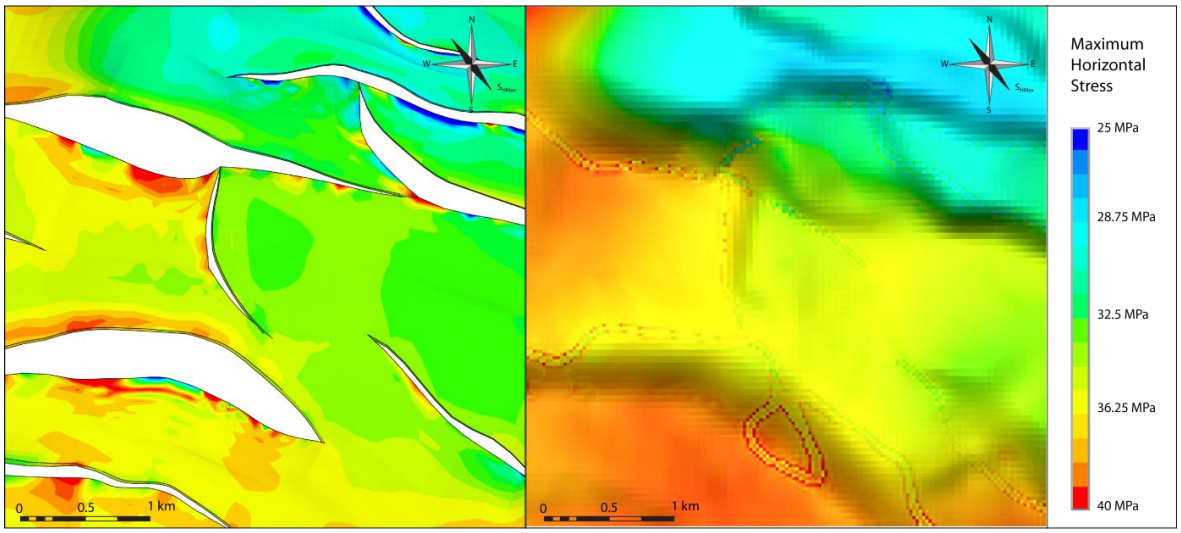

Fig. 11.2: Comparison of total stress distribution of maximum horizontal stress at mid-reservoir level computed with Ansys® (left) and Visage® (right).

The comparison of the distribution of total minimum horizontal stress at mid-reservoir level leads to similar observations (Fig. 11.3). Correlation with depth is evident for both models, with magnitudes increasing from the northern part of the reservoir towards the southern part. Local perturbations are significantly pronounced in the NE quadrant of the reservoir in the Ansys® model, whereas the same area in Visage® only follows the depth tendency.

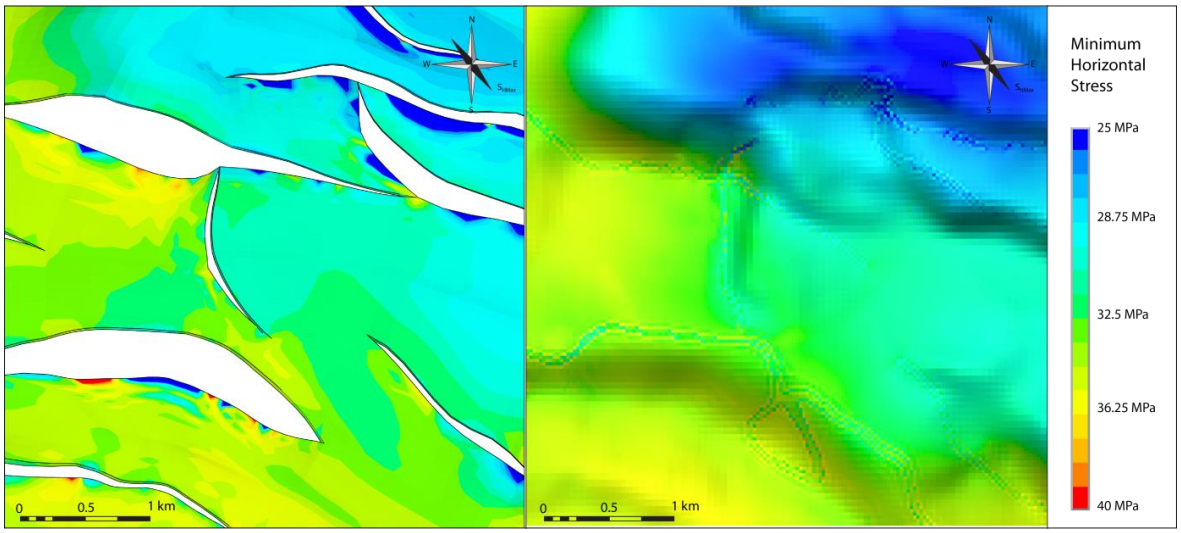

Fig. 11.3: Comparison of total stress distribution of minimum horizontal stress at mid-reservoir level computed with Ansys® (left) and Visage® (right).

Visualization of the orientation of maximum horizontal stress orientation at mid-reservoir level looks instead quite different, a representative fault has been taken as example (Fig. 11.4). First of all, the different setups of the two model results in a different resolution of the vectors orientation. Indeed, Ansys® model has an uneven distribution as each vector is displayed at the center of the corresponding cell and that reflects the non-uniform mesh of the model. In contrast, Visage® model that is generated with a spatially uniform grid shows the same resolution in the entire area. Besides different resolutions, different results are also computed as already seen for

the local perturbations in magnitude, only captured by Ansys® model. Looking at the footwall of the uppermost fault, maximum stress orientation computed with Ansys® software is strongly affected by local stress rotation, whereas in Visage® model stress rotation is very limited. Several factors could be responsible for those differences: how faults are treated in the two models and the consequent assignment of material properties, slight differences in the geometry due to the geometry transfer.

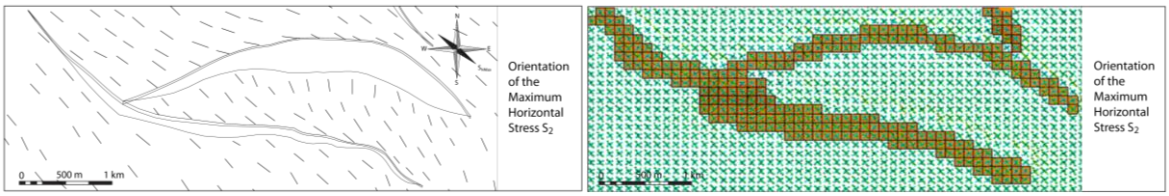

Fig. 11.4: Comparison of maximum horizontal stress orientation computed with Ansys® (left) and Visage® (right). Output of Visage® shows vectors for both maximum and minimum horizontal stress, perpendicular to each other. Stress rotation computed with Ansys® is very limited in software Visage®.

11.3 Stress rotation analysis

A comparison between the modeled orientations of the five major tectonic stages (present-day model and paleostress models) gives the opportunity to attempt an explanation of the occurrence of stress rotation. Generally, the modelled orientation of the maximum horizontal stress tends to follow the orientation of the regional orientation applied as boundary condition to the model (cf. Chap. 9.6.1 and 10.4.1). However, Present-Day model and Paleo 1 model show significant local stress rotations, in particular in the vicinity of faults where stress vectors tend to reorient perpendicular to them. Evidences of local stress rotations are not registered for models Paleo 2 and Paleo 4, although they have a maximum horizontal stress orientation very similar to Present-Day and Paleo 1 models. Model Paleo 3 shows limited stress rotations, but it has completely different maximum horizontal stress orientation that strikes already perpendicular to faults. From these observations, it can be concluded that the relative orientation of faults with respect to maximum horizontal stress direction provides the first factor necessary to cause local stress rotations.

With the aim to take into account in the analysis the anisotropy in magnitude of the two horizontal stresses a parameter is proposed to explain the occurrence of stress rotation. This can be applied for settings that are already favorable to the occurrence of stress rotation i.e. relative orientation between faults and regional stress are not already perpendicular to each other. For this reason, Paleo 3 model is not included in this analyis since, although low anisotropy, the relative orientation between faults and maximum horizontal stress leads in any case to the absence of local stress rotations.

The Differential Horizontal Stress Ratio (Gray et al. 2012) is the weighted ratio of the two horizontal stresses (Fig. 11.5) (Eq. 11-1):

$$DHSR = \frac{S_{HMax} - S_{hmin}}{S_{HMax}} \qquad (Eq.\ 11\text{-}1)$$

Models Present-day and Paleo 1 have a low Differential Stress Ratio (~0.2), whereas the models Paleo2 and Paleo 4 have a high Differential Stress Ratio (>0.25). The influence of the far-field in the occurrence of stress rotation is well described by this parameter and if the reference values for the boundary conditions at reservoir level are analyzed in terms of Differential Horizontal Stress Ratio (DHSR), it becomes clear that stress rotation occurs for DHSR<0.25 (Tab. 11.1) if faults are not oriented perpendicular to the regional stress.

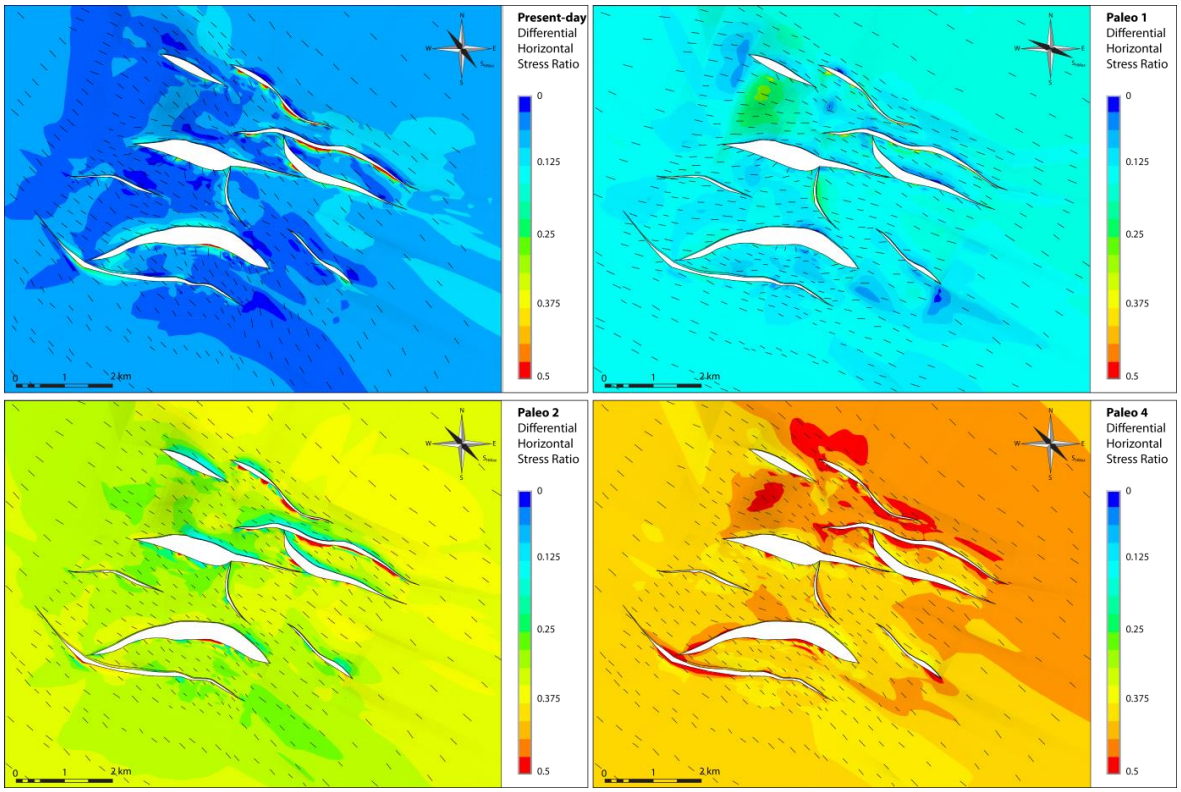

Fig. 11.5: Top view of the mid-reservoir level showing vector plot for the orientation of the maximum horizontal stress S_{HMax} and contour plot of the Differential Horizontal Stress Ratio in a range 0-0.5.

This observation confirms the theory proposed by Yale (2003) stating that for small differential horizontal stresses, geologic and tectonic structures influence more the orientation of the maximum horizontal stresses, whereas large differential stresses lead to orientations consistent with and parallel to the regional field. In his study, Yale used datasets from several sedimentary basins worldwide and focused on present-day stress orientation where the majority of faults strikes parallel to the regional maximum horizontal stress orientation.

	Stress regime	S_V at reservoir level	S_{HMax} at reservoir level	S_{hmin} at reservoir level	DHSR	Stress Rotation
Present-day	Normal Faulting	44.45 MPa	34.06 MPa	31.48 MPa	0.07	Yes
Paleo 1	Reverse faulting	41.42 MPa	55.52 MPa	47.06 MPa	0.15	Yes
Paleo 2	Normal faulting	40.26 MPa	35.28 MPa	23.83 MPa	0.32	No
Paleo 3	Reverse faulting	40.26 MPa	51.09 MPa	43.39 MPa	0.15	No
Paleo 4	Strike-slip faulting	40.26 MPa	43.06 MPa	24.73 MPa	0.42	No

Tab. 11.1: Table summarizing the reference values at reservoir level used for the boundary conditions, the DHSR value and the corresponding occurrence of stress rotation. Model Paleo 3 does not show stress rotation due to the relative orientation between faults and regional stress orientation.

Further causes that could be responsible for the occurrence of stress rotation in the four paleostress models are to be researched directly in the setup and geometric features of the models. Presence of discontinuities in the model, such as faults, their geometry (i.e. the curvature) and their orientation with respect to the orientation of the regional stress field have already been mentioned. Furthermore, the large offset of the faults more affected by stress rotation can be considered as possible reason because of the contrast in mechanical properties at fault plane location if the offset is greater than the thickness of the reservoir formation. The topography of the reservoir level could influence the amount of stress rotation since the two horizontal stresses have different gradients i.e. different magnitudes, affecting the resulting anisotropy.

11.4 Fractures correlation

Generation and development of fractures is mainly controlled by the tectonic stress field: the orientation of principal stresses and the corresponding tectonic stress regime decide the type of fractures and their orientation. Therefore, many fractures and faults existing today have been introduced by previous deformational episodes (Zoback 2010). The dependency of fractures generation on the active stress field is the assumption on the fractures correlation analysis conducted in this thesis. Indeed, the observed fractures can be assigned to the modeled present-day or paleostress distributions that ideally generated them. An estimation of the temporal evolution of the present-day fracture network can therefore be attempted.

According to Anderson faulting theory and Mohr-Coulomb failure criterion, idealized relationship between sets of fractures and orientation of principal stresses can be outlined (Fig. 11.6) (Zoback 2010). Extensional fractures tend to form in a plane normal to the least principal stress, whereas strike of shear fractures depends on the tectonic stress regime. In a normal faulting regime conjugate sets of shear fractures are expected to strike nearly parallel to the direction of S_{HMax} and to dip ~60° from horizontal in the direction of S_{hmin}. In the case of a strike-slip faulting regime, conjugate sets of shear fractures are nearly vertical and strike at an angle of ~30°

with respect to S_{HMax}. Conjugate sets of shear fracture in a reverse faulting regime are expected to strike ~90° with respect to S_{HMax} and to dip ~30° in the S_{HMax} direction.

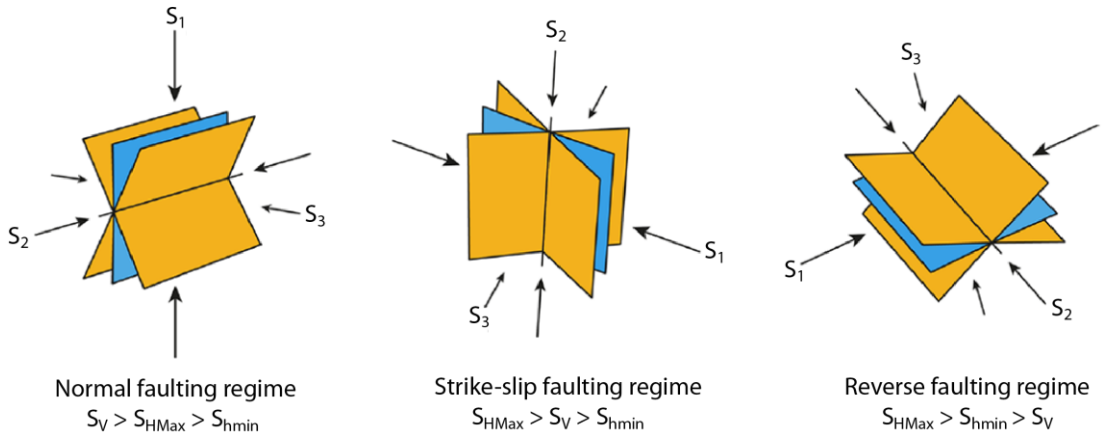

Fig. 11.6: Idealized relationships between fractures and state of stress. Extensional fractures (blues) tend to form perpendicular to the least principal stress. Strike and dip angle of conjugate shear fractures (orange) depend on the orientation of the three principal stresses at the time of generation. Modified after Towse (1980).

A structural analysis of borehole images from well CRC-1 and CRC-2 has been carried out by CO2CRC consortium (Lawrence 2011). This study aims to provide a full fracture characterization of the CO2CRC Otway site and contains description of fractures and faults encountered while logging.

Resistivity borehole images were acquired using the Fullbore Formation MicroImager (FMI™, Schlumberger) over the intervals 511.1-2240.4 m in well CRC-1 and 490.1-1554.5 m in well CRC-2 (Fig. 11.7). Image quality is a direct function of the borehole conditions. Well CRC-1 has moderate to good borehole conditions with intervals of rugosity and washouts, which have resulted in a moderate quality images. Borehole of well CRC-2 has good conditions, resulting in a better image quality than well CRC-1. Borehole images from both wells have been processed using an accelerometer speed correction to remove as many speed irregularities as possible. Lastly, a dynamically-normalized image is generated to highlight the details.

Fractures can be interpreted on borehole images due to the resistivity contrast between the host rock and the fracture. Planar fractures cutting the wellbore have sinusoidal appearance with dip direction towards the lowest point of the sinusoid (Fig. 11.7). The amount of dip depends on the diameter of the well and the height of the fracture as measured at the top and bottom of its intersection with the wellbore. Fractures parallel to the wellbore axis (e.g. vertical fractures in vertical wells) are not visible in borehole images due to sampling bias.

A total of 57 fractures have been interpreted from CRC-1 borehole images and 14 for well CRC-2. However, some fractures have a low level of confidence and are not taken into account in this study. As a consequence, only 25 fractures from well CRC-1 and 9 from well CRC-2 are used for the fractures correlation analysis. The dominant fracture type in both wells are conductive fractures that are generally interpreted as open but filled with conductive drilling mud, closed due to a conductive mud smear

fill or closed due to precipitation of sulphide minerals. From core inspection, mud infill is considered to be the most likely cause of conductive fractures fill.

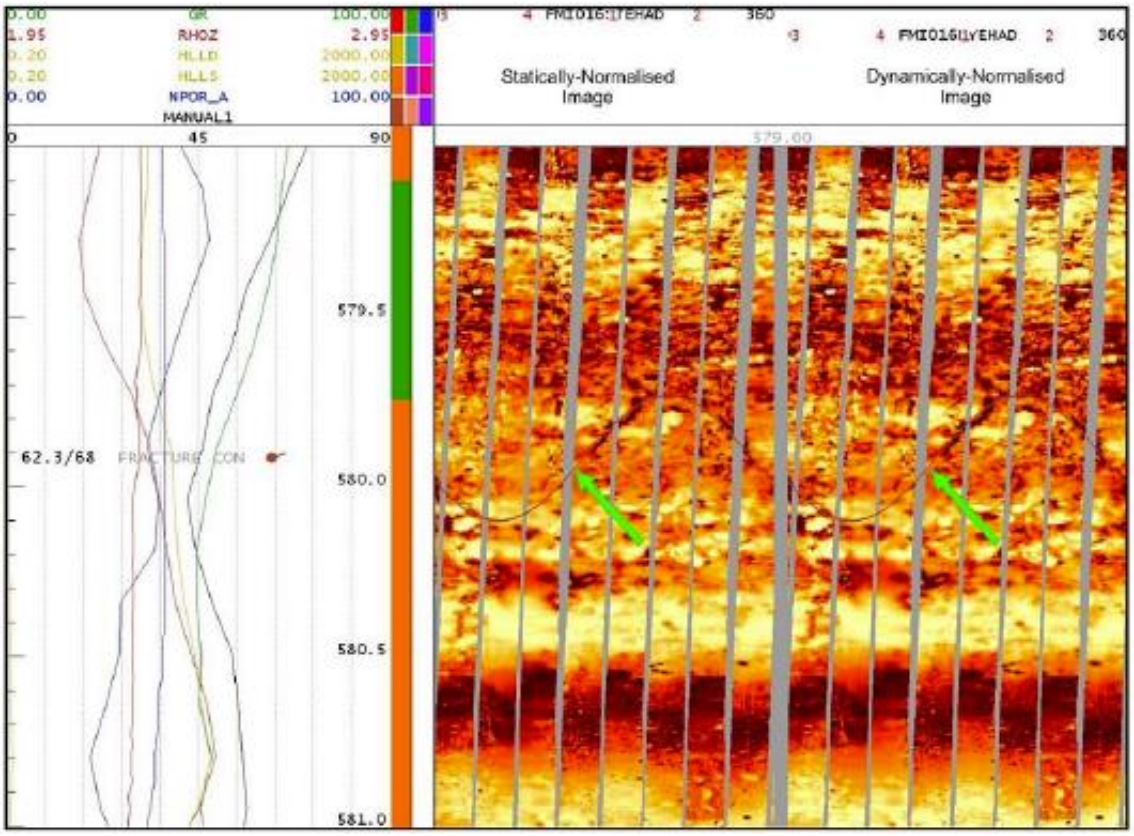

Fig. 11.7: Example of borehole image from well CRC-1. Green arrows indicate a resistive discontinuous fracture interpreted from the FMI™ log. (Lawrence 2011).

Fractures orientation is represented as roseplots where strike azimuths are plotted (Fig. 11.8). The dominant strike directions are W-E to NW-SE in well CRC-1, while in well CRC-2 are NNW-SSE and NNE-SSW.

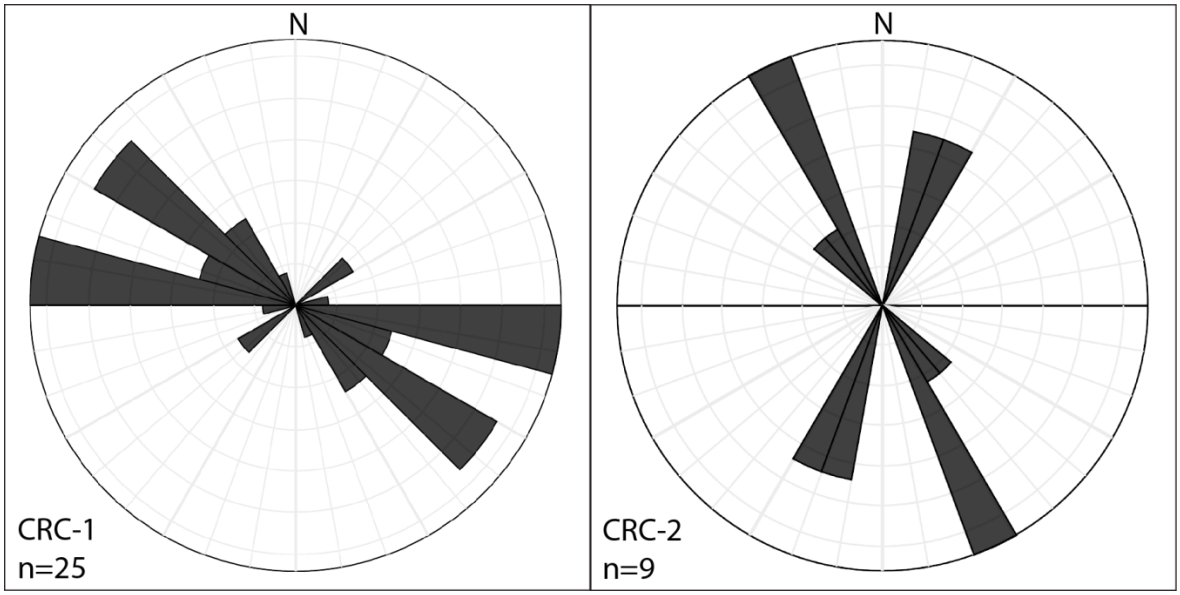

Fig. 11.8: Fractures orientations roseplots for wells CRC-1 (left) and CRC-2 (right). Data are plotted as strike azimuths.

Orientation of fractures is the first parameter used for sorting the different sets of fractures interpreted in the two wells. The second distinctive parameters is the dip angle that gives preliminary information about the possible stress regime that generated those fractures (e.g. a fracture dipping ~60° was most likely generated in a normal faulting regime). The fractures are assumed to be shear fracture or hybrid between shear and extensional fractures. In a vertical wellbore, due to sampling bias, extensional fractures generated in normal and strike-slip regime would be undersampled. It has also to be taken into account that structural dip of the lithostratigraphic layers is not perfectly horizontal and could affect the interpretation of fractures, in particular the dip angle that could have been tilted after the generation of fractures.

The majority of fractures crossing well CRC-1 strikes NW-SE to W-E, with a dip angle close to 60°, typical for normal faulting regime (Fig. 11.9). The major tectonic stages undergoing a normal faulting regime are the present-day stress field (maximum horizontal stress orientation of 142°) and model Paleo 2 (maximum horizontal stress orientation of 135°). Fractures are assigned accordingly to the two major tectonic stages, although it is also possible that fractures were generated during the extensional period from Late Cretaceous to Miocene (model Paleo 2) and then reactivated during Quaternary under the present-day stress field.

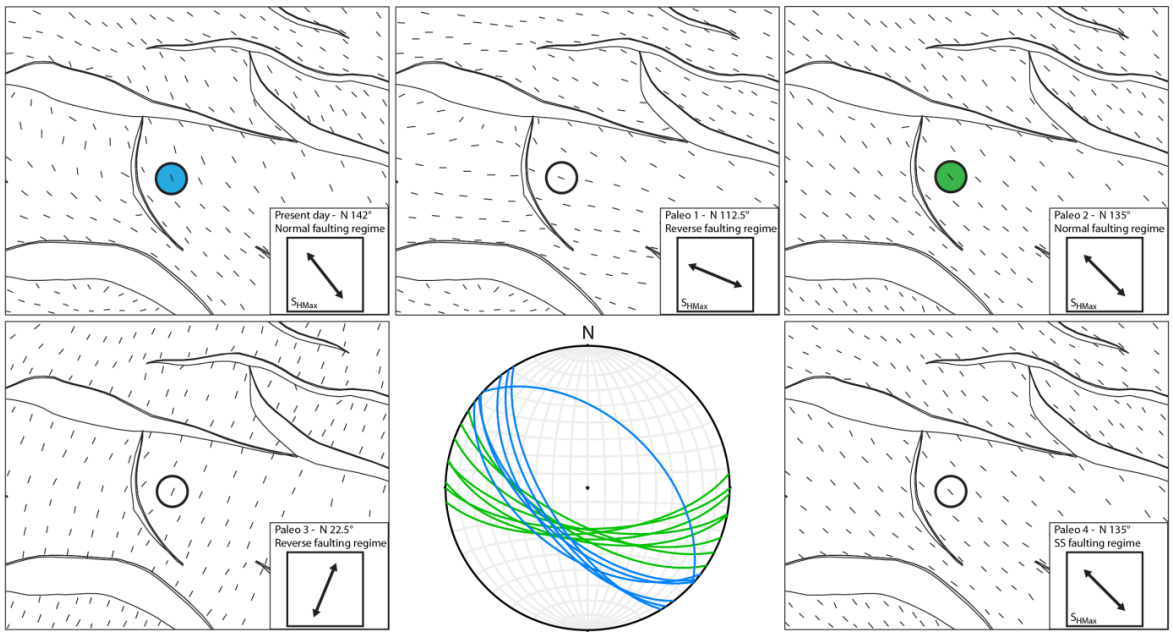

Fig. 11.9: Details of modeled maximum horizontal stress orientation in the vicinity of CRC-1 well for the five major tectonic stages (present-day model and paleostress models). The stereoplot shows two sets of fractures developed under a normal faulting regime and their fit with present-day model (blue) and Paleo1 model (green).

The second identified set of fractures in well CRC-1 comprise two steeply-dipping (>70°) fractures (Fig. 11.10), indication of generation during a strike-slip faulting regime period. One fracture strikes at NNW-SSE, while the other fractures strike in ENE-WSW direction. This setup can be associated with the sinistral transcurrent faulting developed during the rifting the extension modeled with Paleo 4 model.

Indeed, this conjugate set of strike-slip fractures strikes at angle of ~30° with respect to the modelled S_{HMax}.

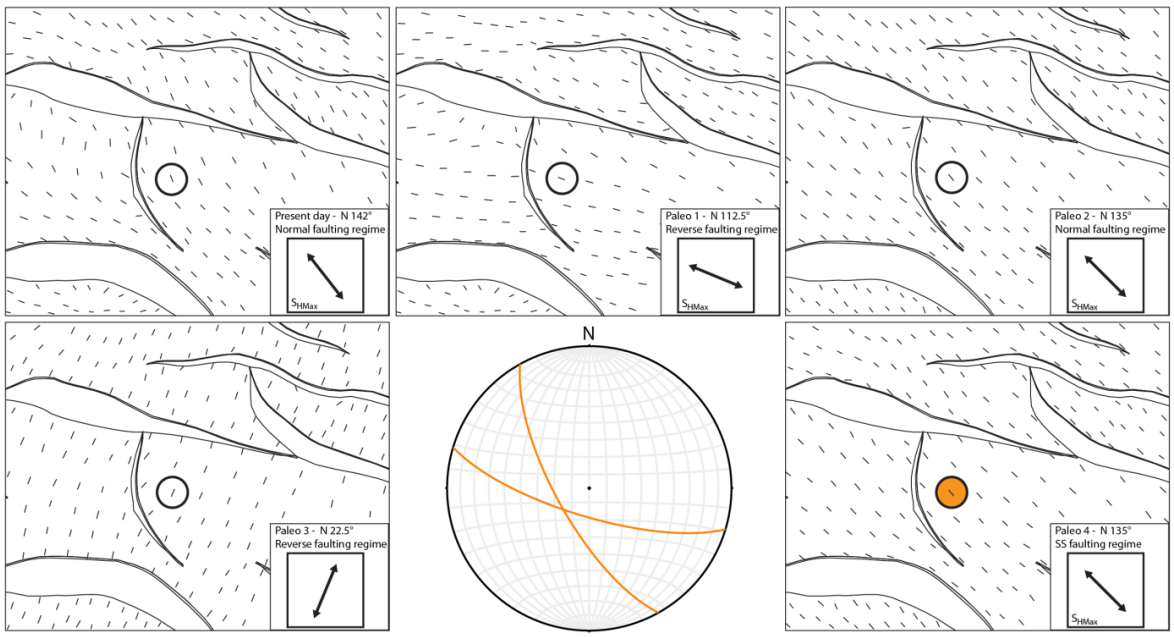

Fig. 11.10: Details of modeled maximum horizontal stress orientation in the vicinity of CRC-1 well for the five major tectonic stages (present-day model and paleostress models). The stereoplot shows two fractures developed under a strike-slip faulting regime and their fit with Paleo4 model (orange).

The third identified set of fractures in well CRC-1 comprises fractures orientated W-E with a low dip angle (~30°), typical of reverse faulting regime (Fig. 11.11). It has his best fit with model Paleo 3 that has a S_{HMax} orientation approximately N-S (90° from the strike of fractures).

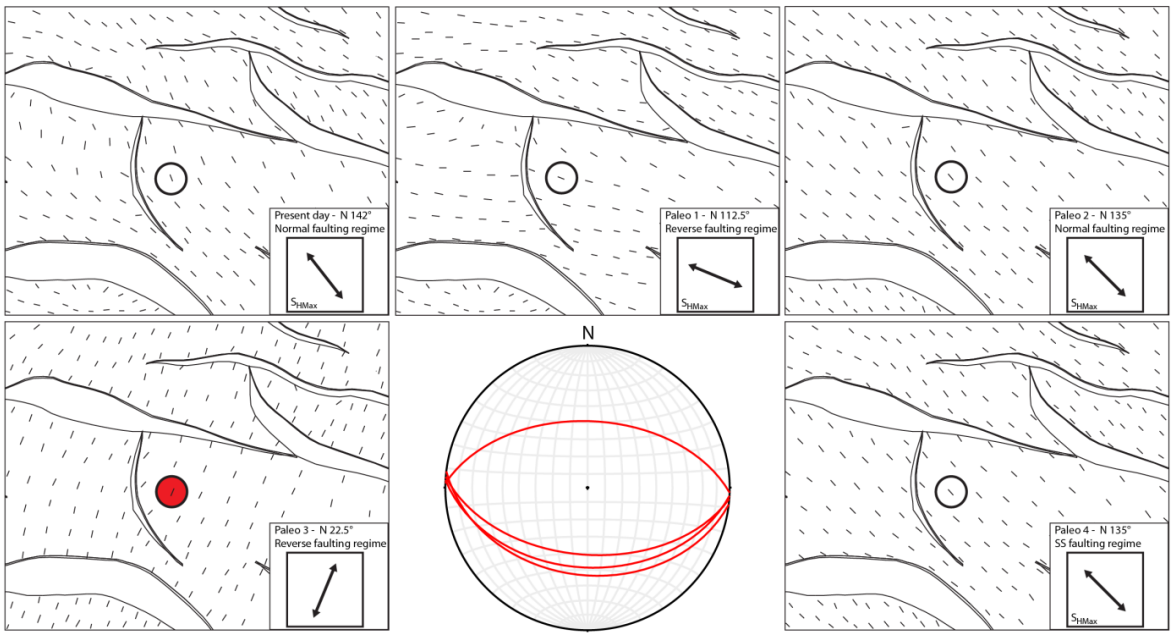

Fig. 11.11: Details of modeled maximum horizontal stress orientation in the vicinity of CRC-1 well for the five major tectonic stages (present-day model and paleostress models). The stereoplot shows a set of fractures developed under a reverse faulting regime and their fit with Paleo3 model (red).

The last set of fractures from well CRC-1 is a conjugate set of fracture striking NW-SE and NE-SW with a high dip angle (>70°), typical of strike-slip stress regime (Fig. 11.12). The best fit for this set has been found in Paleo 1 model that has an orientation of S_{HMax} ENE-WSW, although representing a reverse fault regime for which fractures are expected to strike 90° from the regional stress orientation and to have a low dip angle. Instead, a strike ~30° from the maximum horizontal stress orientation and high-angle could be explain as a fluctuation of magnitudes of the minimum horizontal stress S_{hmin} in the transition from the reverse faulting regime in place during Miocene and the present-day normal faulting regime. This progressive decrease in magnitude, lower than vertical stress magnitude, would actually establish a strike-slip faulting regime with the same S_{HMax} orientation that could have generated this set of fractures.

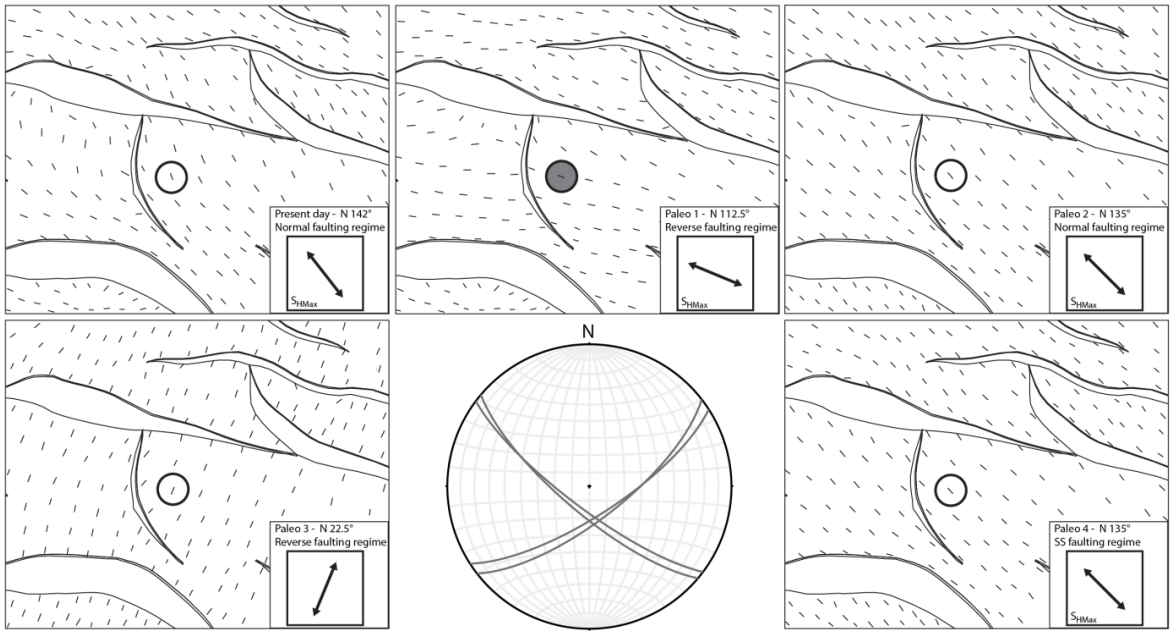

Fig. 11.12: Details of modeled maximum horizontal stress orientation in the vicinity of CRC-1 well for the five major tectonic stages (present-day model and paleostress models). The stereoplot shows a conjugate set of strike-slip shear fractures developed under a strike-slip faulting regime and their fit the orientation of Paleo1 model (grey). Further explanation is provided in the text.

In well CRC-2 9 fractures have been identified and sorted in two different families. The first set of fractures has a mean strike oriented NW-SE to NNW-SSE and a dip angle that varies from ~60° to slightly higher values (Fig. 11.13). This set has been most likely generated in a normal faulting regime, therefore can be correlated with the present-day regional stress that strikes approximately NW-SE. Fractures with a steep dip angle (>70°) could correspond to hybrid fractures at the boundary between shear fractures and extensional fractures.

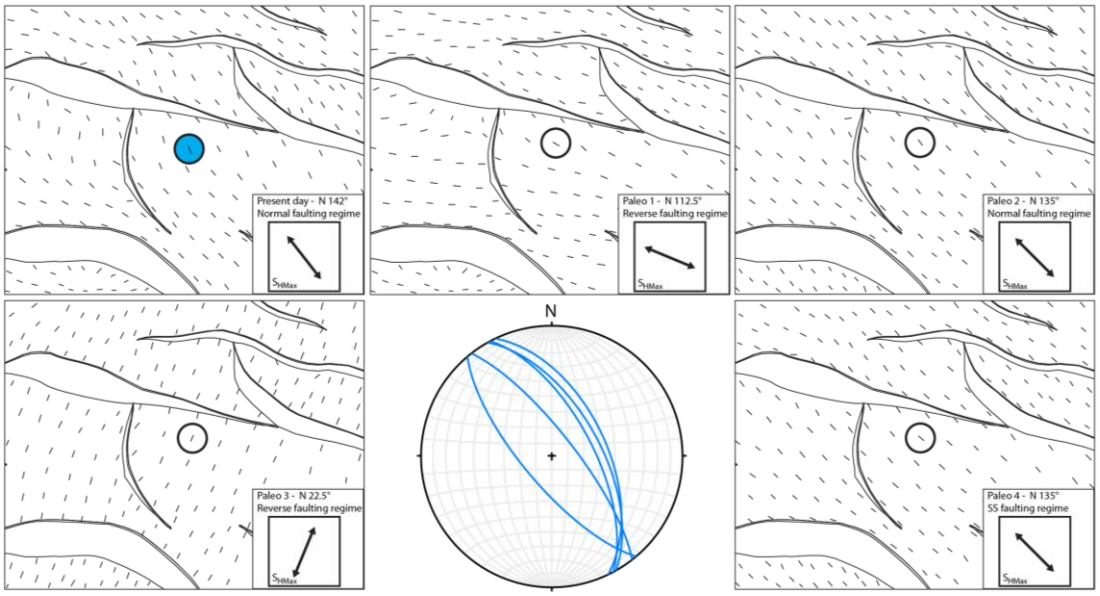

Fig. 11.13: Details of modeled maximum horizontal stress orientation in the vicinity of CRC-2 well for the five major tectonic stages (present-day model and paleostress models). The stereoplot shows fractures developed under a normal faulting regime and their fit present-day model (blue).

The second set of fractures from well CRC-2 comprises a conjugate set of shear fracture striking NNE-SSE with a dip angle ~60°, typical of a normal faulting stress regime (Fig. 11.14). The best fit is with Paleo 3 model that share the same S_{HMax} orientation, although representing a reverse faulting regime for which fractures are expected to strike 90° from the regional stress orientation and to have a low dip angle. However, generation of these conjugate shear fractures could be the result of a transition phase between the Eocene inversion (Paleo 3 model) and the following normal stress regime in place until Miocene. A decrease of both S_{HMax} and S_{hmin} magnitude would cause a change in stress regime, with the same maximum horizontal stress orientation.

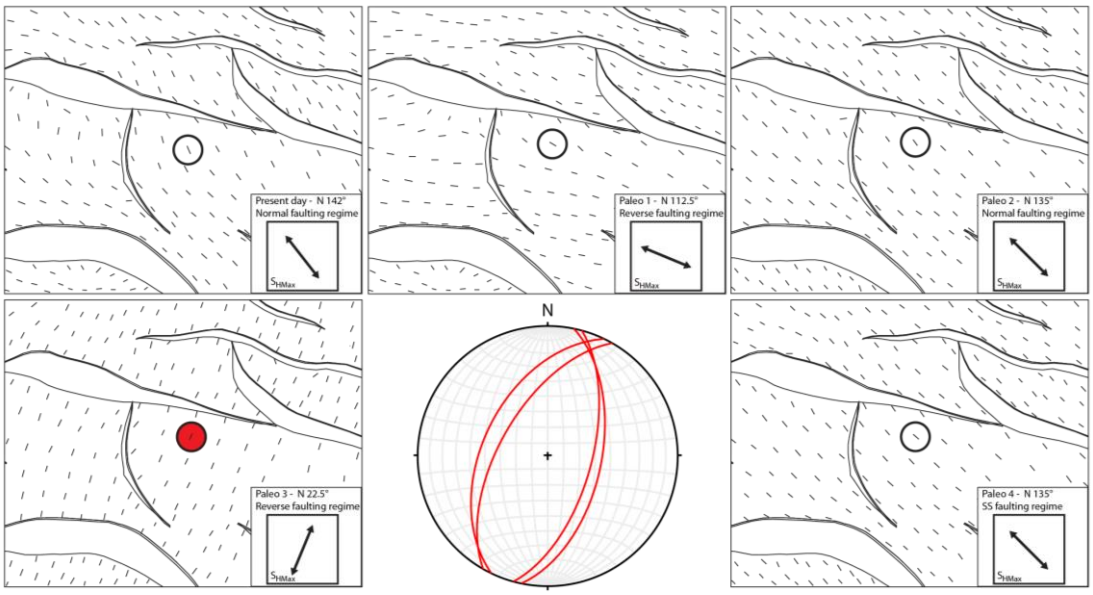

Fig. 11.14: Details of modeled maximum horizontal stress orientation in the vicinity of CRC-2 well for the five major tectonic stages (present-day model and paleostress models). The stereoplot shows a conjugate set of normal shear fractures developed under a normal faulting regime and their fit the orientation of Paleo3 model (red). Further explanation is provided in the text.

12 Conclusion

A geomechanical characterization of the CO2CRC Otway project site was successfully accomplished through the application of two different geomechanical approaches, one that describes changes in effective stresses due to CO_2 injection (Chap. 7), the other one that takes into account only the contribution of total stresses acting on the reservoir and its surroundings (Chap. 9). The workflow followed for this case study has high relevance as it can be applied virtually to any reservoir geometry. Knowledge of the local stress field is nowadays required prior to wellbore construction to increase operation safety and to prevent for example wellbore failure, sand production. Incorporation of a flow model in the coupled simulation allows to compute changes in stress related to production and injection of fluids, expanding its applicability to oil and gas industry.

3D seismic interpretation has been carried out and, following a depth-conversion of the seismic cube, a 3D geological and structural model (Chap. 6) has been built providing the first input data needed for the geomechanical model: the geometry of reservoir and overlying layers. According to the different aim of the two geomechanical approaches proposed, different model sizes have been used.

As main outcome, a comprehensive 3D description of the stress field at different scale is now available. The inclusion of the entire geometry and mechanical stratigraphy up to the ground surface, instead of a simple lithostatic load as top boundary condition, allow to have a good level of confidence for the stress field calculated not only at reservoir level, but also in the overburden. Hence, results of the modelling could be use for borehole planning in future operation where knowledge of stress acting along the entire depth is considered to be crucial. In the light of the objectives stated for this thesis, the main results are here summarized.

The reservoir response to CO_2 injection has been quantified in terms of changes in effective stresses through a one-way flow and geomechanics coupled simulation (Chap. 7). A flow model simulated the injection of CO_2 in the subsurface and the computed pressures were transferred as input to the geomechanical simulator to calculate the corresponding effective stresses. This workflow has been applied to the entire development history of the reservoir comprising both production and injection operations. The computed state of stress has been checked against the Mohr-Coulomb failure criterion to assess both caprock integrity and fault stability. This is made possible by the incorporation of faults in the model as 3D cells with specific fault properties, for which state of stress is singularly calculated. The present-day scenario indicates that caprock integrity is not jeopardized, whereas potential fault reactivation could occur if a critical pore fluid pressure is exceeded. This critical pore pressure has been quantified for the numerical geomechanical model and for two analytical models, one that considers stresses constant during injection and one that includes the reservoir stress path in the stress calculation (Chap. 8). The critical pore pressure in the numerical model is 1.15 times the original pore pressure equivalent to a final Bottom-Hole Pressure (BHP) of 22.73 MPa, while the analytical model

predicts values of 1.2 and 1.35 for constant and variable stress fields, corresponding respectively to a BHP of 23.93 MPa and 26.80 MPa. From the determination of the critical pore pressure it is also possible to derive an upper boundary to the injection rate to be chosen during injection operations. BHP obtained from the critical pressure calculation is used as control mode in a new set of flow simulations. As a result, daily injection rate could be increased up to ~90000 sm^3/day if numerical results of BHP are used, or ~100000 sm^3/day and ~140000 sm^3/day if BHP results from the two analytical models, constant stresses and variable stresses respectively, are taken into consideration.

Critical pore pressure and allowable injection rate calculations differ quite significantly whether a numerical or analytical approach is used. Possible reasons have been investigated, in particular in relation to how stresses are calculated and incorporation of heterogeneity (Chap. 11.1). Degree of complexity that can be included in numerical models is much higher with respect to analytical models: variability of rock properties, topographic effect and presence of discontinuities can be taken into account only in numerical simulators. Furthermore, analytical models do not consider interaction between adjacent cells, thus neglecting a component that needs to be included when an accurate state of stress has to be computed. Indeed, impact of results accuracy on risk analysis for potential fault reactivation and caprock failure is highly relevant. For a CCS injection scenario, which requires the most conservative estimates of allowable fluid pressures to be determined, it is recommended to perform numerical modeling when possible.

The present-day stress field has been described also in term of total stresses with the aim to understand the contribution of tectonic stress in the local stress field (Chap. 9). Although results are analyzed only at mid-reservoir level, such information is available throughout the depth of the model. Generally, distribution of principal stress magnitudes shows a good correlation with depth. Local stress perturbations in magnitude are generated due to presence of discontinuities (i.e. faults) and occur mostly at footwall location. Magnitude of perturbations could be enhanced by numerical noise due to curvature of faults and a subsequent non-perfect correspondence between contact and target elements. Indeed, in this geomechanical simulation faults are implemented as 2D distinct elements, characterized by a coefficient of friction that allows them to slip during the modelling. Vectors describing the orientation of the maximum horizontal stress can be derived from the modelling results. The general trend follows the orientation of the regional stress field applied as boundary condition, however evidence of local stress rotation can be found, in particular around faults with significant displacement. Further stress quantities such as mean stress and differential stress are derived as well and again, a good correspondence with depth is found. However these derived quantities show less intense magnitude perturbations. Planar nature of modelled faults allows to compute directly normal and shear stresses acting on faults plane. These last two components are then used to characterize the fault behavior, from a structural point of view, in terms of slip and dilation tendency. For a coefficient of friction of 0.6 (literature-

matching scenario) slip tendency is <0.3 in a range from 0 to 1, whereas if a coefficient of friction of 0.2 is used, slip tendency increases reaching also locally a value of 1. This confirms the strong dependency of potential slip on friction coefficient, considered to be source of uncertainty in the geomechanical analysis. Impact of mechanical stratigraphy is also influencing the distribution of slip tendency: within each layer is possible to recognize a zonation increasing with depth. On contrast, dilation tendency does not show an appreciable dependency on coefficient of friction, with values mostly >0.5 (in a range from 0 to 1) and a distribution almost identical if a coefficient of friction of either 0.6 or 0.2 is used. For the literature-matching scenario (coefficient of friction=0.6), higher values of dilation tendency with respect to slip tendency indicate a prevailing normal stress acting on faults with respect to shear stress. Curvature and orientation of faults are also factors that contribute to control fault behavior.

The same workflow used to build the steady-state present-day geomechanical model has been applied to reproduce paleostresses in place during the past (Chap. 10). A revision of the geodynamic history of the Otway basin led to the identification of a total of four major tectonic stages. A decompaction analysis and the use of backstripping technique helped to update the model in terms of density and depth for each tectonic stage. A complete update of the geometry would be theoretically possible by taking into account fault restoration to reproduce the exact geometry of the horizons through time. However, this information is not yet available for the Otway Basin and furthermore, it would require a separate and new build up for each tectonic stage. About the update of rock properties, same values from the present-day stress modelling have been used for Young's Modulus and Poisson Ratio due to the lack of data or correlation with density. The major outcome of the paleostress modeling is the distribution of stress magnitudes and orientation at local scale. Magnitude and orientation of the three principal stresses have then been used, together with the results from the present-day stress field modelling, to understand the generation and development of fracture network through time (Chap. 11.4). Analysis of strike and dip angle of fractures allows the correlation between fractures sets and corresponding tectonic stages.

Examination and comparison of all the results obtained from the steady-state models (i.e. present-day and paleostress models) allows to investigate possible reasons for the occurrence of local stress rotation (Chap. 11.3). Indeed, two models out of five show occurrence of stress rotation, mainly around faults with significant displacement. Possible sources have been identified in the presence of discontinuities, orientation of faults with respect to model stress field, contrast in mechanical properties and far-field influence. The latter has been more accurately analyzed and the Differential Horizontal Stress Ratio (DHSR) is proposed as parameter to predict occurrence of stress rotation for given boundary conditions. Generally, local stress rotation is more likely to occur if orientation of faults is not perpendicular to the orientation of stress field and, satisfied this first condition, if

DHSR<0.25 (i.e. small differential stress promotes the occurrence of local stress rotation).

Results obtained from the 3D geomechanical models can be compared with previous analytical geomechanical studies conducted on the Otway Basin (Tab. 12.1). As the first published 3D geomechanical model, it represents a breakthrough in understanding the distribution of the local stress field in terms of magnitude and orientation that is proposed here for the first time. Nevertheless, a comparison with previous studies (Chap. 3.3) can be still carried out, but only in terms of fault stability analysis. Values for critical pore pressure sustainable by faults within the reservoir differ significantly between the studies that progressively incorporate new available data, thus increasing the level of confidence. The first geomechanical analysis of Naylor Field by van Ruth and Rogers (2006) reported that cohesionless faults were not able to withstand a pressure increase without reactivation occurring, but they also acknowledge that "it may be a result of the methodology used". Furthermore, the geomechanical model is considered to be poorly constrained due to lack of lab testing and well logs. Following the availability of in situ test a new report was published (van Ruth et al. 2007) for pre-injection assessment. For cohesionless faults and magnitude horizontal stress calculated from leak-off test, the critical pore pressure for optimally oriented faults has a value of 5.6 MPa. The same critical pore pressure is reported in the subsequent report (Vidal-Gilbert 2008) for cohesionless faults and constant horizontal stresses during injection. The introduction of reservoir stress path (A=0.5) in the calculation leads to an increase in the value of the estimated critical pore pressure up to 18.5 MPa. Additional scenarios testing different stress path are described in Vidal-Gilbert et al. (2010). For a reservoir stress path equal to 0 (constant stresses) the reactivation pressure is 5.3 MPa for a normal faulting regime. Increasing the reservoir stress path, also the critical pore pressure increases: for A=0.4 the reactivation pressure is 12.9 MPa for a normal faulting regime. Those last results can be directly compared with the results presented in this thesis for analytical models. For constant horizontal stresses (A=0) the critical pore pressure calculated is 4.35 MPa, whereas for a variable reservoir stress path comprised in a range 0.25-0.60 the reactivation pressure is 7.22 MPa. On contrast with previous studies where the reservoir stress path was assigned with a constant value, a range of values is provided because it varies spatially in the reservoir. This accounts for differences in calculated critical pore pressure between this thesis and previous reports, together with a different methodology used for deriving magnitude of horizontal stresses. Furthermore, it has to be taken into account that for this study the critical pore pressure is calculated at well location, whereas is not reported the reference location for the previous analytical studies. However, high permeability of the reservoir should reduce potential differences in reference locations. When results from the numerical model are analyzed, they indicate that an increase in pore pressure of 3.15 MPa would be sufficient for initiating failure of faults. This reflects the increase in confidence provided by numerical modelling that is able to incorporate more complexity in the calculation. As a consequence, it is recommended to perform numerical modelling for a more accurate risk assessment.

	Reservoir stress path	CCP for faults
Van Ruth and Rogers 2006	0	0 MPa
Van Ruth et al. 2007	0	5.6 MPa
Vidal-Gilbert 2008	0	5.6 MPa
	0.5	18.5 MPa
Vidal-Gilbert et al. 2010	0	5.3 MPa
	0.4	12.9 MPa
Aruffo (this work)	0	4.35 MPa
	0.25-0.60 (analytical)	7.22 MPa
	0.25-0.60 (numerical)	3.15 MPa

Tab. 12.1: Summary table of the Critical Pore Pressure (CPP) for faults calculated in the geomechanical models of Naylor Field. A Results depends mainly on methodology chosen for estimating magnitude of maximum horizontal stress, values assigned to reservoir stress path and type of analysis (analytical or numerical).

13 Perspectives

The workflow proposed for 3D geomechanical modelling can be easily applied to other reservoir geometries to be exploited for production of injection of fluids. Although it already provides reliable results, areas of possible improvements and topic of future research for the general workflow and for the Otway basin case study have been identified and outlined below.

The one-way coupled flow and geomechanics simulation is nowadays often used to study the interaction between changes in pressure and changes in stress in active reservoirs. The current workflow could be potentially improved by performing a fully-coupled simulation, where not only pressures computed in the flow model are transferred to the geomechanical simulator, but also changes in porosity and permeability in the geomechanical model are transferred back to the fluid model. In this way, the flow simulation can be constantly updated to produce more accurate results. Furthermore, for reservoirs with a strong dependence on temperature i.e. geothermal reservoirs, temperature could be also included in the coupling to refine the fluid model.

The workflow followed for the steady-state geomechanical model could also be significantly improved, in particular in the geometry transfer and model setup. The actual configuration does not allow the incorporation of vertical and lateral variation of material properties within the same layer, with loss in accuracy. Given the importance of a more realistic rock properties distribution, this topic is currently under research at TU Darmstadt (Weber, in prep.). Moreover, update of the geometry (i.e. revision of seismic interpretation) requires at this moment a significant effort in terms of time and model re-construction. Generally, a more straightforward geometry transfer would be beneficial in this sense, allowing to reduce significantly model-building time. The same issue applies for the re-definition of the geometry in paleostress modeling, which at the moment is very limited as only depth of the top of the model can be easily modified. However, a more accurate paleostress modelling would require first a fault restoration analysis to obtain geometry of horizons through time. A retrodeformation study is currently undergoing at LIAG (Leibniz Institute for Applied Geoscience), part of PROTECT Research Group. Incorporation of pore pressure in the steady-state model would also be beneficial and results could be compared with those provided by the one-way coupled model. Similarly to the population of rock properties, vertical and horizontal variation should be included to actually reproduce changes in pressure occurring inside the reservoir.

Workflow for paleostress modeling would also require some adjustments, mainly in terms of model geometry, material parameters and absolute magnitudes. Issues about the model geometry have been already addressed above and could be useful especially in modelling older paleostresses that require the complete restoration/removal of shallower layers. Update of material parameters at the moment involves only the density, thanks to decompaction and backstripping techniques. The establishment of correlation between density and elastic parameters

(Young's Modulus and Poisson Ratio) would improve the material population of the model. Definition of absolute magnitude of paleostress is also a crucial point and would concur to the improvement of the paleostress modeling.

Besides the workflow, the geomechanical model of the CO2CRC Otway Site could be improved with additional analyses, however more data – currently not available – are needed. Calibration could sensibly improved in the case of new drilled wells that can provide new stress data. In particular, mini-frac and leak-off tests are recommended to measure magnitude of minimum principal stress, whereas magnitude of maximum horizontal stress could be constrained by studying the occurrence of drilling-induced tensile fractures and/or width of wellbore breakouts in borehole images. New well data would also help to improve the population of material parameters and to increase the accuracy of lateral variation, currently highly dependent on the algorithm chosen. Laboratory testing could directly provide information about rock properties, however if unavailable geophysical logs can be used to estimate those properties. Dynamic elastic moduli can be derived from P-wave and S-wave velocities, subsequently using further correlation static values can be estimated. Rock strength can be determined from P-waves velocity, Young's Modulus and porosity data. Coefficient of friction of faults is a sensible parameter and analyses on drilled core fault would be beneficial to better model fault characteristics.

14 Bibliography

[2009] Release Area S09-7, Western Otway Basin, South Australia. E. a. T. Department of Resources (ed.), pp. 31. Australian Goverment.

[2011] Regional Geology of the Otway Basin. E. a. T. Department of Resources (ed.), pp. 19. Australian Government.

Addis, M. A. [1997] The stress-depletion response of reservoirs - SPE 38720. *SPE Annual Technical Conference and Exhibition,* San Antonio - Texas, pp. 11.

Allen, P. A. and Allen, J. R. [2013] Basin analysis: principles and application to petroleum play assessment. John Wiley & Sons, pp. 642.

Allen, T. I., Gibson, G. and Cull, J. P. [2005] Stress-field constraints from recent intraplate seismicity in southeastern Australia. *Australian Journal of Earth Sciences* 52(2), p. 217-229.

Altmann, J. B., Müller, B. I. R., Müller, T. M., Heidbach, O., Tingay, M. R. P. and Weisshardt, A. [2014] Pore pressure stress coupling in 3D and consequences for reservoir stress states and fault reactivation. *Geothermics* 52, p. 195-205.

Amadei, B. and Stephansson, O. [1997] Rock Stress and Its Measurement. Springer Netherlands, pp. 490.

Anderson, E. M. [1951] The dynamics of faulting and dyke formation with application to Britain. Oliver and Boyd, Edinburgh, pp. 206.

Ansys [2012] Ansys 14.0 Release - Ansys Contact Technology Guide. pp. 105.

Ansys [2012] Ansys 14.0 Release - Help files. pp. 10396.

Aruffo, C. M., Rodriguez-Herrera, A., Tenthorey, E., Krzikalla, F., Minton, J. and Henk, A. [2014] Geomechanical modelling to assess fault integrity at the CO2CRC Otway Project, Australia. *Australian Journal of Earth Sciences* 61(7), p. 987-1001.

Ashworth, P., Rodriguez, S. and Miller, A. [2010] Case study of the CO2CRC Otway project. CSIRO RPT 10-2362, pp. 10.

Barnhill, R. E. [1982] Coon's patches. *Computers in industry* 3, p. 37-43.

Bérard, T., Jammes, L., Lecampion, B., Vivalda, C. and Desroches, J. [2007] CO_2 Storage Geomechanics for Performance and Risk Management - SPE 108528. *Offshore Europe,* Aberdeen, Scotland UK, pp. 8.

Bérard, T., Sinha, B. K., van Ruth, T., John, Z. and Tan, C. [2008] Stress Estimation at the Otway CO_2 Storage Site, Australia - SPE 116422. *SPE Asia Pacific Oil and Gas Conference and Exhibition,* Perth, Australia, pp. 26.

Bernecker, T. and Moore, D. H. [2003] Linking Basement and Basin fill: implications for hydrocarbon prospectivity in the Otway Basin region. *The APPEA Journal* 43(1), p. 39-58.

Biot, M. [1941] General thory of three-dimensional consolidation. *Journal of Applied Physics* 12(2), p. 155-164.

Bouquet, S., Gendrin, A., Labregere, D., Le Nir, I., Dance, T., Xu, J. and Cinar, Y. [2009] CO2CRC Otway Project, Australia: parameters influencing dynamic modeling of CO2 injection into a depleted gas reservoir. *2009 SPE Offshore Europe Oil & Gas Conference & Exhibition,* Aberdeen, UK, pp. 19.

Brodie, J. and White, N. J. [1994] Sedimentary basin inversion caused by igneous underplating: Northwest continental shelf. *Geology* 22, p. 147–150.

Brudy, M. and Zoback, M. D. [1999] Drilling-induced tensile wall-fractures: implications for determination of in-situ stress orientation and magnitude. *International Journal of Rock Mechanics and Mining Sciences* 36(2), p. 191-215.

Bryan, S. E., Constantine, A. E., Stephens, C. J., Ewart, A., Schön, R. W. and Parianos, J. [1997] Early Cretaceous volcano-sedimentary successions along the eastern Australian continental margin: Implications for the break-up of eastern Gondwana. *Earth and Planetary Science Letters* 153(1–2), p. 85-102.

Cardozo, N. [2005] Backstrip http://www.ux.uis.no/~nestor/work/programs.html

Chadwick, R. A., Holloway, S., M., B. and Kirby, G. [2004] The case of underground CO_2 sequestration in northern Europe. Geological society of London, Special Publication, B. S. J. (ed.), p. 17-28, London.

Chiaramonte, L., Johnson, S. and White, J. A. [2011] Preliminary geomechanical analysis of CO_2 injection at Snohvit, Norway. *45th U.S. Rock Mechanics/Geomechanics Symposium* San Francisco, California, USA, pp. 9.

Clark, D. and McCue, K. [2003] Australian paleoseismology: towards a better basis for seismic hazard estimation. *Annals of Geophysics* 46(5), p. 1087-1105.

CO2CRC. www.co2crc.com.au.

Coblentz, D. D., Zhou, S., Hillis, R. R., Richardson, R. M. and Sandiford, M. [1998] Topography, boundary forces, and the Indo-Australian intraplate stress field. *Journal of Geophysical Research* 103(B1), p. 919-931.

Cook, J., Frederiksen, R. A., Hasbo, K., Green, S., Judzis, A., Martin, J. W., Suarez-Rivera, R., Herwanger, J., Hooyman, P., Lee, D., Noeth, S., Sayers, C., Koutsabeloulis, N., Marsden, R., Stage, M. G. and Tan, C. P. [2007] Rocks matter: ground truth in geomechanics. *Schlumberger Oilfield review* (3), p. 19.

Cooper, G. T. and Hill, K. C. [1997] Cross-section balancing and thermochronological analysis of the Mesozoic development of the eastern Otway Basin. *The APPEA Journal* (37), p. 390–414.

Dake, L. P. [1978] Fundamentals of Reservoir Engineering. Elsevier Scientific Pub. Co., Amsterdam, pp. 462.

Daniel, R. F. [2007] Carbon dioxide seal capacity study, CRC-1, CO2CRC Otway Project, Otway Basin, Victoria. CO2CRC RPT07-0629, pp. 10.

Darcy, H. [1856] Les fontaines publiques de la Ville de Dijon. Dalmont, Paris, pp. 657.

Davis, R. O. and Selvadurai, A. P. S. [1996] Elasticity and Geomechanics. Cambridge University Press, pp. 216.

Drucker, D. C. and Prager, W. [1952] Soil mechanics and plastic analysis for limit design. *Quarterly of Applied Mathematics* 10(2), p. 157-165.

Duddy, I.R. [1997] Focusing exploration in the Otway Basin: Understanding timing of source rock maturation. *Journal of the Australian Petroleum Production and Exploration Association* 37, p. 178-191.

Dyksterhuis, S., Muller, R. D. and Albert, R. A. [2005] Paleostress field evolution of the Australian continent since the Eocene. *Journal of Geophysical Research-Solid Earth* 110(B5), p. 1978-2012.

Economides, M. J., Nolte, K. G. and Ahmed, U. [1989] Reservoir stimulation. Prentice Hall, pp. 856.

Eshelby, J. D. [1957] The determination of the elastic field of an ellipsoidal inclusion and related problems. *Proceedings of the Royal Society* A241, p. 376-396.

Fischer, K. [2013] Dissertation - Geomechanical reservoir modeling - workflow and case study from the North German Basin. TU Darmstadt, pp. 230.

Fjaer, E., Holt, R. M., Horsrud, P., Raaen, A. M. and Risnes, R. [2008] Petroleum Related Rock Mechanics. pp. 514.

Gallagher, S. J., Duddy I. R., Quilty P. G., Smith A. J., Wallace M. W., Holdgate G. R., and Boult P. J. [2004] The use of foraminiferal coloration index (FCI) as a thermal indicator and correlation with vitrinite reflectance in the Sherbrook Group, Otway Basin, Victoria, in Boult P. J., Johns D. R., and Lang S. C., Eastern Australasian basins symposium II: Petroleum Exploration Society of Australia Special Publication, p. 643–653.

Goodman, J. E. and O' Rourke, J. [2004] Handbook of discrete and computational geometry, 2nd ed. Chapman&Hall/CRC, pp. 1560.

Gray, D., Anderson, P., Logel, J., Delbecq, F., Schmidt, D. and Schmid, R. [2012] Estimation of stress and geomechanical properties using 3D seismic data. *First Break* (32), p. 59-68.

Halliday, D., Resnick, R. and Walker, J. [2010] Fundamentals of Physics. John Wiley & Sons, pp. 1232.

Hansen, O., Eiken, O., Ostmo, S., Johansen, R. I. and Smith, A. [2011] Monitoring CO_2 injection into a fluvial brine-filled sandstone formation at the Snohvit Field, Barents Sea. *SEG Annual Meeting*,San Antonio, USA, pp. 5.

Henk, A. [2010] Geomechanical reservoir models - a case study from the Sirte Basin, Lybia. *Oil Gas European Magazin* 1, p. 18-22.

Henk, A. and Fischer, K. [2011] Building and calibrating 3D geomechanical reservir models - a worked example. *73rd EAGE Conference & Exhibition*,Wien, pp. 4.

Herwanger, J. and Koutsabeloulis, N. [2011] Seismic geomechanics - How to build and calibrate geomechanical models using 3D and 4D seismic data. EAGE Publications, Houten, pp. 181.

Hillis, R. R. and Reynolds, S. [2000] The Australian Stress Map. *Journal of the Geological Society of London* (157), p. 915–921.

Hillis, R. R. and Reynolds, S. [2003] In situ stress field of Australia. *Geological society of Australia Special Publications* 22, p. 43-52.

Hillis, R. R., Sandiford, M., Reynolds, S. and Quigley, M. C. [2008] Present-day stresses, seismicity and Neogene-to-Recent tectonics af Australia´s "passive" margins: intraplate deformation controlled by plate boundary forces. Geological Society, London, Special Publication, p. 71-89. Geological Society, London.

Jaeger, J. C., Cook, N. G. W. and Zimmerman, R. W. [2007] Fundamentals of Rock Mechanics, 4th edition. Blackwell pp. 488.

Jenkins, C. R., Cook, P. J., Ennis-King, J., Undershultz, J., Boreham, C., Dance, T., de Caritat, P., Etheridge, D. M., Freifeld, B. M., Hortle, A., Kirste, D., Paterson, L., Pevzner, R., Schacht, U., Sharma, S., Stalker, L. and Urosevic, M. [2012] Safe storage and effective monitoring of CO2 in depleted gas fields. *Proceedings of the National Academy of Sciences* 109(2), p. E35-E41.

Johnston, A. C. [1994] Seismotectonic interpretations and conclusions from the stable continental region seismicity database. Electric Power Research Institute (Report TR-102261-1), pp. 4.

Jones, R. M., Boult, P. J., Hillis, R. R. and Mildren, S. [2000] Integrated hydrocarbon seal evaluation in the Penola Trough, Otway Basin. *The APPEA Journal* 40(1-2), p. 194-212.

Judd, W. R. [1964] Rock stress, rock mechanics and research. State of stress in the Earth's crust, p. 5-54. Elsevier, New York.

Kaldi, J., Daniel, R., Tenthorey, E., Michael, L., Schacht, U., Nicol, A., Undershultz, J. and Backé, G. [2011] IEAGHG, Caprock Systems for CO_2 Geological Storage. pp. 149.

Kopsen, E. and Scholefield, T. [1990] Prospectivity of the Otway Supergroup in the central and western Otway Basin. *The APPEA Journal* (30), p. 263–279.

Koutsabeloulis, N. and Zhang, X. [2009] 3D Reservoir Geomechanical Modeling in Oil/Gas field production - SPE 126095. *SPE Saudi Arabia Section Technical Symposium and Exhibition*,Alkhobar, Saudi Arabia, pp. 14.

Krawczyk, C. M., Tanner, D. C., Henk, A., Trappe, H. and Urosevic, M. [2011] Sub-/seismic deformation prediction - Development of a new seismo-mechancal workflow

in the Otway Basin for verification of communication between reservoir and surface. *1st Sustainable Earth Science*,Valencia, pp. 3.

Lavin, C. J. [1997] The Maastrichtian breakup of the Otway Basin margin - a model developed by integrating seismic interpretation, sequence stratigraphy and thermochronological studies. *Exploration Geophysics* 28, p. 252–259.

Lavin, C. J. [1998] Geology and prospectivity of the western Victorian Voluta Trough, Otway Basin, for the 1998 Acreage Release. Department of Natural Resources and Environment (Australia), pp.

Lawrence, M. J. F. [2011] Structural Analysis of Borehole Images from CO2CRC Otway Project Wells CRC-1 and CRC-2. CO2CRC RPT11-2833. pp.40.

Lippmann, A. [2013] Fracture and fault mapping by curvature and coherency analysis. CO2CRC Research Symposium, Hobart, Tasmania, Poster.

Lyon, P. J., Boult, P. J., Watson, M. and Hillis, R. R. [2005] A systematic fault seal evaluation of the Ladbroke Grove and Pyrus traps of the Penola Trough, Oway Basin. *The APPEA Journal* 45, p. 459–476.

Manning, J. C. [1997] Applied principles of hydrology. Prentice Hall, Upper Saddle River, pp. 276.

Marsden, D. [1989] Layer cake depth conversion, Part I. *The Leading Edge* 8(1), p. 10-14.

Marsden, D. [1992] V_0 + k method of depth conversion. *Geophysics: the Leading Edge of Exploration*, p. 53-54.

Mavko, G., Mukerji, T. and Dvorkin, J. [2009] The Rock Physics Handbook: Tools for Seismic Analysis of Porous Media. Cambridge University Press, pp. 522.

Mehin, K. and Constantine, A. E. [1999] Hydrocarbon potential of the western onshore Otway Basin in Victoria: 1999-Acreage Release. Victorian Initiative for Mineralsand Petroleum Report 62. Australian Government - Department of Natural Resources and Environment., pp. 76.

Mildren, S. D., Hillis, R. R., Lyon, P. J., Meyer, J. J., Dewhurst, D. N. and Boult, P. J. [2005] FAST: A new technique for geomechanical assessment of the risk of reactivation-related breach of fault seals. Evaluating Fault and Cap Rock Seals (Boult P. amd Kaldi J.), p. 73-85. The American Association of Petroleum Geologists.

Miyazaki, S., Lavering, I. H., Stephenson, A. E. and Pain, L. [1990] Australia Petroleum Accumulation Report 6 - Otway Basin, South Australia, Victoria and Tasmania. E. a. T. Department of Resources (ed.), pp. 80.

Moeck, I., Kwiatek, G. and Zimmermann, G. [2009] Slip tendency analysis, fault reactivation potential and induced seismicity in a deep geothermal reservoir. *Journal of Structural Geology* 31(10), p. 1174-1182.

Moore, D. H. [2002] Basement-basin relationship in the Otway Basin, Victoria, Australia. Department of Natural Resources and Environment (Australia), pp. 24.

Morris, A., Ferrill, D. A. and henderson, D. B. [1996] Slip tendency analysis and fault reactivation. *Geology* 24(3), p. 275-278.

Müller, R. D., Dyksterhuis, S. and Rey, P. [2012] Australian paleo-stress fields and tectonic reactivation over the past 100 Ma. *Australian Journal of Earth Sciences* 59(1), p. 13-28.

Müller, R. D., Lim, V. S. L. and Isern, A. R. [2000] Late Tertiary tectonic subsidence on the northeast Australian passive margin: response o dynamic topography? *Marine Geology* (162), p. 337–352.

Nelson, E., Hillis, R. R., Sandiford, M., Reynolds, S. and Mildren, S. [2006] Present-day state-of-stress of Southeast Australia. *The APPEA Journal* 46, p. 283–305.

Nelson, E. J. and Hillis, R. R. [2005] In situ stresses of the West Tuna area, Gippsland Basin. *Australian Journal of Earth Sciences* 52(2), p. 299-313.

Norvick, M. and Smith, M. A. [2001] Mapping the plate tectonic reconstructions of southern and southeastern Australia and implications for petroleum system. *The APPEA Journal* 41, p. 15–35.

Nur, A. and Byerlee, J. D. [1971] An exact effective stress law for elastic deformation of rock with fluids. *Journal of Geophysical Research* 76, p. 6414-6419.

Pacala, S. and Socolow, R. [2004] Stabilization wedges: solving the climate problem for the next 50 years with current technologies. *Science* 305, p. 968-972.

Partridge, A. [2001] Revised stratigraphy of the Sherbrook Group, Otway Basin. Eastern Australasian Basins Symposium: a refocussed energy perspective for the future, p. 455-464. Petroleum Exploration Society of Australia.

Pollard, D. D. and Fletcher, R. C. [2005] Fundamentals of Structural Geology. Cambridge University Press, pp. 514.

Ranasinghe, N. [2008] Master thesis - Regulating carbon dioxide capture and storage in Australia. Griffith University, Australia, pp. 96.

Rankin, L. R. [1993] Polda Basin. The Geology of South Australia, volume 1 the Phanerozoic, J. F. Drexel and W. V. Preiss (eds.), p. 202–203. Geological Survey Bullettin.

Reynolds, S. D., Mildren, S. D., Hillis, R. R. and Meyer, J. J. [2006] Constraining stress magnitudes using petroleum exploration data in the Cooper-Eromanga Basins, Australia. *Tectonophysics* 415(1-4), p. 123-140.

Rinaldi, A. P. and Rutqvist, J. [2013] Modeling of deep fracture zone opening and transient ground surface uplift at KB-502 CO_2 injection well, In Salah, Algeria. *International Journal of Greenhouse Gas Control* 12, p. 155-167.

Rockfield. www.rockfield.co.uk.

Roxar. http://www2.emersonprocess.com/en-US/brands/roxar/Pages/Roxar.aspx.

Rudnicki, J. K. [1999] Alteration of regional stress by reservoirs and other inhomogeneities:stabilizing or destabilizing? *9th International Congress in Rock Mechanics*,Paris, France, pp. 9.

Rutqvist, J. [2012] The Geomechanics of CO_2 storage in Deep Sedimentary Formations. *Geotechnical and Geological Engineering* 30, p. 525-551.

Rutqvist, J. and Tsang, C.-F. [2002] A study of caprock hydromechanical changes associated with CO2-injection into a brine formation. *Environmental Geology* 42(2-3), p. 296-305.

Rutqvist, J., Vasco, D. W. and Myer, L. [2010] Coupled reservoir-geomechanical analysis of CO_2 injection and ground deformations at In Salah, Algeria. *International Journal of Greenhouse Gas Control* 4, p. 225-230.

Samier, P., Onaisi, A. and Fontaine, G. [2003] Coupled analysis of geomechanics and fluid flow in reservoir simulation. *SPE Reservoir Simulation Symposium,* Houston, Texas, pp. 16.

Sandiford, M. [2003] Geomorphic constraints on the Late Neogene tectonics of the Otway Range, Victoria. *Australian Journal of Earth Sciences* 50(1), p. 69-80.

Sandiford, M., Wallace, M. W. and Coblentz, D. [2004] Origin of the in situ stress field in southeastern Australia. *Basin Research* (16), p. 325–338.

Santarelli, F. J., Tronvoll, J. T., Svennekjaer, M., Skeie, H., Henriksen, R. and Bratli, R. K. [1998] Reservoir stress path: the depletion and the rebound. *SPE/ISRM Eurock '98*,Trondheim (Norway), pp. 7.

Schlumberger [2009] ECLIPSE Blackoil Reservoir Simulation 2.0. pp. 308.

Schneider, C. L., Hill, K. C. and Hoffman, N. [2004] Compressional growth of the Minerva Anticline, Otway Basin, Southeast Australia-evidence of oblique rifting. *The APPEA Journal* 44, p. 463–480.

Sibson, R. H. [1974] Frictional constraints on thrust, wrench and normal faults. *Nature* 249, p. 542-544.

amagawa, T. and Pollard, D. D. [2008] Fracture permeability created by perturbed stress fields around active faults in a fractured basement reservoir. *AAPG Bulletin* 92(6), p. 743-764.

Tassone, D. R., Holford, S. P., Duddy, I. R., Green, P. F. and Hillis, R. R. [2014] Quantifying Cretaceous-Cenozoic exhumation in the Otway Basin, southeastern Australia, using sonic transit time data: Implication for conventional and unconventional hydrocarbon prospectivity. *AAPG Bullettin* 98(1), p. 67-117.

Teasdale, J., Pryer, L., Stuart-Smith, P., Romine, K., Loutit, T., Etheridge, M., Shi, Z., Foss, C., Vizy, J., Henley, P. and Kyan, D. [2002] Otway & Sorell Basins SEEBASE Project. SRK Consulting, pp. 46.

Tenthorey, E., Dance, T., Cinar, Y., Ennis-King, J. and Strand, J. [2014] Fault modelling and geomechanical integrity associated with the CO2CRC Otway 2C injection experiment. *International Journal of Greenhouse Gas Control* 30, p. 72-85.

Tenthorey, E., Maney, B. and Dewhurst, D. [2011] Description of geomechanical properties for the Paaratte and surrounding formations. CO2CRC RPT11-3124, pp. 26.

Tenthorey, E., Vidal-Gilbert, S., Backé, G., Puspitasari, R., Pallikathekathil, Z. J., Maney, B. and Dewhurst, D. [2013] Modelling the geomechanics of gas storage: a case study from the Iona gas field, Australia. *International Journal of Greenhouse Gas Control* 13, p. 138-148.

Terzaghi, K. [1925] Principles of soil mechanics. Engineering News-Record, pp. 95.

Teufel, L. W., Rhett, D. W. and Farrel, H. E. [1991] Effect of reservoir depletion and pore pressure drawdown on in situ stress and deformation in the Ekofisk Field, North Sea. *32th Symposium on Rock Mechanics (USRMS)*,Norman, Oklaoma, pp. 10.

Thiercelin, M. C. and Roegiers, J.-C. [1989] Formation Characterization: Rock Mechanics. Reservoir stimulation, p. 35. Prentice Hall.

Townend, J. and Zoback, M. D. [2000] How faulting keeps the crust strong. *Geology* 28, p. 399-402.

Towse, D. [1980] A review of the mechanics and occurence of natural fractures in rock as applied to the development of the tight Western gas sands. Lawrence Livermore Laboratory, University of California (UCRL-52908), pp. 32.

Trupp, M. A., Spence, K. W. and Gidding, M. J. [1994] Hydrocarbon prospectivity of the Torquay Sub-Basin, Offshore Victoria. *The APPEA Journal* (34), p. 479–494.

Tupper, N. P., Padley, D., Lovibond, R., Duckett, A. K. and McKirdy, D. M. [1993] A key test of Otway Basin Potential: the Eumeralla-sourced Play on the Charma Terrace. *The APPEA Journal* (33), p. 77–93.

Urosevic, M., Pevzner, R., Shulakova, V., Kepic, A., Caspari, E. and Sharma, S. [2011] Seismic monitoring of CO2 injection into a depleted gas reservoir–Otway Basin Pilot Project, Australia. *Energy Procedia* 4(0), p. 3550-3557.

Van der Pluijm, B. A. and Marshak, S. [2004] Earth structure: an introduction to structural geology and tectonics, 2nd edition. W. W. Norton New York, pp. 672.

van Ruth, P. [2007] CRC-1 Extended Leak-off Test Report. CO2CRC RPT07-0608, pp. 8.

van Ruth, P. and Rogers, C. [2006] Geomechanical analysis of the Naylor structure, Otway Basin Australia. CO2CRC RPT06-0039, pp. 26.

van Ruth, P., Tenthorey, E. and Vidal-Gilbert, S. [2007] Geomechanical Analysis of the Naylor structure, Otway Basin, Australia - Pre-injection. CO2CRC RPT07-0966, pp. 27.

Vasco, D. W., Ferretti, A. and Novali, F. [2008] Reservoir monitoring and characterization using satellite geodetic data: interferometric synthetic aperture radar observation from the Krechba field, Algeria. *Geophysics* 73(6), p. WA113-WA122.

Verdon, J. P., Kendall, J.-M., Stork, A. L., Chadwick, R. A., White, D. J. and Bissell, R. C. [2013] Comparison of geomechanical deformation induced by megatonne-scale CO_2 storage at Sleipner, Weyburn and InSalah *Proceedings of the National Academy of Sciences* 30(110), p. E2762-E2771.

Verdon, J. P., Kendall, J. M., White, D. J. and Angus, D. A. [2011] Linking microseismic event observations with geomechanical models to minimise the risks of storing CO2 in geological formations. *Earth and Planetary Science Letters* 305(1–2), p. 143-152.

Vidal-Gilbert, S. [2008] Reservoir Stress Path and Geomechanical Risking - Part 1. CO2CRC RPT08-1135, pp. 17.

Vidal-Gilbert, S., Tenthorey, E., Dewhurst, D., Ennis-King, J., Van Ruth, P. and Hillis, R. [2010] Geomechanical analysis of the Naylor Field, Otway Basin, Australia: Implications for CO2 injection and storage. *International Journal of Greenhouse Gas Control* 4(5), p. 827-839.

Von der Borch, C. C., Conolly, J. R. and Dietz, R. S. [1970] Sedimentation and Structure of Continental Margin in Vicinity of Otway-Basin, Southern Australia. *Marine Geology* 8(1), p. 59-83.

Wang, Z. and Nur, A. [2000] Seismic and acoustic velocities in reservoir rocks. Society of Exploration Geophysicists, Tulsa, Oklaoma, USA, pp. 633.

Williamson, P. E., Swift, M. G., O'Brien, G. W. and Falvey, D. A. [1990] Two-Stage Early Cretaceous Rifting of the Otway Basin Margin of Southeastern Australia - Implications for Rifting of the Australian Southern Margin. *Geology* 18(1), p. 75-78.

Yale, D. P. [2003] Fault and stress magnitude controls on variations in the orientation of in situ stress. *Geological Society, London, Special Publications* 209(1), p. 55-64.

Yeow, L., Johar, Z., Wu, B., Tan, C. and Yaakub, M. [2004] Sand production prediction study using empirical and laboratory approach for a multi-field gas development. *SPE Asia Pacific Conference on Integrated modelling for Asset Management,* Kuala Lumpur - Malaysia, pp. 14.

Yu, S. M. [1988] Structure and development of the Otway Basin. *The APEA Journal* 28(1), p. 243-253.

Zhang, X., Koutsabeloulis, N., Kristiansen, T., Heffer, K., Main, I., Greenhough, J. and Hussein, A. [2011] Modelling of depletion-induced microseismic events by coupled reservoir simulation: application to Valhall field - SPE 143378. *SPE EUROPEC/EAGE Annual Conference and Exhibition,* Vienna - Austria, pp. 16.

Ziesch, J., Aruffo, C. M., Tanner, D. C., Beilecke, T., Dance, T., Henk, A., Weber, B., Tenthorey, E., Lippmann, A. and Krawczyk, C. M. [subm.] Geological structure of the CO2CRC Otway Project site, Australia: fault kinematics based on quantitative 3D seismic interpretation. *Basin Research* in review, p. 25.

Zoback, M. D. [2010] Reservoir geomechanics. Cambridge University Press, Cambridge, pp. 449.

Zoback, M. D., Barton, C. A., Brudy, M., Castillo, D. A., Finkbeiner, T., Grollimund, B. R., Moos, D. B., Peska, P., Ward, C. D. and Wiprut, D. J. [2003] Determination of stress orientation and magnitude in deep wells. *International Journal of Rock Mechanics and Mining Sciences* 40(7-8), p. 1049-1076.

Zoback, M. D., Day-Lewis, A. D. F. and Kim, S. [2008] Predicting changes in hydrofrac orientation in depleting oil and gas reservoirs. Google Patents.

Zoback, M. D. and Gorelick, S. M. [2012] Earthquake triggering and large-scale geologic storage of carbon dioxide. *Proceedings of the National Academy of Sciences* 109(26), p. 10164-10168.

Zoback, M. L. [1992] First- and Second-Order Patterns of Stress in the Lithosphere: The World Stress Map Project. *Journal of Geophysical Research* 97(B8), p. 11703-11728.

15 Appendix

The appendix to this thesis is provided on the attached DVD. The following files are included:

Dissertation in PFD format

3D PDF of the Geological model

Plots of the following results of the geomechanical models:

Steady-state models (Present-day and paleostress models):

- Magnitude of the three total principal stress
- Orientation of the maximum horizontal stress
- Magnitude of mean stress and differential stress
- Differential Horizontal Stress Ratio
- Normal stress and shear stress acting on faults
- Slip Tendency and Dilation Tendency

One-way coupled model:

Magnitude of horizontal total stresses

- Magnitude of horizontal effective stresses
  - Pre- and post- production
  - Pre-a and post-injection
- Magnitude of mean effective stress
  - Pre- and post- production
  - Pre-a and post-injection

Statement of Authorship

I hereby certify that this thesis has been composed by myself and describes my own work unless otherwise acknowledged in the text. All references and verbatim extracts have been quoted and all sources of information have been specifically acknowledged. This thesis has not been accepted in any previous application for a degree.

Hiermit versichere ich, dass ich die vorliegende Arbeit selbstständig und ohne Benutzung anderer als der angegebenen Hilfsmittel angefertigt habe. Stellen, die wörtlich oder sinngemäß aus anderen Schriften entnommen sind, sind als solche kenntlich gemacht. Die Arbeit ist in gleicher oder ähnlicher Form noch nicht als Prüfungsarbeit eingereicht worden.

Darmstadt,_____Signature _____

Curriculum vitae

Work experience

July 2013 - September 2013

Schlumberger, Geomechanics Centre of Excellence. Bracknell,UK

Internship

September 2011 - November 2011

Roma Tre University for Petrobras

Consultant

Education

March 2012 - February 2015

TU Darmstadt

PhD student – Engineering Geology

February 2009 - May 2011

Roma Tre University

M.Sc. Field and Resources Geology (Petroleum Geology)

110/110 cum laude

January 2010 - June 2010

University of Leeds

Erasmus student - M.Sc. Exploration Geophysics

September 2005 - February 2009

Roma Tre University

B.Sc. Geological Sciences

109/110

Software skills

OS Windows and Mac, MS Office

Petrel, PetrelRG (Visage), PetrelRE (Eclipse), Kingdom Suite, Ansys, Adobe Illustrator

Memberships

AAPG, EAGE, SPE